JANUARY-MARCH 2023 VOL. 15 № 1 (56)

ISSN 2075-8251

ActaNaturae

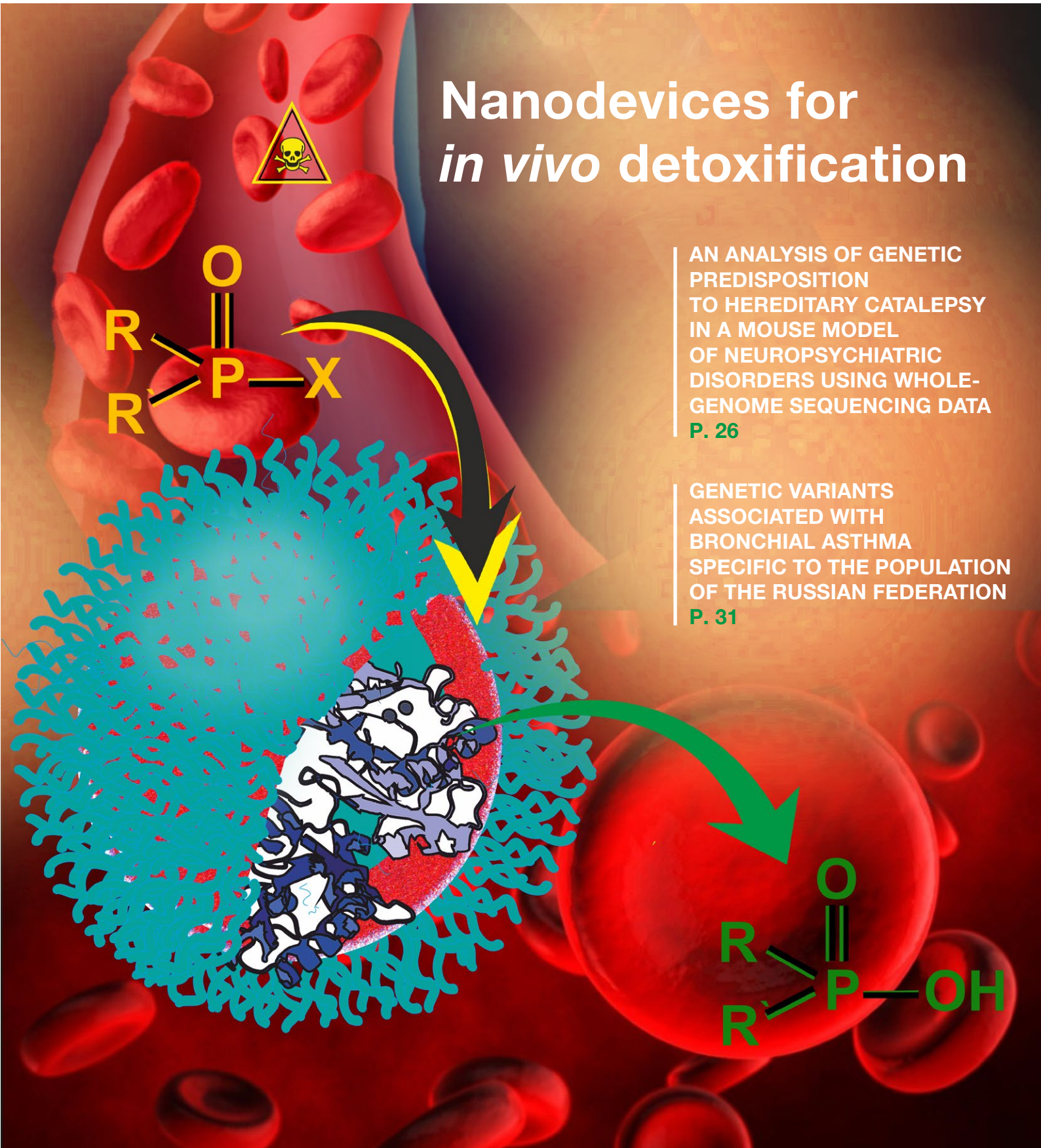

Creation of Recombinant Biocontrol Agents by Genetic Programming of Yeast

S. O. Pipiya, N. Z. Mirzoeva, M. N. Baranova, I. E. Eliseev, Yu. A. Mokrushina, O. V. Shamova, A. G. Gabibov, I. V. Smirnov, S. S. Terekhov

Antibiotics based on antimicrobial peptides (AMPs) are of particular interest due to their genetically encoded nature. Recombinant technologies enable the creation of genetically programmable AMP producers for large-scale generation of recombinant AMPs (rAMPs) or the creation of rAMP-producing biocontrol agents. The methylotrophic yeast *Pichia pastoris* was genetically modified for the secreted production of rAMP. Constitutive expression of the sequence encoding the mature AMP protegrin-1 provided the yeast strain that effectively inhibits the growth of target gram-positive and gram-negative bacteria. The heterologous production of rAMPs opens up new avenues for creating effective biocontrol agents and screening antimicrobial activity using ultrahigh-throughput technologies.

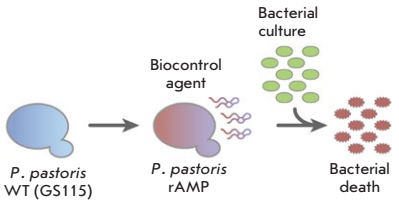

Schematic representation of the genetic programming of *P. pastoris* yeast strains and the creation of a recombinant biocontrol agent

Evaluation of the Effectiveness of Various Autophagy Inhibitors in A549 Cancer Stem Cells

K. V. Aleksandrova, I. I. Suvorova

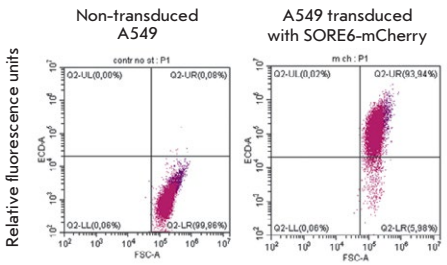

The effect of autophagy inhibitors on Sox2 and Oct4 expression in A549 cancer cells

In the present work, authors selected a panel of autophagy inhibitors (Autophinib, SBI-0206965, Siramesine, MRT68921, and IITZ-01), some of which have been recently identified as effective autophagy inhibitors in cancer cells. Using A549 cancer cells, which express the core stem factors Oct4 and Sox2, authors evaluated the effect of these drugs on the survival and preservation of the original properties of cancer stem cells. Among the agents selected, only Autophinib demonstrated a significant toxic effect on cancer stem cells. The obtained results demonstrate that autophagy inhibition by Autophinib downregulates the expression of the Sox2 protein in A549 cells, and that this downregulation correlates with a pronounced induction of apoptosis. Moreover, Autophinib-treated A549 cells are unable to form spheroids, which indicates a reduction in stemness. Thus, among the drugs studied, only Autophinib can be considered a potential agent against cancer stem cells.

Distortion of Population Statistics due to the Use of Different Methodological Approaches to the Construction of Genomic DNA Libraries

F. S. Sharko, K. V. Zhur, V. A. Trifonov, E. B. Prokhortchouk

In this paper, authors compare the results of a sequencing of the aDNA libraries of a Bronze Age sample from the Caucasian burial ground Klady, prepared using three different approaches: (1) shotgun sequencing, (2) strategies for selecting target genomic regions, and (3) strategies for selecting target genomic regions, including DNA pre-treatment with a mixture of uracil-DNA glycosylase (UDG) and endonuclease VIII. The impact of the studied approaches to genomic library preparation on the results of a secondary analysis of the statistical data, namely F4 statistics, ADMIXTURE, and principal component analysis (PCA), was analyzed. It was shown that preparation of genomic libraries without the use of UDG can result in distorted statistical data due to postmortem chemical modifications of the aDNA. This distortion can be alleviated by analyzing only the single nucleotide polymorphisms caused by transversions in the genome.

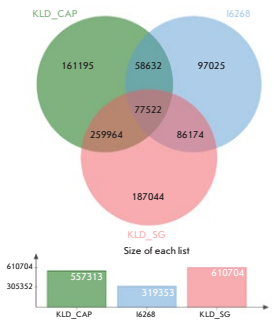

Venn diagrams for the SNPs of the three libraries KLD_CAP, KLD_SG, and I6268

ActaNaturae
JANUARY–MARCH 2023 VOL. 15 № 1 (56)
since april 2009, 4 times a year

Founders
Acta Naturae, Ltd,
National Research University
Higher School of Economics

Adress: 101000, Moscow, Myasnitskaya Ulitsa, 13, str. 4
Phone/Fax: +7 (495) 727 38 60
E-mail: actanaturae@gmail.com

Номер подписан в печать 30 марта 2023 г.
Тираж 15 экз. Цена свободная.
Отпечатано в типографии: НИУ ВШЭ,
г. Москва, Измайловское шоссе, 44, стр. 2

Founder and Chairman
of the Editorial Board (from 2009 to 2023)
of the journal Acta Naturae
Academician Grigoriev Anatoly Ivanovich

Indexed in PubMed, Web of Science, Scopus, and RISC

Impact Factor: 2.204

CONTENTS

REVIEWS

RESEARCH ARTICLES

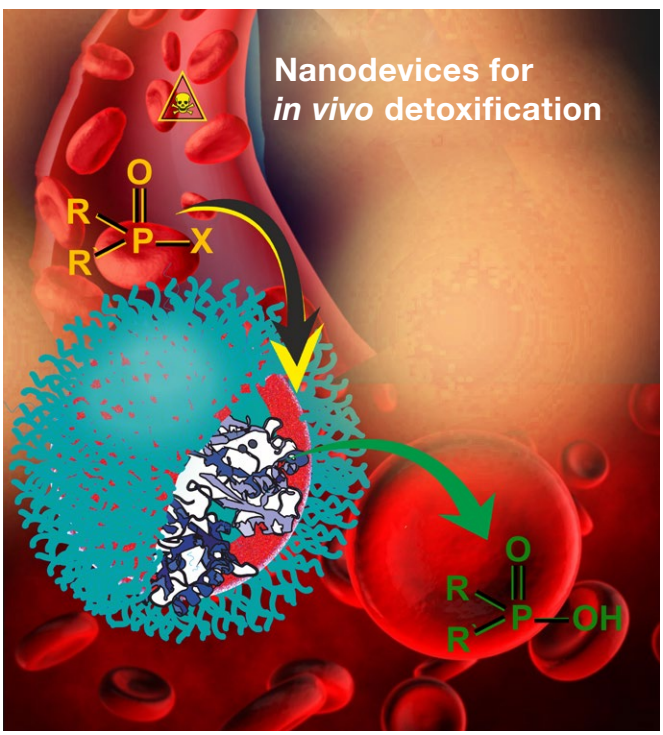

IMAGE ON THE COVER PAGE
(see the article by Pashirova et al.)

Biomedical Nanosystems for *In Vivo* Detoxification: From Passive Delivery Systems to Functional Nanodevices and Nanorobots

T. N. Pashirova[1*], Z. M. Shaihutdinova[1,2], V. F. Mironov[1], P. Masson[2]
[1]Arbuzov Institute of Organic and Physical Chemistry, FRC Kazan Scientific Center of RAS, Kazan, 420088 Russian Federation
[2]Kazan (Volga Region) Federal University, Kazan, 420008 Russian Federation
[*]E-mail: tatyana_pashirova@mail.ru
Received February 15, 2023; in final form, March 21, 2023
DOI: 10.32607/actanaturae.15681

ABSTRACT **The problem of low efficiency of nanotherapeutic drugs challenges the creation of new alternative biomedical nanosystems known as robotic nanodevices. In addition to encapsulating properties, nanodevices can perform different biomedical functions, such as precision surgery, *in vivo* detection and imaging, biosensing, targeted delivery, and, more recently, detoxification of endogenous and xenobiotic compounds. Nanodevices for detoxification are aimed at removing toxic molecules from biological tissues, using a chemical- and/or enzyme-containing nanocarrier for the toxicant to diffuse inside the nanobody. This strategy is opposite to drug delivery systems that focus on encapsulating drugs and releasing them under the influence of external factors. The review describes various kinds of nanodevices intended for detoxification that differ by the type of poisoning treatment they provide, as well as the type of materials and toxicants. The final part of the review is devoted to enzyme nanosystems, an emerging area of research that provides fast and effective neutralization of toxins *in vivo*.**
KEYWORDS **detoxification, nanodevices, delivery systems, enzyme.**
ABBREVIATIONS **LE – lipid emulsions; RM-PL – erythroliposome; LSPD – peritoneal dialysis with liposomes; OP – organophosphorus compounds; E – enzyme; T – toxicant.**

INTRODUCTION

For a long time, human disease prevention and treatment had mostly been based on the administration of chemical or biological drugs. Since the discovery of first liposomal systems in 1964, the current nanomedicine strategy has focused on encapsulating and stabilising small molecule drugs or macromolecules in various types of nanocarriers to overcome biological barriers, increase bioavailability, reduce unwanted toxicity to healthy tissues, and target delivery [1, 2]. Despite the fact that a number of nanotherapeutic drugs have already been approved for clinical uses and/or are undergoing clinical studies [3, 4], nanomedicine still faces low efficiency in many for example, only 0.7% of cytotoxic drugs encapsulated into nanocarriers reach solid tumors [5]. Since 2008, there has been a significant increase in publications describing the production of new-generation nanotherapeutic drugs called "smart nanocarriers" that have been modified with various ligands to provide targeted delivery and sensitivity to various stimuli [6, 7].

Today, there is a demand for alternative biomedical systems such as robotic nanodevices. Unlike traditional passive nanotherapeutic drugs, these robotic nanodevices perform various biomedical functions, including precision surgery, biosensing, *in vivo* detection and imaging, targeted drug delivery, and, recently, detoxification [8, 9]. For a long time, nanorobotics remained a fantasy. The concept of microscopic mechanical surgeons moving through a blood vessel was first put forward in 1959 by Richard Feynman, a Nobel Prize winner in physics. Shortly after, in 1966, the concept of "surgeon" was introduced in the science fiction film *Fantastic Voyage*. In the film, a miniature submarine was used to remove a clot from a blood vessel. Over the past few decades, science fiction has

become a reality. Nanodevices of various shapes and sizes have been developed using different types of materials, technologies, and control methods. They are often referred to as micro/nanomotors [10], micro/nano swimmers [11], micro/nano machines [12], micro/nano pumps [13], micro/nano rockets [14], etc [15].

There are many definitions for nanodevices. Nanomachines are nanoscale mechanical devices able to transform energy into precise mechanical motion [16]. Micro/nano biomedical devices often characterize structures that can be controlled and propelled within a living organism through chemical or bio-hybrid sources [17]. They are tiny nanomaterial-based integrated structures engineered in a way so that they can move autonomously and perform programmed tasks efficiently even at hard-to-reach organ/tissues/cellular sites [18]. In summary, robotic nanodevices are next-generation tools propelled and/or guided by endogenous and exogenous stimuli for targeted and personalized therapeutic applications. However, their use for practical clinical applications is still in its infancy [19]. For the development and successful applications and clinical use of biomedical therapeutic nanodevices, the following key factors must be considered:

- biocompatibility with the patient's body;
- ability to load/release drugs, imaging agents, etc.;
- motion control and tracking in real time using medical imaging techniques;
- controlled degradation without any toxic metabolite formation in the patient's body.

The nomenclature of micro/nanodevices is based on their design, geometry, mechanism of motion and rotation. As a rule, their self-propulsion is provided by:

a) The conversion of chemical and enzymatic [20, 21] reactions into mechanical actions [22]. Such nanodevices move in a certain direction using the energy of enzymatic or various chemical reactions [23, 24]; e.g., i) nanodevices moved by gas-bubble formation (hydrogen, oxygen, etc.); ii) self-electrophoresis-propelled nanodevices operating on the principle of redox potential difference; iii) self-diffusion nanodevices moving thanks to a concentration gradient;

b) The influence of external stimuli (magnetic, acoustic, light field); i.e., they are stimulus-sensitive nanodevices [25];

c) Biological/biohybrid nanodevices, whose movement is generated by microorganisms and cellular components such as cilia, flagella, etc [26–29].

More recently, biomedical nanosystems designed for detoxification/neutralization have started to be explored. They are able to capture toxic molecules and reduce their concentration in an organism thanks to their large surface area and high affinity for active ingredients. Such systems have been designed to treat tumor and inflammatory diseases [30–32], drug overdoses [33], xenobiotic detoxification, including industrial toxicants and chemical warfare agents, etc. Typically, drug delivery systems aim at encapsulating therapeutic agents and release them in target tissues under external stimuli control. A completely opposite approach is assumed for detoxification nanodevices. These nanocarriers ensure the removal of drugs and xenobiotics from biological tissues [34]. This review provides the proof of concept and potential applications of micro/nanodevices for detoxification.

TYPES OF NANODEVICES FOR DETOXIFICATION IN MEDICINE

Based on the general principles of therapy, detoxification is administered using:

a) antidote therapy or toxic-compound neutralization;

b) accelerated toxin elimination (hemodialysis, peritoneal dialysis, and hemosorption); and

c) symptomatic therapy; i.e., restoration of impaired functions.

Nanosystems as nonspecific antidotes

At present, the so-called antidotes, compounds and formulations capable of preventing or reducing the side effects of an overdose of drugs, are in demand. Nonspecific antidotes such as lipid emulsions, liposomes, and nanosponges are effectively capable of capturing drug molecules through nonspecific interactions (hydrogen bonds, hydrophobic effect, electrostatic interactions). Thus, non-specific antidotes have a broad spectrum of action for detoxification and drug overdose treatment.

Nanoemulsions. Lipid emulsion resuscitation therapy is recommended for the treatment of lipophilic drug overdoses; specifically, lipid emulsions (LE) are administered intravenously as non-specific antidotes, in the form of an "oil-in-water" type of drops [35]. LEs have been used for overdose treatment and to reduce the concentration of lipophilic antiarrhythmic, psychotropic, antimalarial drugs, local anesthetics, calcium channel blockers such as propranolol [36], cocaine [37, 38], diltiazem [39], buprenorphine, fentanyl and butorphanol [40], bupivacaine [41], ivermectin [42, 43], and ropivacaine [44, 45]. LEs rapidly decrease the threshold for seizure activity, amoxapine toxicity [46], and improve cardiac activity during heart transplantation [47]. They are also administered in cases of acute poisoning with neurotoxic organophosphorus compounds [48]. In a recent case, active toxic molecules have been

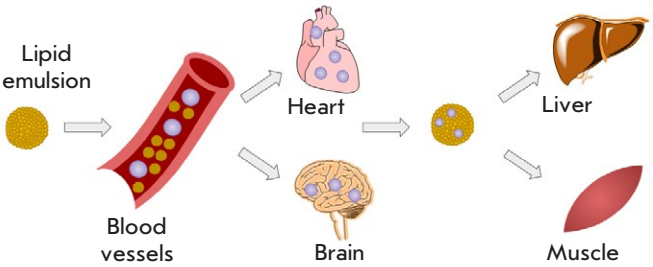

Fig. 1. LE action mechanism in human body: the toxins are captured by lipid emulsion in high-perfusion organs, such as the heart and brain, to be transported to the liver and muscles for further redistribution. Adapted from [49]

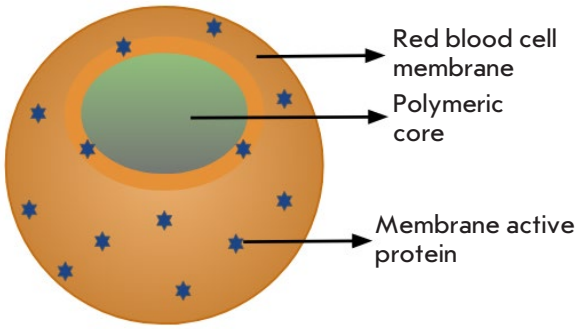

Fig. 2. Nanosponge structure that consists of a polymer-covered core with an erythrocyte membrane shell. Redrawn and modified from [55]

removed from biological tissues using a lipophilic amine nanocarrier that is able to react with the toxin (cargo-aldehyde) inside the LEs, forming a lipophilic imine conjugate in the oil core. Successful elimination of highly toxic aliphatic aldehyde 4-hydroxynonenal from living cells is evidence in favor of the concept of living cells detoxification [34].

LE action mechanism in human body is shown in *Fig. 1*. The emulsion captures highly lipid-soluble drugs from highly perfused organs such as the heart, brain, and kidneys and then transports them to the liver and muscles, contributing to enhanced toxins redistribution.

Recently, a dynamic multimodal LE action mechanism has been introduced. In this case, LEs capture not only toxins/drugs, but also change their pharmacokinetic profiles, exhibit a post-conditioning effect along with cardiotonic and vasoconstrictive properties, have a positive inotropic effect, reduce the release of nitric oxide, weaken mitochondrial dysfunction, phosphorylation of kinase-3β-glycogen synthase, etc. [50]. The effect of LE on the pharmacokinetic characteristics of drugs could be a guide for their clinical applications [33]. Despite the fact that LEs relieve a wide range of lipophilic drug intoxications, nevertheless, their optimal dosage, duration of administration, treatment initiation and administration have not been determined yet [51].

Nanocapsules. For the purpose of detoxification, nanocapsules (oil core/silica shell) have been synthesized [52]. The authors of [52] found that nanocapsules of smaller diameter absorbe toxins more efficiently than larger nanocapsules. The distribution of drug/toxin in nanocapsules is proportional to the area of interfacial surface and does not depend on the concentration of oil phase. In addition, the drug distribution decreases when the thickness of shell increases, since there is a decrease of drug penetration into the nanocapsules with a thicker shell [52]. For the treatment of alcohol intoxication, nanocapsules imitating hepatocyte detoxifying functions were developed to deliver enzymes (alcohol oxidase, catalase, and aldehyde dehydrogenase) to the liver. Alcohol oxidase and catalase contributed to the rapid removal of alcohol. The resulting acetaldehyde was effectively oxidized by aldehyde dehydrogenase. Administration of the developed antidote to mice suffering alcoholic intoxication provided a significant decrease alcohol concentration in the bloodstream without acetaldehyde accumulation [53].

Nanosponges. Nanosponges are a naturally degradable 3D scaffold formed in solution by crosslinkers. [54]. For the first time, nanosponges covered by a natural cell membrane and functioning through biomimicry were proposed by Zhang L. in [55]. "The nanosponge acts as a toxin bait *in vivo* and is a new way to remove toxins from the bloodstream", Zhang L said. "Instead of building specific products to treat individual toxins, we are developing a platform that can neutralize the toxins produced by a wide range of pathogens". The nanosponges developed by Zhang L and colleagues consist of poly(lactic-co-glycolic acid) polymer core (PLGA) and an outer shell of red blood cell membrane that attract toxins like a bait (*Fig. 2*).

In tests on mice, prophylactic administration of nanosponges reduced mortality down to 11%, compared to 100% mortality without treatment. With nanosponges, mortality in mice dropped to 56% after toxin injection. Suggestively, the nanosponges containing the isolated toxin accumulated in the liver, where, in the absence of any damage, the toxin was safely metabolized and eliminated from the body [55, 56].

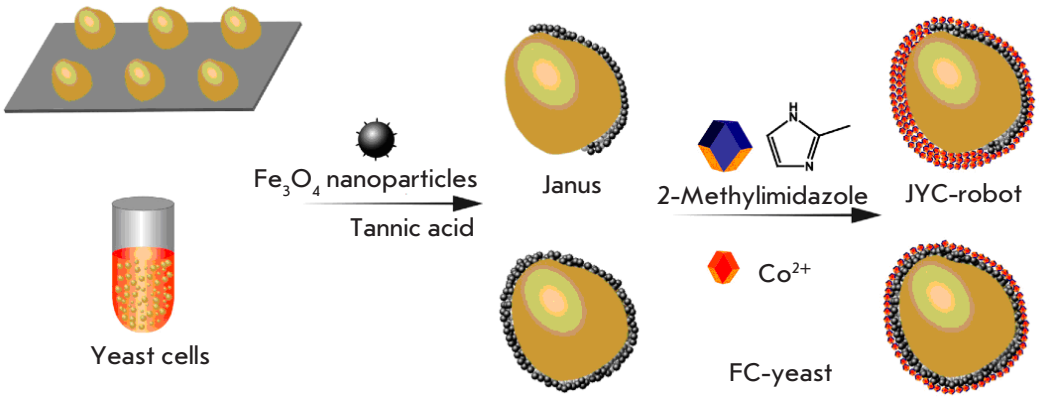

Fig. 3. Designing biomimetic hybrid systems for the neutralization of mycotoxins. Adapted from [73]

Nanosponges were effectively used for detoxification of bacterial toxins [57, 58]. They were able to bind and neutralize low-molecular-weight compounds [59], autoimmune antibodies [60], inflammatory cytokines [61], bacteria and viruses [62, 63], and neurotoxins (tetrodotoxin, botulinum toxin, and saxitoxin) [64]. Nanosponges for the neutralization of neurotoxins consist of a polymer core covered by a membrane of neurons; namely, neuro-2a cells. The use of this mouse neural crest-derived cell line increased the mice's survival rate in the absence of acute toxicity [64]. Two-modal detoxification with nanosponges that possess an oil core and are coated with an erythrocyte membrane (Oil-NS) was more effective [65]. This Oil-NS construction combines the specific binding capacity of biological receptors on the cell membrane with the non-specific absorption of oil core. Together, they increase the overall detoxification capacity.

A nanosponge-gel hybrid system also neutralizes toxins. Its use for both therapeutic and prophylactic purposes has led to a significant improvement in the treatment of toxin-related skin damage [66]. A subject for further study is a biomimetic detoxification strategy based on the creation of nanoparticles coated with a platelet membrane. Such systems can be promising as additional therapy for patients with a methicillin-resistant *Staphylococcus aureus* infection [67].

Erythroliposomes. Erythroliposomes (RM-PL) are a biomimetic platform consisting of artificial lipid membranes and natural erythrocyte membranes. Such systems have been successfully used to neutralize various hemolytic pore-forming toxins [68]. The toxins absorbed by RM-PL are transferred to the liver and spleen, where they undergo endocytosis and are digested by macrophages. In mice, administration of RM-PL eliminates initial toxicity in target organs, allowing the animals to survive.

Biomimetic hybrid systems. Janus micromotors are magnesium and gold particles coated with a red blood cell membrane (RBC-Mg) that acts as a bait and absorbs and neutralizes biological toxins in water and biological media. RBC-Mg nanomotors have been used to rapidly detoxify α-toxin and methylparaoxon, models of membrane-damaging toxins and chemical warfare agents, respectively [69, 70]. Hybrid biomembrane nanorobots with an acoustic drive and a membrane consisting of two types of cells (erythrocytes and platelets) effectively bind to both toxins and pathogens in the blood. To eliminate simultaneously pathogenic bacteria and toxins the proteins located in the hybrid membrane are used. They bind to pathogens and neutralize pore-forming toxins [71, 72]. There are examples [73] of microrobots with Fe_3O_4 nanoparticles covering yeast cells and creating a zeolite imidazolate framework-67 (ZIF-67) to neutralize mycotoxins (*Fig. 3*).

Nanodialysis systems for improved detoxification

Liposomes. Designing liposomal dialysates is an emerging area of research. Liposomes without drugs, "empty liposomes", were used as scavengers for exogenous and endogenous toxic molecules. Some of these studies have reached clinical trials. It is quite possible that liposomes will be medically used as nanoantidotes in the next decade [74]. The introduction of "empty" liposomes contributes to reservoir formation for toxin binding. Liposomes bind toxins through electrostatic interactions and a hydrophobic effect in the membrane or through ion trapping into the hydrophilic core. Non-ionized molecules penetrate the liposome membrane. They are captured by a hydrophilic, pH-controlled core of liposomes. For example, a weakly basic drug molecule, upon entering a hydrophilic core with an acidic pH value can be ionized and

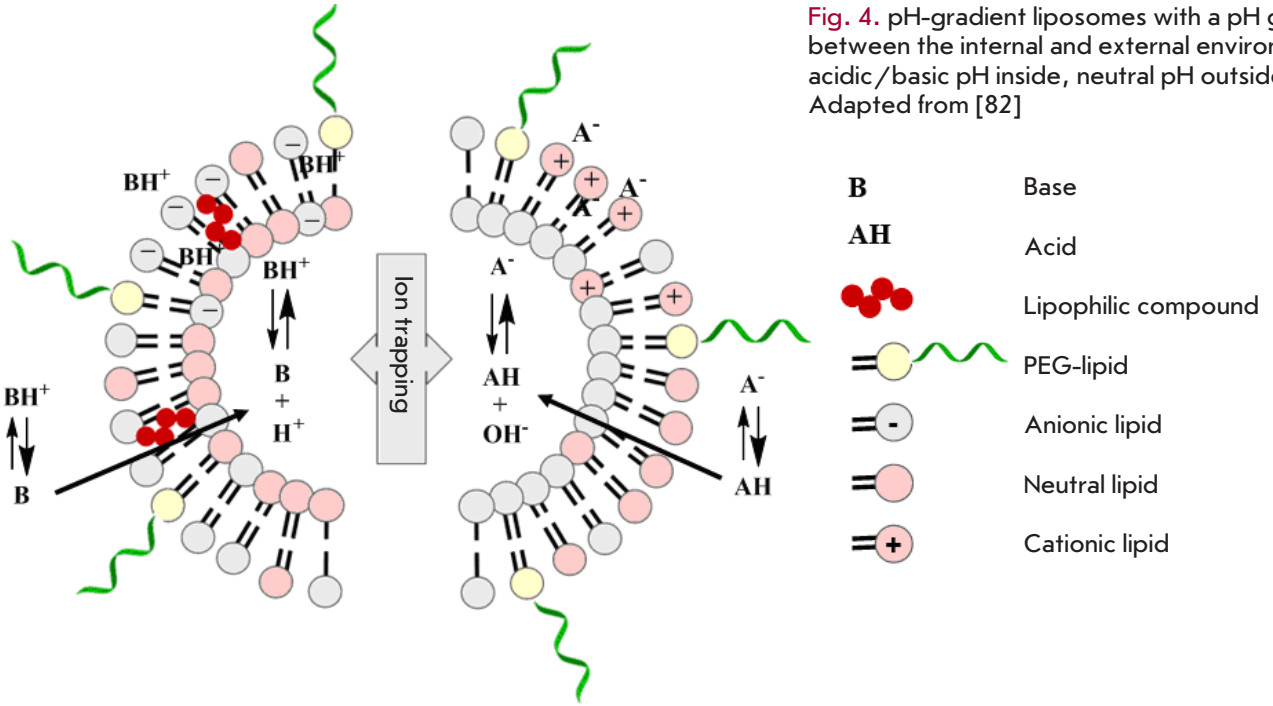

Fig. 4. pH-gradient liposomes with a pH gradient between the internal and external environments: acidic/basic pH inside, neutral pH outside. Adapted from [82]

lose its ability to diffuse through the lipid bilayer of liposome membrane (*Fig. 4*).

For the first time, a hemodialysis method including liposomes and antioxidants has been presented as a unique strategy for removing toxins. Its application *in vitro* resulted in a further noticeable decrease in the amount of oxidation products and removal of platelets and bilirubin when compared to conventional hemodialysis [75]. *In vivo* experiments in rats suffering from uremia confirmed that the addition of liposomes to the dialysate as an adjunct to conventional hemodialysis facilitated the removal of protein-bound uremic solutes. The developed nanosystem has unique advantages in comparison with albumin and other alternatives that use sorbents [76]. Modified by linoleic acid [77] and decorated with polyethyleneimine, liposomes demonstrated significantly higher binding rates and rapid clearance of protein-bound uremic toxins [78]. Preclinical evaluation of transmembrane liposomes with a pH gradient for the ammonia concentration confirmed the ability of liposome-supported peritoneal dialysis (LSPD) to reduce plasma ammonia levels in pigs with artificially induced hyperammonemia [79]. LSPD, in particular its peritoneal dialysate, enriched with pH-gradient liposomes, i.e., with a pH gradient between the internal and external environments of liposomes (acid inside, neutral outside), alleviated the symptoms of poisoning in animal models in [80, 81]. An apparent increase in the concentrations of haloperidol, verapamil, and amitriptyline in the dialysate using LSPD was observed in rats compared to a peritoneal dialysate without augmentation [80, 81]. LSPD was used to remove toxins/highly plasma protein bound drugs. Amitriptyline was chosen as a drug that highly binds to plasma proteins. It was shown that LSPD increases amitriptyline extraction *in vivo* in [82].

Polyethylene glycol-modified liposomes encapsulated with phosphate-binding iron (III) citrate trap the circulating phosphate ions into the inner liposomal core. These traps reduce the concentration of free phosphate ions in solution and in serum [83] (*Table 1*).

ENZYME NANODEVICES FOR DETOXIFICATION

A detailed description of nanoparticles with encapsulated enzymes is present in our recently published review [85], where nanoparticle types, materials, results of clinical studies, etc., were considered. Therefore, in this part of this review, we want to focus on such systems as enzymatic nanodevices for neutralizing toxins. Enzyme encapsulation in nanocarriers opens up possibilities for the creation of nanoreactors, nanodevices that contain the molecules needed to support anomalous diffusion and abide by kinetic laws. Such systems are capable of performing single or cascade reactions either for biosynthesis or for degradation of toxic substrates [86]. Nanobiotechnology of enzyme nanoreactors is a new, rapidly developing area of research. For example, recently, alcohol oxidase and catalase enzymes-containing liposomes supporting peritoneal

Table 1. Types of detoxification nanodevices, materials and enzyme/drug library

Nanodevices	Material	Neutralization	*In vivo* model	Ref.
LE	Lipoamine	Cargo-aldehyde	-	[34]
	Intralipid	Propranolol	White rabbits	[36]
	Intralipid	Cocaine	Clinical trial	[37]
	Intralipid	Cocaine	Dog	[38]
	Intralipid	Diltiazem	Clinical trial	[39]
	Intralipid	Buprenorphine, fentanyl, butorphanol	-	[40]
	Intralipid	Bupivacaine	Pigs	[41]
	Intralipid	Ivermectin	Pogona vitticeps	[42]
	Intralipid	Ropivacaine	Pigs	[44]
	Intralipid	Sevoflurane, isoflurane	Rats	[45]
	Intralipid	Amoxapine	Clinical trial	[46]
	Intralipid	Organophosphates	Clinical trial	[48]
Nanocapsules	Tetramethoxysiloxane, octadecyltrimethoxysilane, ethyl-butyrate, lecithin, Tween-80	Quinoline	-	[52]
	Acrylamide, APm, N,N'–methylenebisacrylamide, enzymes (Alcohol oxidase, Catalase, Aldehyde dehydrogenase)	Ethanol	C57BL/6 mice	[53]
Nanosponges	RBC membrane, PLGA	Bacterial toxins (melittin, α-hemolysin, listeriolysin O, streptolysin O)	-	[57]
	RBC membrane, PLGA	Bacterial toxins	CD-1 mice	[58]
	RBC membrane, PLGA	Bichlorvos	CD-1 mice	[59]
	RBC membrane, PLGA	Autoantibodies	CD-1 mice	[60]
	Peripheral blood neutrophils membrane, PGLA	Proinflammatory cytokines	ICR mice	[61]
	Bacterial membrane, PLGA	Bacteria	C57BL/6 mice	[62]
	Lung epithelial cells membrane/macrophage membrane, PLGA	SARS-CoV-2	C57BL/6NHsd mice	[63]
	Neuro-2a cells membrane, PLGA	Tetrodotoxin	ICR mice	[64]
	RBC membrane, olive oil	Organophosphates (paraoxon, diisopropyl fluorophosphate, dichlorvos)	ICR mice	[65]
	RBC membrane, PLGA, Pluronic F127	Pore-forming toxins	ICR mice	[66]
	Platelet membrane, PLGA	S. aureus	CD-1 mice	[67]
Erythroliposomes	RBC membrane, cholesterol, phosphatidylcholine, mPEG-DSPE EPC,	Pore-forming toxins	ICR mice	[68]
Janus micromotors	RBC membrane, Mg, Au, chitosan	α-toxin	-	[69]
	RBC membrane, Au, citric acid	Melittin	-	[70]
Hybrid biomembrane nanorobots	RBC membrane, Au	Pore-forming toxins	-	[71]
	RBC and platelet membrane, Au	Pore-forming toxins	-	[72]
Janus microrobots	Yeast cell membrane, Fe_3O_4, 2-methylimidazole	Mycotoxins	-	[73]
Liposomes	Lecithin, cholesterol, deoxysodium cholate	Protein-bound uremic toxins	Sprague Dawley rats	[76]
	Lecithin, cholesterol, linoleic acid, Tween-80	Protein-bound uremic toxins	-	[77]
	Lecithin, cholesterol, linoleic acid, polyethylenimine, Tween-80	Protein bound uremic toxins	-	[78]
LSPD	DPPC, cholesterol, mPEG-DSPE, citric acid	Ammonia	Göttingen minipig	[79]
	DPPC, cholesterol, DSPE-mPEG	Ammonia	Sprague Dawley rats	[80]
	DPPC, cholesterol, DSPE-mPEG	Amitriptyline	Sprague Dawley rats	[81]
	DOPG, cholesterol	Amitriptyline	Sprague Dawley rats	[82]
	Phosphatidylcholine, cholesterol, DSPE-mPEG, iron citrate	Phosphate ions	-	[83]
	DOPE-NHS, β-octylglucoside, enzymes (Alcohol oxidase, Catalase)	Ethanol	Sprague Dawley rats	[84]

dialysis have been investigated. In this nanoreactor, H_2O_2 addition accelerates ethanol removal for H_2O_2 to be rapidly decomposed into O_2 by the catalase, while enzymatic liposomes enhance ethanol metabolism. In a model of rodent intoxication with ethanol, enzyme liposomes enhanced ethanol metabolism, as was evidenced by increased production of acetaldehyde, the main metabolite of ethanol [84].

In our laboratory, we focus on the design and development of injectable therapeutic enzyme nanoreactors for the neutralization of toxicants like organophosphorous (OP) pesticides [87]. Enzymes capable of detoxifying OPs can be used as bioscavengers. They act either as stoichiometric, pseudocatalytic or catalytic traps for OP molecules [88, 89]. These enzymes, phosphotriesterases and cholinesterases, are the active components of these therapeutic nanodevices. Encapsulation of bioscavengers in such vehicles is first intended to overcome the fast clearance and immune response after injection of soluble heterologous therapeutic enzymes. The aim of enzyme encapsulation into nanoreactors is also to provide a high concentration of reactive enzyme in stable nanocontainers. Determining the concentration of the encapsulated enzyme inside nanocarriers is an important step in designing an efficient *in vivo* nanoreactor. In presence of an injectable nanoreactor, the toxicant present in the bloodstream diffuses across the nanoreactor's membrane, and the enzyme-mediated detoxification reaction takes place inside the sealed compartment [90]. Enzyme concentration (E) inside a nanobody can be either low or much higher than that of the toxicant (T). The reaction inside the nanoreactor occurs either under first ((E) << (T)) or second-order conditions ((E) ≈ (T)) with respect to toxicant concentration (T). However, partial enzyme encapsulation may occur as well and, in this case, an enzymatic "corona" forms on the outer surface of the nanoreactors, which can complicate the process and lead to the undesirable, rapid clearance and possible adverse immune responses to heterologous enzymes. Thus, the permeability of the nanoreactor membrane for substrates and reaction products, possible osmotic effects, the effects of viscosity and crowding, and the formation of an enzymatic "corona" are important technological problems that have not yet been fully resolved. [90].

CONCLUSION

The number of publications devoted to the development of alternative, efficient, and multifunctional biomedical systems such as robotic nanodevices for detoxification is on the rise. This review shows that the proposed concept of nanodetoxification requires an interdisciplinary approach and the borrowing of knowledge from many different fields, such as nanosystem design, biochemistry, biotechnology, micro- and optoelectronics, etc. One of the possible directions in acute poisoning treatment is the development of "empty" nanomedical preparations based on materials and compounds that have been approved for clinical use. In addition, designing nanodevices opens up new opportunities in the treatment of bacterial and viral infections.

However, there is still a long way before highly sensitive, easily controlled, and safe nanodevices are created and such problems as moving in narrow and hard-to-reach places (e.g., capillary blood vessels), performing complex functions, being flexible and cost-effective are resolved. ●

T.N. Pashirova., Z.M. Shaihutdinova, V.F. Mironov acknowledge the financial support received from the government assignment for FRC Kazan Scientific Center of Russian Academy of Sciences.
The work of P. Masson (Enzyme nanodevices for detoxification) is carried out in accordance with the Strategic Academic Leadership Program "Priority 2030" of the Kazan Federal University of the Government of the Russian Federation

REFERENCES

1. Zhang C., Yan L., Wang X., Zhu S., Chen C., Gu Z., Zhao Y. // Nano Today. 2020. V. 35. P. 101008.
2. Shan X., Gong X., Li J., Wen J., Li Y., Zhang Z. // Acta Pharm. Sin. B. 2022. V. 12. № 7. P. 3028–3048.
3. Moosavian S.A., Bianconi V., Pirro M., Sahebkar A. // Semin. Cancer Biol. 2021. V. 69. P. 337–348.
4. Halwani A.A. // Pharmaceutics. 2022. V. 14. № 1. P. 106.
5. Wilhelm S., Tavares A.J., Dai Q., Ohta S., Audet J., Dvorak H.F., Chan W.C.W. // Nat. Rev. Mater. 2016. V. 1. № 5. P. 16014.
6. Chen Z., Wang Z., Gu Z. // Acc. Chem. Res. 2019. V. 52. № 5. P. 1255–1264.
7. Wicki A., Witzigmann D., Balasubramanian V., Huwyler J. // J. Control. Release. 2015. V. 200. P. 138–157.
8. Sun Z., Hou Y. // Adv. Ther. 2022. V. 5. № 7. P. 2100228.
9. Li J., Esteban-Fernández de Ávila B., Gao W., Zhang L., Wang J. // Sci. Robot. 2017. V. 2. № 4. P. eaam6431
10. Gao W., Wang J. // Nanoscale. 2014. V. 6. № 18. P. 10486–10494.
11. Li T., Li J., Zhang H., Chang X., Song W., Hu Y., Shao G., Sandraz E., Zhang G., Li L., et al. // Small. 2016. V. 12. № 44. P. 6098–6105.
12. Wang H., Pumera M. // Adv. Funct. Mater. 2018. V. 28. № 25. P. 1705421.
13. Wong F., Dey K.K., Sen A. // Annu. Rev. Mater. Res.

2016. V. 46. № 1. P. 407–432.
14. Li J., Rozen I., Wang J. // ACS Nano. 2016. V. 10. № 6. P. 5619–5634.
15. Halder A., Sun Y. // Biosens. Bioelectron. 2019. V. 139. P. 111334.
16. Pedrero M., Gamella M., Serafín V. // The Detection of Biomarkers. Past, Present and the Future Prospects, Chapter 19 - Nanomachines and nanorobotics: improving cancer diagnosis and therapy, AcademicPress, 2022, Elsevier Inc., P. 503–543.
17. Agrahari V., Agrahari V., Chou M.-L., Chew C.H., Noll J., Burnouf T. // Biomaterials. 2020. V. 260. P. 120163.
18. Shivalkar S., Chowdhary P., Afshan T., Chaudhary S., Roy A., Samanta S.K., Sahoo A.K. // Colloids Surfaces B Biointerfaces. 2023. V. 222. P. 113054.
19. Sitti M. // Nat. Rev. Mater. 2018. V. 3. № 6. P. 74–75.
20. Jimenez-Falcao S., Joga N., García-Fernández A., Llopis Lorente A., Torres D., de Luis B., Sancenón F., Martínez-Ruiz P., Martínez-Máñez R., Villalonga R. // J. Mater. Chem. B. 2019. V. 7. № 30. P. 4669–4676.
21. Zhao X., Gentile K., Mohajerani F., Sen A. // Acc. Chem. Res. 2018. V. 51. № 10. P. 2373–2381.
22. Arqué X., Patiño T., Sánchez S. // Chem. Sci. 2022. V. 13. № 32. P. 9128–9146.
23. Wu H., Greydanus B., Schwartz D.K. // Proc. Natl. Acad. Sci. USA. 2021. V. 118. № 27. P. e2101807118.
24. Cai L., Xu D., Chen H., Wang L., Zhao Y. // Eng. Regen. 2021. V. 2. P. 109–115.
25. Magdanz V., Khalil I.S.M., Simmchen J., Furtado G.P., Mohanty S., Gebauer J., Xu H., Klingner A., Aziz A., Medina-Sánchez M., et al. // Sci. Adv. 2020. V. 6. № 28. P. aba5855.
26. Xu W., Qin H., Tian H., Liu L., Gao J., Peng F., Tu Y. // Appl. Mater. Today. 2022. V. 27. P. 101482.
27. Li D., Liu C., Yang Y., Wang L., Shen Y. // Light Sci. Appl. 2020. V. 9. № 1. P. 84.
28. Abdelmohsen L.K.E.A., Nijemeisland M., Pawar G.M., Janssen G.J.A., Nolte R.J.M., Van Hest J.C.M., Wilson D.A. // ACS Nano. 2016. V. 10. № 2. P. 2652–2660.
29. Luo M., Li S., Wan J., Yang C., Chen B., Guan J. // Langmuir. 2020. V. 36. № 25. P. 7005–7013.
30. Yang J., Su T., Zou H., Yang G., Ding J., Chen X. // Angew. Chemie Int. Ed. 2022. V. 61. № 47. P. e202211136
31. Feng Y., Liao Z., Zhang H., Xie X., You F., Liao X., Wu C., Zhang W., Yang H., Liu Y. // Chem. Eng. J. 2023. V. 452. P. 139506.
32. Ouyang Y., Fadeev M., Zhang P., Carmieli R., Li J., Sohn Y.S., Karmi O., Nechushtai R., Pikarsky E., Fan C., et al. // ACS Nano. 2022. V. 16. № 11. P. 18232–18243.
33. Li Z., Li M., Sun H., Yang Z., Huo Q., Bai Y., Mei Y., Li Y., Quan P., Zhang J., et al. // J. Control. Release. 2022. V. 346. P. 148–157.
34. Liu F., Anton N., Niko Y., Klymchenko A.S. // ACS Appl. Bio Mater. 2023. V. 6. № 1. P. 246–256.
35. Fettiplace M.R., Weinberg G. // Reg. Anesth. Pain Med. 2018. V. 43. № 2. P. 138–149.
36. Harvey M.G., Cave G.R. // J. Med. Toxicol. 2008. V. 4. № 2. P. 71–76.
37. Jakkala-Saibaba R., Morgan P.G., Morton G.L. // Anaesthesia. 2011. V. 66. № 12. P. 1168–1170.
38. Royle K., Bandt C. // Can. Vet. J., 2020. V. 61. № 1. P. 49–52.
39. Montiel V., Gougnard T., Hantson P. // Eur. J. Emerg. Med. 2011. V. 18. № 2. P. 121–123.
40. Tikhomirov M., Jajor P., Śniegocki T., Poźniak B. // Sci. Rep. 2022. V. 12. № 1. P. 18683.
41. De Diego C., Zaballos M., Quintela O., Sevilla R., Callejo D., González-Panizo J., Anadón M.J., Almendral J. // Cardiovasc. Toxicol. 2019. V. 19. № 5. P. 432–440.
42. DeMel D., Gleeson M., Schachterle K., Thomer A. // J. Vet. Emerg. Crit. Care. 2022. V. 32. № 5. P. 680–684.
43. Sohn J.-T. // Am. J. Emerg. Med. 2022. V. 58. P. 331–332.
44. Zaballos M., Fernández I., Rodríguez L., García S., Varela O., Quintela O., Anadón M.-J., Almendral J. // Clin. Toxicol. 2022. V. 60. № 8. P. 902–911.
45. Hori K., Matsuura T., Tsujikawa S., Hino H., Kuno M., Oda Y., Nishikawa K., Mori T. // Clin. Toxicol. 2022. V. 60. № 6. P. 716–724.
46. Matsuoka M., Imai T., Iwabuchi S., Kinoshita K. // J. Emerg. Med. 2023. V. 64. № 1. P. 62-66.
47. Cobey F.C., Kawabori M., Schumann R., Couper G., Bonney I., Fettiplace M.R., Weinberg G. // J. Cardiothorac. Vasc. Anesth. 2021. V. 35. № 10. P. 3139–3141.
48. Pannu A.K., Garg S., Bhalla A., Dhibar D.P., Sharma N. // Clin. Toxicol. 2022. V. 60. № 5. P. 602–608.
49. Liu Y., Zhang J., Yu P., Niu J., Yu S. // Front. Med. 2021. V. 8. P. 756866.
50. Sohn J.-T. // J. Emerg. Med. 2021. V. 60. № 5. P. e137–e138.
51. Mégarbane B., Oberlin M., Alvarez J.-C., Balen F., Beaune S., Bédry R., Chauvin A., Claudet I., Danel V., Debaty G., et al. // Ann. Intensive Care. 2020. V. 10. № 1. P. 157.
52. Jovanovic A. V., Underhill R.S., Bucholz T.L., Duran R.S. // Chem. Mater. 2005. V. 17. № 13. P. 3375–3383.
53. Xu D., Han H., He Y., Lee H., Wu D., Liu F., Liu X., Liu Y., Lu Y., Ji C. // Adv. Mater. 2018. V. 30. № 22. P. 1707443.
54. Shanuja J., Singh K., Sai Nandhini R., Palanivelu J. // Nanotechnol. Life Sci. 2021. P. 87–104.
55. Hu C.-M.J., Fang R.H., Copp J., Luk B.T., Zhang L. // Nat. Nanotechnol. 2013. V. 8. № 5. P. 336–340.
56. Wang S., Wang D., Duan Y., Zhou Z., Gao W., Zhang L. // Adv. Mater. 2022. V. 34. № 13. P. 2107719.
57. Chen Y., Chen M., Zhang Y., Lee J.H., Escajadillo T., Gong H., Fang R.H., Gao W., Nizet V., Zhang L. // Adv. Health. Mater. 2018. V. 7. № 13. P. 1701366.
58. Chen Y., Zhang Y., Chen M., Zhuang J., Fang R.H., Gao W., Zhang L. // Small. 2019. V. 15. № 6. P. 1804994.
59. Pang Z., Hu C.M.J., Fang R.H., Luk B.T., Gao W., Wang F., Chuluun E., Angsantikul P., Thamphiwatana S., Lu W., et al. // ACS Nano. 2015. V. 9. № 6. P. 6450–6458.
60. Copp J.A., Fang R.H., Luk B.T., Hu C.-M.J., Gao W., Zhang K., Zhang L. // Proc. Natl. Acad. Sci. USA. 2014. V. 111. № 37. P. 13481–13486.
61. Zhang Q., Dehaini D., Zhang Y., Zhou J., Chen X., Zhang L., Fang R.H., Gao W., Zhang L. // Nat. Nanotechnol. 2018. V. 13. № 12. P. 1182–1190.
62. Zhang Y., Chen Y., Lo C., Zhuang J., Angsantikul P., Zhang Q., Wei X., Zhou Z., Obonyo M., Fang R.H., et al. // Angew. Chemie Int. Ed. 2019. V. 58. № 33. P. 11404–11408.
63. Zhang Q., Honko A., Zhou J., Gong H., Downs S.N., Vasquez J.H., Fang R.H., Gao W., Griffiths A., Zhang L. // Nano Lett. 2020. V. 20. № 7. P. 5570–5574.
64. Wang D., Ai X., Duan Y., Xian N., Fang R.H., Gao W., Zhang L. // ACS Nano. 2022. V. 16. № 11. P. 19145–19154.
65. Chen Y., Zhang Y., Zhuang J., Lee J.H., Wang L., Fang R.H., Gao W., Zhang L. // ACS Nano. 2019. V. 13. № 6. P. 7209–7215.
66. Zou S., He Q., Wang Q., Wang B., Liu G., Zhang F., Cheng X., Wang B., Zhang L. // Int. J. Nanomed. 2021.

V. 16. P. 4239–4250.
67. Kim J.-K., Uchiyama S., Gong H., Stream A., Zhang L., Nizet V. // Engineering. 2021. V. 7. № 8. P. 1149–1156.
68. Liu C., Ruan S., He Y., Li X., Zhu Y., Wang H., Huang H., Pang Z. // Acta Pharm. Sin. B. 2022. V. 12. № 11. P. 4235–4248.
69. Wu Z., Li J., de Ávila B.E.-F., Li T., Gao W., He Q., Zhang L., Wang J. // Adv. Funct. Mater. 2015. V. 25. № 48. P. 7497–7501.
70. Wu Z., Li T., Gao W., Xu T., Jurado-Sánchez B., Li J., Gao W., He Q., Zhang L., Wang J. // Adv. Funct. Mater. 2015. V. 25. № 25. P. 3881–3887.
71. Esteban-Fernández de Ávila B., Angsantikul P., Ramírez-Herrera D.E., Soto F., Teymourian H., Dehaini D., Chen Y., Zhang L., Wang J. // Sci. Robot. 2018. V. 3. № 18, P. eaba6137.
72. Refaai M.R.A., Manjunatha M.N., Radjarejesri S., Ramesh B., Subbiah R., Adugna N. // Adv. Mater. Sci. Eng. 2022. V. 2022. P. 1–12.
73. Lu D., Tang S., Li Y., Cong Z., Zhang X., Wu S. // Micromachines. 2021. V. 12. № 7. P. 797.
74. Hart K., Harvey M., Tang M., Wu Z., Cave G. // Pharmaceutics. 2021. V. 13. № 3. P. 395.
75. Wratten M. Lou, Sereni L., Tetta C. // Artif. Organs. 2000. V. 24. № 9. P. 685–690.
76. Shi Y., Wang Y., Ma S., Liu T., Tian H., Zhu Q., Wang W., Li Y., Ding F. // Artif. Organs. 2019. V. 43. № 5. P. 490–503.
77. Shen Y., Shen Y., Bi X., Li J., Chen Y., Zhu Q., Wang Y., Ding F. // Int. J. Artif. Organs. 2021. V. 44. № 6. P. 393–403.
78. Shen Y., Shen Y., Li J., Ding F., Wang Y. // J. Biomed. Mater. Res. Part A. 2022. V. 110. № 4. P. 976–983.
79. Matoori S., Forster V., Agostoni V., Bettschart-Wolfensberger R., Bektas R.N., Thöny B., Häberle J., Leroux J.-C., Kabbaj M. // J. Control. Release. 2020. V. 328. P. 503–513.
80. Forster V., Signorell R.D., Roveri M., Leroux J.-C. // Sci. Transl. Med. 2014. V. 6. № 258.
81. Chapman R., Harvey M., Davies P., Wu Z., Cave G. // J. Liposome Res. 2019. V. 29. № 2. P. 114–120.
82. Cave G., Kee R., Harvey M., Wu Z. // Int. J. Mol. Sci. 2022. V. 23. № 19. P. 11577.
83. Tzror-Azankot C., Anaki A., Sadan T., Motiei M., Popovtzer R. // Materials (Basel). 2022. V. 15. № 21. P. 7779.
84. Pratsinis A., Zuercher S., Forster V., Fischer E.J., Luciani P., Leroux J.-C. // Biomaterials. 2017. V. 145. P. 128–137.
85. Pashirova T.N., Bogdanov A., Masson P. // Chem. Biol. Interact. 2021. V. 346. P. 109577.
86. Chauhan K., Zárate Romero A., Sengar P., Medrano C., Vazquez-Duhalt R. // ChemCatChem. 2021. V. 13. № 17. P. 3732–3748.
87. Pashirova T., Shaihutdinova Z., Mansurova M., Kazakova R., Shambazova D., Bogdanov A., Tatarinov D., Daudé D., Jacquet P., Chabrière E., et al. // ACS Appl. Mater. Interfaces. 2022. V. 14. № 17, P. 19241–19252.
88. Masson P., Rochu D. // Acta Naturae. 2009. V. 1. № 1. P. 68–79.
89. Masson P., Lushchekina S.V. // Chem. Biol. Interact. 2016. V. 259. P. 319–326.
90. Shajhutdinova Z., Pashirova T., Masson P. // Biomedicines. 2022. V. 10. № 4. P. 784.

B Cell Profiling in Patients with Pemphigus Vulgaris

V. A. Abrikosova[1], Y. A. Mokrushina[1,2], L. A. Ovchinnikova[1], E. N. Larina[1], S. S. Terekhov[1], M. N. Baranova[1], Y. A. Lomakin[1], D. S. Balabashin[1], T. V. Bobik[1], E. N. Kaliberda[1], V. D. Knorre[1], M. V. Shpilevaya[3], T. K. Aliev[1,2], D. G. Deryabin[3], A. E. Karamova[3], A. A. Kubanov[3], M. P. Kirpichnikov[1,4], I. V. Smirnov[1,5*]

[1]Shemyakin–Ovchinnikov Institute of Bioorganic Chemistry of the Russian Academy of Sciences, Moscow, 117997 Russian Federation

[2]Faculty of Chemistry, Lomonosov Moscow State University, Moscow, 119991 Russian Federation

[3]State Research Center of Dermatovenereology and Cosmetology, Moscow, 107076 Russian Federation

[4]Faculty of Biology, Lomonosov Moscow State University, Moscow, 119991 Russian Federation

[5]Endocrinology Research Center, Moscow, 117292 Russian Federation

*E-mail: smirnov.mx.ibch@gmail.com

Received December 20, 2022; in final form, March 10, 2023

DOI: 10.32607/actanaturae.11890

ABSTRACT **Pemphigus vulgaris is a severe, socially significant autoimmune disease associated with autoantibodies to the desmoglein 3 antigen. The disease affects all age groups, beginning at 18 years of age; the mortality rate of pemphigus can reach as high as 50%, depending on a patient's age and a number of other factors. There is no highly selective or personalized therapy for pemphigus vulgaris at the moment. One of the well-known therapeutic approaches to the disease is to use rituximab, an anti-CD20 antibody that can help achieve B cell depletion in peripheral blood. To solve the problem of nonspecific elimination of B cells in patients with pemphigus vulgaris, it is reasonable to use specific immunoligands, their choice being based on an assessment of the level of autoantibodies specific to each of the fragments of desmoglein. In this work, the proportion of autoreactive B cells in patients diagnosed with pemphigus vulgaris is found to be 0.09–0.16%; a positive correlation was revealed between the antibody level and the number of autoreactive B cells to various fragments of desmoglein.**

KEYWORDS **desmoglein 3, pemphigus vulgaris, targeted therapy, immunoligands.**

INTRODUCTION

Pemphigus vulgaris is the most common form of bullous dermatosis, involving the appearance of blisters with serous content and a thin flaccid roof on unaltered skin and/or mucous membrane; once opened, they form painful erosions that do not heal for a long time.

According to state statistical monitoring data, 1.9–2.4 new pemphigus vulgaris cases per 100,000 adult population (aged at least 18 years) are annually reported in Russia; the prevalence of the disease ranges from 4.8 to 6.3 cases per 100,000 population [1].

IgG autoantibodies targeting the major structural protein of desmosomes in stratified squamous epithelium, desmoglein 3 (Dsg3), play a key pathogenetic role in the development of pemphigus vulgaris [2]. The interaction between the autoantibodies and the extracellular domains of desmoglein 3 results in desmosomal degradation, followed by acantholysis (degenerative alterations in the stratum spinosum that manifests themselves as rupturing of intercellular bridges and lead to the formation of intraepidermal bullae) [3].

The standard therapy used for pemphigus vulgaris today consists of long-term administration of systemic corticosteroids, either as a monotherapy or in combination with other immunosuppressants, causing a number of serious adverse effects and being ineffective against forms of the disease that are resistant to systemic glucocorticoid (GC) therapy [4].

Monoclonal antibody-based drugs that enable personalized therapy of pemphigus vulgaris and other autoimmune diseases by targeting autoantibody-producing cells (B cells) are currently being developed to reduce the course dose of GCs. So far only rituximab

is recommended for clinical application with pemphigus vulgaris patients, its active principle being chimeric monoclonal antibodies specific to B lymphocyte antigen CD20 [5]. However, the serious problem posed by rituximab use is that both the pathological (autoreactive) and normal B cells are systemically suppressed, thus leading to systemic immunodeficiency that is caused by a lack of circulating immunoglobulins. A series of cases have been reported when specific immunoactive agents were applied for a targeted elimination of pathological lymphocytes [6, 7]. Treatment specificity depends on the effectiveness of the interaction between the immunoactive drug and the target population of autoreactive B cells. It has been reported that there are differences in the level of antibodies specific to different desmoglein domains in patients diagnosed with pemphigus vulgaris [8, 9]. This fact can be used to enhance the immunotherapy specificity when performing targeted delivery of immunoactive agents comprising a specific variant of the desmoglein fragment. Immunosorption based on the elimination of autoreactive antibodies using highly selective immunosorbents from the blood of pemphigus vulgaris patients was proposed as a treatment option [10]. Therefore, it becomes necessary to determine the correlation between the antibody level and the proportion of autoreactive B cells targeting fragments of desmoglein and identify the specificity profile of the autoreactive B cells in pemphigus vulgaris patients.

EXPERIMENTAL

The full-length recombinant extracellular fragment of human Dsg3 (EC1–EC5) and isolated domains EC1, EC2, and EC3–EC4 fused with the Fc fragment of human IgG1 were obtained in the CHO cell-based expression system using genetic constructs based on the pcDNA3.4 vector (Thermo Scientific, USA). Recombinant proteins were purified to remove the culture medium on a MabSelect SuRe column (GE Healthcare, USA). Protein purity was confirmed by size-exclusion chromatography and electrophoresis.

The total serum level of anti-Dsg3 antibodies in patients was characterized using the Anti-Desmoglein 3 ELISA IgG test kit (Euroimmun, Germany) and presented as relative activity units (RU/mL) according to the absorbance of the reference serum supplied together with the test kit. The resulting recombinant proteins were used to assess the immunoreactivity of serum samples from patients with pemphigus vulgaris by two-step competitive enzyme-linked immunosorbent assay (ELISA) [11]. Dsg3, as well as its fragments EC1, EC2, and EC3–EC4, fused with the Fc fragment of human IgG1 at a concentration of 1 μg/mL, as well as bovine serum albumin (BSA) at the same concentration for controlling nonspecific binding, were sorbed onto the wells of a polystyrene plate (Greiner Bio-One GmbH, Germany) overnight at +4°C. After removing the sorbed contents, the wells were washed once with phosphate-buffered saline (PBS) and blocked with a 0.1% casein solution. After the blocking, the wells were washed once with phosphate-buffered saline supplemented with 0.005% Tween-20 (PBST). The studied sera were diluted (1 : 100) in PBS supplemented with 1% BSA and incubated in a thermostated shaker at +24°C for 18 h at a rate of 200 rpm. Once the incubation was completed, the entire studied serum samples were transferred into the wells of the plate supplied with the reference test kit to repeatedly assess the level of antibodies that had not reacted with full-length Dsg3. Calibration samples with activities of 20 and 200 RU/mL were loaded to the additional wells and incubated using the same procedure as the one described previously (18 h, +24°C, 200 rpm). After the incubation, the plate was washed thrice with a PBST solution and antibodies specific to the kappa and lambda light chains of horseradish peroxidase-conjugated human antibodies were added. HRP-conjugated rabbit antibodies against full-length human IgG supplied with the reference test kit were added to the plate. After the 60-min incubation (+24°C, 200 rpm), the plate wells were washed thrice, supplemented with the substrate solution (tetramethylbenzidine, TMB), and incubated overnight in the dark for 30 min. The reaction was stopped by adding a 4 N phosphoric acid solution; the optical density (OD) in the wells was measured at a wavelength of 450 nm (OD_{450}) on a plate reader. The OD values of the calibration curves with activities of 20 and 200 RU/mL recorded on the reference plate were used to plot a calibration curve that allowed one to determine the activity of each studied serum sample in relative activity units (RU/mL). The results were used to calculate the proportion (%) of autoreactive antibodies that specifically interacted with individual epitopes of the Dsg3 molecule and are detected by competitive ELISA:

$$[1 - (A_{Pos} - A_R) / (A_{Pos} - A_{Neg})] \times 100,$$

where A_R is serum activity after preincubation in the plate with an immobilized epitope protein, A_{Pos} is serum activity after preincubation with Dsg3 in the reference test kit, and A_{Neg} is serum activity after preincubation with BSA.

Venous blood samples collected from three patients with a clinical and laboratory diagnosis of L10.0 Pemphigus vulgaris were used in this study. All the patients had provided written informed consent to be

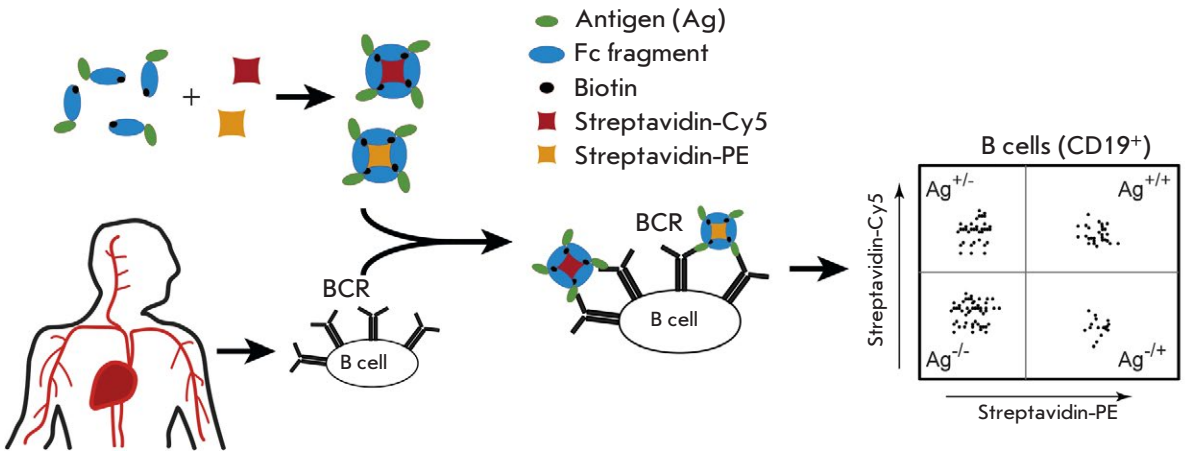

Fig. 1. Schematic of B cell specificity assay workflow using double-positive antigen staining

included in the research; the study was conducted in compliance with current legal and ethical standards.

The number of autoreactive B cells was assessed by flow cytometry using biotinylated recombinant proteins (subdomains EC1, EC2, EC3, and EC4 fused with the constant domain of human immunoglobulin).

Peripheral blood mononuclear cells from pemphigus vulgaris patients and healthy donors were isolated using the Ficoll–Paque PLUS density gradient medium (GE Healthcare). The cells were washed, counted, resuspended in phosphate-buffered saline supplemented with Human Seroblock (Bio-Rad, USA), 0.5% BSA, and 2 mM EDTA (2×10^6 cells per 100 μL of solution), and incubated on ice for 30 min. For a tetrameric complex to form, the preparations EC1-Fc, EC2-Fc, EC3-4-Fc, and Dsg3-Fc, purified and chemically biotinylated using the Sulfo-NHS-LC-Biotin reagent (Thermo Fisher Scientific), were mixed with Streptavidin-PE (Invitrogen, USA) and Streptavidin-Cy5 (Abcam, UK) at a 4 : 1 molar ratio and incubated at +4°C in the dark for 30 min. The tetrameric immune complex with Streptavidin-PE and tetrameric immune complex with Streptavidin-Cy5 were added to the cells being stained until concentrations of 4 nM and 10 nM, respectively, were achieved; the cells were incubated at +4°C under constant stirring for 15 min. Fluorescent anti-CD45-APC-Cy7 (1 : 300 dilution) (Sony, USA) and anti-CD19-PE-Cy7 (1 : 1000 dilution) (Biolegend, USA) antibodies and the SYTOX™Green fluorescent dead cell stain (1 : 1000 dilution) (Biolegend, USA) were then added to the samples being analyzed and additionally incubated at +4°C in the dark for 30 min. Next, the samples were washed with 0.5 mL of PBS supplemented with 2 mM EDTA. The fluorescence intensity was assessed on a ACEA Novocyte fluorimeter (ACEA Biosciences, USA).

Table 1. The results of enzyme-linked immunosorbent assay of a pemphigus vulgaris patient's serum using full-length desmoglein and its fragments as an antigen, represented in RU/ml

Antigen	P1	P2	P3
Dsg3	700	20	1500
EC1	588	-	300
EC2	203	-	450
EC3-4	98	-	750

RESULTS AND DISCUSSION

The number of B cells autoreactive to desmoglein was determined in the venous blood of patients diagnosed with pemphigus vulgaris (P1–P3); blood from a healthy donor (HD) was used as a control sample. Mononuclear cells were isolated from all the samples to further perform staining and a flow cytometry assay (*Fig. 1*).

Serum samples for measuring the level of antibodies specific to Dsg3 and its fragments were collected separately (*Table 1*).

One can see in *Table 1* that the patients had different profiles of antibody response to the full-length protein and desmoglein 3 domains. Patient P2 was found to exhibit only a weak immune response to full-length Dsg3, equal to the diagnostically significant threshold value of 20 RU/mL, while patients P1 and P3 had a strong immune response that differed from the distal (EC1 and EC2) or proximal (EC3-4) extracellular domain of this protein.

In order to establish a correlation between the levels of antibodies specific to different desmoglein variants and the number of antigen-specific autoreactive B cells, the mononuclear cell fraction was stained with immunoactive ligands and antibodies specific to B cell surface antigens (CD19). It was shown earlier that the proportion of antigen-specific B cells is 0.05–0.5% of the entire B cell pool [12]. A tetrameric form of the immunoligand was designed using a fluorescently labeled streptavidin molecule (*Fig. 1*). A single molecule of the complex interacts with several molecules of the B cell receptor, thus increasing ligand avidity and, therefore, enhancing staining efficiency. Another key feature was employing the double-positive staining approach. Two streptavidin-fused antigenic complexes labeled with different fluorescent tags (phycoerythrin (PE) and cyanine dye Cy5) were used in this case. This approach significantly increased the level of specific staining of B cells. The staining mechanism reported in this study can be used to efficiently detect B cells targeting any identified antigens, including when searching for antibodies specifically bound to viral proteins, facilitating virus neutralization. The final scheme for staining/analyzing each sample involved the following: (i) isolating the area according to the cell size, (ii) isolating the area corresponding to live leukocytes after co-staining with the SYTOX™Green dye and anti-CD45-APC-Cy7 antibodies, (iii) isolating the area corresponding to single cells, (iv) isolating the area corresponding to CD19+ B cells, and (v) assessing double-positive antigen-specific B cells (*Fig. 2*).

According to the results presented in *Fig. 2B*, the highest proportion of B cells specific to full-length desmoglein belonged to patient P3 while the lowest was true applied to patient P2; in general, these findings agree with the ELISA data (*Table 1*). The proportion of B cells specific to different domains of desmoglein was also different in all patients (*Fig. 3*).

The highest proportion of EC2-specific B cells was detected in patient P1; meanwhile, the proportion of cells EC1-specific and EC3-4-specific cells was lower: 0.12 and 0.11%, respectively. Patient P2 had no EC1-specific cells (the level being comparable to that of the control); the proportion of EC2-specific and EC3-4-specific cells was 0.13 and 0.10%. In patient P3, the proportion of B cells specific to all the domains was comparable to that in patient P1; however, the proportion of EC2-specific and EC3-4-specific B cells was the highest (0.15 and 0.16%, respectively).

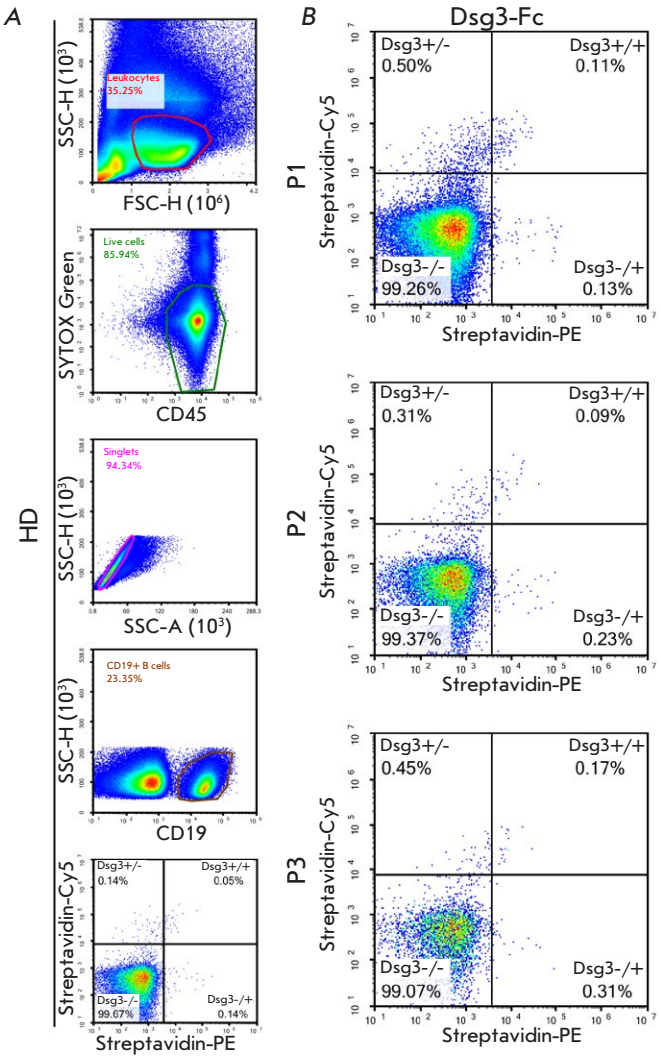

Fig. 2. Flow cytometry analysis of a healthy donor (*A*) and pemphigus vulgaris patients (P1, P2, P3) to identify full-length Dsg3-specific B cells (*B*). The boundary condition for the plots in the Streptavidin-Cy5 and Streptavidin-PE scales were chosen as 0.05% positive events in the gate with "double positive" signal (+/+) for the control sample (healthy donor, HD)

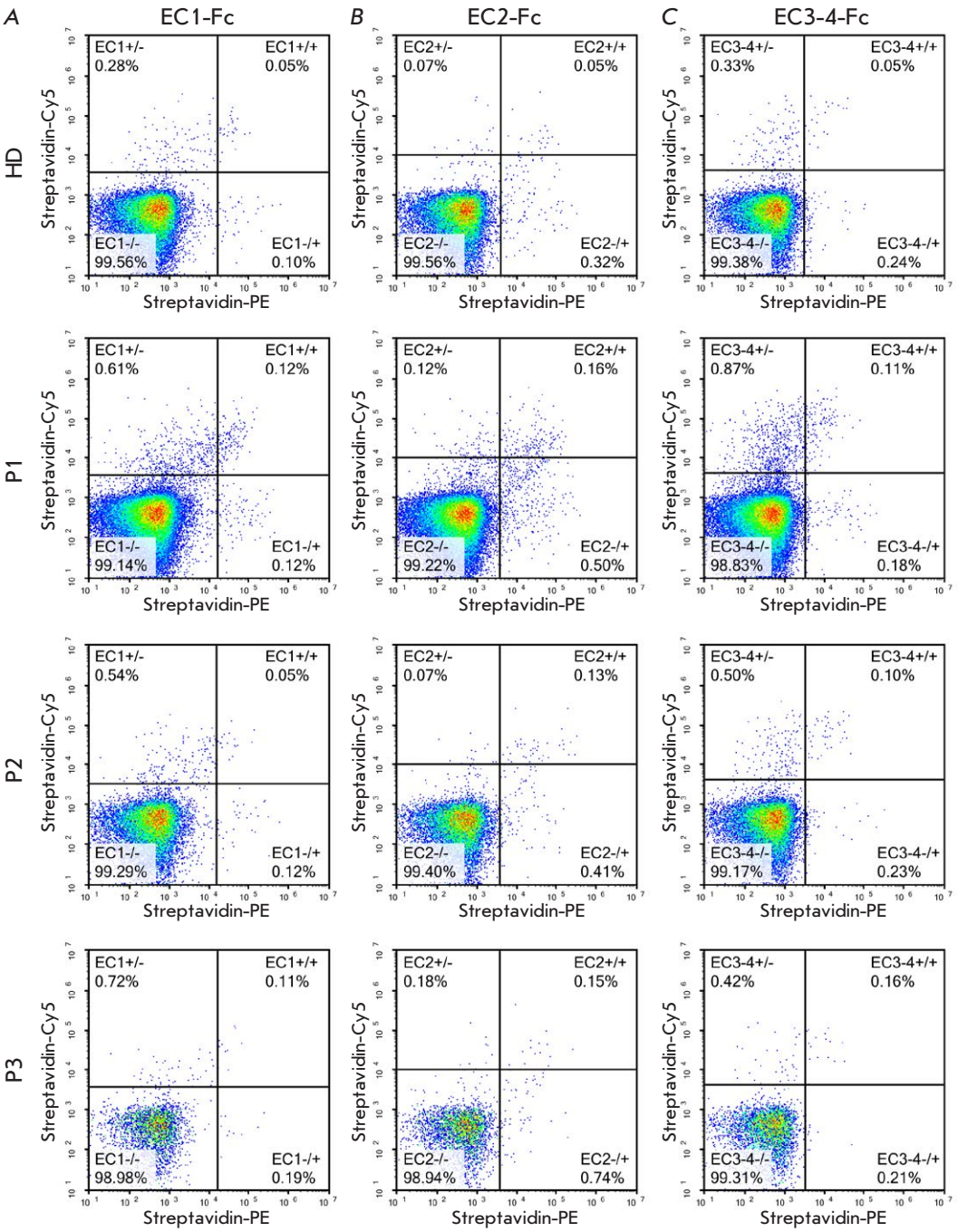

Fig. 3. Flow cytometry analysis of a healthy donor (HD) and pemphigus vulgaris patients (P1, P2, P3) to identify EC1-specific (*A*), EC2-specific, and EC3-4-specific (*B*) B cells. The boundary condition for the plots in the Streptavidin-Cy5 and Streptavidin-PE scales were chosen as 0.05% positive events in the gate with "double positive" signal (+/+) for the control sample (healthy donor)

CONCLUSIONS

Hence, the profile analysis of the specificity of antibodies and B cells showed that there exists a generally positive correlation between the blood titer of specific antibodies and the proportion of antigen-specific B cells (*Fig. 4*).

Meanwhile, the proportion of autoreactive B cells in pemphigus patients was in the range of 0.09–0.16%. A noticeable level of nonspecific binding was also detected in a healthy donor (0.05%); however, the double-positive antigen staining approach has made it possible to determine the antigen-specificity profile of

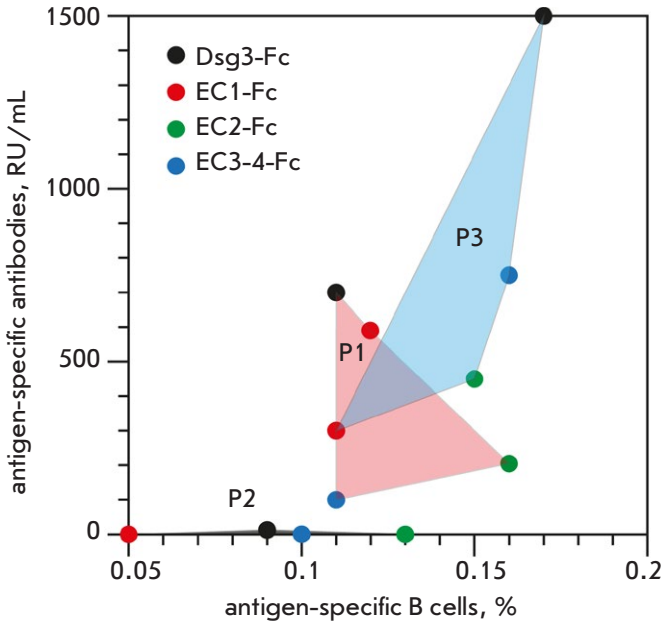

Fig. 4. Profile analysis of the specificity of antibodies and B cells. Samples analyzed for full-length desmoglein 3 and its domains are color-coded. Lines connect values related to the same patient

B cells in pemphigus vulgaris patients. The results are important in elaborating a strategy of personalized pemphigus therapy using cytotoxic immunoligands based on recombinant desmoglein domains fused with the Fc fragment of human IgG1. It is likely that patient P2 will be insensitive to therapy with EC1-Fc, while one may expect the elimination of autoreactive B cells when using EC2-Fc and EC3-4-Fc in patients P1 and P3, respectively. B cell profiling in patients with autoimmune diseases, and pemphigus vulgaris in particular, opens up broad prospects for choosing a personalized treatment strategy. ●

This work was supported by the Ministry of Science and Higher Education of the Russian Federation (Agreement No. 05.607.21.0325, unique project ID RFMEFI60719X0325). The part of the work involving differential staining and flow cytometry analysis of the number of autoreactive B cells to Dsg3 and its fragments was specifically funded by the Russian Foundation for Basic Research (project No. 20-04-60468).

REFERENCES

1. Aleksandrova G.A., Kubanov A.A., Melekhina L.E., Bogdanova E.V., Polikarpov A.V., Ohryzko E.V., Golubev N.A., Pronina T.V., Gladkikh T.E., Grincheva A.V. Resources and activities of medical organizations of the dermatovenerological profile. The incidence of sexually transmitted infections, contagious skin diseases and skin diseases: statistical materials. M.: Ministry of Health of the Russian Federation, 2015. 212 p.
2. Satyam A., Khandpur S., Sharma V.K., Sharma A. // Immunol. Invest. 2009. V. 38. № 6. P. 498–509.
3. Herrero-González J.E., Iranzo P., Benítez D., Lozano F., Herrero C., Mascaró J.M., Jr. // Acta Derm. Venereol. 2010. V. 90. № 4. P. 401–405.
4. Leventhal J.S., Sanchez M.R. // J. Drugs Dermatol. 2012. V. 11. № 10. P. 1200–1206.
5. Sorce M., Aricò M., Bongiorno M.R. // Dermatol. Ther. 2008. V. 21. № S1. P. S6–S9.
6. Stepanov A.V., Belogurov A.A., Jr., Ponomarenko N.A., Stremovskiy O.A., Kozlov L.V., Bichucher A.M., Dmitriev S.E., Smirnov I.V., Shamborant O.G., Balabashin D.S., et al. // PLoS One. 2011. V. 6. № 6. P. e20991.
7. Stepanov A.V., Belogurov A.A. Jr., Kothapalli P., Shamborant O.G., Knorre V.D., Telegin G.B., Ovsepyan A.A., Ponomarenko N.A., Deyev S.M., Kaveri S.V., et al. // Acta Naturae. 2015. V. 7. № 2. P. 74–79.
8. Cho A., Caldara A.L., Ran N.A., Menne Z., Kauffman R.C., Affer M., Llovet A., Norwood C., Scanlan A., Mantus G., et al. // Cell Rep. 2019. V. 28. № 4. P. 909–922. e1–e6.
9. Müller R., Svoboda V., Wenzel E., Gebert S., Hunzelmann N., Müller H.-H., Hertl M. // Exp. Dermatol. 2006. V. 15. № 8. P. 606–614.
10. Abramova T.V., Spilevaya M.V., Kubanov A.A. // Acta Naturae. 2020. V. 12. № 2. P. 63–69.
11. Kubanov A.A., Deryabin D.G., Shpilevaya M.V., Karamova A.E., Nikonorov A.A., Larina E.N., Aliev T.K., Dolgikh D.A., Bobik T.V., Smirnov I.V., et al. // Bull. Exp. Biol. Med. 2021. V. 171. № 4. P. 475–479.
12. Franz B., May K.F., Jr., Dranoff G., Wucherpfennig K. // Blood. 2011. V. 118. № 2. P. 348–357.

Evaluation of the Effectiveness of Various Autophagy Inhibitors in A549 Cancer Stem Cells

K. V. Aleksandrova, I. I. Suvorova*
Institute of Cytology, Russian Academy of Sciences, St. Petersburg, 194064 Russian Federation
*E-mail: irsuvorov@yandex.ru
Received December 20, 2022; in final form, February 20, 2023
DOI: 10.32607/actanaturae.11891

ABSTRACT **Numerous studies have already established that autophagy plays a central role in the survival of all cells, including malignant ones. Autophagy is a central cog in the general mechanism that provides the intracellular proteostasis determining cellular physiological and phenotypic characteristics. The accumulated data show that autophagy largely contributes to cancer cell stemness. Thus, autophagy modulation is considered one of the promising pharmacological targets in therapy aimed at cancer stem cell elimination. However, autophagy is a multi-stage intracellular process that involves numerous protein participants. In addition, the process can be activated simultaneously by various signaling modules. Therefore, it is no small feat to select an effective pharmacological drug against autophagy. What's more, the search for potential chemotherapeutic agents that could eliminate cancer stem cells through pharmacological inhibition of autophagy is still under way. In the present work, we selected a panel of autophagy inhibitors (Autophinib, SBI-0206965, Siramesine, MRT68921, and IITZ-01), some of whom have been recently identified as effective autophagy inhibitors in cancer cells. Using A549 cancer cells, which express the core stem factors Oct4 and Sox2, we evaluated the effect of these drugs on the survival and preservation of the original properties of cancer stem cells. Among the agents selected, only Autophinib demonstrated a significant toxic effect on cancer stem cells. The obtained results demonstrate that autophagy inhibition by Autophinib downregulates the expression of the Sox2 protein in A549 cells, and that this downregulation correlates with a pronounced induction of apoptosis. Moreover, Autophinib-treated A549 cells are unable to form spheroids, which indicates a reduction in stemness. Thus, among the drugs studied, only Autophinib can be considered a potential agent against cancer stem cells.**

KEYWORDS **tumor cells, cancer stem cells, autophagy, Sox2, Oct4, Autophinib.**
ABBREVIATIONS **Vps34 – phosphatidylinositol 3-kinase catalytic subunit type 3.**

INTRODUCTION

Currently, autophagy is considered a promising molecular target for cancer cell therapy. Autophagy is known to play a crucial role at all stages of oncogenesis: i.e., during dissemination of cancer cells from the primary tumor, and, accordingly, during the formation of dissociated tumor cells, and during epithelial-mesenchymal transition, and, thus, during metastasis. In addition, it also maintains the cancer stem cell phenotype, thus, providing drug resistance and renewal of tumor. Considering that autophagy is the basis of the various phenotypic and physiological characteristics of cancer cells, in this work we studied the impact of autophagy inhibition on cancer cell elimination *in vitro*. Using literature data, we arrived at a panel of poorly studied pharmacological drugs that inhibit autophagy and can serve as anti-cancer agents. The pharmacological agent Autophinib, which was synthesized in 2017, seems to be a promising autophagy inhibitor (IC_{50} = 90 and 40 nM); it acts through the inhibition of lipid kinase Vps34 (IC_{50} = 19 nM *in vitro*) [1, 2]. Vps34 is involved in the formation of the pre-autophagosomal membrane, which serves as the basis for the production of autophagosomes, and is regulated by the kinases Ulk1 and Ulk2 [3]. Ulk1 and Ulk2 induce autophagy; therefore, inhibition of both Ulk1/2 and Vps34 blocks autophagy at its very early stage. We used two Ulk1/2 inhibitors in our study: SBI-0206965 (IC_{50} = 108 and 711 nM for Ulk1 and Ulk2, respectively) and MRT68921 (IC_{50} = 2.9 and 1.1 nM for Ulk1 and Ulk2, respectively). It was determined in 2015 that MRT68921 and SBI-0206965 are specific autophagy inhibitors; later, they were identified as potential anti-tumor agents [4–8]. In 2018, IITZ-01 was

shown to act as an effective autophagy inhibitor [9]. IITZ-01 demonstrated high anti-tumor activity by inhibiting autophagy through lysosomal destabilization in *in vitro* and *in vivo* experiments in breast cancer models [9]. The drug Siramesine was first synthesized in 1995 as an anxiolytic, due to its ability to act as a selective sigma-2 receptor agonist, which recruits various psychotropic substances in the brain [10]. It is currently known that Siramesine effectively blocks autophagy through lysosomal destabilization in tumor cells [11]. Thus, Siramesine and IITZ-01 inhibit autophagy at late stages, when mature autophagosomes are unable to fuse with lysosomes due to disintegration of the latter for further degradation of the intercellular material. Cells with blocked autophagy are usually characterized by a high amount of autophagosomal structures accumulated in the cytoplasm.

Thus, according to numerous reports, the above autophagy inhibitors can effectively eliminate tumor cells both *in vitro* and *in vivo*. However, these agents have not been studied sufficiently enough to make a conclusion on the effectiveness of their use in cancer therapy. The ability of the selected pharmacological agents to effectively eliminate tumor cells was studied in A549 cancer cells, which demonstrate stemness. Cancer stem cells are very resistant to chemotherapy; hence, there is a good model system for *in vitro* screening for potential anti-tumor agents.

EXPERIMENTAL

Cell cultures

A549 cancer cells were cultured in DMEM medium (Biolot, Russia) supplemented with 10% fetal bovine serum (FBS, Hyclone, USA) at 37°C and 5% CO_2. Cells were obtained from the Center for Collective Usage "Vertebrate Cell Culture Collection". The following inhibitors were used in the study: Autophinib (5 μM), SBI-0206965 (1 μM), Siramesine (0.5 μM), MRT68921 (1 μM), and IITZ-01 (1 μM). All inhibitors were purchased from Selleckhem (USA).

Cells transduction and analysis

Lentiviral vector carrying the SORE6-mCherry reporter was kindly provided by Gordeev S.A. (Institute of Cytology of the Russian Academy of Sciences). A549 cells were transduced with the lentiviral vector using the protocol described in [12]. The fluorescence of mCherry was detected using a Becton Dickinson FACscan flow cytometer (USA) in the ECD-A channel.

Spheroid formation

A549 cells were cultured in hanging drops in non-adherent Sarstedt plates (Germany). Cells were pre-treated with the indicated concentrations of autophagy inhibitors for three days. Cells were then detached from the plates using 1 : 1 trypsin–versene solution and seeded at a density of 4,000 cells per drop. Spheroid colonies of ⩾ 50 μm were analyzed after seven days using an inverted TS100-F microscope (Nicon, Japan).

Cell viability assay

The number of viable and dead cells was assessed by flow cytometry. Cells were detached from the plates with 1 : 1 trypsin–versene solution and centrifuged. DAPI (1 μg/μl) was added to the suspension of viable cells; cells were incubated for 20 min at room temperature and analyzed on a Becton Dickinson FACscan flow cytometer (USA). The DAPI stain passes through the membrane of permeabilized cells, which makes it possible to identify dead cells.

RT-PCR

Total RNA was isolated using TRIZOL reagent (Evrogen, Russia) according to the manufacturer's protocol. Reverse transcription was performed using MMLV reverse transcriptase, 2.5 μg of RNA, and 1 μg of random hexaprimers based on the manufacturer's instructions (Evrogen). Quantitative RT-PCR was carried out using real-time PCR kit from Evrogen containing SYBR Green on a 7500 Real-time PCR System (Applied Biosystems, USA). The following primers were used:
sox2 (F) – TTGCTGCCTCTTTAAGACTAGGA,
s*ox2* (R) – CTGGGGCTCAAACTTCTCTC;
gapdh (F) – GAGGTCAATGAAGGGGTCAT,
gapdh (R) – AGTCAACGGATTTGGTCGTA.

In vitro analysis of Caspase-3 activity

Cells were lysed in a buffer containing 50 mM HEPES (ICN, USA) pH 7.4, 0.1% CHAPS (Sigma), 0.5% IGEPAL-100 (ICN), and 5 mM DTT (Sigma) for 30 min at 4°C. An equal quantity of proteins from lysates was added to the reaction solution (40 mM HEPES pH 7.4, 0.1% CHAPS, 1 ммMM DTT, and 40 μM of AcDEVD-AMC fluorogenic substrate (Sigma)). The mixture was incubated for 1 h at 37°C. Fluorescence was measured using a GloMax®-Multi Jr detection system.

Immunoblotting

Cells were lysed in PBS containing 1% NP-40, 0.5% sodium deoxycholate, 0.1% SDS, protease, and phosphatase inhibitors and then centrifuged. Protein concentrations in samples were estimated using the Bradford assay; an equal amount of protein from each sample was loaded on the gel. Antibodies against

Oct4, Sox2 (Santa Cruz, USA), LC3 (Cell Signaling, USA), and α-tubulin (Sigma) were used as primary antibodies. Anti-mouse rabbit antibodies and anti-rabbit goat antibodies conjugated to horseradish peroxidase were used as secondary antibodies. Proteins were detected by enhanced chemiluminescence (ECL, Amersham, United Kingdom). The obtained results were densitometry analyzed using ImageJ software. Values were normalized to the control load (α-tubulin) and expressed in relative units.

Statistical data analysis

The obtained data were analyzed using GraphPad Prism version 8 software package. The results are presented as a mean ± standard error of the mean. Mean values were compared using Student's t-test with Bonferroni correction.

RESULTS

Autophinib exerts a pronounced cytotoxic effect on A549 cancer cells

Working concentrations of the pharmacological agents Autophinib, SBI-0206965, Siramesine, MRT68921, and IITZ-01 were selected from published data based on the following principles: (1) the selected concentration does not cause death in > 50% of cells after 24 h, and (2) the selected concentration makes it possible to study stemness of surviving cells after 3 days of treatment. The obtained data showed that Autophinib (5 μM), SBI-0206965 (1 μM), Siramesine (0.5 μM), MRT68921 (1 μM), and IITZ-01 (1 μM) caused the death of ⩽ 30% of A549 cells after one day of treatment (*Fig. 1A*). The number of dead A549 cells increased to 40% three days after treatment with SBI-0206965, Siramesine, MRT68921, and IITZ-01 (*Fig. 1A*). Autophagy inhibitor Autophinib exerted a pronounced cytotoxic effect on both day 1 (slightly > 30% of dead cells) and day 3 after treatment (~60% of dead cells) (*Fig. 1A*). Caspase-3 activity assay *in vitro* showed that all autophagy modulators above activate apoptosis in A549 cells, with Autophinib demonstrating the most pronounced pro-apoptotic effect (*Fig. 1B*). SBI-0206965, Siramesine, MRT68921, and IITZ-01 enhanced caspase-3 activation approximately twofold compared to the control 1 day after treatment; Autophinib increased caspase-3 activity approximately 3-fold (*Fig. 1B*). Thus, Autophinib showed the highest effectiveness in eliminating A549 cancer cells.

In order to assess the effectiveness of autophagy inhibition by the selected concentration range of the pharmacological agents Autophinib, SBI-0206965,

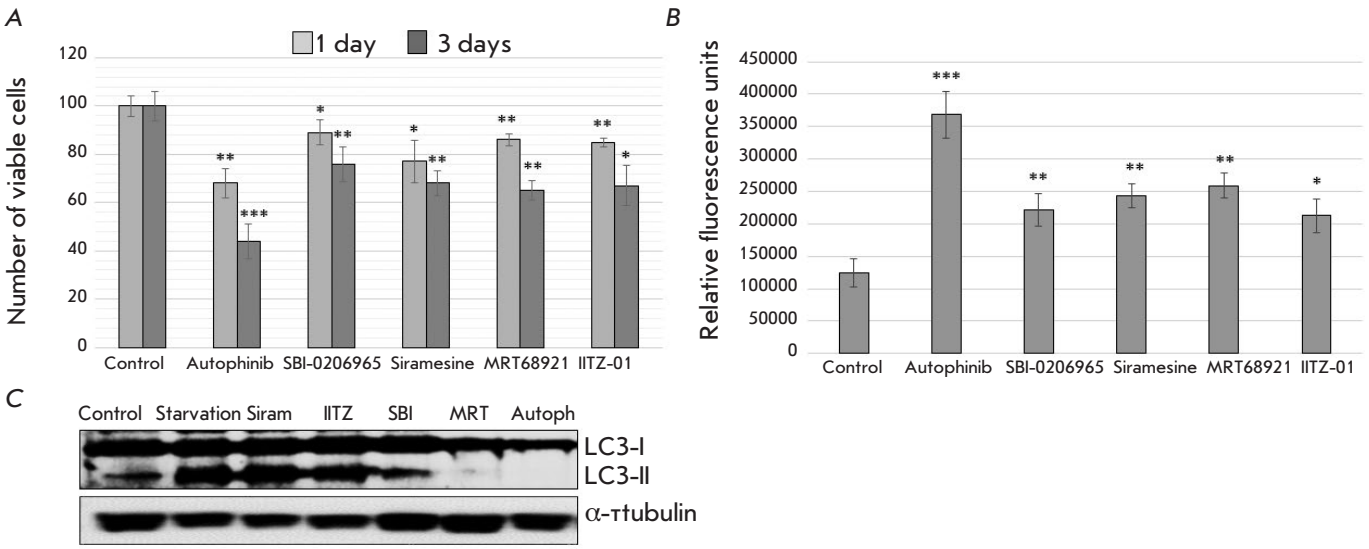

Fig. 1. The effect of autophagy inhibitors on A549 cancer cell survival. (*A*) – Flow cytometry analysis of the number of living cells after treatment with Autophinib, SBI-0206965, Siramesine, MRT68921, and IITZ-01. Results are obtained after DAPI staining of the cell population. The cells were counted on days 1 and 3 of treatment with the indicated agents (n = 10,000 events). Error bars correspond to mean ± SEM (n = 3), * $p < 0.05$, ** $p < 0.05$, *** $p < 0.005$. (*B*) – *In vitro* caspase-3 assay in the control A549 cells and A549 cells treated with Autophinib, SBI-0206965, Siramesine, MRT68921, and IITZ-01 after 1 day. Error bars correspond to mean ± SEM (n = 3), * $p < 0.05$, ** $p < 0.05$, *** $p < 0.005$. (*C*) – Immunoblotting of cell lysates obtained from the control A549 cells and A549 cells under conditions of serum starvation for 4 h. The A549 cells were treated with Autophinib, SBI-0206965, Siramesine, MRT68921, and IITZ-01 for 4 h under conditions of serum starvation. The Anti-LC3-I/II and -α-tubulin antibodies were used

Siramesine, MRT68921, and IITZ-01, we used anti-LC3 protein antibodies. The second form of this protein, LC3-II, is known to be formed through conjugation of the cytosol form of LC3 (LC3-I) with phosphatidylethanolamine on the surface of newly formed autophagosomes. Therefore, LC3-II is assumed to specifically label autophagosomes and autophagolysosomes and can be an indication of enhanced autophagy in cells. Based on the obtained results, it appears that the autophagic activity in A549 cells induced by 4-h serum starvation is effectively inhibited by Autophinib, SBI-0206965, and MRT68921 (*Fig. 1C*). Treatment with Siramesine and IITZ-01 resulted in LC3-II accumulation in cells similar to serum starvation in the absence of the abovementioned agents. This is apparently due to the fact that the mechanism of autophagy inhibition by Siramesine and IITZ-01 mainly has to do with lysosomal destabilization and, thus, does not interfere with autophagy at early stages until the accumulation of LC3-II-labeled autophagosomes. It is interesting to note that, of all the Ulk1/Ulk2 inhibitors used, MRT68921 showed the highest effectiveness in inhibiting autophagy in A549 cells compared to SBI-0206965 (*Fig. 1C*). Autophinib fully prevents LC3-II accumulation, which is an indication of effective suppression of this process in cells.

Autophinib downregulates Sox2 expression in A549 cancer cells

Transcription factors with robust expression in embryonic stem cells are considered stemness drivers in cancer cells. Moreover, Sox2 and Oct4 expression levels correlate with the histological degree of tumor malignancy; these proteins are often used as prognostic markers of cancer cell response to therapy and disease outcome [13, 14]. In order to fully characterize the Sox2 and Oct4 expression levels in A549 cancer cells, the cells were transduced with a lentiviral vector carrying the SORE6-mCherry fluorescent reporter [12]. SORE6-mCherry contains six repeats of promoter region sequences for binding Sox2 and Oct4. Recruitment of these transcription factors results in the induction of transcription of the red fluorescent protein mCherry. This fluorescent protein has been designed for the detection of cancer stem cells [12]. *Figure 2A* shows that transduced A549 cells have a significant fluorescence intensity in the red spectrum, which allows for the identification of the Oct4 and Sox2 activities. According to the obtained results, lentiviral transduction does not change the Sox2 expression at neither the gene nor protein level, which indicates the applicability of the model used in this study (*Fig. 2B* and *C*). We further studied the effect of Autophinib, SBI-0206965, Siramesine, MRT68921, and IITZ-01 on the Oct4 and Sox2 protein levels in A549 cells 3 days after treatment. The Oct4 protein level was shown to remain the same after treatment with each of the pharmacological agents, while the Sox2 level decreased in A549 cells after treatment with Autophinib and did not change in the presence of SBI-0206965, Siramesine, MRT68921, or IITZ-01 (*Fig. 2D*). Analysis of the Oct4 and Sox2 expression levels in A549 cells transduced with the SORE6-mCherry lentiviral vector confirmed a decrease in stemness in cancer cells in the presence of Autophinib (*Fig. 2E*). Transformed A549 cells were cultured in the presence of the autophagy inhibitors Autophinib, SBI-0206965, Siramesine, MRT68921, and IITZ-01 for 3 days and then analyzed using flow cytometry. Based on the obtained data, the fluorescence intensity of the reporter vector SORE6-mCherry decreases significantly in A549 cells after treatment with Autophinib (*Fig. 2E*). Western blotting results (*Fig. 2D*) allow us to assume that the decrease in fluorescence intensity is associated with a reduction in Sox2, but not Oct4, activity: the level of the latter remains the same in the presence of Autophinib. We can assume that the cytotoxic effect of Autophinib is accompanied by a decrease in cell stemness and, therefore, has a pronounced effect. Thus, the obtained data demonstrate that, of the selected panel of autophagy inhibitors, only Autophinib altered the stemness characteristics of A549 cells.

Treatment of A549 cells with Autophinib inhibits the formation of tumor spheroids

Tumor spheroids are three-dimensional (3D) structures formed by cancer cells that imitate solid tumors *in vivo* in numerous key aspects such as heterogeneous architecture, internal gradients of signaling factors, nutrients, and oxygenation. Tumor spheroids are a more adequate model of drug resistance compared to monolayer cultures [15]. To evaluate the malignant potential of the surviving A549 cells after treatment with Autophinib, SBI-0206965, Siramesine, MRT68921, and IITZ-01, we analyzed the ability of cancer cells to form spheroids. A549 cells were pre-cultured in the presence of the abovementioned agents for 3 days, dissociated, and cultured in special conditions for the formation of 3D structures. The obtained data shows that A549 cells treated with SBI-0206965, Siramesine, MRT68921, and IITZ-01 could form spheroids of $\geqslant$ 50 μm, although to a lesser extent compared to the control (*Fig. 3*). Apparently, the reduced number of spheroids formed from the pretreated A549 cells is due to the apoptotic program initiated by these agents, which had been preserved in the cells used for the formation of the 3D structures. Autophinib can significantly

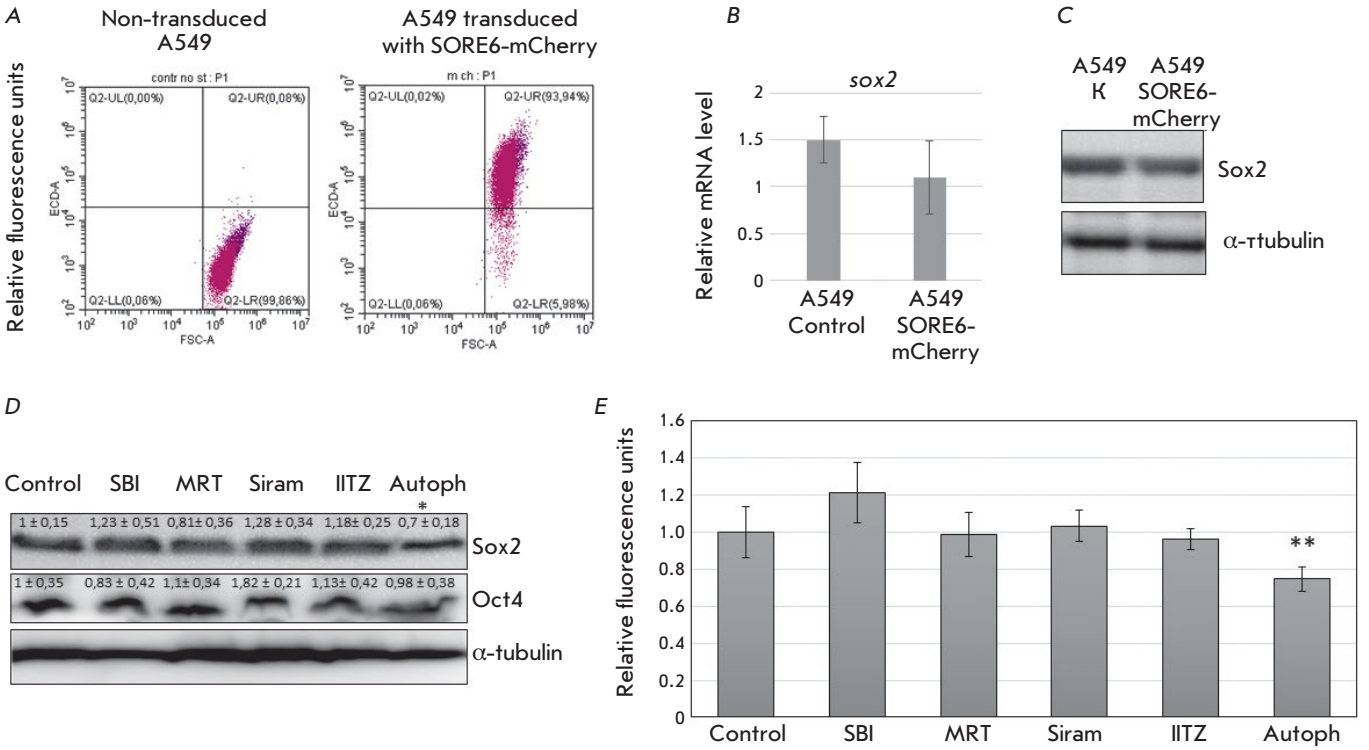

Fig. 2. The effect of autophagy inhibitors on Sox2 and Oct4 expression in A549 cancer cells. (*A*) – Flow cytometry analysis of non-transduced A549 cells and cells transduced with the lentiviral SORE6-mCherry vector. Fluorescence was detected in the red (ECD-A) channel. (*B*) – Analysis of *sox2* mRNA expression by quantitative RT-PCR in the control A549 cells and cells treated for 1 and 3 days with the indicated drugs. Expression was normalized to *gapdh*. (*C*) – Immunoblotting of cell lysates for the Sox2 protein in non-transduced A549 cells and cells transduced with the SORE6-mCherry vector. *α-tubulin* was used as a load control. (*D*) – Immunoblotting of cell lysates for the Sox2, Oct4, and α-tubulin proteins in A549 cells after treatment with the indicated drugs for three days. The results are densitometric and presented as mean ± SEM (n = 3), * $p < 0.05$. (*E*) – Flow cytometry analysis of fluorescent emission of the reporter vector SORE6-mCherry in A549 cells after treatment with the indicated drugs for three days. Flow cytometry results are presented as diagrams. The mean fluorescence value was determined based on three independent experiments, excluding cell autofluorescence. Error bars correspond to mean ± SEM (n = 3), ** $p < 0.05$

block the potential of cancer cells to form spheroids, which may be due to severe impairment of intracellular proteostasis in A549. Apparently, Autophinib can have an irreversible impact on cancer cells, leading to their inability to restore homeostasis and resulting in their elimination.

DISCUSSION

Recently, numerous autophagy-inhibiting compounds have been developed. Their use is hoped to result in the massive death of cancer cells, accompanied by low toxicity for healthy human cells [16, 17]. Some autophagy-modulating drugs are already utilized in clinical practice (rapamycin, chloroquine, and hydroxychloroquine), while others are undergoing clinical trials (mTOR kinase inhibitors) [17, 18]. The fact that around 70% of clinical studies are now focused on the role of autophagy in oncogenesis points to the high expectations vested in the use of autophagy modulation in the treatment of cancer [19].

This study was an attempt to assess the potential therapeutic significance of Autophinib, SBI-0206965, Siramesine, MRT68921, and IITZ-01 in the elimination of A549 cancer stem cells. We showed that only Autophinib – among all the examined autophagy inhibitors – exerts a pronounced antitumor effect by decreasing cancer cell stemness, inducing apoptosis in tumor, and preventing cancer cell population renewal. Apparently, the antitumor effects of Autophinib are achieved through severe disruption of the cellular proteostasis caused by the inhibition of Vps34, followed by the inhibition of not only autophagy. This is because lipid kinase Vps34 is one of the main producers of phosphatidylinositol-3-phosphate in the cell, which, in turn, recruits the corresponding proteins to the membranes. Thus, Vps34 plays a key role not only

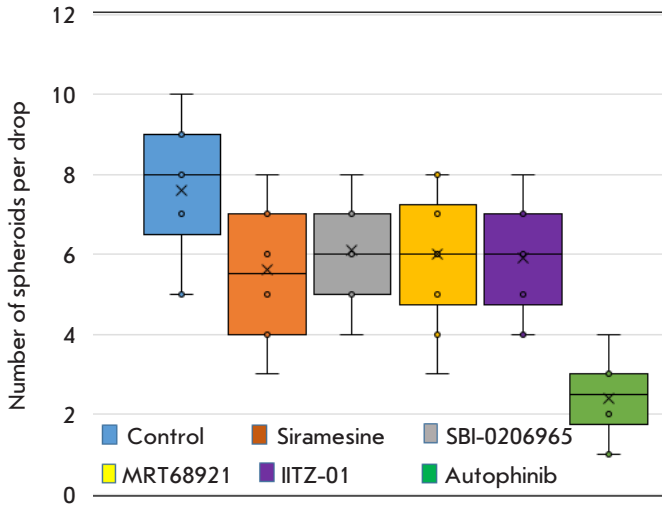

Fig. 3. Effect of autophagy inhibitors on the ability of A549 cells to form spheroids. The results are presented as box plots. Spheres with a size of at least 50 μm were counted in one drop

in autophagy induction and formation of the primary membrane with recruitment of membrane protein complexes, but also in endocytosis [20, 21]. For this reason, Vps34 inhibition leads to the suppression of membrane vesicle formation, which is necessary in both autophagy and endocytosis, since it disrupts intracellular homeostasis. In addition, endocytosis mostly mediates the interaction between cells in the tumor, and its impairment can separate cancer cells [22]. Apparently, inability of A549 cells to form spheroids after they are treated with Autophinib is also due to the damage caused to intercellular communication. Thus, the antitumor effect of Autophinib is associated with not only autophagy inhibition, but also the functioning of other signaling pathways. For this reason, pharmacological agents such as SBI-0206965 and MRT68921 that block autophagy through a targeted inhibition of proteins Ulk1 and Ulk2 turn out to be less toxic to A549 cancer stem cells than Autophinib. It is interesting to note that Siramesine and IITZ-01 also demonstrated a poor tumor elimination activity in A549 cells, despite the fact that their action is associated with a destabilization of lysosomes, which are required in both autophagy and endocytic pathways. Nevertheless, inhibition of kinase Vps34 has turned out to be a less effective strategy in eliminating cancer stem cells in both our study and other works. Vps34 activity is shown to be necessary for the expansion of cancer stem cells in the liver: RNA-interference of this protein has the opposite effect in the form of tumor growth suppression *in vivo* [23]. In addition, pharmacological inhibition of Vps34 effectively eliminates the cancer stem cell population in the liver and also inhibits tumor growth *in vivo* [23]. Inhibition of Vps34 activity effectively eliminates cancer stem cells in the presence of combination therapy in a model of tumor spheroids [24]. A combination therapy with 5-fluorouracil and the drug 36-077, which is a Vps34 inhibitor, mainly kills tumor cells with the stem cell phenotype [24].

The results obtained and data published by us indicate that a pharmacological approach to autophagy inhibition in cancer cells should be aimed at cross-signaling pathways. Monotherapy based on autophagy inhibition is currently considered ineffective [19]. The main reasons for this are the following: (1) the dual role of autophagy in cancer, (2) the absence of therapeutically suitable autophagy inhibitors, and (3) the lack of knowledge about cross-interactions between autophagy and other signaling pathways in the cell. Co-inhibition of autophagy and endocytic pathways through Vps34 inhibition can be a good strategy for eliminating cancer stem cells. Therefore, the study of autophagy in terms of vesicular transport can be considered a promising research path. ●

This study was financially supported by the Ministry of Science and Higher Education of the Russian Federation (grant agreement No. 075-15-2020-773). Cell lines were obtained from the Center for Collective Usage "Vertebrate Cell Culture Collection" supported by the Ministry of Education and Science of the Russian Federation (agreement No. 075-15-2021-683).

REFERENCES

1. Robke L., Laraia L., Corrales M.A., Konstantinidis G., Muroi M., Richters A., Winzker M., Engbring T., Tomassi S., Watanabe N., et al. // Angew. Chem. Int. Ed. Engl. 2017. V. 56. № 28. P. 8153–8157.
2. Li H., Li M., Chen K., Li Y., Yang Z., Zhou Z. // Med. Oncol. 2022. V. 39. № 12. P. 244.
3. Russell R.C., Tian J., Yuan H., Park H.W., Chang Y-Y., Kim J., Kim H., Neufeld T.P., Dillin A., et al. // Nat. Cell. Biol. 2013. V. 15. № 7. P. 741–750.
4. Petherick K.J., Conway O.J.L., Mpamhanga C., Osborne S.A., Kamal A., Saxty B., Ganley I.G. // J. Biol. Chem. 2015. V. 290. № 18. P. 11376–11383.
5. Egan D.F., Chun M.G.H., Vamos M., Zou H., Rong J., Miller C.J., Lou H.J., Raveendra-Panickar D., Yang C.-C., Sheffler D.J., et al. // Mol. Cell. 2015. V. 59. № 2. P. 285–297.
6. Chen Y., Xie X., Wang C., Hu Y., Zhang H., Zhang L., Tu S., He Y., Li Y. // Cell. Death Dis. 2020. V. 11. № 8. P. 712.
7. Singha B., Laski J., Ramos Valdés Y., Liu E., DiMattia

G.E., Shepherd T.G. // Am. J. Cancer Res. 2020. V. 10. № 5. P. 1384–1399.
8. Zheng Y., Liu L., Wang Y., Xiao S., Mai R., Zhu Z., Cao Y. // Cell Biosci. 2021. V. 11. № 1. P. 63.
9. Guntuku L., Gangasani J.K., Thummuri D., Borkar R.M., Manavathi B., Ragampeta S., Vaidya J.R., Sistla R., Vegi N.G.M. // Oncogene. 2019. V. 38. № 4. P. 581–595.
10. Perregaard J., Moltzen E.K., Meier E., Sánchez C. // J. Med. Chem. 1995. V. 38. № 11. P. 1998–2008.
11. Ostenfeld M.S., Høyer-Hansen M., Bastholm L., Fehrenbacher N., Olsen O.D., Groth-Pedersen L., Puustinen P., Kirkegaard-Sørensen T., Nylandsted J., Farkas T., et al. // Autophagy. 2008. V. 4. № 4. P. 487–499.
12. Tang B., Raviv A., Esposito D., Flanders K.C., Daniel C., Nghiem B.T., Garfield S., Lim L., Mannan P., Robles A.I., et al. // Stem Cell Reports. 2015. V. 4. № 1. P. 155–169.
13. Zhao X., Lu H., Sun Y., Liu L., Wang H. // Medicine (Baltimore). 2020. V. 99. № 42. P. e22804.
14. Yuan D., Wang J., Yan M., Xu Y. // Int. J. Biol. Markers. 2021. V. 36. № 4. P. 45–53. https://doi.org/10.1177/17246008211042899
15. Ishiguro T., Ohata H., Sato A., Yamawaki K., Enomoto T., Okamoto K. // Cancer Scie. 2017. V. 108. № 3. P. 283–289.
16. Ariosa A.R., Lahiri V., Lei Y., Yang Y., Yin Z., Zhang Z., Klionsky D.J. // Biochim. Biophys. Acta Mol. Basis Dis. 2021. V. 1867. № 12. P. 166262.
17. Mohsen S., Sobash P.T., Algwaiz G.F., Nasef N., Al-Zeidaneen S.A., Karim N.A. // Curr. Oncol. 2022. V. 29. № 3. P. 1695–1708.
18. Amaravadi R.K. // Autophagy. 2022. V. 18. № 6. P. 1470–1471.
19. Marinković M., Šprung M., Buljubašić M., Novak I. // Oxid. Med. Cell. Longev. 2018. V. 2018. P. 8023821.
20. Lindmo K., Stenmark H. // J. Cell. Sci. 2006. V. 119. № 4. P. 605–614.
21. Nascimbeni A.C., Codogno P. // FEBS J. 2017. V. 284. № 9. P. 1267–1278.
22. Wu B., Wang Q., Shi X., Jiang M. // Cell Commun. Signaling. 2022. V. 20. № 1. P. 161.
23. Liu F., Wu X., Qian Y., Jiang X., Wang Y., Gao J. // Cell Death Dis. 2020. V. 11. № 6. P. 427.
24. Kumar B., Ahmad R., Sharma S., Gowrikumar S., Primeaux M., Rana S., Natarajan A., Oupicky D., Hopkins C.R., Dhawan P., et al. // Cancers (Basel). 2021. V. 13. № 9. P. 2168.

An Analysis of Genetic Predisposition to Hereditary Catalepsy in a Mouse Model of Neuropsychiatric Disorders Using Whole-Genome Sequencing Data

T. V. Andreeva[1,2*], F. E. Gusev[1,2], N. A. Sinyakova[3], A. V. Kulikov[3], A. P. Grigorenko[2], I. Yu. Adrianova[2], D. V. Bazovkina[4], E. I. Rogaev[2,5]

[1]Center for Genetics and Life Science, Sirius University of Science and Technology, Sochi, 354340 Russian Federation

[2]Vavilov Institute of General Genetics RAS, Department of Human Genomics and Genetics, Moscow, 119991 Russian Federation

[3]Institute of Cytology and Genetics RAS, Department of Genetic Collection of Neuropathologies, Novosibirsk, 630090 Russian Federation

[4]Institute of Cytology and Genetics RAS, Laboratory of Neurogenomics of Behavior, Novosibirsk, 630090 Russian Federation

[5]UMass Chan Medical School, Department of Psychiatry, Shrewsbury, MA, 01545, USA

[*]E-mail: an_tati@vigg.ru, Evgeny.Rogaev@umassmed.edu

Received December 12, 2022; in final form, January 23, 2023

DOI: 10.32607/actanaturae.11875

ABSTRACT **Catalepsy is a behavioral condition that is associated with severe psychopathologies, including schizophrenia, depression, and Parkinson's disease. In some mouse strains, catalepsy can be induced by pinching the skin at the scruff of the neck. The main locus of hereditary catalepsy in mice has recently been linked to the 105–115 Mb fragment of mouse chromosome 13 by QTL analysis. We performed whole-genome sequencing of catalepsy-resistant and catalepsy-prone mouse strains in order to pinpoint the putative candidate genes related to hereditary catalepsy in mice. We remapped the previously described main locus for hereditary catalepsy in mice to the chromosome region 103.92–106.16 Mb. A homologous human region on chromosome 5 includes genetic and epigenetic variants associated with schizophrenia. Furthermore, we identified a missense variant in catalepsy-prone strains within the *Nln* gene. *Nln* encodes neurolysin, which degrades neurotensin, a peptide reported to induce catalepsy in mice. Our data suggest that *Nln* is the most probable candidate for the role of major gene of hereditary, pinch-induced catalepsy in mice and point to a shared molecular pathway between catalepsy in mice and human neuropsychiatric disorders.**

KEYWORDS **catalepsy, mice, genome, brain, neurolysin.**

INTRODUCTION

Catalepsy is a natural condition characterized by a prolonged freezing reaction and the inability to correct an externally imposed awkward posture; it is a passive, defensive behavior found in most vertebrates. In humans, the defensive role of catalepsy is lost and it is a symptom of a number of severe mental and nervous diseases, such as schizophrenia and depression [1, 2].

In rodents, catalepsy can be caused by dopamine D2 receptor blockade with neuroleptics such as haloperidol or morphine [3–6]. Drug-free catalepsy in mice (Supplementary file 1. Mouse with pinch-induced catalepsy (video file), see https://evolgenomics.org/catalepsy/)) can be induced by pinching the skin at the scruff of the neck [7], and there are significant differences between strains, in terms of their predisposition to this type of catalepsy. Mice of the most common inbred strains, such as C57BL/6J, DBA/2, and AKR/J, are resistant to pinch-induced catalepsy, but about 50% of CBA/Lac mice

show hereditary catalepsy associated with depressive-like features and sensitivity to chronic antidepressant drug treatment [8–11].

The main locus of hereditary catalepsy in mice has recently been mapped through QTL analysis to the distal part (61–70 cM) of chromosome 13 [12]. The genetic linkage was verified by the selective breeding experiment in [13] and transferring of the CBA-derived distal fragment of chromosome 13 between the D13Mit74 and D13Mit214 genetic markers to the genome of the catalepsy-resistant strain AKR. About 50% of mice of the congenic AKR.CBA-D13Mit76 strain showed severe catalepsy, similar to CBA mice [10]. The ASC/Icg (Antidepressant Sensitive Catalepsy) strain was created by selective breeding of CBA × (CBA × AKR) backcrosses for predisposition to catalepsy. Hereditary catalepsy in CBA mice was shown to come with depressive-like features and sensitivity to chronic antidepressant drug treatment [2, 9, 11, 14]. About 80–85% of ASC mice exhibited catalepsy [13], but the candidate genes for pinch-induced catalepsy in mice remain poorly understood.

Here, we performed whole-genome sequencing of the catalepsy-resistant (AKR/J) and catalepsy-prone mouse strains (CBA, AKR.CBA-D13Mit76, and ASC) in order to identify the putative candidate genes or chromosomal loci involved in the mechanisms of hereditary catalepsy in mice.

EXPERIMENTAL PROCEDURES

Animals

Mice of the catalepsy-resistant (AKR/J) and catalepsy-prone (CBA/LacJ) strains which were maintained for more than 50 years at the Institute of Cytology and Genetics (Novosibirsk, Russia) and animals of the congenic AKR.CBA-D13Mit76 strain, with the CBA-derived fragment of chromosome 13 carrying the major gene of catalepsy transferred to the AKR genome and ASC strain created for hereditary predisposition to catalepsy, were used in this study. All animal experiments were approved by the Ethics Committee of the Institute of Cytology and Genetics RAS. All the experimental procedures were performed in compliance with the European Communities Council Directive dated November 24, 1986 (86/609/EEC). The animals were tested for catalepsy (including the AKR/J strain for the absence of catalepsy) as described earlier [15]. The test was regarded as positive if the mouse retained the imposed posture for at least 20 s. The animals with a positive pinch response (except for the control line AKR) were selected.

Table 1. Genome sequencing statistics for the four mouse strains

Sample (strain)	Total reads	% mapped Grcm38/mm10	Mean genome coverage
HT76	561995272	99.56	19 ×
ASC	720038088	99.35	23 ×
CBA	555706906	97.95	17 ×
AKR	986011514	99.49	33 ×

Whole-genome sequencing

Genomic DNA was extracted from mouse tail fragments (3–4 mm long). One tail fragment was used for DNA extraction for the animals of the AKR and D13Mit76C strains, and mixtures of tail fragments from two animals were used for DNA preparation for the ASC and CBA strains. DNA was purified using QIAamp DNA Mini columns (QIAGEN, Hilden, Germany). A total of 1.5 μg of genomic DNA was used for library preparation using the TruSeq DNA Sample Preparation kit v2 (Illumina, San Diego, CA, USA). Paired-end DNA libraries with a mean insert size of 350 bp were sequenced on an Illumina HiSeq2000 platform as paired-end 101 base reads. The sequence data generated for this study were submitted to the NCBI SRA (http://www.ncbi.nlm.nih.gov/sra) under accession number PRJNA900682.

Sequencing data analysis and statistics

The raw data were aligned to the reference mouse genome (Grcm38/mm10) using a BWA v. 0.7.17 [16] and Sarek v.2.7.1 workflow [17]. PCR duplicates were marked using the Picard tool (http://broadinstitute.github.io/picard/). Genetic variants were called using the GATK v. 4.1.7.0 [18] and annotated using the VEP software [19]. Structural variants were predicted with Manta 1.6.0 [20]. Whole-genome sequencing on an Illumina HiSeq2000 system resulted in a mean mouse genome coverage of 17–33× (*Table 1*).

RESULTS AND DISCUSSION

Fine mapping of the main cataleptic locus

It was shown previously that hereditary catalepsy is a homozygous recessive condition [8]; therefore, we used only the homozygous variants that were found in the distal fragment of chromosome 13 in mice of

Table 2. Missense homozygous variants in the major catalepsy locus of chromosome 13 found in all cataleptic mice genomes but not in the non-cataleptic mice genome

Variant	Existing variation	Gene	Consequence	SIFT [23]
13:104069202 T/C	rs50518036	*Nln*	H148R	tolerated(0.35)
13:104111134 G/A	rs51459950	*Sgtb*	C7Y	deleterious(0.01)
13:104111173 A/G	rs50301687	*Sgtb*	N20S	tolerated(0.99)
13:104174454 T/C	rs51569005	*Shld3*	I150V	tolerated(0.41)
13:104174470 G/T	rs219600951	*Shld3*	S144R	tolerated(0.68)
13:104220239 T/C	rs221133823	*Ppwd1*	E256G	tolerated(0.23)
13:104220303 A/G	rs49763463	*Ppwd1*	Y235H	tolerated(0.11)
13:104230784 G/T	rs48594661	*Cenpk*	V43L	tolerated(1)
13:104312759 T/A	rs45772491	*Adamts6*	S226T	tolerated(0.29)

all three catalepsy-prone strains (CBA, D13Mit76C, and ASC), but were absent in the AKR mouse strain, to search for the candidate catalepsy genes in this region.

Earlier, the main gene of catalepsy was mapped on the terminal fragment of mouse chromosome 13; the CBA-derived fragment of this chromosome, marked with D13Mit76, was then transferred to the genome of AKR, and the AKR.CBA-D13Mit76 recombinant line was created. The major gene of catalepsy was mapped further between 105.8 and 115.3 Mb of mouse chromosome 13 using the microsatellite mapping technique [10]. However, because microsatellite mapping is not sufficiently precise, the boundaries of the transferred fragment could be different. In order to remap the previously identified main catalepsy locus, we analyzed the distribution of parental (AKR and CBA-specific) homozygous variants in both the ASC and AKR.CBA-D13Mit76 strains on the distal fragment of chromosome 13 and found homozygous CBA-specific variants at the 103.92–106.16 Mb fragment in both the ASC and AKR.CBA-D13Mit76 strains.

We have determined that this locus is homologous to the human chromosome 5 region between 63.24 Mb and 65.93 Mb (according to the human reference genome GRCh38) and have screened this locus against a database of human GWAS [21]. Among others, we observed several statistically significant associations with educational attainment and cognitive performance, but also nominally significant associations with schizophrenia and major depressive disorder (Supplementary table S1. Genetic associations in the human genome region homologous to the main catalepsy region). Next, we overlapped this region with the recently reported [22] schizophrenia brain ChIP-seq data for histone 3 lysine 27 acetylation (H3K27ac), a marker of active enhancers. We found that five out of 76 H3K27ac peaks within the locus are epigenetically dysregulated in schizophrenia, specifically in neuronal cells, and that seven out of 114 H3K27ac peaks are dysregulated in bulk brain tissue (Supplementary table S2. H3K27ac regions dysregulated in schizophrenia found in the human genome region homologous to the main catalepsy region). Overall, these data indicate a shared molecular pathway between pitch-induced catalepsy in mice and human neuropsychiatric disorders.

Coding variants in the chromosome 13 cataleptic locus

In total, we observed 13,147 genomic positions harboring short variants (SNPs and indels) in this main locus of hereditary catalepsy. We found that 6,087 of those have an allele present in all three sequenced genomes from cataleptic strains in the homozygous state but absent in the non-cataleptic strain (Supplementary table S3. Candidate short genetic variants). We also observed 239 putative structural variants in this locus, with 21 variants specific to catalepsy strains (found in all three, but not in the non-cataleptic genome). However, neither of them affects the protein-coding

sequence (Supplementary table S4. Candidate large structural variants).

For further analysis, we prioritized the variations observed in protein-encoding regions and found nine of those to affect protein-coding genes in catalepsy-prone mice strains compared with non-catalepsy AKR mouse (*Table 2*). We analyzed all the coding variants in the GenBank genome assemblies for 14 reference mouse strains (DBA_2J_v3, BALB_cJ_v3, A_J_v3, CBA_J_v3, C3H_HeJ_v3, AKR_J_v3, NOD_ShiLtJ_v3, FVB_NJ_v3, Mm_Celera, LP_J_v1, PWK_PhJ_v3, WSB_EiJ_v3, CAST_EiJ_v3, and C57BL/6J), including the known catalepsy-resistant (C57BL/6J, DBA/1J) and catalepsy-prone (C3H/HeJ, A/He, BALB/cLac) strains [8]. The catalepsy-prone C3H/HeJ strain carries the total list of these coding variants, just like the CBA strain does, but all variants are missing in the catalepsy-prone lines A/He, BALB/cJ, except for the *Nln* gene mutation. In total, a single-nucleotide variant T > C (rs50518036) in the coding region of the neurolysin gene *Nln* was found in CBA, AKR. CBA-D13Mit76, and ASC mice, as well as in C3H/HeJ, A/He, BALB/cJ mouse strain genome assemblies, while it's absent in the GenBank genomes of catalepsy-resistant mice strains (AKR/J, C57BL/6J, and DBA/1J).

Neurolysin is a metalloendopeptidase, which plays a role in the degradation of neurotensin and bradykinin; both are pharmacological inductors of catalepsy in mice [24–27]. All catalepsy-prone strains contained histidine at position 146 of *nln*, while the catalepsy-resistant AKR strain contained arginine. Neurolysin has never previously been implicated in catalepsy, but this enzyme degrades neurotensin, the peptide that can induce catalepsy [24]. Consequently, the *Nln* gene emerges as the strongest candidate to be the major gene of hereditary pinch-induced catalepsy in mice.

CONCLUSIONS

Whole-genome sequencing of the catalepsy-prone and catalepsy-resistant mouse strains yielded valuable data for remapping the earlier identified main locus for hereditary pinch-induced catalepsy in mice on chromosome 13 to the chromosome region between 103.92–106.16 Mb and uncovered a single, potentially causing mutation in the neurolysin gene *Nln* in the main locus of catalepsy on chromosome 13. The major gene of catalepsy defined about 20% of catalepsy penetrance [10]. Meanwhile, the trait penetrance was 50% in recombinant D13Mit76 mice and 80% in catalepsy-prone ACS mice. The remaining penetrance is obviously the result of other genes and/or the impact of gene regulatory regions. Whole-genome data for the mouse model of hereditary behavior-trait-related depression and schizophrenia in humans should provide another resource for further identification of the genetic and epigenetic factors behind human psychiatric disorders. ●

The present study was supported in part by the Russian Science Foundation Research Project No. 19-75-30039 (bioinformatics analysis of databases and human genome regulatory elements).

The Supplementary Material for this article can be found online https://evolgenomics.org/catalepsy/

REFERENCES

1. Singerman B., Raheja R. // Ann. Clin. Psychiatry. 1994. V. 6. № 4. P. 259–266.
2. Kolpakov V.G., Gilinsky M.A., Alekhina T.A., Barykina N.N., Nikulina E.M., Voitenko N.N., Kulikov A.V., Shtilman N.I. // Behav. Processes. 1987. V. 14. № 3. P. 319–341.
3. Sanberg P.R., Bunsey M.D., Giordano M., Norman A.B. // Behav. Neurosci. 1988. V. 102. № 5. P. 748–759.
4. Klemm W.R. // Prog. Neurobiol. 1989. V. 32. № 5. P. 403–422.
5. VanderWende C., Spoerlein M.T. // Neuropharmacology. 1979. V. 18. № 7. P. 633–637.
6. de Ryck M., Teitelbaum P. // Behav. Neurosci, 1984. V. 98. № 2. P. 243–261.
7. Ornstein K., Amir S. // J. Comp. Physiol. Psychol. 1981. V. 95. № 5. P. 827–835.
8. Kulikov A.V., Kozlachkova E.Y., Maslova G.B., Popova N.K. // Behav. Genet. 1993. V. 23. № 4. P. 379–384.
9. Bazovkina D.V., Kulikov A.V., Kondaurova E.M., Popova N.K. // Genetics. 2005. V. 41, № 9. P. 1222–1228.
10. Kulikov A.V., Bazovkina D.V., Kondaurova E.M., Popova N.K. // Genes. Brain. Behav. 2008. V. 7. № 4. P. 506–512.
11. Tikhonova M.A., Kulikov A.V. // Chin. J. Physiol. 2012. V. 55. № 4. P. 284–293.
12. Kulikov A.V., Bazovkina D.V., Muazan M.P., Mormed P. // Bulletin of the Russian Academy of Sciences. 2003 V. 293. P. 134–137.
13. Kondaurova E.M., Bazovkina D.V., Kulikov A.V., Popova N.K. // Genes. Brain. Behav. 2006. V. 5. № 8. P. 596–601.
14. Kulikov A.V., Kozlachkova E.Yu., Popova N.K. // Genetics. 1989. V. 25, № 8. P. 1402–1408.
15. Kulikov A.V., Kozlachkova E.Y., Kudryavtseva N.N., Popova N.K. // Pharmacol. Biochem. Behav. 1995. V. 50. № 3. P. 431–435.
16. Li H., Durbin R. // Bioinformatics. 2009. V. 25. № 14. P. 1754–1760.
17. Garcia M., Juhos S., Larsson M., Olason P. I., Martin M., Eisfeldt J., DiLorenzo S., Sandgren J., Díaz De Ståhl T., Ewels P., et al. // F1000Research. 2020. V. 9. P. 63.
18. McKenna A., Hanna M., Banks E., Sivachenko A.,

Cibulskis K., Kernytsky A., Garimella K., Altshuler D., Gabriel S., Daly M., et al. // Genome Res. 2010. V. 20. № 9. P. 1297–1303.
19. McLaren W., Gil L., Hunt S.E., Singh Riat H., Ritchie G.R.S., Thormann A., Flicek P., Cunningham F. // Genome Biol. 2016. V. 17. № 122. P. 1–14.
20. Chen X., Schulz-Trieglaff O., Shaw R., Barnes B., Schlesinger F., Källberg M., Cox A.J., Kruglyak S., Saunders C.T. // Bioinformatics. 2016. V. 32. № 8. P. 1220–1222.
21. Buniello A., MacArthur J.A.L., Cerezo M., Harris L.W., Hayhurst J., Malangone C., McMahon A., Morales J., Mountjoy E., Sollis E., et al. // Nucl. Acids Res. 2019. V. 47. № D1. P. 1005–1012.
22. Girdhar K., Hoffman G.E., Bendl J., Rahman S., Dong P., Liao W., Hauberg M.E., Sloofman L., Brown L, Devillers O., et al. // Nat. Neurosci. 2022. V. 25. № 4. P. 474–483.
23. Adzhubei I.A., Schmidt S., Peshkin L., Ramensky V.E., Gerasimova A., Bork P., Kondrashov A.S., Sunyaev S.R. // Nat. Methods. 2010. V. 7. № 4. P. 248–249.
24. Dunn A.J., Snijders R., Hurd R.W., Kramarcy N.R. // Ann. N. Y. Acad. Sci. 1982. V. 400. № 1. P. 345–353.
25. Snuders R., Kramarcy N.R., Hurd R.W., Nemeroff C.B., Dunn A.J. // Neuropharmacology. 1982. V. 21. № 5. P. 465–468.
26. Bhattacharya S.K., Rao P.J.R.M., Brumleve S.J., Parmar S.S. // Pharm. Res. 1986. V. 3. № 3. P. 162–166.
27. Dixon A.K. // Br. J. Med. Psychol. 1998. V. 71. № 4. P. 417–445.

Genetic Variants Associated with Bronchial Asthma Specific to the Population of the Russian Federation

Y. N. Akhmerova[1*#], T. A. Shpakova[1#], K. S. Grammatikati[1#], S. I. Mitrofanov[1#], P. G. Kazakova[1], A. A. Mkrtchian[1], P. U. Zemsky[1], M. N. Pilipenko[1], N. V. Feliz[1], L. V. Frolova[1], A. A. Frolovskaya[1], V. S. Yudin[1], A. A. Keskinov[1], S. A. Kraevoy[1], S. M. Yudin[1], V. I. Skvortsova[2]

[1]Federal State Budgetary Institution "Center for Strategic Planning and Management of Biomedical Health Risks" of the Federal Medical Biological Agency (Center for Strategic Planning of FMBA of Russia), Moscow, 119121 Russian Federation

[2]Federal Medical Biological Agency (FMBA of Russia), Moscow, 123182 Russian Federation

#These authors contributed equally.

*E-mail: YUAhmerova@cspfmba.ru

Received November 7, 2022; in final form, January 9, 2023

DOI: 10.32607/actanaturae.11853

ABSTRACT **Bronchial asthma (BA) is a disease that still lacks an exhaustive treatment protocol. In this regard, the global medical community pays special attention to the genetic prerequisites for the occurrence of this disease. Therefore, the search for the genetic polymorphisms underlying bronchial asthma has expanded considerably. As the present study progressed, a significant amount of scientific medical literature was analyzed and 167 genes reported to be associated with the development of bronchial asthma were identified. A group of participants (n = 7,303) who had voluntarily provided their biomaterial (venous blood) to be used in the research conducted by the Federal Medical Biological Agency of Russia was formed to subsequently perform a bioinformatic verification of known associations and search for new ones. This group of participants was divided into four cohorts, including two sex-distinct cohorts of individuals with a history of asthma and two sex-distinct cohorts of apparently healthy individuals. A search for polymorphisms was made in each cohort among the selected genes, and genetic variants were identified whose difference in occurrence in the different cohorts was statistically significant (significance level less than 0.0001). The study revealed 11 polymorphisms that affect the development of asthma: four genetic variants (rs869106717, rs1461555098, rs189649077, and rs1199362453), which are more common in men with bronchial asthma compared to apparently healthy men; five genetic variants (rs1923038536, rs181066119, rs143247175, rs140597386, and rs762042586), which are more common in women with bronchial asthma compared to apparently healthy women; and two genetic variants (rs1219244986 and rs2291651) that are rare in women with a history of asthma.**

KEYWORDS **bronchial asthma, polymorphism, phenotype–genotype associations, genetic variants.**

ABBREVIATIONS **BA – bronchial asthma; WHO – World Health Organization; AHR – airway hyperreactivity; GCs – glucocorticoids; IGCs – inhaled glucocorticoids; FEV – forced expiratory volume; bp – base pair; SNP – single-nucleotide polymorphism; PAF – platelet-activating factor.**

INTRODUCTION

Bronchial asthma (BA) is a chronic, recurrent disease whose pathogenesis is associated with altered bronchial reactivity caused by both specific immunological and nonspecific mechanisms. The major (essential) clinical sign of BA involves choking episodes that result from bronchial spasm, mucus hypersecretion, and edema of the bronchial mucosa [1].

The WHO considers bronchial asthma to be among the most serious chronic, non-communicable diseases. Most deaths due to BA occur in low- and middle-income countries, which are characterized by insufficiently efficient diagnosis and treatment capabilities for the disease, as well as the healthcare system in general [2]. Up to 350 million people worldwide currently have BA [1], and this figure may increase to 450 million by 2025 [3].

According to official statistics, there are 1.3 million patients with BA in Russia. This means that the prevalence of this disease in Russia is less than 1%, while

the proportion of people with BA is less than 0.4% of all patients with asthma worldwide. Meanwhile, the European Respiratory Society has estimated the incidence of BA in a number of European countries at 5% among adults and more than 7% among children. A trend towards growing rates of disability and death due to BA is observed in many countries. Thus, the rate of BA deaths in Great Britain has increased sevenfold over the past 20 years, and two- to threefold, in North America. More than 5,000 people die due to BA in the U.S. each year.

BA develops due to a number of factors, including the intensity of allergen exposure, habitat destruction, overactive immune response, and individual genetic features [3]. It has been demonstrated that there is a 25% risk that a child whose parent suffers from bronchial asthma also develop this disease. If both parents have asthma, the risk increases to 50% [4]. Furthermore, it has been proved that there exists an association between the increasing incidence rate of BA and aggravated soil, air, and water contamination [5].

In 2018, the direct expenses of the Russian healthcare system for BA treatment amounted to ~ 8.5 billion rubles; two-thirds of this amount was spent on hospital stays. Moreover, substantial funds are needed to cover temporary disability leaves and disability payments [6]. Early diagnosis and prevention of BA will make it possible both to reduce these costs and the prevalence of bronchial asthma in Russia.

EXPERIMENTAL

Building the cohorts

The manifestation and course of BA is significantly different in men than it is in women, which is largely due to the different contributions of reproductive hormones to the pathogenesis of BA [7]. Therefore, our study participants were divided into cohorts according to such factors as history of BA and sex.

The 7,303 study participants were allotted to four cohorts:

1A – women with a confirmed diagnosis of BA (mean age, 52 ± 10 years), n = 218;

2A – men with a confirmed diagnosis of BA (mean age, 41 ± 12 years), n = 70;

3H – apparently healthy women without a history of BA or other diagnoses with a similar clinical presentation (mean age, 52 ± 8 years), n = 4,015;

4H – apparently healthy men without a history of BA or other diagnoses with a similar clinical presentation (mean age, 44 ± 6 years), n = 3,000.

An inclusion criterion for groups 1A and 2A was a history of bronchial asthma in the anamnesis. Groups 3H and 4H contained visibly healthy men and women; the exclusion criteria for these cohorts were medical records indicating that a patient had a history of diseases whose symptoms were similar to manifestations of BA, such as acute bronchitis, pulmonary emphysema, allergic rhinitis, gastroesophageal reflux, tracheoesophageal fistula, congenital heart disease, tracheomalacia and bronchomalacia, cystic fibrosis, primary ciliary dyskinesia, bronchiectasis of other etiologies, tuberculosis, lung cancer, a vascular ring anomaly, sarcoidosis, intrathoracic lymphadenopathy, bronchopulmonary dysplasia, allergic bronchopulmonary aspergillosis, systemic anaphylaxis, primary immunodeficiency, vocal cord dysfunction, psychogenic cough, and affective respiratory paroxysms [8].

Biomaterial sampling and personal data of study participants

Samples from collections previously created by the Center for Strategic Planning of FMBA of Russia were used in this study. In all cases, the data were collected in full compliance with the procedural requirements: the following respective data were included and verified for each donor: sex, age, region of residence, nationality, past medical history, informed consent (signed by the donor) for biomaterial sampling, handling, transportation, storage and personal data use; proper procedures for sample (venous blood) collection, handling, transportation, and storing was ensured, per the State Standard GOST R53079.4-2008.

All the specimens selected for the final study sample were checked to make sure that the donor's ID code and the information deciphered in that code were unique. Furthermore, it was guaranteed that the biomaterial had no signs of hemolysis or lipemia. The samples were transported under constant temperature control.

Creating a candidate gene list

Over 150 genes associated with the development of BA have been reported thus far. The following tentative gene groups are of special interest:

the atopy-related genes. These genes include *IL4, IL5, IL13, IL4RA, CHI3L1, RAD50*, etc. and are responsible for the blood level of total and specific IgE, as well as the development of allergic responses;

the genes related to bronchial hyperreactivity, including *ADRB2, TNF, IL5, IL9, NOS1, NPSR1, TAC1, TACR2, TACR1, TACR3, ADAM33, ACE*, etc., being responsible for bronchial hyperresponsiveness, which is tightly related to the blood IgE level and inflammation;

the inflammation-related genes such as *TNF, IL4, IL5, IL13, ORMDL3, SCGB3A2, CCL11, IRAK3, CSF2,*

ALOX5, CYSLTR1, CYSLTR2, LTC4S, STAT3, STAT6, etc., being responsible for the level of inflammatory mediators by their role in regulating the immune response and behavior of inflammatory cells in body fluids [8].

A list comprising 167 candidate genes was created according to 107 references to search for phenotype–genotype associations. The list of these genes, with a brief description of the functions of the proteins encoded by them, is provided in Discussion.

DNA isolation, construction of genomic libraries, and sequencing

DNA was isolated from whole blood samples using a MagAttract HMW DNA Kit (Qiagen, Germany). The DNA isolation protocol was automated on the Tecan Freedom EVO workstation (Tecan, Switzerland). The concentration and purity of the isolated DNA were measured on a Tecan Infinite® F Nano Plus microplate reader (Tecan, Switzerland).

The genomic libraries for sequencing were prepared using a Nextera DNA Flex kit (Illumina, USA), in accordance with the manufacturer's recommendations. Each sample in the flow cell was labelled using indexes from the IDT-ILMN Nextera DNA UD kit (Illumina, USA).

The concentrations of the genomic libraries were measured using a Tecan Infinite® F Nano Plus spectrophotometer. The size of the genomic libraries was determined on an Agilent TapeStation 4200 system using an Agilent DNA 1000 kit (Agilent, USA). The library pools consisting of 24 samples were combined on a Tecan Freedom EVO robotic platform.

Genome-wide sequencing was performed on a NovaSeq 6000 sequencing system and a S4 reagent kit (300 cycles) (Illumina, USA) for paired-end reads 2 × 150 bp.

Bioinformatic analysis of the whole-genome sequencing data

Demultiplication was performed at the first stage of the analysis of the primary sequencing data. During this procedure, the initial reads of the NovaSeq 6000 sequencing system was converted from the BCL format to the FASTQ format using the Illumina bcl2fastq conversion software v2.20 [9]. The Illumina Sequencing Analysis Viewer software v2.4.7 was employed to control the overall sequencing quality of the entire cell [10]. The quality of individual reads was controlled using the FastQC v0.11.9 bioinformatic tool [11].

The final sample contained blood specimens that had undergone quality control for such parameters as homogeneity of the nucleotide distribution in the reads and GC composition.

Read alignment against a reference genome was performed at the second stage of the bioinformatic analysis using the DRAGEN platform [12]. The GRCh38.d1.vd1 sequence was used as the reference genome. Blood samples with average coverage over genome < ×30 were excluded from the study.

The CrosscheckFingerprints software (Picard) [13] was used to check whether the sample contained any duplicates. All duplicate specimens were excluded from the study.

Search for short genetic variations

The Strelka software was used to process VCF files and search for short genetic variations (SNPs, indels up to 50 bp long) [14].

Finally, 380,564 short genetic variations were detected in 167 candidate genes (7,303 samples); 253,628 of those were found more than once.

The procedure for searching for genetic variations whose frequency was statistically significantly different in different cohorts was employed to identify the polymorphisms associated with BA. The Fisher's exact test was used to determine the significance level of the differences.

The case with identical occurrence of the "zero" variant in all four cohorts was assumed to be the null hypothesis. The significance level at which the null hypothesis was rejected was set equal to 10^{-4}. The calculations were performed using the R programming language.

RESULTS

Comparison of male cohorts

Our analysis revealed four genetic variants in the introns of the *TACR3, ZNF257, FOXP1*, and *EGFR* genes; their frequencies differ statistically significantly (the *p* value being no higher than the significance level of 10^{-4}) in the cohorts of men with a verified diagnosis of BA and in the cohort of apparently healthy men. These genetic variants are found significantly more frequently in cohort 2A (more than fivefold) (*Table 1*) than in cohort 4H.

The *TACR3* gene that encodes tachykinin receptors and has an indirect effect on the bronchial tone [15, 16] was found to carry the rs1461555098 deletion (chr4:g.103629850_103629861del). According to our calculations, the relative risk of developing BA in individuals carrying this deletion stands at 6.9, while this parameter is normally equal to 1.0. The deletion rs1461555098 (chr4:g.103629850_103629861del) was detected in cohort 2A twice as frequently as in cohort 4H.

The *ZNF257* gene encoding the transcription factor (a zinc finger motif-containing protein) was

Table 1. SNPs associated with bronchial asthma in the cohorts of men

Chromosome	Polymorphism ID number	Gene	Frequency		*p*
			cohort 2A, %	cohort 4H, %	
chr3	rs869106717 (del)	*FOXP1*	5.71	0.17	1.1×10^{-5}
chr4	rs1461555098 (del)	*TACR3*	12.86	2.07	2.9×10^{-5}
chr7	rs189649077 (G>T)	*EGFR*	4.29	0.03	2.4×10^{-5}
chr19	rs1199362453 (T>C)	*ZNF257*	4.29	0.00	4.5×10^{-5}

Table 2. SNPs associated with bronchial asthma in the cohorts of women

Chromosome	Polymorphism ID number	Gene	Frequency		*p*
			cohort 1A, %	cohort 3H, %	
chrX	rs1923038536 (G>A)	*CYSLTR1*	2.29	0.05	6.7×10^{-6}
chr1	rs1219244986 (T>C)	*MUC1*	1.83	9.46	1.5×10^{-5}
chr3	rs2291651 (G>C)	*MUC4*	83.03	91.88	5.0×10^{-5}
chr3	rs181066119 (A>G)	*IL5RA*	1.83	0.05	9.5×10^{-5}
chr8	rs143247175 (T>A)	*NRG1*	1.83	0.05	9.5×10^{-5}
chr15	rs140597386 (dup)	*HDC*	4.13	0.67	6.0×10^{-5}
chr2	rs762042586 (del)	*DPP10*	1.83	0.05	9.5×10^{-5}

found to carry the genetic variant rs1199362453 (chr19:g.22076863T>C), which was encountered three times in cohort 2A but was absent in cohort 4H.

The *FOXP1* gene encoding the transcription factor and expressed in the proximal airway epithelium [18] was found to carry the genetic variant rs869106717 (chr3:g.71465326del), which was encountered in cohort 2A 33.6 times more frequently than in cohort 4H. The relative risk of developing BA in individuals carrying this mutation is 36.0.

In the *EGFR* gene that encodes the transmembrane receptor binding extracellular ligands belonging to the epidermal growth factor group [19], the frequency of the genetic variant rs189649077 (chr7:g.55168296G>T) in cohort 2A was 143-fold higher compared to that in cohort 4H. The relative risk of developing BA in individuals carrying this mutation is 34.3.

Comparison of female cohorts

It was demonstrated that in the cohort of women with a confirmed diagnosis of BA, five genetic variants were six times more frequent compared to the cohort of apparently healthy women (the *p* value is no higher than the significance level of 10^{-4}). These genetic variants resided in the *CYSLTR1, IL5RA, NRG1, HDC*, and *DPP10* genes (*Table 2*).

The *CYSLTR1* gene that encodes the protein affecting the secretion of inflammatory mediators (leukotrienes) [16, 20] was found to carry the rs1923038536 (chrX:g.78306516G>A) variant, which was detected in cohort 1A 45.8 times more frequently compared to cohort 3H. The relative risk of developing BA in individuals carrying this mutation is 14.2.

The genetic variant rs181066119 (chr3:g.3102851A>G) was found in the *IL5RA* gene encoding the subunit of the heteromeric receptor of interleukin 5, a cytokine that plays a crucial role in eosinophil differentiation [21]; this variant occurred in cohort 1A 36.6 times more frequently than in cohort 3H. The relative risk of developing asthma in individuals carrying this mutation is 13.2.

The genetic variant rs143247175 (chr8:g.32692193T>A) was found in the *NRG1* gene encoding mucin production by airway goblet cells [22]; like the previous genetic variant, it was found in cohort 1A 36.6 times more frequently than in cohort 3H. The relative risk of developing BA in individuals carrying this mutation is also 13.2.

The *HDC* gene codes for the enzyme catalyzing histamine synthesis from L-histidine [23]. The genetic variant rs140597386 (chr15:g.50261726dup) was identified for this gene; it occurred in cohort 1A 6.2 times more frequently than in cohort 3H. The relative risk of developing BA in individuals carrying this mutation was 5.0.

The genetic variant rs762042586 (chr2:g.115490670del) was identified in the *DPP10* gene encoding membrane-anchored serine protease

[16], which was found in cohort 1A 36.6 times more frequently than in cohort 3H. The relative risk of developing BA in individuals carrying this mutation is 13.2.

The genetic variants rs2291651 (chr3:g.195751141G>C) and rs1219244986 (chr1:g.155189991T>C) of the *MUC1* and *MUC4* genes occurred in women with asthma much less frequently than in apparently healthy women. This means that the identified genetic variants can be considered protective in individuals with BA [24]. The *MUC1* and *MUC4* genes encode mucins. The *MUC1* gene is responsible for the anti-inflammatory effect in patients with bronchial and lung diseases. *MUC4* exhibits a mediated effect on the proliferation of airway epithelial cells [25]. The genetic variant rs2291651 (chr3:g.195751141G>C) of the *MUC4* gene in cohort 1A occurred somewhat more rarely than in cohort 3H. The relative risk of developing BA in individuals carrying this mutation is 0.5, while normally this parameter is 1.0. This indicates that the risk of developing bronchial asthma is down twofold in women carrying the genetic variant rs2291651. The relative risk of developing BA in females carrying the genetic variant rs1219244986 (chr1:g.155189991T>C) is 0.2 (i.e., lower than 1), corresponding to the fivefold reduction in the risk of developing the disease.

However, allowance should be made for the fact that the identified variants in the *MUC1* and *MUC4* genes reside in GC-rich regions. This region negatively affects sequencing quality and, therefore, the quality of the genetic variant detection.

DISCUSSION

We have analyzed the candidate genes potentially associated with BA. Eleven polymorphisms whose frequency differs significantly in individuals diagnosed with BA and those not diagnosed with the condition have been identified. Nine of the identified genetic variants increase the risk of developing BA, while two variants reduce it. These nine variants increase the risk of developing BA at least fivefold. The identified variants are specific to the population of Russia.

Arathimos et al. [26] reported that up to 45% of females with bronchial asthma experience an aggravation of their condition before their menstrual period. In 2020, the polymorphism rs2291651 in the *MUC4* gene was described to be an accompanying sign of endometriosis in South Korean women [27]. The relationship between the single nucleotide polymorphisms in the *MUC1* and *MUC4* genes and endometriosis risk was analyzed in this study. Screening identified eight genetic variants of *MUC4*, including rs2291651, whose presence correlated with the development of endometriosis. Women of childbearing age using oral contraceptive pills tended to experience milder asthma attacks [28]. A number of studies [29, 30] also demonstrated that variations in the estradiol and progesterone levels during the menstrual cycle affected the severity of bronchial asthma symptoms. That means that when studying the genetic predisposition to a severe BA course in women, one should pay particular attention to the genes associated with female sex hormones.

In this study, we have analyzed 167 candidate genes associated with bronchial asthma. These genes include *HNMT, MS4A2, HRH1, HRH2, HRH3, HRH4, AOC1,* and *HDC*, which code for the histamine receptors that are involved in the regulation of histamine release [16, 23, 31–33].

The *HDC* gene encodes the enzyme histidine decarboxylase catalyzing histamine formation from L-histidine; the HDC mRNA level is elevated in patients with asthma [23];

the *IL3, IL4, IL4R, IL5, IL9, IL13, IL17, IL21R, IL18, IL18R1, IL2RB, IL1RL1, IL5RA, IL33, SCGB3A2, TNF, CCL11, IRAK3, CSF2,* and *TSLP* genes encode the cytokines involved in inflammation. Thus, IL5 stimulates eosinophil release into the bloodstream, while IL5RA regulates their activity. Stimulation of the airways with allergens increases the local IL5 concentration, which correlates with the severity of airway eosinophilia, while *IL4RA* codes for the α chain of the IL4 receptor, which can bind IL4 and IL13 to regulate the IgE production [4, 16, 21, 23, 34–40];

the *IL17F* gene encodes the pro-inflammatory cytokine involved in pathophysiological manifestations of asthma. *In vivo* and *in vitro* studies have shown that IL17F is involved in the pathogenesis of allergic airway inflammation [41];

the *ADRB2* gene encodes the β2-adrenoceptors that play a crucial role in airway contractility. β2-adrenoceptors act as a target for β2-agonists exhibiting a marked bronchodilator and bronchoprotective activity, which is important for assessing the effectiveness of BA therapy [16];

the *PLA2G7* gene encodes the platelet-activating factor acetylhydrolase. This enzyme catalyzes the cleavage of PAF by hydrolyzing the acetyl group down to biologically inactive products [31];

the *ALOX5, CYSLTR1, CYSLTR2,* and *LTC4S* genes encode the proteins that affect the production of inflammatory mediators (leukotrienes), contributing to various allergic and hypersensitivity reactions. It has been shown that altered expression of some of these genes may cause bronchoconstriction of the airways and hyperresponsiveness to bronchoconstricting

agents such as histamine, increased vascular permeability, edema, eosinophilia and neutrophilia, smooth muscle cell proliferation, collagen deposition and fibrosis in different tissue areas, mucin secretion by goblet cells, metaplasia of goblet cells, and hypertrophic changes in the respiratory epithelium [16, 20, 42];

the *PTGER2* and *PTGDR* genes encode prostaglandin receptors and are involved in the pathogenesis of BA [16, 43];

the *TBX21* and *TBX5* genes encode transcriptional activators; their expression is downregulated in airway-resident T cells in asthma patients [16, 44];

the *STAT6* gene encodes the STAT family transcription factor; expression of this gene is significantly upregulated in patients with severe BA [16];

the *STAT3* gene encodes the STAT family transcription factor mediating the cellular responses to interleukins and regulates the inflammatory response [45, 46];

the *STAT4* gene encodes the STAT family transcription factor; expression of this gene is downregulated in patients with BA [47];

the *NPSR1* gene encodes the neuropeptide S receptor; the upregulated expression of this gene in airway epithelium leads to the activation of matrix metalloproteinases, which are involved in the pathogenesis of BA [16, 48];

the *TAC1, TACR2, TACR1*, and *TACR3* genes encode receptors for tachykinins, which are found in sensory nerve endings, are activated by inflammatory mediators (histamine, platelet-activating factor, and leukotrienes), and add the axon reflex mechanism to the pathogenesis of asthma, thus leading to aggravation and spread of the initial inflammation. Tachykinins affect the bronchial tone and vascular permeability [16];

the *CHI3L1* gene encodes the glycoprotein belonging to the glycoside hydrolase family and contributes to the development of the Th2-type inflammatory response [16, 49];

the *DENND1B* gene encodes the protein interacting with tumor necrosis factor and plays a crucial role in suppressing T-cell receptors on Th2 cells [50, 51];

the *ADAM33* gene codes for metalloprotease. *ADAM33* is expressed by various types of airway cells. *ADAM33* expression is elevated in patients with BA; the impaired function of this metalloprotease can be associated with bronchial hyperresponsiveness and airway wall remodeling, thus contributing to early manifestation of bronchial asthma [52];

the *ORMDL1*, *ORMDL2*, and *ORMDL3* genes encode ORM-like proteins, the key regulators of serine palmitoyltransferase, which catalyzes the first step of sphingolipid biosynthesis. Sphingolipids play an important role in signal transduction in response to stress and affect the mechanical properties of cell membranes. Dysregulation of sphingolipid biosynthesis is associated with several diseases, including allergies, inflammation, and asthma [53, 54];

the *VIP* gene encodes the vasoactive intestinal peptide responsible for the relaxation of smooth muscles [55];

the genes belonging to the *NOS* family encode nitric oxide synthases. Mutations in the *NOS1* gene reduce the nitric oxide concentration in non-eosinophilic phenotype patients, which is a marker of bronchial asthma, and cause bronchial hyperresponsiveness [56–58];

the *ACE* gene encodes angiotensin, which converts angiotensin I to the vasoactive angiotensin II, and is involved in the pathogenesis of BA as it causes proliferation and increases smooth muscle contractility, thus leading to lung obstruction [59];

protein RAD50 encoded by the *RAD50* gene is involved in double-strand DNA break repair. It was shown in transgenic mice that the fragment of the 3'-terminus of this gene is the Th2 locus control region (LCR), which regulates cytokine gene expression [60];

the *PTAFR* gene encodes the receptor for the platelet-activating factor, a chemotactic phospholipid mediator exhibiting strong inflammatory, contractile, and hypotensive activities with respect to smooth muscles. The PAF receptor is involved in various pathological processes, such as allergies, asthma, septic shock, arterial thrombosis, and inflammation [16];

the *OPN3* gene encodes the G-protein-coupled receptor. Upregulated *OPN3* expression was detected in bronchial epithelium and immune cells. Mutations in the *OPN3* gene increase the risk of bronchial asthma [20, 61];

the *GSDMB* gene encodes the protein whose overexpression in bronchial epithelial cells increases expression of the genes that are crucial for both airway remodeling and airway hyperresponsiveness [16, 62];

the *PKN2* gene encodes serine/threonine-specific protein kinase and regulates apical junction formation in human bronchial epithelium [63];

the *PTK2* gene codes for tyrosine protein kinase and plays a crucial role in airway hyperresponsiveness and airway remodeling [63];

the *ALPP* gene encodes the placental alkaline phosphatase catalyzing the hydrolysis of phosphoric acid monoesters; the expression level of this gene is associated with childhood asthma [63];

the *PTEN* gene encodes phosphatidylinositol-3,4,5-triphosphate-3-phosphatase [20]. A low *PTEN* expression level is considered to be among the independent factors of BA development [64];

the *PRMT1* gene encodes an important epigenetic regulator, protein arginine methyltransferase-1, which contributes to inflammation and airway remodeling in patients with BA [65];

the *HSPD1* gene encodes the heat shock protein that can modulate the immune and inflammatory responses, be involved in pathogenesis, and/or be a risk factor or a prognostic marker for several diseases, including BA [66];

the *TLR2* and *TLR4* genes encode proteins belonging to the Toll-like receptor family, which are essential for pathogen recognition and activation of the innate immune system. Some polymorphisms in these genes are associated with the risk of developing BA [67];

the *ZNF208, ZNF257, ZNF676, ZNF729, ZNF98, ZNF492, ZNF99, ZNF723, ZNF728, ZNF730*, and *ZNF91* genes encode zinc finger proteins residing within the region of the transcription factor cluster area and are associated with the pathogenesis of BA [17];

the *B4GALT1* gene encodes beta-1,4-galactosyltransferase and is associated with the atopic phenotypes and inflammatory conditions [68];

the *IGFBP3* gene codes for a protein binding insulin-like growth factor and inhibits the specific physiological effects of asthma in an IGF-independent manner [69];

genes belonging to the *MUC* family encode mucins. *MUC7* codes for salivary mucin; the frequency of the *MUC7* allele with five tandem repeats is significantly reduced in patients with asthma [20, 70]. During the late stages of bacterial infection, MUC1 exhibits an anti-inflammatory activity in the airways, which is initiated and mediated by inhibition of Toll-like receptor signaling [24]. Mucin MUC4 was identified as a ligand-activating receptor tyrosine kinase, which modulates the proliferation of airway epithelial cells in patients with asthma [25]; *MUC19* is mainly expressed in the cells of submucous glands in the trachea and salivary glands; in patients with allergic rhinitis and chronic otitis media, this gene is expressed in the epithelium. *MUC5AC* is expressed in the goblet cells of tracheal and bronchial epithelium. *MUC5B* is also expressed in the submucosal epithelium and ducts and, to a lesser extent, in the goblet cells of both tracheal and bronchiolar epithelium. Many individuals with a confirmed diagnosis of bronchial asthma have elevated levels of MUC5AC mRNA but reduced levels of MUC5B mRNA [71];

the *NRG1* gene encodes the protein-inducing production of mucins MUC5AC and MUC5B by human airway goblet cells, so its inhibition can be regarded as a novel therapeutic approach to reducing mucus hypersecretion in patients with respiratory diseases [22];

the *DACT1*, *DACT2*, and *DACT3* genes code for the proteins involved in the pathogenesis of BA. The tissue levels of DACT1, DACT2, and DACT3 mRNA are significantly elevated in asthma patients [72];

the *CYP* genes encode the cytochrome proteins involved in the metabolism of many drugs, including nonsteroidal anti-inflammatory drugs, oral anticoagulants and angiotensin receptor blockers, as well as in the synthesis of cholesterol, steroids, and other lipids [20, 70, 73–77];

the *CHML* gene codes for Rab geranylgeranyltransferase regulating the intracellular transport of membrane structures. Polymorphisms in this gene are associated with the development of BA [61];

the *GSTT2* and *GSTP1* genes encode glutathione S-transferase theta 2 and glutathione S-transferase P; polymorphisms in these genes may be risk factors for BA [78];

the *NAT2* gene codes for N-acetyltransferase 2; polymorphisms in this gene are associated with the development of atopic asthma [79];

the *PYHIN1* gene encodes the interferon-inducible HIN-200 protein, which is involved in the production of proinflammatory cytokines in airway epithelial cells [80];

the *SMAD3* gene promoter is significantly hypermethylated in patients with BA [81];

the *PGAP3* gene encodes a glycosylphosphatidylinositol-specific phospholipase predominantly residing in the Golgi apparatus. The PGAP3 and ORMDL3 proteins can contribute to the development of BA [82];

the *ERBB2* gene encodes the epidermal growth factor receptor tyrosine kinase. The *ERBB2* expression level in freshly isolated airway epithelium in asthma patients is lower than that in healthy individuals [83];

the *COL15A1* gene coding for the alpha chain of collagen type XV, a member of the FACIT collagen family [16], is involved in the metabolism of the drugs used to treat lung diseases [84];

the *FOXP1* gene encodes the transcription factor belonging to the FOXO family, which is expressed in the proximal airway epithelium of the lungs; downregulated expression of *FOXP1* inhibits early differentiation of secretory cells [18];

the *ACOT7* gene encodes a protein belonging to the acyl-coenzyme family; an epigenome-wide association study revealed an association between the degree of methylation and the development of bronchial asthma [85];

the *MTHFR* gene codes for the methyltetrahydrofolate reductase. Polymorphisms in the *MTHFR* gene

are associated with predisposition to bronchial asthma and glucocorticoid responsiveness in humans [86];

the *DICER1* gene encodes RNA helicase involved in cytokine production and signal transduction in patients with BA [87];

the *SERPINC1* gene encodes antithrombin III, which inhibits clotting factors; variations in its level may induce thrombosis or pulmonary embolism [88];

the *SYNM* gene codes for an intermediate filament; there is a hypothesis that the degree of methylation of this gene is associated with the development of BA [89];

the *GATA3* gene encodes a transcription factor belonging to the GATA family. The *GATA3* expression level in the airways is significantly increased in patients with asthma. The increased *GATA3* expression level correlates with changes in *IL5* expression and the development of bronchial hyperresponsiveness [90];

the *FOXP3* gene encodes an activating transcription factor; the expression level of this gene is downregulated in asthma patients [91];

the *CCDC80*, *DAPK3*, *LOXL1*, *PROC*, *FUCA2*, *SP100*, and *ITCH* genes encode proteins associated with antigen presentation to T lymphocytes. The degree of methylation of these genes was found to be increased in asthma patients [76];

the *VDR* gene codes for the vitamin D3 receptor. Genetic variants of the *VDR* gene are often found in children with BA; their presence inversely correlates with asthma severity [92];

the *DPP10* gene encodes a membrane protein belonging to the serine protease family. Mutations in this gene increase the risk of BA [16, 93];

the genetic variants of the *PHF11*, *SPP1*, and *PLAUR* genes are associated with elevated IgE levels [94];

the *SLC22A5* gene encodes an organic cation transporter; its expression level in the bronchial epithelium is reduced in asthma patients [95];

the *EPHX1* gene codes for microsomal epoxide hydrolase. A high *EPHX1* expression level is associated with an increased risk of developing BA at any time in one's life [96];

the *CTLA4* gene encodes one of the proteins from the immunoglobulin superfamily. According to the meta-analysis data, some polymorphisms in this gene are risk factors for developing BA [16, 97];

the *MMP9* gene encodes a matrix metalloprotease involved in local proteolysis of the extracellular matrix, leukocyte migration, and airway remodeling [98];

the *SOCS5* gene codes for a protein belonging to the family of cytokine signaling inhibitors. The single-nucleotide polymorphisms identified in this gene are associated with the development of BA [99];

the polymorphisms in the *FCER2* gene encoding CD23 are associated with atopy, higher risk of exacerbation in patients with asthma, and a high serum IgE level [100];

the *VEGFA* gene encodes the heparin binding protein, one of the PDGF/VEGF growth factors. An elevated expression level of this gene is detected in patients with BA [101];

the *ASB3* gene codes for the protein involved in smooth muscle cell proliferation and muscle cell development. A genome-wide association study revealed an association between polymorphisms in this gene and the development of BA [102];

the *CRISPLD2* gene encodes the secretory protein LCCL, which increases glucocorticoid sensitivity and regulates the immune response [103];

according to a genome-wide association study, polymorphisms in the *APOBEC3B*, *APOBEC3C*, and *EDDM3B* genes are associated with asthma exacerbations [104];

a whole-genome association study revealed an association between polymorphisms in the *BBS9* gene and the effectiveness of asthma treatment in children [105];

the *PRKG1* gene encodes cGMP-dependent protein kinase, a key mediator of the nitric oxide (NO)/cGMP signaling pathway, and contributes to smooth muscle relaxation [16];

the *DNAH5* gene codes for the dynein protein. The *DNAH5* expression level in the bronchial epithelium is reduced in asthma patients compared to that in the control group [106];

the *JAK1* and *JAK2* genes encode the tyrosine kinases involved in the inflammatory cytokine signaling pathways associated with a higher frequency of asthma exacerbation and increased susceptibility to allergic sensitization and environmental antigens [107, 108];

the *CHRNA1* and *CHRNA3* genes code for nicotinic acetylcholine receptors. Polymorphisms in these genes are considered to be genetic risk factors for bronchial obstruction [109];

the *TGF-β* gene encodes a secreted ligand belonging to the TGF-β protein superfamily. TGF-β isoforms play a role in the regulation of airway inflammation and remodeling [110];

variants in the *HHIP* gene are associated with chronic obstructive pulmonary disease [111];

the *SOD3* gene encodes superoxide dismutase. The *SOD3* expression level is elevated in patients with BA, and some genetic variants of this gene affect the distribution of extracellular superoxide dismutase in the

lungs and reduce the risk of manifesting BA symptoms [112];

the *EGFR* gene encodes a transmembrane receptor binding extracellular ligands belonging to the epidermal growth factor group. Biopsy specimens from asthma patients often contain regions of epithelial damage that are immunostained with EGFR; an elevated *EGFR* expression level is also observed in the morphologically intact epithelium of asthma patients [19];

the *SLC11A1* gene codes for the divalent metal transporter protein carrying iron and manganese. A number of studies have revealed an association between polymorphisms in this gene and the development of lung diseases [113]; and

the *ZPBP2* gene encodes a protein expressed in the bronchial glandular epithelium. The degrees of methylation of this gene are different in healthy individuals than they are in patients with BA [114].

CONCLUSIONS

The genetic variants of a number of genes identified in this study, which increase and reduce the relative risk of developing BA, may facilitate early diagnosis of bronchial asthma and accurate diagnosis-making in case of ambiguity. In the long run, analysis of the samples collected from residents of different regions will help assess the geographic distribution of the risk-editing genetic variants and not only perform mapping of BA prevalence, but also adequately allocate financial and material resources, as well as qualified medical staff, across regions. Timely, including prenatal, detection of individuals genetically predisposed to BA and accurate diagnosis-making will improve the quality of medical care, reduce the rates of disability and death due to bronchopulmonary events, and decrease the direct and indirect cost of combatting bronchial asthma. ●

REFERENCES

1. Interregional public organization Russian Respiratory Society, All-Russian public organization Association of Allergists and Clinical Immunologists, All-Russian public organization Union of Pediatricians of Russia, Scientific Council of the Ministry of Health of the Russian Federation. Clinical guidelines. Bronchial asthma. M., 2021. P. 7.
2. Vos T., Lim S.S., Abbafati, C., Abbas K.M., Abbasi M., Abbasifard M., Abbasi-Kangevari M., Abbastabar, H., Abd-Allah F., Abdelalim A., et al. // Lancet. 2020. V. 396. № 10258. P. 1204–1222.
3. Zaikina M.V. Bronchial asthma in young men: early changes in the functional state of the cardiorespiratory system, Perm State Medical University named after Academician E.A. Wagner of the Ministry of Health of the Russian Federation, 2017. 153 p.
4. Asanov A.Yu., Namazova L.S., Pinelis V.G., Zhurkova N.V., Voznesenskaya N.I. // Pediatric Pharmac. 2008. V. 5. № 4. P. 31–37.
5. The European Community Respiratory Health Survey II // Eur. Resp. J. Eur. Resp. Soc. 2002. V. 20. № 5. P. 1071–1079.
6. Belevsky A.S., Zaitsev A.A. // Med. advice. 2018. № 15. P. 60–68.
7. Yung J.A., Fuseini H., Newcomb D.C. // Ann. Allergy Asthma Immunol. 2018. V. 120. № 5. P. 488–494.
8. Chuchalin A.G., Abelevich M.M., Arkhipov V.V., Astafieva N.G., Asherova I.K., Balabolkin I.I., Baleva L.S., Baskakova A.E., Blokhin B.M., Bogorad A.E. et al. National program Bronchial asthma in children. Treatment strategy and prevention. M., 2012. P. 11.
9. Holtgrewe M., Messerschmidt C., Nieminen M., Beule D. // Bioinformatics. 2020. V. 36. № 6. P. 1983–1985.
10. Wright M.N., Gola D., Ziegler A. // Statistical Human Genetics. 2017. V. 1666. P. 629–647.
11. de Sena Brandine G., Smith A.D. // F1000Res. 2021. V. 8. P. 1874.
12. Miller N.A., Farrow E.G., Gibson M., Willig L.K., Twist G., Yoo B., Marrs T., Corder S., Krivohlavek L., Walter A., et al. // Genome Medicine. 2015. V. 7. № 1. P. 100.
13. Najafov J., Najafov A. // Nature. 2017. V. 7. P. 5855.
14. Saunders C.T., Wong W.S.W., Swamy S., Becq J., Murray L.J., Cheetham R.K. // Bioinformatics. 2012. V. 28. № 14. P. 1811–1817.
15. Ramalho R., Soares R., Couto N., Moreira A. // BMC Pulm Med. 2011. V.11. P. 41–48.
16. Stelzer G., Rosen N., Plaschkes I., Zimmerman S., Twik M., Fishilevich S., Stein T.I., Nudel R., Lieder I., Mazor Y., et al. // Curr. Protoc. Bioinformatics. 2016. V. 54. P. 1.30.1–1.30.33.
17. Karunas A.S. Identification of genes of predisposition to bronchial asthma in various ethnic groups of the Volga-Ural region of Russia // Russian Fund for Basic Research. 2013. Grant № 13-04-01397.
18. Li S., Wang Y., Zhang Y., Lu M.M., DeMayo F.J., Dekker J.D., Tucker P.W., Morrisey E.E. // Development. 2012. V. 139. № 14. P. 2500–2509.
19. Puddicombe S.M., Polosa R., Richter A., Krishna M.T., Howarth P.H., Holgate S.T., Davies D.E. // FASEB J. 2000. V. 14. № 10. P. 1362–1374.
20. UniProt Consortium. // Nucl. Acids Res. 2021. V. 49. P. D480–D489.
21. Cheong H.S., Kim L.H., Park B.L., Choi Y.H., Park H.S., Hong S.J., Choi B.W., Park C.S., Shin H.D. // J. Hum. Genet. 2005. V. 50. № 12. P. 628–634.
22. Zuiker R.G., Tribouley C., Diamant Z., Boot J.D., Cohen A.F., van Dyck K., De Lepeleire I., Rivas V.M., Malkov V.A., Burggraaf J., et al. // Eur. Clin. Respir. J. 2016. V. 3. P. 31324.
23. Yamauchi K. // Nihon Rinsho. 1996. V. 54. № 2. P. 377–388.
24. Kato K., Lillehoj E.P., Lu W., Kim K.C. // J. Clin. Med. 2017. V. 6. № 12. P. 110.
25. Damera G., Xia B., Sachdev G.P. // Respiratory Res. 2006. V. 7. № 1. P. 39.
26. Arathimos R., Granell R., Haycock P., Richmond R.C., Yarmolinsky J., Relton C.L., Tilling K. // Thorax. 2019. V. 74. № 7. P. 633–642.

27. Yen C.-F., Kim M.-R., Lee C.-L. // Gynecol. Minim. Invasive Ther. 2019. V. 8. № 1. P. 4–11.
28. Nwaru B.I., Tibble H., Shah S.A., Pillinger R., McLean S., Ryan D.P., Critchley H., Price D.B., Hawrylowicz C.M., Simpson C.R., et al. // Thorax. 2021. V. 76. № 2. P. 109–115.
29. Chowdhury N.U., Guntur V.P., Newcomb D.C., Wechsler M.E. // Eur. Respir. Rev. 2021. V. 30. № 162. P. 210067.
30. Yung J.A., Fuseini H., Newcomb D.C. // Ann. Allergy Asthma Immunol. 2018. V. 120. № 5. P. 488–494.
31. Amberger J.S., Bocchini C.A., Schiettecatte F., Scott A.F., Hamosh A. // Nucl. Acids Res. 2015. V. 43. № 7. P. 89–98.
32. Yoshikawa T., Nakamura T., Yanai K. // Int. J. Mol. Sci. 2019. V. 20. № 3. P. 737.
33. Szczepankiewicz A., Bręborowicz A., Sobkowiak P., Popiel A. // Clin. Mol. Allergy. 2010. V. 8. P. 14.
34. Freihat L.A., Wheeler J.I., Wong A., Turek I., Manallack D.T., Irving H.R. // Sci. Rep. Nature. 2019. V. 9. № 1. P. 15468.
35. Matucci A., Bormioli S., Nencini F., Maggi E., Vultaggio A. // Expert. Rev. Clin. Immunol. 2021. V. 17. № 1. P. 63–71.
36. Borish L., Steinke J.W. // Curr. Allergy Asthma Rep. 2011. V. 11. № 1. P. 7–11.
37. Matera M.G., Rogliani P., Calzetta L., Cazzola M. // Drugs. 2020. V. 80. № 5. P. 449–458.
38. Gordon E.D., Palandra J., Wesolowska-Andersen A., Ringel L., Rios C.L., Lachowicz - Scroggins M.E., Sharp L.Z., Everman J.L., MacLeod H.J., et al. // JCI Insight. 2016. V. 1. № 14. P. 87871.
39. Zhang Y., Moffatt M.F., Cookson W.O.C. // Curr. Opin. Pulmonary Med. 2012. V. 18. № 1. P. 6–13.
40. Elena-Pérez S., Heredero-Jung D.H., García-Sánchez A., Estravís M., Martin M.J., Ramos-González J., Triviño J.C., Isidoro-García M., Sanz C., Dávila I. // Front. Med. (Lausanne). 2021. V. 7. P. 624576.
41. Ota K., Kawaguchi M., Matsukura S., Kurokawa M., Kokubu F., Fujita J., Morishima Y., Huang S.K., Ishii Y., Satoh H., et al. // J. Immunol. Res. 2014. V. 2014. P. 602846.
42. Theron A.J., Steel H.C., Tintinger G.R., Gravett C.M., Anderson R., Feldman C. // J. Immunol. Res. 2014. V. 2014. P. 608930.
43. García-Solaesa V., Sanz-Lozano C., Padrón-Morales J., Hernández-Hernández L, García-Sánchez A., Rivera-Reigada M.L., Dávila-González I., Lorente-Toledano F., Isidoro-García M. // Allergol. Immunopathol (Madrid). 2014. V. 42. № 1. P. 64–68.
44. Edris A., de Roos E.W., McGeachie M.J., Verhamme K.M.C., Brusselle G.G., Tantisira K.G., Iribarren C., Lu M., Wu A.C., Stricker B.H., Lahousse L. // Clin. Exp. Allergy. 2022. V. 52. № 1. P. 33–45.
45. Nikolskii A.A., Shilovskiy I.P., Barvinskaia E.D., Korneev A.V., Sundukova M.S., Khaitov M.R. // Biochemistry (Moscow). 2021. V. 86. № 11. P. 1489–1501.
46. Saik O.V., Demenkov P.S., Ivanisenko T.V., Bragina E.Y., Freidin M.B., Dosenko V.E., Zolotareva O.I., Choynzonov E.L., Hofestaedt R., Ivanisenko V.A. // J. Integr. Bioinform. 2018. V. 15. № 4. P. 20180054.
47. Trophimov V.I., Mineyev V.N., Sorokina L.N., Nema M.A., Lim V.V., Yeremeyeva A.V. // Med. Acad. J. 2013. V. 13, № 1. P. 6767–72.
48. Pietras C.O., Vendelin J., Anedda F., Bruce S., Adner M., Sundman L., Pulkkinen V., Alenius H., D'Amato M., Söderhäll C., et al. // BMC Pulm. Med. 2011. V. 11. P. 39.
49. Komi D.E.A., Kazemi T., Bussink A.P. // Curr. Allergy Asthma Rep. 2016. V. 16. № 8. P. 57.
50. Sleiman P.M., Flory J., Imielinski M., Bradfield J.P., Annaiah K., Willis-Owen S.A., Wang K., Rafaels N.M., Michel S., Bonnelykke K., et al. // N. Engl. J. Med. 2010. V. 362. № 1. P. 36–44.
51. Fiuza B.S.D., de Silva M.J., Alcântara-Neves N.M., Barreto M.L., Costa R.D.S., Figueiredo C.A. // Mol. Immunol. 2017. V. 90. P. 33–41.
52. Sharma N., Tripathi P., Awasthi S. // Allergy Rhinol. (Providence). 2011. V. 2. № 2. P. 63– 70.
53. Paulenda T., Draber P. // Allergy. 2016. V. 71. № 7. P. 918–930.
54. Luthers C.R., Dunn T.M., Snow A.L. // Front. Immunol. 2020. V. 11. P. 597945.
55. Pavón-Romero G.F., Serrano-Pérez N.H., García-Sánchez L., Ramírez-Jiménez F., Terán L.M. // Front. Cell. Dev. Biol. 2021. V. 9. P. 663535.
56. Ferraro V., Carraro S., Bozzetto S., Zanconato S., Baraldi E. // Asthma Res. Pract. 2018. V. 4. P. 9.
57. Batozhargalova B.T., Diakova S.E., Petrova N.V., Mizernitsky Yu.L., Zinchenko R.A. // Russian Bulletin of Perinatology and Pediatrics. 2019. V. 64. № 5. P. 55–68.
58. Bouzigon E., Monier F., Boussaha M., Le Moual N., Huyvaert H., Matran R., Letort S., Bousquet J., Pin I., Lathrop M., et al. // PLoS One. 2012. V. 7. № 5. P. 36672.
59. Sardaryan I.S., Zhelenina L.A., Galustyan A.N., Korostovtsev D.S., Ivashchenko T.E. // Russian Bulletin of Perinatology and Pediatrics. 2008. V. 53. № 1. P. 44 –48.
60. Li X., Howard T.D., Zheng S.L., Haselkorn T., Peters S.P., Meyers D.A., Bleecker E.R. // J. Allergy Clin. Immunol. 2010. V. 125. № 2. P. 328–335.
61. White J.H., Chiano M., Wigglesworth M., Geske R., Riley J., White N., Hall S., Zhu G., Maurio F., Savage T., et al. // Hum. Mol. Genet. 2008. V. 17. № 13. P. 1890–1903.
62. Das S., Miller M., Beppu A.K., Mueller J., McGeough M.D., Vuong C., Karta M.R., Rosenthal P., Chouiali F., Doherty T.A., et al. // Proc. Natl. Acad. Sci. USA. 2016. V. 113. № 46. P. 13132–13137.
63. Krautenbacher N., Flach N., Böck A., Laubhahn K., Laimighofer M., Theis F.J., Ankerst D.P., Fuchs C., Schaub B. // Allergy. 2019. V. 74. № 7. P. 1364–1373.
64. Wen X., Yan J., Han X.-R., Zheng G.-H., Tang R., Liu L.-F., Wu D.-M., Lu J., Zheng Y.-L. // J. Thorac. Dis. 2018. V. 10. № 1. P. 202–211.
65. Zhai W., Sun H., Li Z., Li L., Jin A., Li Y., Chen J., Yang X., Sun Q., Lu S., et al. // J. Immunol. 2021. V. 206. № 1. P. 11–22.
66. Wancheng T., Weici L. // Respirilogy. 2001. V. 5. P. 227–230.
67. Yang M., Wu T., Cheng L., Wang F., Wei Q., Tanguay R.M. // Respirat. Res. 2005. V. 6. № 1. P. 18.
68. Hansel N.N., Diette G.B. // Proc. Am. Thorac. Soc. 2007. V. 4. № 1. P. 32–36.
69. Lee Y.-C., Jogie-Brahim S., Lee D.-Y., Han J., Harada A., Murphy L.J., Oh Y. // J. Biol. Chem. 2011. V. 286. № 20. P. 17898–17909.
70. Mcguckin M., Thornton D., Whitsett J. // Mucosal Immunol. Cambridge: Acad. Press Books, 2015. V. 1. P. 231–250.
71. Bonser L.R., Erle D.J. // J. Clin. Med. 2017. V. 6. № 12. P. 112.
72. Zhang C., Yang P., Chen Y., Liu J., Yuan X. // Exp. Ther. Med. 2018. V. 15. № 3. P. 2674–2680.
73. Yildirim Yaroğlu H., Calikoğlu M., Tamer Gümüş L. // Med. Princ. Pract. 2011. V. 20. № 1. P. 39–42.

74. Niewiński P., Patkowski J., Orzechowska-Juzwenko K., Hurkacz M., Wolańczyk-Medrala A., Nittner-Marszalska M. // Adv. Clin. Exp. Med. 2005. V. 14. P. 1175–1180.
75. Yim E.-Y., Kang H.-R., Jung J.-W., Sohn S.-W., Cho S.-H. // Asia PacAllergy. 2013. V. 3. № 4. P. 231–240.
76. Ntontsi P., Photiades A., Zervas E., Xanthou G., Samitas K. // Internat. J. Mol. Sci. 2021. V. 22. № 5. P. 2412.
77. Laitinen T. // Meth. Mol. Biol. 2007. V. 376. P. 213–234.
78. Liang S., Wei X., Gong C., Wei J., Chen Z., Chen X., Wang Z., Deng J. // Respirology. 2013. V. 18. № 5. P. 774–783.
79. Pawlik A., Juzyszyn Z., Gawronska-Szklarz B. // Arch. Med. Res. 2009. V. 40. № 4. P. 264–267.
80. Massa D., Baran M., Bengoechea J.A., Bowie A.G. // J. Biol. Chem. 2020. V. 295. № 14. P. 4438–4450.
81. DeVries A., Wlasiuk G., Miller S.J., Bosco A., Stern D.A., Lohman I.C., Rothers J., Jones A.C., Nicodemus-Johnson J., Vasquez M.M., et al. // J. Allergy Clin. Immunol. 2017. V. 140. № 2. P. 534–542.
82. Stein M.M., Thompson E.E., Schoettler N., Helling B.A., Magnaye K.M., Stanhope C., Igartua C., Morin A., Washington C., Nicolae D., et al. // J. Allergy Clin. Immunol. 2018. V. 142. № 3. P. 749–764.
83. Inoue H., Hattori T., Zhou X., Etling E.B., Modena B.D., Trudeau J.B., Holguin F., Wenzel S.E. // J. Allergy Clin. Immunol. 2019. V. 143. № 6. P. 2075–2085.
84. Maghsoudloo M., Azimzadeh Jamalkandi S., Najafi A., Masoudi-Nejad A. // Mol. Med. 2020. V. 26. № 1. P. 9.
85. Cardenas A., Sordillo J.E., Rifas-Shiman S.L., Chung W., Liang L., Coull B.A., Hivert M.-F., Lai P.S., Forno E., Celedón J.C., et al. // Nat. Commun. 2019. V. 10. № 1. P. 3095.
86. Li M., Tang Y., Zhao E.-Y., Chen C.-H., Dong L.-L. // Zhongguo Dang Dai Er Ke Za Zhi. 2021. V. 23. № 8. P. 802–808.
87. Hudon Thibeault A.-A., Laprise C. // Genes (Basel). 2019. V. 10. № 11. P. 932.
88. Bai J., Zhong J.-Y., Liao W., Hu R., Chen L., Wu X.-J., Liu S.-P. // Mol. Med. Rep. 2020. V. 22. № 5. P. 3607–3620.
89. Gunawardhana L.P., Gibson P.G., Simpson J.L., Benton M.C., Lea R.A., Baines K.J. // Epigenetics. 2014. V. 9. № 9. P. 1302–1316.
90. Ray A., Cohn L. // J. Clin. Invest. 1999. V. 104. № 8. P. 985–993.
91. Vale-Pereira S., Todo-Bom A., Geraldes L., Schmidt-Weber C., Akdis C.A., Mota-Pinto A. // Clin. Exp. Allergy. 2011. V. 41. № 4. P. 490–496.
92. Hou C., Zhu X., Chang X. // Exp. Ther. Med. 2018. V. 15. № 3. P. 2773–2776.
93. Allen M., Heinzmann A., Noguchi E., Abecasis G., Broxholme J., Ponting C.P., Bhattacharyya S., Tinsley J., Zhang Y., Holt R., et al. // Nat. Genet. 2003. V. 35. № 3. P. 258–263.
94. Holloway J.W., Beghe B., Holgate S.T. // Clin. Exp. Allergy. 1999. V. 29. P. 1023–1032.
95. Mukherjee M., Brown A., Pritchard D.I., Bosquillon C. // Physiological Soc. 2013. V. 30. P. 11.
96. Salam M.T., Lin P.-C., Avol E.L., Gauderman W.J., Gilliland F.D. // Thorax. 2007. V. 62. № 12. P. 1050–1057.
97. Zheng Y., Wang H., Luo L., Liao L., You L., Wang J., Li Q. // Medicine (Baltimore). 2018. V. 97. № 28. P. 11380.
98. Ohbayashi H., Shimokata K. // Curr. Drug Targets Inflamm. Allergy. 2005. V. 4. № 2. P. 177–181.
99. Averyanov A.B., Cherkashina I.I., Nikulina S.Yu., Maksimov V.N., Shestovitsky V.A. // Therapeutic archive. 2019. V. 3. P. 27–30.
100. Chan M.A., Gigliotti N.M., Aubin B.G., Rosenwasser L.J. // Am. J. Respir. Cell. Mol. Biol. 2014. V. 50. № 2. P. 263–269.
101. Ding Q., Sun S., Zhang Y., Tang P., Lv C., Ma H., Yu Y., Xu S., Deng Z. // COPD. 2020. V. 15. P. 357–365.
102. Israel E., Lasky-Su J., Markezich A., Damask A., Szefler S.J., Schuemann B., Klanderman B., Sylvia J., Kazani S., Wu R., et al. // Am. J. Respir. Crit. Care Med. 2015. V. 191. № 5. P. 530.
103. Kachroo P., Hecker J., Chawes B.L., Ahluwalia T.S., Cho M.H., Qiao D., Kelly R.S., Chu S.H., Virkud Y.V., Huang M., et al. // Nat. Heart, Lung, Blood Inst. TransOmics for Precision Med. Consortium. 2019. V. 156. № 6. P. 1068–1079.
104. Hernandez-Pacheco N., Farzan N., Francis B., Karimi L., Repnik K., Vijverberg S.J., Soares P., Schieck M., Gorenjak M., Forno E., et al. // Clin. Exp. Allergy. 2019. V. 49. № 6. P. 789–798.
105. Perez-Garcia J., Espuela-Ortiz A., Lorenzo-Diaz F., Pino-Yanes M. // Pharmgenomics Pers. Med. 2020. V. 13. P. 89–103.
106. Lee J.H., McDonald M.-L.N., Cho M.H., Wan E.S., Castaldi P.J., Hunninghake G.M., Marchetti N., Lynch D.A., Crapo J.D., Lomas D.A., et al. // Respir. Res. 2014. V. 15. № 1. P. 97.
107. Dengler H.S., Wu X., Peng I., Rinderknecht C.H., Kwon Y., Suto E., Kohli P.B., Liimatta M., Barrett K., Lloyd J., et al. // Sci. Transl. Med. 2018. V. 10. № 468. P. 2151.
108. Tabèze L., Marchand-Adam S., Borie R., Justet A., Dupin C., Dombret M.-C., Crestani B., Taillé C. // Eur. Respir. J. 2019. V. 53. № 6. P. 1802248.
109. Finsterer J. // Orphanet. J. Rare Dis. 2019. V. 14. P. 57.
110. Al-Alawi M., Hassan T., Chotirmall S.H. // Respir. Med. 2014. V. 108. № 10. P. 1409–1423.
111. Li X., Howard T.D., Moore W.C., Ampleford E.J., Li H., Busse W.W., Calhoun W.J., Castro M., Chung K.F., Erzurum S.C., et al. // J. Allergy Clin. Immunol. 2011. V. 127. № 6. P. 1457–1465.
112. Gaurav R., Varasteh J.T., Weaver M.R., Jacobson S.R., Hernandez-Lagunas L., Liu Q., Nozik-Grayck E., Chu H.W., Alam R., Nordestgaard B.G., et al. // JCI Insight. 2017. V. 2. № 17. P. 95072.
113. Smit J.J., Folkerts G., Nijkamp F.P. // Trends Immunol. 2004. V. 25. № 7. P. 342–347.
114. Moussette S., Al Tuwaijri A., Kohan-Ghadr H.-R., Elzein S., Farias R., Bérubé J., Ho B., Laprise C., Goodyer C.G., Rousseau S., et al. // PLoS One. 2017. V. 12. № 2. P. 0172707.

Analysis of the Involvement of NMDA Receptors in Analgesia and Hypothermia Induced by the Activation of TRPV1 Ion Channels

E. A. Ivanova*, A. I. Matyushkin, T. A. Voronina
V.V. Zakusov Research Institute of Pharmacology, Moscow, 125315 Russian Federation
*E-mail: iwanowaea@yandex.ru
Received September 09, 2022; in final form, January 09, 2023
DOI: 10.32607/actanaturae.11829

ABSTRACT **NMDA glutamate receptors play an important role in normal and pathophysiological nociception. At the periphery, they can interact with TRPV1 ion channels. The blockade of TRPV1 ion channels decreases NMDA-induced hyperalgesia, and NMDA receptor antagonists suppress the pain response to the TRPV1 agonist capsaicin. Since TRPV1 ion channels and NMDA receptors can functionally interact at the periphery, it would be interesting to investigate the possibility that they interact in the CNS. A single subcutaneous injection of 1 mg/kg of capsaicin was found to raise the thermal pain threshold in the tail flick test in mice, which reproduces the spinal flexion reflex, owing to the ability of capsaicin to cause long-term desensitization of nociceptors. Preventive administration of either noncompetitive NMDA receptor antagonists (high-affinity MK-801 20 μg/kg and 0.5 mg/kg subcutaneously; low-affinity hemantane 40 mg/kg intraperitoneally) or the selective TRPV1 antagonist BCTC (20 mg/kg intraperitoneally) inhibit the capsaicin-induced increase in the pain threshold. Capsaicin (1 mg/kg, subcutaneous injection) induces transient hypothermia in mice, which is brought about by hypothalamus-triggered vegetative reactions. This effect is prevented by BCTC but not by the noncompetitive NMDA receptor antagonists.**
KEYWORDS **NMDA receptors, TRPV1 ion channels, capsaicin, mice, nociception, thermoregulation.**
ABBREVIATIONS **MK-801 – (5S,10R)-(+)-5-methyl-10,11-dihydro-5H-dibenzo[a,d]cyclohepten-5,10-imine hydrogen maleate; BCTC – 4-(3-chloro-2-pyridinyl)-N-[4-(1,1-dimethylethyl)phenyl]-1-piperazinecarboxamide.**

INTRODUCTION

The interaction between glutamate and glutamate receptors is central for excitatory transmission in the central nervous system (CNS) and plays a crucial role in normal and pathophysiological nociception. In particular, the long-term activation of nociceptors, induced by either damage to tissues and nerves or inflammation, leads to a continuous release of glutamate; together with released neuropeptides, this may cause prolonged membrane depolarization, might eliminate the voltage-gated block of the ion channel of NMDA glutamate receptors by magnesium, and ensure their activation [1]. NMDA glutamate receptors are located on primary afferents [2–5], and their stimulation leads to nociceptor activation or sensitization [2, 6–9]. At the periphery, NMDA glutamate receptors can interact with TRPV1 ion channels in the calcium/calmodulin-dependent protein kinase type II (CaMKII) and protein kinase C (PKC) pathways; administration of AMG9810, an antagonist of TRPV1 ion channels, suppresses NMDA (N-methyl-D-aspartic acid)-induced mechanical hyperalgesia in rats [10]. Injection of antagonists of ionotropic NMDA and AMPA or metabotropic mGluR1 glutamate receptors into the plantar surface in rats decreases thermal hyperalgesia induced by capsaicin, a TRPV1 ion channel agonist, and inhibits the elevation of the glutamate level in subcutaneous perfusate observed after the injection of capsaicin into the animals' metatarsal region [11]. Noncompetitive antagonists of NMDA receptors (high-affinity (5S,10R)-(+)-5-methyl-10,11-dihydro-5H-dibenzo[a,d]cyclohepten-5,10-imine hydrogen maleate (MK-801) and low-affinity N-(2-adamantyl)-hexamethyleneimine hydrochloride (hemantane)) reduce the duration of the pain response to the sub-

cutaneous injection of a capsaicin solution into the metatarsal region of mice when applied dermally, systemically (intraperitoneally for hemantane and subcutaneously for MK-801), and via the subcutaneous intraplantar route [12].

TRPV1 ion channels are voltage-gated non-selective cation channels that are expressed by primary afferent neurons, activated by vanilloids, low pH values (pH < 6.5), changes in osmolarity, arachidonic acid metabolites, endocannabinoids, as well as temperatures above 42°C [13–17], and are regarded as a potential signal integrator under pathological conditions (in particular, that is indicated by the possibility of their functional interaction with NMDA glutamate receptors in trigeminal afferent neurons in mechanical hyperalgesia [10]). Like NMDA glutamate receptors, TRPV1 ion channels are abundant in the CNS [17]. Taking into account the ability of TRPV1 ion channels and NMDA glutamate receptors to functionally interact at the periphery, it is rather interesting to study their interplay in the CNS.

The aim of this work was to evaluate the ability of noncompetitive antagonists of NMDA receptors (the high-affinity MK-801 and low-affinity hemantane) to influence the effects of capsaicin, an agonist of TRPV1 ion channels, at the CNS level: alter the pain response threshold in the tail flick test and rectal temperature in mice. The effect of the antagonists of NMDA receptors was compared to the selective antagonist of TRPV1 ion channels, 4-(3-chloro-2-pyridinyl)-N-[4-(1,1-dimethylethyl)phenyl]-1-piperazinecarboxamide (BCTC), which is capable of penetrating the blood–brain barrier (BBB) [18].

MATERIALS AND METHODS

Animals

Mature male ICR mice (weight, 23–26 g) procured from the Stolbovaya husbandry of laboratory animals, Research Center of Biomedical Technologies, Federal Medical and Biological Agency (Moscow Region, Russia), were used in this study. The animals were handled in compliance with the State Standard GOST 33216-2014 "Guidelines for Accommodation and Care of Laboratory Animals. Species-Specific Provisions for Laboratory Rodents and Rabbits," State Standard GOST 33215-2014 "Guidelines for Accommodation and Care of Animals. Environment, Housing and Management," and Directive 2010/63/EU of the European Parliament and the Council of the European Union, dated September 9, 2010, on the protection of animals used for scientific purposes. Experiment conduct was approved by the Biomedical Ethics Commission of the Zakusov Research Institute of Pharmacology (Protocol No. 01 dated January 28, 2022).

Study objects, doses, and administration routes

NMDA receptor antagonists were the noncompetitive high-affinity antagonist (5S,10R)-(+)-5-methyl-10,11-dihydro-5H-dibenzo[a,d]cyclohepten-5,10-imine hydrogen maleate (MK-801; Sigma Aldrich, USA) and noncompetitive low-affinity antagonist N-(2-adamantyl)-hexamethyleneimine hydrochloride (hemantane; synthesized and provided by the Chemical–Technological Laboratory of the Zakusov Research Institute of Pharmacology). The antagonist of TRPV1 ion channels was 4-(3-chloro-2-pyridinyl)-N-[4-(1,1-dimethylethyl)phenyl]-1-piperazinecarboxamide (BCTC; Sigma Aldrich, USA). The agents were administered 30 min prior to injecting the capsaicin solution: MK-801 was injected subcutaneously at doses of 20 μg/kg and 0.5 mg/kg; hemantane was injected intraperitoneally at a dose of 40 mg/kg; and BCTC was injected intraperitoneally at a dose of 20 mg/kg.

The TRPV1 ion channel agonist capsaicin (Sigma Aldrich, USA), diluted in a saline–ethanol mixture (9:1, v/v), was injected subcutaneously at a dose causing transient hypothermia in mice (1 mg/kg) [14].

Tail flick test

The tail flick test is based on the spinal flexion reflex in response to a progressively increasing thermal radiation stimulation of skin and is widely used for assessing the analgesic effect of various agents [19, 20]. Thermoreceptors, C- and Ad-fibers of polymodal nociceptors, and high-threshold mechanoreceptors are sequentially activated in this test. Local pain stimulation of the tail was induced by thermal radiation using a TSE-system analgesiometer (Germany). Stimulation intensity was 27%, which corresponded to a gradual temperature increase ranging from 51 to 61°C during 15 s. The latent period (LP) until tail withdrawal (15 s) was considered the maximum possible time of stimulation. The maximum possible effect (MPE) was calculated using the formula:

$$MPE\ (\%)=(LP_{exp} - LP_{control})\times 100/(MAXtime - LP_{control}),$$ where

LP_{exp} was the latent period of response in mice 30 min after administering the capsaicin solution or NMDA receptor and TRPV1 ion channel antagonists;

$LP_{control}$ was the latent period for mice in the control group that received the solvent; and

MAXtime was the maximum possible time of stimulation (15 s).

The experimental investigation of the effect of noncompetitive NMDA receptor antagonists on changes in the pain response threshold in the tail flick test induced by capsaicin (a TRPV1 ion channel agonist) involved two stages. The influence of BCTC, a TRPV1 ion channel antagonist, and NMDA receptor antagonists on the sensitivity to thermal stimulation of the mouse tail was assessed 30 min after their administration at the first stage. At the second stage, their effect on the pain response threshold in the animals, increased by capsaicin administration, was evaluated 30 min after injecting the TRPV1 ion channel agonist. Mice that had subcutaneously received an equivalent volume (10 mL/kg) of solvents were used as control groups. Saline was used as a solvent in the first experiment. In the second experiment, saline was employed as a solvent for BCTC, hemantane, and MK-801, and a saline–ethanol mixture (9:1, v/v) was used for capsaicin; in other words, the animals received saline instead of BCTC, hemantane, or MK-801, and a saline–ethanol mixture (9:1, v/v) instead of capsaicin.

Rectal temperature in mice was measured using a digital rectal thermometer (Kent Scientific Corp., USA). Groups of animals that had received solvents (saline and saline–ethanol mixture (9:1, v/v)), saline and capsaicin, and groups of animals that received capsaicin 30 min after administration of the tested antagonists of NMDA receptors and TRPV1 ion channels were included in the experiment. The effects of antagonists of NMDA receptors and TRPV1 ion channels on the rectal temperature in mice that had received saline only were also compared. The rectal temperature was measured prior to injecting the saline, capsaicin, NMDA receptor antagonists, and BCTC, and every 30 min after administration of the solvent, NMDA antagonists, BCTC, and capsaicin (2 h), or every 30 min after administration of capsaicin (when injected together with NMDA receptor antagonists and BCTC (2 h)).

Statistical analysis of the experimental data was carried out using the Statistica 10.0 software. Data were checked for normal distribution using the Shapiro–Wilk test, followed by an evaluation of intergroup equality using the Levene's test. For normal distribution in the groups and the homogeneity of intergroup variance, further statistical analysis was performed using a one-way analysis of variance (ANOVA), followed by group comparison using the Newman–Keuls test. The Kruskal–Wallis test, a nonparameteric alternative to one-way ANOVA, was used in the case of non-normal distribution. If statistically significant intergroup differences were detected using the Kruskal–Wallis test, we carried out pairwise comparison of samples using the Mann–Whitney U test. Intergroup differences were considered statistically significant at $p < 0.05$. The figures were created using the GraphPad Prism V. 8.4.3 software.

RESULTS AND DISCUSSION

Expression of TRPV1 ion channels is maximal in the dorsal roots of the spinal cord of mice [21]; their short-term stimulation induces a long-lasting increase in the presynaptic level of calcium (Ca^{2+}) ions and potentiates glutamate release into the synaptic gap [22]. In turn, activation of NMDA glutamate receptors in spinal dorsal horns is needed in order to trigger central sensitization [23–26].

The spinal flexion reflex was chosen as a nociceptive reaction that occurs at the spinal cord level and whose mechanism involves TRPV1 ion channels and NMDA glutamate receptors. The tail flick test reproducing this reflex [20, 27] allows one to assess the ability of NMDA receptor antagonists to affect TRPV1 activation-induced changes in the animals' sensitivity to thermal stimulation. $VR^{-/-}$ mice (lacking TRPV1 ion channels) are known to produce an abnormal response to thermal pain stimulation. The C fibers in $VR^{-/-}$ mice are characterized by a lower threshold of the response to thermal stimulation, while the latency of the tail flick response in the tail immersion test at water temperatures of 50 and 52°C (but not 46 and 48°C) and animals' response in the hot plate test at temperatures of 52.5, 55, and 58°C (but not 50°C) is statistically significantly increased [14]. Therefore, in our experiment (the tail flick test), thermal stimulation was performed by exposing the animals' tails to thermal radiation, with the temperature gradually increased from 51 to 61°C (during 15 s).

A single intraperitoneal administration of 20 mg/kg BCTC (a TRPV1 ion channel antagonist) was found to significantly increase the latency of the tail flick response in mice – by 36.4% – compared to the control group; the maximum possible effect (MPE) was 15.09% (*Table 1*). TRPV1 ion channel antagonists are known to possess an analgesic effect [28]. In particular, our findings agree with the data on the efficacy of single intraperitoneal injection of BCTC at doses of 3, 10, and 30 mg/kg for the rat model of thermal hyperalgesia [29].

The low-affinity NMDA receptor antagonist hemantane, injected intraperitoneally at a dose of 40 mg/kg,

Table 1. The effect of NMDA receptor antagonists (hemantane and MK-801) and the TRPV1 ion channel antagonist (BCTC) on the thermal pain threshold in the tail flick test in ICR mice. Median (Q1; Q3)

Group	Number of mice per group	Latency of tail flick response, s	MPE, %
Control	10	4.40 (3.90; 5.10)	0.00 (-4.72; 6.60)
BCTC, 20 mg/kg	8	6.00 (5.20; 7.35)*	15.09 (7.55; 27.83)*
Hemantane, 40 mg/kg	8	7.20 (6.30; 10.05)*	26.42 (17.92; 53.30)*
MK-801, 20 μg/kg	9	4.60 (4.10; 5.20)	1.89 (-2.83; 7.55)
MK-801, 0.5 mg/kg	9	4.00 (3.80; 4.40)	-3.77 (-5.66; 0.00)

Note: control – saline; MPE – maximum possible effect.
*$p < 0.05$ vs. Control group; Mann–Whitney U test.

Table 2. The effect of NMDA receptor antagonists (hemantane and MK-801) and the TRPV1 ion channel antagonist (BCTC) on the capsaicin-induced increase in the thermal pain threshold in ICR mice. Median (Q1; Q3)

Group	Number of mice per group	Latency of tail flick response, s	MPE, %
Saline + saline/ethanol	11	4.60 (4.50; 4.80)	0.00 (-0.96; 1.92)
Saline + capsaicin, 1 mg/kg	13	7.70 (6.80; 15.00)*	29.81 (21.15; 100.00)*
BCTC 20 mg/kg + capsaicin, 1 mg/kg	8	6.35 (5.90; 7.45)*#	16.83 (12.50; 27.40)*#
Hemantane 40 mg/kg + capsaicin, 1 mg/kg	11	5.60 (4.90; 9.20)*#	9.62 (2.88; 44.23)*#
MK-801 20 μg/kg + capsaicin, 1 mg/kg	14	4.60 (3.90; 4.90)#	0.00 (-6.73; 2.88)#
MK-801 0.5 mg/kg + capsaicin, 1 mg/kg	13	3.80 (3.40; 4.60)*#	-7.69 (-11.54; 0.00)*#

*$p < 0.05$ vs. group "Saline + saline/ethanol," Mann–Whitney U test.
#$p < 0.05$ vs. group "Saline + capsaicin, 1 mg/kg," Mann–Whitney U test.

increased the latency of the flick tail response in mice by 63.6% compared to the control group; the MPE was 26.42%. No significant intergroup differences between animals that received 20 mg/kg BCTC and 40 mg/kg hemantane were detected (*Table 1*). Single intraperitoneal administration of 20 and 40 mg/kg hemantane shortened the duration of the pain response to subcutaneous injection of a capsaicin solution into the metatarsal region in mice in a dose-dependent manner; therefore, the 40 mg/kg dose of the agent was used in this study [12].

A single subcutaneous injection of the high-affinity NMDA receptor antagonist MK-801 at a dose of 20 μg/kg (at this dose, it reduced the duration of the capsaicin-induced pain behavior in mice [12]) and a larger dose (0.5 mg/kg) had no significant effect on the thermal pain threshold in the tail flick test in mice (*Table 1*). Interestingly, single administration of MK-801, the high-affinity NMDA receptor antagonist, induced both the pronociceptive [30] and antinociceptive effects in rats [31].

Single subcutaneous administration of 1 mg/kg capsaicin substantially raised the thermal pain threshold in mice. The latency of the tail flick response to capsaicin administration was 67.4% longer than that in control group mice that had received solvents (saline + saline/ethanol mixture (9:1, v/v)) (*Table 2*). The detected effect of capsaicin in the tail flick test in mice is attributed to the ability of this agent to induce long-lasting desensitization of nociceptors [32]. Capsaicin did not increase the thermal pain threshold in mice that had preventively received BCTC (a selective TRPV1 ion channel antagonist) or NMDA receptor antagonists (hemantane and MK-801). The effectiveness of BCTC administered to mice 30 min prior to a subcutaneous injection of capsaicin was almost identical to that in the group of animals that had received BCTC only. Thus, the latency of the tail flick response in the group "BCTC, 20 mg/kg + capsaicin, 1 mg/kg" was significantly higher (by 38.04%) compared to the control group (group "saline + saline/ethanol"); the MPE was 16.83%. Hemantane administered at a dose of 40 mg/kg 30 min prior to capsaicin injection increased the latency of the tail flick response in mice by 21.7% compared to the control group; the MPE was 9.62% (*Table 2*). Although the latency of the tail flick response in animals that had received hemantane prior to capsaicin injection was lower than that in the animals that had been given hemantane only, no significant differences in the MPE were observed in these groups (*Tables 1* and *2*). Administration of MK-801 at both doses 30 min prior to capsaicin injection did not increase the thermal pain threshold in mice in the tail flick test (*Table 2*).

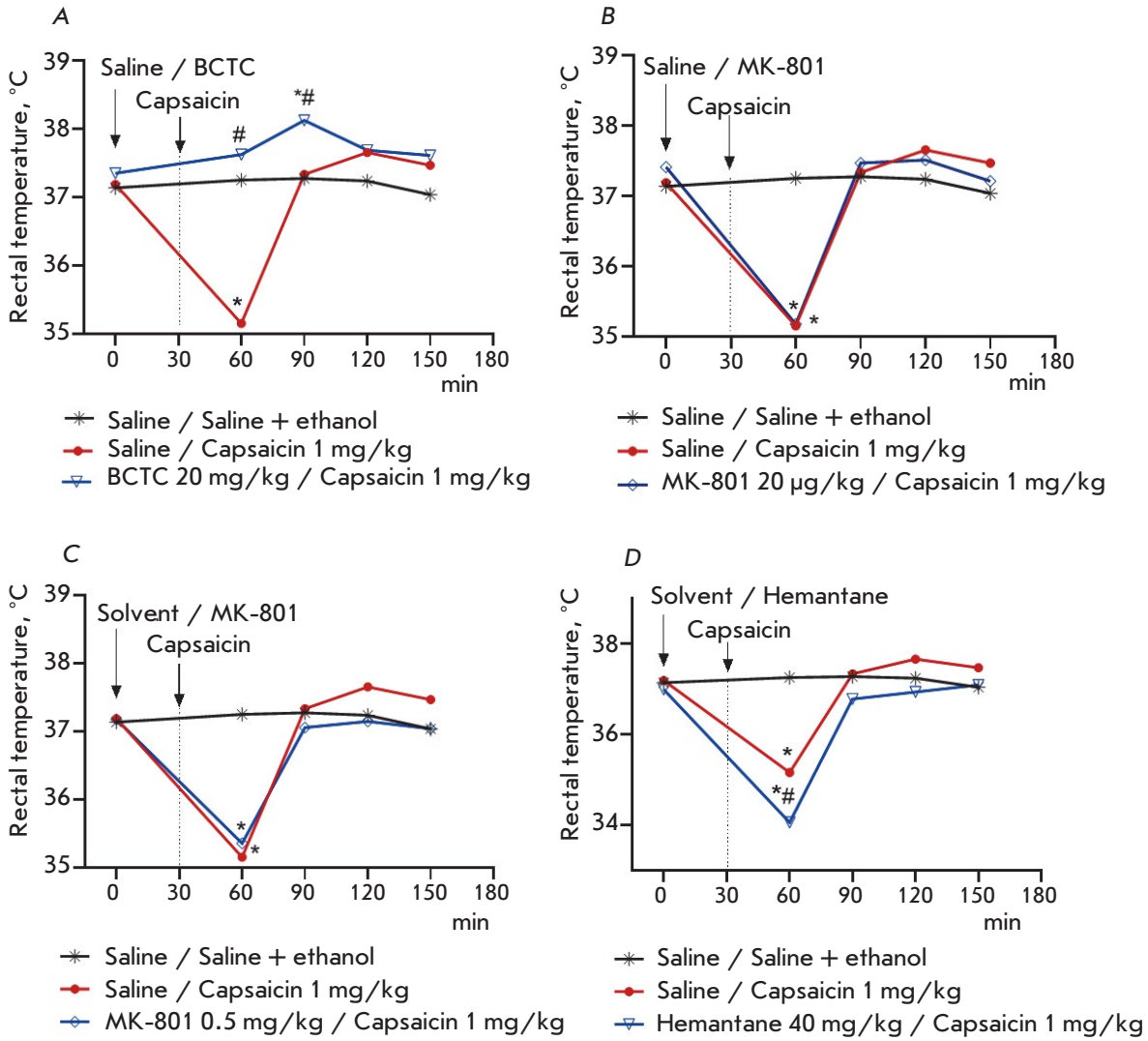

Fig. 1. Effect of the TRPV1 antagonist BCTC and NMDA receptor antagonists hemantane and MK-801 on the capsaicin-induced decrease in the rectal temperature in mice. $^{*}p < 0.05$ compared to the group "Saline / Saline + ethanol", the Newman–Keuls test. $^{\#}p < 0.05$ compared to the group "Saline / Capsaicin 1 mg/kg", the Newman–Keuls test

In the groups of mice that had received NMDA receptor antagonists (hemantane and MK-801) and BCTC before capsaicin injection, the latency of the tail flick response was significantly lower than that in the group of mice that had received capsaicin and saline (*Table 2*).

Hence, the thermal pain threshold was significantly lower in the group of animals that had preventively (before capsaicin injection) been administered the selective TRPV1 ion channel antagonist (BCTC) or NMDA receptor antagonists (hemantane and MK-801) than that in mice that had received capsaicin and saline. This demonstrates that NMDA receptor antagonists and BCTC (a TRPV1 ion channel antagonist) exhibit similar activities. These agents suppressed the effect of capsaicin on TRPV1 ion channels that causes their desensitization and, therefore, significant increase in the thermal pain threshold.

One of the functions of TRPV1 is to get involved in thermoregulation through central and peripheral mechanisms [33–35]. Systemic administration of cap-

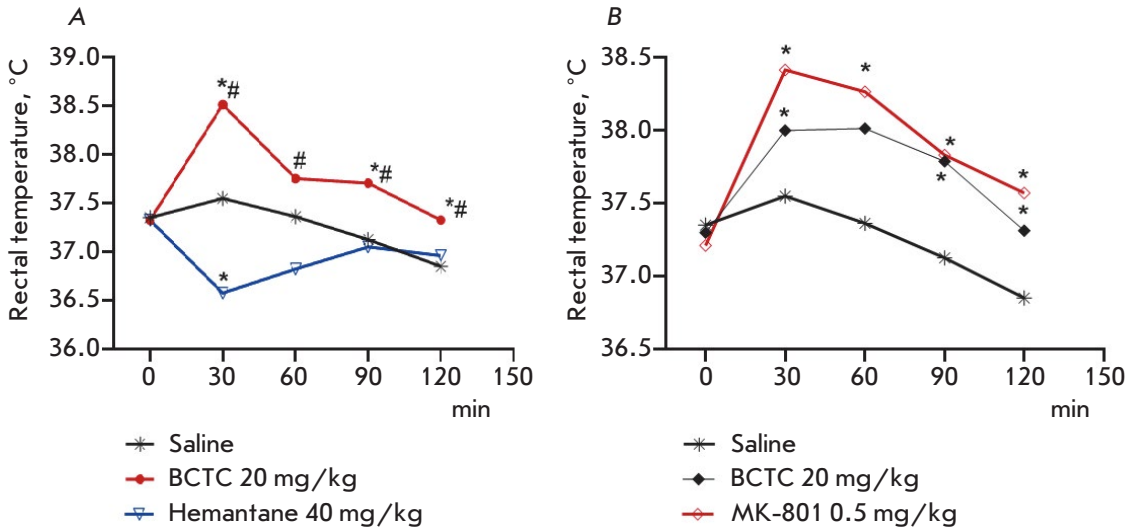

Fig. 2. Effect of the TRPV1 antagonist BCTC and NMDA receptor antagonists hemantane and MK-801 on the rectal temperature in mice. $^{*}p < 0.05$ compared to the group "Saline", the Newman–Keuls test. $^{\#}p < 0.05$ compared to the group "Hemantane 40 mg/kg", the Newman–Keuls test

saicin leads to a rapid transient decline in body temperature, which is brought about by hypothalamus-triggered vegetative reactions, such as vasodilation and hypersalivation [14, 36].

Glutamate receptors in the raphe pallidus nucleus (RPa) mediate the thermogenesis of brown adipose tissue induced by the activation of dorsomedial hypothalamic neurons: microinjections of NMDA or kainic acid into RPa increase the temperature of brown adipose tissue in rats [37]. Preventive administration of LY 235959, a selective NMDA receptor antagonist, weakens hyperthermia induced by icilin (AG-3-5), an agonist of TRPM8 and TRPA1 channels, in rats [38].

In our experiment, a single subcutaneous administration of 1 mg/kg capsaicin to mice induced transient hypothermia, which was observed 30 min after the injection: the rectal temperature decreased by 2°C compared both to its background value (before capsaicin injection) and its value in the control group of mice that had received solvents: saline + saline/ethanol mixture (9:1, v/v). The rectal temperature returned to normal 60 min after capsaicin administration (*Fig. 1*).

A preventive single intraperitoneal dose (20 mg/kg) of BCTC, the selective TRPV1 ion channel antagonist, which is capable of penetrating the BBB [18], suppressed the hypothermic effect of capsaicin. In mice that had sequentially received BCTC and then capsaicin (subcutaneously), the rectal temperature at 30 and 60 min post-injection was significantly higher than that in the animal group receiving capsaicin and saline (by 2.5 and 0.8°C, respectively) (*Fig. 1A*). Like other TRPV1 ion channel antagonists, BCTC induces hyperthermia, whose formation mechanism remains unclear [32]. Thus, in our experiment, a significant increase in the rectal temperature (compared to the control group of animals) was observed in mice that had received a single intraperitoneal dose (20 mg/kg) of BCTC 30, 90, and 120 min post-injection: by 1, 0.6, and 0.5°C, respectively (*Fig. 2A*).

A preventive single-dose administration of non-competitive NMDA receptor antagonists (the high-affinity MK-801 and low-affinity hemantane) did not suppress the hypothermic effect of capsaicin that was observed 30 min after its injection. The rectal temperature in mice that had received the high-affinity NMDA receptor antagonist MK-801 at doses of 20 μg/kg and 0.5 mg/kg prior to capsaicin injection was 35.18 and 35.36°C, respectively, after the injection; in the animals in the group "Capsaicin", the rectal temperature was 35.16°C (*Fig. 1B,C*). Meanwhile, similarly to BCTC, MK-801 induced hyperthermia in mice at both doses (*Fig. 2A,B*). The rectal temperature in animals that had received the high-affinity NMDA receptor antagonist at a dose of 0.5 mg/kg significantly exceeded that in the control group of mice, from minutes 30–120 of follow-up; at a dose of 20 μg/kg, 30, 90, and 120 min after administration of MK-801 (*Fig. 2B*). It is known that MK-801 can induce both hyperthermia, when administered

to rats at doses up to 1.2 mg/kg [39, 40], and hypothermia, when its dose is increased to 3 mg/kg [40]. In our study, the observed elevation of the rectal temperature in mice in response to the injection of the high-affinity NMDA receptor antagonist MK-801 may have to do with its dopamine-positive effect. It has been demonstrated for rat striatal synaptosomes that both the noncompetitive NMDA receptor antagonist MK-801 and the competitive NMDA receptor antagonist (+/-)-CPP (3-(2-carboxypyperazin-4-yl)-propyl-1-phosphonic acid) inhibit dopamine reuptake [41]. The dopaminergic system plays a crucial role in body temperature regulation in rats; agonists of D1- and D2-dopaminergic receptors induce hyperthermia in rats [42].

Single-dose preventive intraperitoneal administration of hemantane (40 mg/kg) 30 min prior to capsaicin injection significantly potentiated capsaicin-induced hypothermia: hemantane significantly decreased the rectal temperature in mice by 1.1°C compared to the group "Capsaicin" 30 min after administration of the TRPV1 agonist (*Fig. 1D*). Meanwhile, when administered intraperitoneally as a single dose (40 mg/kg) to intact animals, hemantane significantly reduced the rectal temperature by 1°C 30 min post-injection; 60 min after hemantane administration, the rectal temperature of mice rose to a value that did not significantly differ from the rectal temperature in the control group (*Fig. 2A*). Therefore, capsaicin administered 30 min after hemantane injection increases the duration of the hypothermic effect of hemantane to 60 min. After this period (60 min after capsaicin injection), there was no significant difference in rectal temperature between animals that had received hemantane and the control group or the group "Capsaicin" (*Fig. 1D*).

It was found earlier that single-dose intraperitoneal administration of 20 mg/kg hemantane reduces the levels of serotonin and its metabolite, 5-hydroxyindolacetic acid, in the striatum of C57Bl/6 mice [43]. Therefore, the detected hypothermic effect of hemantane would be apparently attributed to its effect on the serotonergic system, since hypothalamic serotonergic neurons control the body temperature homeostasis, while serotonin injection into the thermosensitive anterior hypothalamic area induces hyperthermia [44].

Excitation of the capsaicin-sensitive peripheral nerves (cutaneous somatosensory afferents and afferent vagus nerve fibers in the abdominal cavity) transmitting signals via the polysynaptic pathways into the preoptic area of the hypothalamus that is responsible for thermoregulation is considered to be a potential mechanism of TRPV1-induced hypothermia [35]. Furthermore, capsaicin, when penetrating the BBB [45], can activate the TRPV1 ion channels of hypothalamic neuronal cells and, therefore, affect thermosensitivity [35]. Thus, capsaicin injection into the preoptic area of the hypothalamus of rats leads to a rapid decline in body temperature; repeated injections of this TRPV1 agonist decrease its intensity [46].

Preliminary administration of NMDA receptor antagonists suppressed the capsaicin-induced increase in the threshold of pain sensitivity in the tail flick test reproducing the spinal flexion reflex in mice and shortened the duration of their response (paw licking) to the injection of a capsaicin solution into the metatarsal region in our earlier study [12]. Intradermal injection of capsaicin into a the paw in rats induced phosphorylation of the NR1 subunit of the NMDA receptors in the neurons of the dorsal horns of the spinal cord and the spinothalamic tract catalyzed by protein kinase A (PKA)- and PKC, which was detected 30 min after capsaicin injection [47, 48]. According to the reported facts of the functional interplay between NMDA receptors and TRPV1 ion channels, we put forward a hypothesis that preliminary administration of NMDA receptor antagonists MK-801 and hemantane would reduce the severity of capsaicin-induced hypothermia by weakening nerve impulse transmission from the periphery (in particular, in the spinal cord) to the preoptic area of the hypothalamus. This, however, did not occur: preliminary administration of NMDA receptor antagonists to the animals did not prevent transient capsaicin-induced hypothermia. Therefore, in the mechanism of transient capsaicin-induced hypothermia in mice, we uncovered no functional interplay between TRPV1 ion channels and NMDA receptors that would be similar to that detected in the experiments aiming to assess the pain response in mice in the tail flick test or the duration of the response in mice when the studied TRPV1 agonist was injected into the metatarsal region [12]. Therefore, our data prove that when administered systemically, capsaicin, a selective TRPV1 ion channel agonist, can penetrate the BBB and act on the neurons in the preoptic area of the hypothalamus, thus affecting thermosensitivity.

CONCLUSIONS

It has been established in the tail flick test reproducing the spinal flexion reflex in mice that preventive administration of noncompetitive NMDA receptor antagonists (the high-affinity MK-801 and low-affinity hemantane) and the selective TRPV1 ion channel antagonist BCTC inhibits the increase in the ther-

mal pain threshold induced by capsaicin, a TRPV1 agonist. Taking into account the interplay between NMDA receptors and TRPV1 ion channels at the periphery, the effect observed in the tail flick test in mice can be attributed to the effect exhibited by the tested compounds on afferent innervation. Further studies are needed to evaluate this interplay at the CNS level.

Single-dose subcutaneous injection of capsaicin induces transient hypothermia in mice, and preliminary administration of BCTC, a selective TRPV1 ion channel antagonist, but not the noncompetitive NMDA receptor antagonists MK-801 and hemantane, this effect. Our findings prove that there can be a functional interplay between NMDA receptors and TRPV1 ion channels in the capsaicin-induced antinociceptive response, but this interplay is absent in the case of transient capsaicin-induced hypothermia, whose mechanism is attributed to hypothalamus-triggered vegetative reactions. ●

REFERENCES

1. Chrizh B.A. // Amino Acids. 2002. V. 23. № 1–3. P. 169–176.
2. Carlton S.M., Hargett G.L., Coggeshall R.E. // Neurosci. Lett. 1995. V. 197. № 1. P. 25–28.
3. Coggeshall R.E., Carlton S.M. // J. Comp. Neurol. 1998. V. 391. № 1. P. 78–86.
4. Kinkelin I., Bröcker E.B., Koltzenburg M., Carlton S.M. // Neurosci. Lett. 2000. V. 283. № 2. P. 149–152.
5. Ma Q.P., Hargreaves R.J. // Neuroscience. 2000. V. 101. № 3. P. 699–707.
6. Du J., Koltzenburg M., Carlton S.M. // Pain. 2001. V. 89. № 2–3. P. 187–198.
7. Lawand N.B., Willis W.D., Westlund K.N. // Eur. J. Pharmacol. 1997. V. 324. № 2–3. P. 169–177.
8. Zhou S., Bonasera L., Carlton S.M. // Neuroreport. 1996. V. 7. № 4. P. 895–900.
9. Christoph T., Reissmüller E., Schiene K., Englberger W., Chizh B.A. // Brain Res. 2005. V. 1048. № 1–2. P. 218–227.
10. Lee J., Saloman J. L., Weiland G., Auh Q.S., Chung M.K., Ro J.Y. // Pain. 2012. V. 153. № 7. P. 1514–1524.
11. Jin Y.H., Yamaki F., Takemura M., Koike Y., Furuyama A., Yonehara N. // J. Pharmacol. Sci. 2009. V. 109. № 2. P. 233–241.
12. Ivanova E.A., Matyushkin A.I., Voronina T.A. // Pharm. Chem. J. 2021. V. 55. P. 857–859.
13. Tominaga M., Caterina M.J., Malmberg A.B., Rosen T.A., Gilbert H., Skinner K., Raumann B.E., Basbaum A.I., Julius D. // Neuron. 1998. V. 21. № 3. P. 531–543.
14. Caterina M.J., Leffler A., Malmberg A.B., Martin W.J., Trafton J., Petersen-Zeitz K.R., Koltzenburg M., Basbaum A.I., Julius D. // Science. 2000. V. 288. № 5464. P. 306–313.
15. Chung M.K., Guler A.D., Caterina M.J. // Nat. Neurosci. 2008. V. 11. № 5. P. 555–564.
16. Chavez A.E., Chiu C.Q., Castillo P.E. // Nat. Neurosci. 2010. V. 13. № 12. P. 1511–1518.
17. Sanchez J.F., Krause J.E., Cortright D.N. // Neuroscience. 2001. V. 107. № 3. P. 373–381.
18. Valenzano K.J., Grant E.R., Wu G., Hachicha M., Schmid L., Tafesse L., Sun Q., Rotshteyn Y., Francis J., Limberis J., et al. // J. Pharmacol. Exp. Ther. 2003. V. 306. № 1. P. 377–386.
19. Mironov A.N., editor. Guidelines for Preclinical Trials of Medicinal Products. // M.: Grif i K, 2012. 944 p. (in Russian).
20. Bannon A.W., Malmberg A.B. // Curr. Protoc. Neurosci. 2007. doi: 10.1002/0471142301.ns0809s41.
21. Sanchez J.F., Krause J.E., Cortright D.N. // Neuroscience. 2001. V. 107. № 3. P. 373–381.
22. Medvedeva Y.V., Kim M.S., Usachev Y.M. // J. Neurosci. 2008. V. 28. № 20. P. 5295–5311.
23. Bleakman D., Alt A., Nisenbaum E.S. // Semin. Cell. Dev. Biol. 2006. V 17. № 5. P. 592–604.
24. Chizh B.A., Headley P.M. // Curr. Pharm. Des. 2005. V. 11. № 23. P. 2977–2994.
25. Salter M.W. // Curr. Top. Med. Chem. 2005. V. 5. № 6. P. 557–567.
26. Woolf C.J. // Anesthesiology. 2007. V. 106. № 4. P. 864–867.
27. Dewey W.L., Harris L.S., Howes J.F., Nuite J.A. // J. Pharmacol. Exp. Ther. 1970. V. 175. № 2. P. 435–442.
28. Trevisani M., Gatti R. // Open Pain J. 2013. № 6 (Suppl 1: M11). P. 108–118.
29. Tekus V., Bölcskei K., Kis-Varga A., Deezsi L., Szentirmay E., Visegrady A., Horvath C., Szolcsanyi J., Petho G. // Eur. J. Pharmacol. 2010. V. 641. № 2–3. P. 135–141.
30. Al-Amin H., Saade N., Khani M., Atweh S., Jaber M. // Brain Res. 2003. V. 981. № 1–2. P. 99–107.
31. Forman L.J. // Life Sci. 1999. V. 64. № 21. P. 1877–1887.
32. Iftinca M., Defaye M., Altier C. // Drugs. 2021. V. 81. № 1. P. 7–27.
33. Kauer J.A., Gibson H.E. // Trends Neurosci. 2009. V. 32. № 4. P. 215–224.
34. Sharif-Naeini R., Ciura S., Bourque C.W. // Neuron. 2008. V. 58. № 3. P. 179–185.
35. Caterina M.J. // Am. J. Physiol. Regul. Integr. Comp. Physiol. 2007. V. 292. № 1. P. R64–R76.
36. Jancso-Gabor A., Szolcsanyi J., Jancso N. // J. Physiol. 1970. V. 206. № 3. P. 495–507.
37. Cao W.H., Morrison S.F. // Neuropharmacology. 2006. V. 51. № 3. P. 426–437.
38. Ding Z., Gomez T., Werkheiser J.L., Cowan A., Rawls S.M. // Eur. J. Pharmacol. 2008. V. 578. № 2–3. P. 201–208.
39. Pechnick R.N., Hiramatsu M. // Eur. J. Pharmacol. 1994. V. 252. № 1. P. 35–42.
40. Hetzler B.E., Burkard H.K. // Pharmacol. Biochem. Be-

hav. 1999. V. 62. № 3. P. 559–573.
41. Kovalev G.I., Abaimov D.A., Voronin M.V., Firstova Yu.Yu., Dolotov O.V. // Neurochem. J. 2007. V. 24. № 2. P. 253–259.
42. Nagashima M., Yamada K., Kimura H., Matsumoto S., Furukawa T. // Pharmacol. Biochem. Behav. 1992. V. 43. № 4. P. 993–997.
43. Abaimov D.A., Zimin I.A., Kudrin V.S., Kovalev G.I. // Eksperimental'naya i Klinicheskaya Farmakologiya. 2009. V. 72. № 1. P. 64–67. (in Russian).
44. Myers R.D. // J. Physiol. (Paris). 1981. V. 77. № 2–3. P. 505–513.
45. Saria A., Skofitsch G., Lembeck F. // J. Pharm. Pharmacol. 1982. V. 34. № 4. P. 273–275.
46. Jancso-Gabor A., Szmrecsanyi J., Jancso N. // J. Physiol. 1970. V. 208. № 2. P. 449–459.
47. Zou X., Lin Q., Willis W.D. // Neuroscience. 2002. V. 115. № 3. P. 775–786.
48. Zou X., Lin Q., Willis W.D. // Brain. Res. 2004. V. 1020. P. 95–105.

RNAcontacts: A Pipeline for Predicting Contacts from RNA Proximity Ligation Assays

S. D. Margasyuk[1], M. A. Vlasenok[1], G. Li[2], Ch. Cao[3], D. D. Pervouchine[1*]
[1]Skolkovo Institute of Science and Technology, Moscow, 121205 Russian Federation
[2]College of Life Sciences, Zhejiang University, Hangzhou, Zhejiang, ZJ310058 China
[3]Key Laboratory of RNA Biology, Institute of Biophysics, Chinese Academy of Sciences, Beijing, 100101 China
[*]E-mail: d.pervouchine@skoltech.ru
Received December 22, 2022; in final form, February 20, 2023
DOI: 10.32607/actanaturae.11893

ABSTRACT **High-throughput RNA proximity ligation assays are molecular methods that are used to simultaneously analyze the spatial proximity of many RNAs in living cells. Their principle is based on cross-linking, fragmentation, and subsequent religation of RNAs, followed by high-throughput sequencing. The generated fragments have two different types of splits, one resulting from pre-mRNA splicing and the other formed by the ligation of spatially close RNA strands. Here, we present RNAcontacts, a universal pipeline for detecting RNA–RNA contacts in high-throughput RNA proximity ligation assays. RNAcontacts circumvents the inherent problem of mapping sequences with two distinct types of splits using a two-pass alignment, in which splice junctions are inferred from a control RNA-seq experiment on the first pass and then provided to the aligner as *bona fide* introns on the second pass. Compared to previously developed methods, our approach allows for a more sensitive detection of RNA contacts and has a higher specificity with respect to splice junctions that are present in the biological sample. RNAcontacts automatically extracts contacts, clusters their ligation points, computes the read support, and generates tracks for visualizing through the UCSC Genome Browser. The pipeline is implemented in Snakemake, a reproducible and scalable workflow management system for rapid and uniform processing of multiple datasets. RNAcontacts is a generic pipeline for the detection of RNA contacts that can be used with any proximity ligation method as long as one of the interacting partners is RNA. RNAcontacts is available via the GitHub repository https://github.com/smargasyuk/RNAcontacts/**

KEYWORDS **RNA, proximity ligation, RNA contacts, splicing, RNA structure.**

ABBREVIATIONS **EEJ – Exon-exon junction; RIC-seq – RNA *in situ* conformation sequencing; RBP – RNA-binding protein**

INTRODUCTION

The rapid evolution of high-throughput sequencing technology enabled the *in vivo* identification of spatial contacts between nucleic acids, including the DNA contacts in the 3D chromatin structure [1–3], functional enhancer-promoter interactions [4, 5], and chromatin-associated RNA–DNA contacts [6, 7]. These methods rest on the basic principle of digestion of nucleic acids cross-linked in macromolecular complexes and subsequent stochastic religation, which occurs predominantly between spatially proximal molecules. Deep sequencing of the resulting chimeric fragments produces hundreds of millions of reads encoding sequence signatures of the interacting loci.

A number of recently developed methods employ RNA proximity ligation to trace back RNA–RNA interactions *in vivo* and *in vitro* (see [8] and [9] for review). Some of them, such as PARIS [10], LIGR-seq [11], SPLASH [12], and COMRADES [13], use psoralen derivatives to induce reversible cross-linking between RNA duplexes to assess pairwise structural interactions *in vivo* with high sensitivity and specificity. In the RIC-seq protocol, the RNA strands are cross-linked through an RNA-binding protein (RBP)

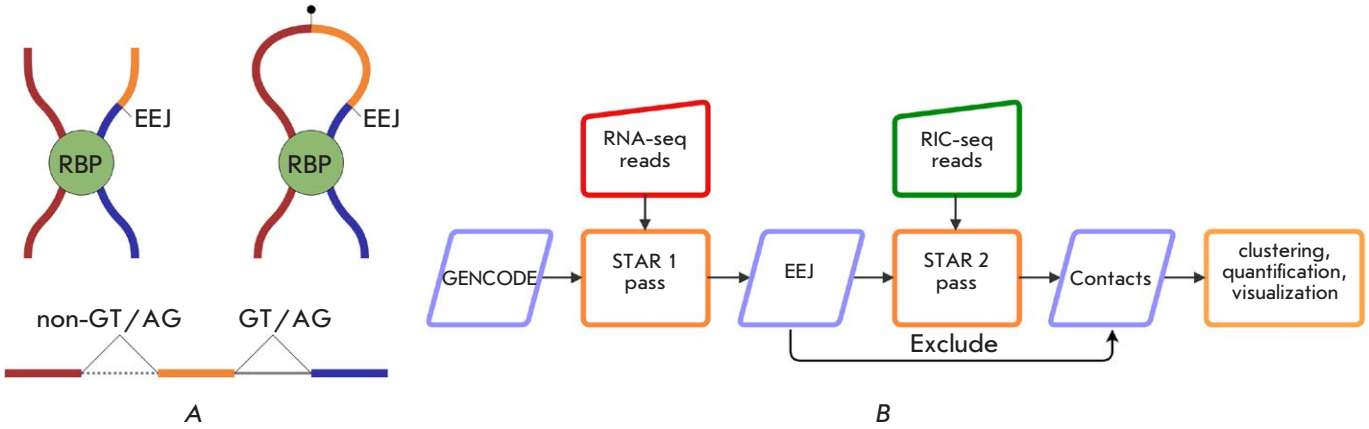

Fig. 1. (*A*) – In RIC-seq protocol [14], an unspliced RNA strand can be cross-linked through an RNA-binding protein (RBP) to a strand with exon-exon junctions (EEJ). The sequence formed by proximity ligation aligns to the reference genome with a non-GT/AG split reflecting the ligation point and a canonical GT/AG split resulting from splicing. (*B*) – The RNAcontacts pipeline. On the first pass, short reads from the control RNA-seq experiment are aligned to the reference genome to identify the expressed splice junctions. The latter are used on the second pass as *bona fide* introns when aligning proximity ligation data to detect ligation junctions, which encode RNA–RNA contacts

[14]. Not only can this approach recapitulate RNA secondary and tertiary structures, but it also helps generate three-dimensional maps of the interacting RNA-RBP complexes. In all these cases, the interactions are encoded within chimeric RNA sequences obtained via digestion and religation.

However, unlike DNA-DNA interactions, which manifest themselves in the sequencing data as split reads that align to a pair of genomic loci, RNA-RNA interactions may produce more sophisticated split alignments because pre-mRNAs are spliced. In particular, the cross-linked fragments may contain both exon-exon junctions and proximity ligation products, thus producing short reads with canonical intronic GT/AG splits resulting from splicing and non-GT/AG splits resulting from religation (*Fig. 1A*). Accurate mapping of such reads is challenging, because most short-read alignment tools can deal only with one type of split. With just one split model, the aligner would have to make a tradeoff between increasing the penalty for non-GT/AG splits to correctly identify introns at the expense of missing RNA-RNA contacts, or relaxing the GT/AG requirement to correctly detect RNA-RNA contacts, while having incorrect intron mappings. Therefore, developing a computational method for mapping short reads with such distinct types of splits is of particular interest. The current work introduces a computational pipeline that makes it possible to achieve such a goal without developing specialized alignment software.

EXPERIMENTAL PART

Genomes and annotations

The hg19 assembly of the human genome (February 2009) and GENCODE transcript annotation v34lift37 were downloaded from the Genome Reference Consortium [15] and GENCODE website [16], respectively. Intron coordinates were taken from STAR output (see below).

High-throughput sequencing data

Two bioreplicates of rRNA-depleted RIC-seq data (GSM3629915 and GSM3629916) in the HeLa cell line [14] were downloaded from the Gene Expression Omnibus under the accession number GSE127188 in FASTQ format. The matched control set of RNA-seq data in the HeLa cell line was downloaded from the ENCODE consortium under the accession numbers ENCLB555ASI and ENCLB555ASJ. On the first pass, the RNA-seq data were mapped to the human genome using the STAR aligner (version 2.7.3a) in paired-end mode with the following additional settings:

```
--runMode alignReads --outSAMtype BAM
SortedByCoordinate --chimOutType Junctions.
```

On the second pass, the RIC-seq data were mapped to the human genome using the same version of STAR aligner with the following additional settings:

--chimSegmentMin 15 --chimJunctionOverhangMin 15 --chimScoreJunctionNonGTAG -1 --scoreGapNoncan -1 --scoreGapATAC -1 --scoreGapGCAG -1 --chimSegmentReadGapMax 3 --outFilterMatchNminOverLread 0.5 --outFilterScoreMinOverLread 0.5.

The parameter --chimSegmentReadGapMax 3 is introduced to account for the mappability of the additional biotinylated cytosine residue in RIC-seq [14]. The penalty score is reduced to -1 for all non-canonical splice junctions on the second pass.

Pipeline implementation

RIC-contacts is implemented in the popular workflow management system Snakemake [17] and is available through the GitHub repository [18]. The input data files are provided through a configuration file in YAML format, which also contains STAR settings and additional parameters that control the minimum distance between two ligation points in a cluster and the cutoff on the distance between neo-junctions to be visualized through UCSC Genome Browser [19]. Neo-junctions were extracted from BAM files using the custom Perl script (neo.pl in RNAcontacts repository) and samtools package v1.14 [20]. The bedops package v2.4.41 was used to cluster ligation points [21]. The number of supporting reads was computed using bedtools package v2.29.0 [22].

Visualization

To visualize the contact maps, we converted the contact lists to the 'cool' format using the cooler package v0.8.11 with 100-bp resolution and visualized the maps with the pygenometracks package v3.7. Split read visualization was performed with IGV v2.11.2 and the UCSC Genome Browser [19]. By default, only co-linear contacts that span not more than 50,000 nts were visualized through a UCSC Genome Browser track hub (see also the manual [18]).

RESULTS

The RNAcontacts pipeline

We have developed RNAcontacts, a computational pipeline for the analysis of RNA proximity ligation data, which circumvents the problem of multiple split types by aligning short reads in a two-pass mode (*Fig. 1B*). The workflow is based on the STAR aligner [23]. On the first pass, RNAcontacts aligns the sample-matched set of RNA-seq data in the paired-end mode to identify the splice junctions expressed in a given biological sample using a strict penalty for non-GT/AG splits. Here, RNA-seq represents a control experiment that does not contain fragments resulting from proximity ligation. On the second pass, the reads generated in an RNA proximity ligation experiment are aligned using a relaxed penalty for non-GT/AG splits. At the same time, the splice junctions identified on the first pass as *bona fide* introns are provided to the input of the second pass, so that the aligner will preferentially make splits at the coordinates from the provided list. Since RNA proximity ligation data may contain chimeric junctions at arbitrary genomic distances or *in trans*, the alignment on the second pass is performed in the single-end mode. All the split alignments obtained on the second pass are parsed to extract RNA–RNA contacts and exclude the splice junctions obtained on the first pass.

Spliced alignment programs usually generate two separate output files corresponding to co-linear and non-co-linear splits. In particular, the STAR aligner reports co-linear splits (same strand, same chromosome, and forward split orientation) within the standard SAM/BAM output, while non-co-linear splits are placed in the chimeric output file, since the BAM format does not allow their representation with a single CIGAR string [23]. RNAcontacts extracts the coordinates of neo-junctions, i.e., co-linear splits that were found on the second pass from the SAM/BAM output, and combines them with the chimeric splits obtained from the chimeric output. Of note, not only *trans,* but also *cis* contacts may be encoded within both neo-junctions and chimeric splits. The combined output of the second pass comprises neo-junctions and chimeric junctions, which are jointly referred to as ligation junctions, with their constituent split positions referred to as ligation points.

In application to the RIC-seq experiment in the HeLa cell line [14], RNAcontacts mapped 94.3% of the ~224 million short reads from the two bioreplicates, with 72.0% of the mapped reads aligned uniquely (see *Table S1* for the complete mapping statistics). At the same time, 18.5% of the uniquely mapped reads contained at least one ligation junction, as compared to 3.5%, 2%, and 0.5% previously reported for LIGR-seq, PARIS, and SPLASH, respectively [24]. It is worth noting that spliced alignment programs may differ in their base-wise mapping accuracy and decisions on gap placement [25]. For example, when using the RIC-seq protocol, gap variability can arise even when mapping read mates overlapping the same ligation point because reading the same sequence from one or the other strand may produce slightly different split coordinates due to the lack of consensus sequences that characterize the split (*Fig. S1*). Furthermore, different copies of the same RNA are digested and religated stochastically, thus resulting in even more considerable variability. Considering this technical and

Table 1. The characterization of clusters of RNA–RNA contacts

δ	Metric	Intragenic	*in cis*	*in trans*
10	n	1369158	1061470	4881920
	s	10.1±2.2	10.1±2.1	10.2±2.2
	$\log_2$d	10.8±3.3	17.6±4.4	N/A
	$\log_2$r	0.8±0.8	0.5±0.7	0.5±0.7
20	n	1313727	1035656	4851697
	s	20.2±2.4	20.2±2.3	20.3±2.4
	$\log_2$d	11.0±3.3	17.6±4.4	N/A
	$\log_2$r	0.8±0.8	0.5±0.7	0.5±0.7

Note: Clustering distance, δ. The number of contacts, n. Cluster lengths, s. Distance between contacting clusters, d. The number of reads supporting the contact, r. The numbers represent the mean ± standard deviation.

biological variation, we expect to observe clusters of ligation points rather than well-defined junctions, as in GT/AG introns.

Indeed, the distribution of distances between two consecutive ligation points has a rapidly decaying tail, with approximately 50% of distances below 9 nts and 90% of distances below 21 nts (*Fig. S2*). We chose to cluster the ligation points using single linkage clustering with distance cutoffs (δ) of 10 nts and 20 nts (*Fig. S3*). A contact was defined as a pair of clusters, with the number of supporting reads equal to the sum of read counts corresponding to ligation junctions.

For each δ, we subdivided the contacts into three groups: intragenic contacts (both ends of a contact belong to an annotated gene), contacts *in cis* (on the same chromosome, but not in the same gene), and contacts *in trans* (on different chromosomes). The number of contacts (n), the cluster length (s), the distance between contacting clusters (d, which is defined only for intragenic and *cis* contacts), and the number of supporting reads (r) were only marginally different for the two values of δ (*Table 1*). On average, we detected 30% more intragenic contacts than contacts *in cis* and more than twofold enrichment of contacts *in trans* with respect to the other two groups. For δ = 10, most clusters had a length of 10 nts (*Fig. S4*), indicating that they comprise only one individual ligation point surrounded by 5-nt-flanks in both directions.

The distances between contacting clusters were distributed differently for neo-junctions and chimeric splits, both in terms of the number of contacts and when weighted by the number of supporting reads (*Fig. S5*). Remarkably, the distributions have two modes, with the first mode at d≈1000 corresponding to the intragenic contacts encoded by both neo-junctions and chimeric splits. Chimeric reads may encode intragenic contacts if the split is in backward orientation, as in circular RNAs [26]. The second mode for neo-junctions was due to the d ⩽ 250 000 condition imposed by the STAR aligner on co-linear splits. However, longer contacts *in cis* were captured by the second mode of the chimeric distribution. At that, most contacts *in cis* and *in trans* were supported by only one read, while most intragenic contacts were supported by two reads (*Fig. S6*). Therefore, the read support in individual RNA proximity ligation assays is generally quite sparse, even after contacts' merging into clusters.

RNAcontacts has higher sensitivity than RICpipe

To compare the performance of RNAcontacts with that of RICpipe, a pipeline originally designed to analyze RIC-seq data, we first analyzed ligation junctions of 50 nts or longer located on the same chromosome and then matched their exact genomic positions obtained by the two pipelines. We excluded junctions in reads mapped to rRNA from RNAcontacts results for this analysis, because RICpipe removes rRNA reads [14]. Only 40% of ligation junctions identified by RNAcontacts (compared with 45% by RICpipe) had exactly the same coordinates as the ligation junctions identified by the other pipeline, indicating the differences in the spliced alignment programs (*Fig. 2A*). However, in terms of the number of short reads supporting the identified ligation junctions, RNAcontacts aligned more reads than RICpipe, indicating an approximately 40% increase in sensitivity (*Fig. 2B*). When performing the comparison using 100-nts windows, i.e., without exact coordinate matching, we found the results of the two pipelines to be largely concordant. This finding is also evidenced by the similarity of contact maps, with a slightly higher number of contacts for RNAcontacts compared to RIC-pipe (*Fig. 2C*).

Additionally, we checked the performance of RNAcontacts on the RIC-seq data in the HeLa cell line with and without the first mapping pass. For this purpose, we ran the second pass of RNAcontacts by supplying only the splice junctions annotated in

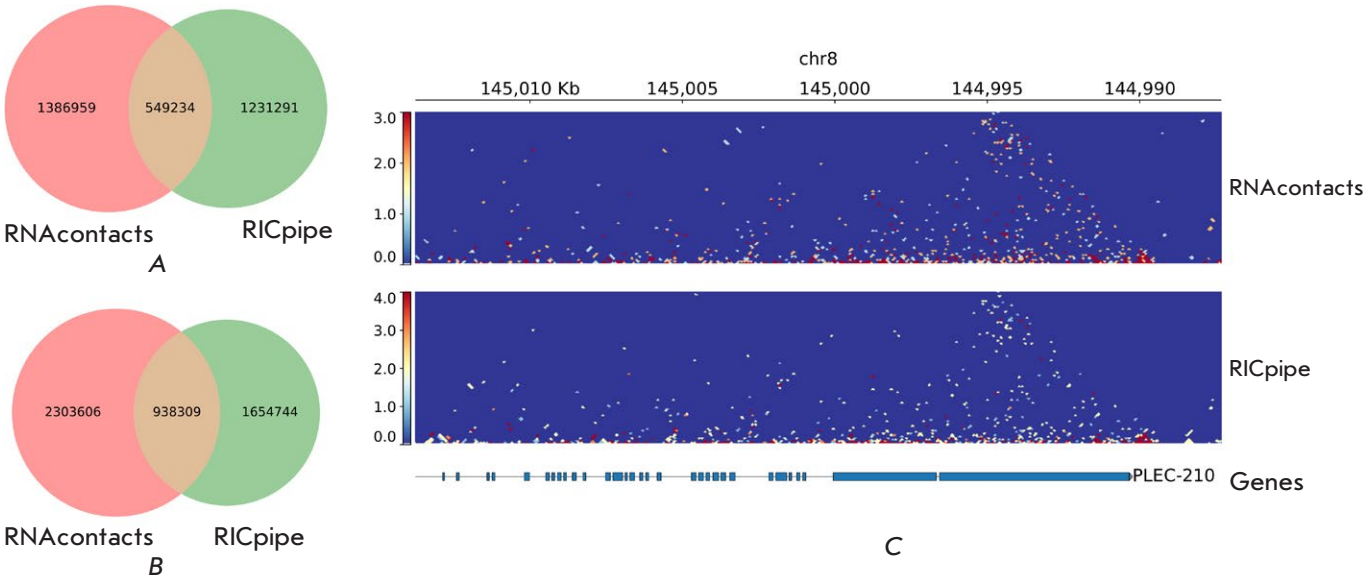

Fig. 2. RNAcontacts vs. RICpipe. (*A*) – Venn diagram of ligation junctions obtained by RNAcontacts and RICpipe. (*B*) – Same as A, but weighted by read support. (*C*) – Contact maps for the PLEC-210 gene obtained by RNAcontacts (top) and RICpipe (bottom)

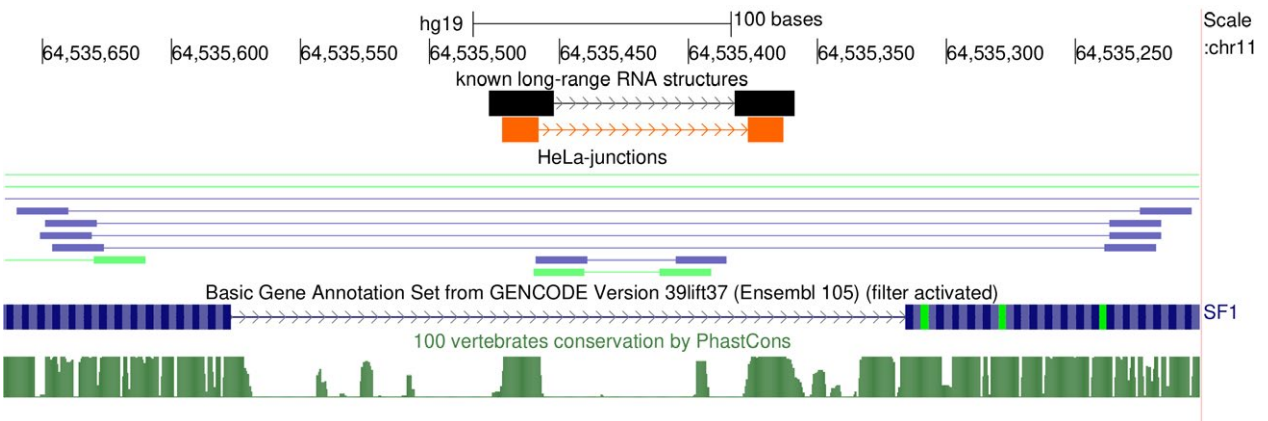

Fig. 3. Ligation junctions supporting the RNA structure in the human SF1 gene [28]. The complementary strands are shown in orange. Ligation junctions in the HeLa cell line are shown under the HeLa junctions track. The reads from the two bioreplicates are shown in blue and green

GENCODE [16], without adding the splice junctions inferred for the HeLa cell line on the first pass. As a result, we obtained approximately 1% of spurious ligation junctions corresponding to the endogenous splice junctions in HeLa. We also found that 16,809 out of ~3.5 million ligation junctions identified by RICpipe could be attributed to exon-exon junctions. While the number of such ligation junctions is not large, they are supported by a considerable fraction (> 30%) of reads. Hence, a conclusion is made that the two-pass method provides higher specificity (lower false positive rate) towards RNA–RNA contacts, especially when the transcriptome expressed differs significantly from the annotated one.

DISCUSSION AND CONCLUSION

In this work, we have presented a conceptual solution to the problem of mapping short reads with two

distinct split types, which are characteristic of RNA proximity ligation assays, using the STAR aligner. However, the approach is not limited to STAR, and any other spliced aligner program can be used instead [25]. We have demonstrated that endogenous splice junctions constitute a large portion of the split read alignments in RIC-seq data, and that RNAcontacts allows one to detect split reads aligning to ligation junctions with greater sensitivity than RIC-pipe. The implementation of RNAcontacts in a reproducible and scalable workflow management system Snakemake allows fast and uniform processing of multiple datasets like RIC-seq.

The nature of RNA proximity ligation data is similar to that of Hi-C. Yet it has important distinctions related to the resolution. While it is a common practice for Hi-C to average chromatin contacts at kilobase or megabase scale, the assessment of RNA–RNA contacts using proximity ligation intrinsically targets single-nucleotide levels. Meanwhile, the read support by RIC-seq in the most naturally occurring contacts, for example, mediated by the RNA structure in the human *SF1* gene [27], is very weak (see example in *Fig. 3*). We observed that most RIC-seq contacts *in cis* and *in trans* were supported by only one read, raising the issue of assessing the statistical significance of the contacting clusters. This issue should be addressed in future studies supported by larger amounts of data. We expect that many more RNA proximity ligation datasets similar to RIC-seq will soon become available to be analyzed using the RNAcontacts pipeline.

To summarize, RNAcontacts implements a generic RNA–RNA contact analysis pipeline that accounts for multiple split types specific to RNA proximity ligation methods. Initially designed for the RIC-seq protocol, the scope of the software can be extended to any method involving proximity ligation in which one of the interacting partners is RNA.

The authors would like to express gratitude to T.M. Ivanov for the additional testing of the software. The study was supported by a research grant from the Russian Ministry of Science and Education (075-10-2021-116) and a research grant from the National Key Research and Development Program of China (2021YFE0114900).

D.P. conceived and supervised the study; G.L. and C.C. provided the data and participated in the analysis; S.M. conducted the data analysis and developed the software. All the authors wrote the manuscript and approved it.

AVAILABILITY OF SUPPORTING DATA AND MATERIALS

The data set supporting the results of this study is available in the Zenodo repository (https://zenodo.org/record/7027475) [27]. ●

REFERENCES

1. Jerkovic I., Cavalli G. // Nat. Rev. Mol. Cell. Biol. 2021. V. 22. № 8. P. 511–528.
2. McCord R.P., Kaplan N., Giorgetti L. // Mol. Cell. 2020. V. 77. № 4. P. 688–708.
3. Han J., Zhang Z., Wang K. // Mol. Cytogenet. 2018. V. 11. P. 21.
4. Lu L., Liu X., Huang W.K., Giusti-Rodríguez P., Cui J., Zhang S., Xu W., Wen Z., Ma S., Rosen J.D., et al. // Mol. Cell. 2020. V. 79. № 3. P. 521–534.
5. Li G., Cai L., Chang H., Hong P., Zhou Q., Kulakova E.V., Kolchanov N.A., Ruan Y. // BMC Genomics. 2014. V. 15 Suppl. 12. P. S11.
6. Bell J.C., Jukam D., Teran N.A., Risca V.I., Smith O.K., Johnson W.L., Skotheim J.M., Greenleaf W.J., Straight A.F. // Elife. 2018. V. 7. P. e27024.
7. Limouse C., Jukam D., Smith O.K., Fryer K.A., Straight A.F. // Meth. Mol. Biol. 2020. V. 2161. P. 115–142.
8. Kudla G., Wan Y., Helwak A. // Annu. Rev. Genomics Hum. Genet. 2020. V. 21. P. 81–100.
9. Xu B., Zhu Y., Cao C., Chen H., Jin Q., Li G., Ma J., Yang S.L., Zhao J., Zhu J., et al. // Sci. China Life Sci. 2022. V. 65. № 7. P. 1285–1324.
10. Lu Z., Zhang Q.C., Lee B., Flynn R.A., Smith M.A., Robinson J.T., Davidovich C., Gooding A.R., Goodrich K.J., Mattick J.S., et al. // Cell. 2016. V. 165. № 5. P. 1267–1279.
11. Sharma E., Sterne-Weiler T., O'Hanlon D., Blencowe B.J. // Mol. Cell. 2016. V. 62. № 4. P. 618–626.
12. Aw J.G., Shen Y., Wilm A., Sun M., Lim X.N., Boon K.L., Tapsin S., Chan Y.S., Tan C.P., Sim A.Y., et al. // Mol. Cell. 2016. V. 62. № 4. P. 603–617.
13. Ziv O., Gabryelska M.M., Lun A.T.L., Gebert L.F.R., Sheu-Gruttadauria J., Meredith L.W., Liu Z.Y., Kwok C.K., Qin C.F., MacRae I.J., et al. // Nat. Methods. 2018. V. 15. № 10. P. 785–788.
14. Cai Z., Cao C., Ji L., Ye R., Wang D., Xia C., Wang S., Du Z., Hu N., Yu X., et al. // Nature. 2020. V. 582. № 7812. P. 432–437.
15. Church D.M., Schneider V.A., Graves T., Auger K., Cunningham F., Bouk N., Chen H.C., Agarwala R., McLaren W.M., Ritchie G.R., et al. // PLoS Biol. 2011. V. 9. № 7. P. e1001091.
16. Harrow J., Frankish A., Gonzalez J.M., Tapanari E., Diekhans M., Kokocinski F., Aken B.L., Barrell D., Zadissa A., Searle S., et al. // Genome Res. 2012. V. 22. № 9. P. 1760–1774.
17. Mölder F., Jablonski K.P., Letcher B., Hall M.B., Tomkins-Tinch C.H., Sochat V., Forster J., Lee S., Twardziok S.O., Kanitz A., et al. // F1000Res. 2021. V. 10. P. 33.
18. Margasyuk S., Pervouchine D. RNAcontacts pipeline. https://doi.org/10.5281/zenodo.6512482. 2022.
19. Raney B.J., Dreszer T.R., Barber G.P., Clawson H.,

Fujita P.A., Wang T., Nguyen N., Paten B., Zweig A.S., Karolchik D., Kent W.J. // Bioinformatics. 2014. V. 30. № 7. P. 1003–1005.
20. Li H., Handsaker B., Wysoker A., Fennell T., Ruan J., Homer N., Marth G., Abecasis G., Durbin R. // Bioinformatics. 2009. V. 25. № 16. P. 2078–2079.
21. Neph S., Kuehn M.S., Reynolds A.P., Haugen E., Thurman R.E., Johnson A.K., Rynes E., Maurano M.T., Vierstra J., Thomas S., et al. // Bioinformatics. 2012. V. 28. № 14. P. 1919–1920.
22. Quinlan A.R., Hall I.M. // Bioinformatics. 2010. V. 26. № 6. P. 841–842.
23. Dobin A., Davis C.A., Schlesinger F., Drenkow J., Zaleski C., Jha S., Batut P., Chaisson M., Gingeras T.R. // Bioinformatics. 2013. V. 29. № 1. P. 15–21.
24. Schönberger B., Schaal C., Schäfer R., Voß B. // F1000Res. 2018. V. 7. P. 1824.
25. Eger N., Schoppe L., Schuster S., Laufs U., Boeckel J.N. // Adv. Exp. Med. Biol. 2018. V. 1087. P. 41–52.
26. Engström P.G., Steijger T., Sipos B., Grant G.R., Kahles A., Rätsch G., Goldman N., Hubbard T.J., Harrow J., Guigó R., et al. // Nat. Methods. 2013. V. 10. № 12. P. 1185–1191.
27. Margasyuk S., Vlasenok M., Li G., Cao C., Pervouchine D. RIC-seq contacts in HeLa. 2022. URL: https://doi.org/10.5281/zenodo.7027475.
28. Pervouchine D.D., Khrameeva E.E., Pichugina M.Y., Nikolaienko O.V., Gelfand M.S., Rubtsov P.M., Mironov A.A. // RNA. 2012. V. 18. № 1. P. 1–15.

The Relationship of Precursor Cluster Concentration in a Saturated Crystallization Solution to Long-Range Order During the Transition to the Solid Phase

M. A. Marchenkova[1*], A. S. Boikova[1], K. B. Ilina[1], P. V. Konarev[1], Yu. V. Pisarevsky[1], Yu. A. Dyakova[2], M. V. Kovalchuk[1,2]

[1]Federal Scientific Research Centre "Crystallography and Photonics", Russian Academy of Sciences, Moscow, 119333 Russian Federation

[2]National Research Centre "Kurchatov Institute", Moscow, 123182 Russian Federation

[*]E-mail: marchenkova@crys.ras.ru

Received October 02, 2022; in final form, January 11, 2023

DOI: 10.32607/actanaturae.11815

ABSTRACT **A model for the transition from disordered liquid state to the solid phase has been proposed based on establishing a correlation between the concentration of precursor clusters in a saturated solution and the features of solid phase formation. The validity of the model has been verified experimentally by simultaneously studying the oligomeric structure of lysozyme protein solutions and the peculiarities of solid phase formation from these solutions. It was shown that no solid phase is formed in the absence of precursor clusters (octamers) in solution; perfect monocrystals are formed at a small concentration of octamers; mass crystallization is observed with an increasing degree of supersaturation (and concentration of octamers); further increase in octamer concentration leads to the formation of an amorphous phase.**

KEYWORDS **oligomers, precursor clusters, crystallization, supersaturation, crystal growth.**

ABBREVIATIONS **SAXS – small-angle X-ray scattering; SANS – small-angle neutron scattering.**

INTRODUCTION

Transition from the liquid disordered state to the solid state is an important area of condensed state physics; it has been researched for many decades [1, 2]. A large number of experimental studies on transition to the solid phase have been conducted for substances such as synthetic, metallic, dielectric, semiconductor, organic, macromolecular (including proteins), etc. Solutions of known compounds morph into a solid phase upon reaching their supersaturated state. It has been established also that the supersaturation degree determines the structure of the resulting solid phase. Monocrystals are formed at low supersaturation degrees. A further increase in the supersaturation degree results in mass crystallization and transition to the amorphous phase. However, there is no generally accepted model for this transition.

The conventional crystallization mechanism, which was once considered valid for all systems, is gradually being replaced by the non-conventional mechanism, which is now believed to be the prevailing mechanism of crystallization from solution and other systems [2–9]. According to the conventional crystal growth theory, any crystal grows through the attachment of new building units (atoms, ions, molecules, and their complexes) to its surface from the environment (solution, melt, vapor, and solid). Non-conventional crystallization models postulate that crystals can grow via the addition of not only single atoms, ions, and molecules to their surface, like in the conventional theory, but also by addition of solid phase blocks. It should be noted that these studies describe the resulting precursors, particles, dense liquid drops with an amorphous structure, as well as the essential features of a series of liquid-to-solid phase transition cases for the processes occurring at the scale of tens of nm and above. These works denote the need to study the processes that take place

in saturated (crystallization) solutions at the nm and tens of nm scale.

For the past decades, crystallization solution structures at a scale of units and tens of nanometers have been studied using the methods of small-angle X-ray scattering (SAXS) and small-angle neutron scattering (SANS), as well as the method of molecular dynamics. Such studies were conducted on the saturated crystallization solutions of a series of proteins [10–15] and potassium dihydrogen phosphate [9]. In these works, three-dimensional (3D) fragments were isolated from the crystallization structure of the compounds under study. The fragments could then be used for monocrystal formation. These ordered formations are found in saturated solutions of lysozyme (octamers [10–15]), thermolysin (hexamers [16]), proteinase (dimers [17]), aminotransferase (dodecamers [18]), and potassium dihydrophosphate (octamers [19]), which was experimental confirmation of the hypothesis on the existence and structure of a precursor cluster in a crystallization solution. The use of molecular dynamics showed that this cluster is stable in a crystallization solution [20]. In particular, it has been shown for lysozyme that only protein dimers and octamers are present in a crystallization solution, while other oligomers (tetra-, hexa-, decamers, etc.) are unstable [21].

The dependence of the concentration of lysozyme dimers and octamers on the temperature and concentration of the solvent and precipitant has been studied in detail by SAXS and SANS. It has been confirmed for a wide range of crystallization solution parameters that a lysozyme solution contains protein monomers, dimers, and octamers, and that their ratio depends on the degree of the solution's saturation [10–15].

The current work represents a study of the relation between the precursor cluster concentration and the features of a solid phase formation exemplified by lysozyme. For this, we performed two series of experiments. We analyzed the lysozyme oligomeric structure (the ratio of monomer, dimer, and octamer concentrations) in ~60 lysozyme solutions with different precipitates by SAXS. The transition of the solutions to the solid phase was also studied (crystals were grown using the method of hanging drop vapor diffusion).

EXPERIMENTAL

Preparation of crystallization solutions of the lysozyme protein

To prepare the solutions, Sigma-Aldrich chicken egg lysozyme was used (CAS# 12650-88-3, USA). Solutions from the crystallization kits *NeXtal-Tubes-Classics-Suite 1* and *NeXtal-Tubes-Classics-Suite 2* (QIAGEN®) and sodium chloride (CAS 7647-14-5, Helicon, Russia) were used as precipitants. Sodium acetate (CAS 6131-90-4, Sigma-Aldrich) and acetic acid (CAS 64-19-7, PanReac AppliChem) were used to prepare sodium acetate buffer. Hereinafter, the precipitant solutions from the crystallization kits will be referred to as CS1 No. and CS2 No., respectively, where No. stands for the solution number in the kit. Lysozyme and NaCl were dissolved in 0.2 M sodium acetate buffer (pH 4.5) prepared using Millipore ultrapure water (water resistance 18 MOhm × cm). Before mixing with the precipitant, the protein solution was centrifuged at 10,000 rpm for 10 min. The initial concentration of the protein stock solution was 80 mg/ml; the solution was then diluted with a buffer to the required concentration.

Prior to SAXS, the lysozyme and stock solutions of the precipitant were mixed in equal volumes.

SAXS measurements

SAXS measurements of lysozyme solutions on a P12 EMBL BioSAXS beamline with a PETRA III synchrotron radiation source (DESY, Hamburg, Germany). Samples with different compositions of precipitants from the CS1 and CS2 kits were measured on a P12 EMBL BioSAXS beamline with a PETRA III synchrotron radiation source (DESY, Hamburg, Germany) [22]. The X-ray energy was 10 keV (λ = 0.124 nm). Data were collected using a PILATUS 6M 2D pixel detector (Dectris, Switzerland) at a sample–detector distance of 3.0 m covering a scattering vector range of $0.02 < s < 7.0$ nm^{-1} ($s = 4\pi\sin\theta/\lambda$, where 2θ is the scattering angle), which corresponds to a resolution of 300–0.9 nm in real space. Measurements were carried out using a special cell for SAXS samples, consisting of a horizontal temperature-controlled (temperature range of 278–323 K) quartz capillary with a wall thickness of 50 μm and a diameter of 1.7 mm, placed in a specialized stainless steel pod for measurements in vacuum. The test solution moved uniformly along the capillary; each time, the beam reached the same site at the capillary but a different part of the sample. A total of 20 measurements were made for each sample. The exposure time was 50 ms. The sample volume for each measurement was 40 μl. All measurements were carried out at a temperature of 20°C and lysozyme concentration of 20 mg/ml.

SAXS measurements of lysozyme solutions on a BM29 BioSAXS beamline with a ESRF synchrotron radiation source (Grenoble, France). Samples with different concentrations of the NaCl precipitant (range, 5–30 mg/ml) were measured on a BM29 BioSAXS beamline with an ESRF synchrotron radiation source

(Grenoble, France). The X-ray energy was 12.4 keV. Data were collected using a Pilatus 1M 2D pixel detector (Dectris). The sample–detector distance was 2.8 m. The studied samples were placed in a special temperature-controlled robotic system [23] in 200-μl polystyrol cells, which were simultaneously heated. The samples were heated to 20°C and then maintained at that temperature. The solution from the cell automatically entered a quartz capillary with a diameter of 1.8 mm, which was used for measurements. The test solution moved uniformly along the capillary; each time, the beam reached the same site at the capillary but a different part of the sample. A total of 10 measurements were made for each sample. The exposure time was 1 s; beam cross-section at the sample was 400 μm^2.

SAXS data processing

The signal from the buffer solution was averaged, subtracted from the data of protein solution scattering, and normalized to the protein concentration using the PRIMUS program of the ATSAS software package [24, 25]. Experimental curves of scattering intensity I(s) were obtained for the protein solutions in different conditions. The addition of precipitants to the lysozyme solution in some specific conditions changes the oligomeric composition of the solution in a way that, in addition to monomeric particles, multimers (oligomers of a higher order: dimers, tetramers, hexamers, and octamers) are formed. For this reason, data were analyzed with account of the presence of several components in the system. After primary data processing, experimental SAXS curves were processed using the OLIGOMER software [25] to determine the volume fractions of monomers and oligomers of various orders. Theoretical curves of oligomeric components were calculated using the CRYSOL software [26]. The crystallographic structure of lysozyme (PDB ID: 4WLD) was used as a monomeric component, while dimer, tetramer, hexamer, and octamer models were obtained using the technique described in [10]. The fit quality χ^2 was evaluated by minimizing the discrepancy between the experimental data and theoretical model approximations using the formula from [14].

Lysozyme crystallization

The stock solutions prepared for measurements by SAXS on a P12 EMBL BioSAXS beamline (DESY, Hamburg, Germany) were also used for lysozyme crystallization. The method of hanging drop vapor diffusion and a Mosquito-LCP crystallization robot (EMBL, Hamburg, Germany) were used for crystallization. The volume of each drop was 200 nl (100 nl of the protein stock solution + 100 nl of the stock precipitant solution). Crystals were grown in the automated imaging system ROCK IMAGER at 19°C. The system makes it possible to observe the growth of protein crystals and take photographs of drops during a long period of time (at day 0 (immediately after loading the crystallization plate) and then on days 1, 3, 7, 14, 28, 54, and 84). The same solutions from the kits *NeXtal-Tubes-Classics-Suite 1* and *NeXtal-Tubes-Classics-Suite 2* were used as precipitants similar to the SAXS analysis of the solutions. Lysozyme was crystallized at two concentrations: 20 and 40 mg/ml. We would like to note that the solutions were analyzed by SAXS at the same concentration (20 mg/ml).

RESULTS AND DISCUSSION

As mentioned in the Introduction, crystallization can be described as a phase process of liquid-to-solid phase transition. Therefore, crystallization is a three-stage process (two-step crystallization): the solution is initially in liquid phase, then the intermediate phase takes shape, followed by the formation of the solid phase at the final stage.

The effect of the precipitant concentration on the supersaturation degree and its dependence on octamer concentration

A number of factors determine the supersaturation degree, which include both physical (e.g. temperature) and chemical parameters (concentrations of the precipitant and protein in the solution, the chemical composition of the solution, and the precipitant type). In this work, we studied the effect of the precipitant type and concentration on the composition of the intermediate phase (the content of monomers, dimers, and octamers in it). The results are presented in *Table 1*.

According to the equation (2) from [27], lysozyme solubility (C_s) and NaCl concentration (C_{NaCl}) in sodium acetate buffer (pH 4.6) at 293 K are related through the following relationship:

$$C_s = -0.0016C_{NaCl}^3 + 0.2146C_{NaCl}^2 - 9.6437C_{NaCl} + 148.06$$

The relation between supersaturation (σ), lysozyme solubility (C_s), and concentration (C) in the solution is described by the following equation: $\sigma = C / C_s$ [24].

The resulting curve of lysozyme solution supersaturation and octamer concentration versus NaCl concentration in the solution is presented in *Fig. 1*.

Both supersaturation and the volume fraction of octamers grow with an increase in the NaCl concentration, with supersaturation increasing not gradually but almost exponentially, starting at a given time

Table 1. Oligomer composition of the lysozyme crystallization solution (volume fractions of monomers, dimers, and octamers) using NaCl as the precipitant, obtained by SAXS

NaCl concentration, mg/ml	R_g, A	Monomer, %	Dimer, %	Octamer, %	χ^2
30	21.0	85.6	10.3	4.1	1.46
25	20.7	87.3	8.9	3.8	1.41
20	20.3	88.8	7.7	3.5	1.30
15	19.5	92.0	5.1	2.9	1.43
5	15.5	95.2	4.5	0.3	1.78

Note. Measurements were carried out at 20°C.
R_g – radius of gyration. χ^2 – fit quality.

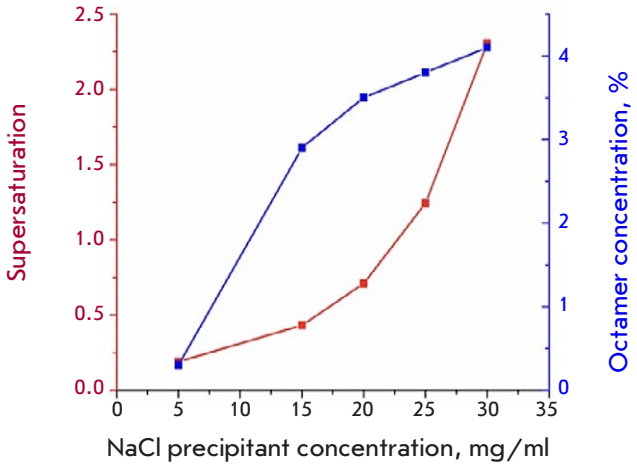

Fig. 1. Lysozyme supersaturation (red curve) and octamer volume fraction (blue curve) in a lysozyme solution at different NaCl concentrations

point. The point of the lowest supersaturation and highest solubility at an NaCl concentration of 5 mg/ml corresponds to the lowest volume fraction of octamers (0.3%), which makes crystallization unlikely.

The volume fraction of octamers in the solution increases from 2.9 to 4.1% with an increase in the NaCl concentration (from 15 to 30 mg/ml). At the same time, an increase in the precipitant concentration leads to a rapid rise in the supersaturation degree, which indicates the instability of this state, when even a slight change in the environment can significantly affect the solution supersaturation degree. In other words, in the region where the volume fraction of octamers exceeds 4%, the probability of aggregation and occurrence of crystals would decrease, while the probability of aggregation and formation of an amorphous precipitate, on the contrary, should increase.

Comparison of results of the transition to a solid phase with octamer concentrations

An analysis of the data obtained by SAXS (oligomeric composition of solutions, radius of gyration (R_g), and fit quality χ^2) of the crystallization solutions with the CS1 and CS2 precipitant kits is presented in *Tables 2–4*. For each case, the *Tables* provide the chemical compositions of the precipitants and crystallization results, which, in our case, could be one of the four variants below:

- clear drops (no crystal, result "–");
- the crystal grew at the study concentration of 20 mg/ml in at least one drop (result "crystal");
- aggregation (mass crystallization, result "aggregation"); and
- denaturation (amorphous precipitant, result "denaturation").

There were 55 such cases out of 67 studied solutions.

In the presence of the remaining 12 precipitants (CS1 13, CS1 55, CS2 16, CS2 14, CS2 15, CS1 36, CS1 26, CS1 54, CS1 38, CS1 40, CS1 12, and CS1 52), no crystal growth was noted in the solution with a protein concentration of 20 mg/ml. However, a crystal was observed at a concentration of 40 mg/ml in the solution with the same precipitant. In the vast majority of cases, a crystal was observed either after a very long period of time (28–56 days) or in one out of three drops.

It is extremely important to note that, in all the cases when no octamers were present in the solution (only monomers and dimers), no crystals were found. In addition, neither aggregation nor denaturation was observed (all three drops remained visually clear during the whole period of exposure). Taking into account the previous studies by SANS [13] and the discovered growth step height (110) for tetragonal crystals (6 nm) [28, 29], we can state that the ***formation of lysozyme octamers is the key stage of lysozyme crystallization*** [10], while dimers cannot be the key element of the protein crystal.

We can distinguish three general cases describing crystallization solutions with different compositions and corresponding to different regions in the phase diagram:

Table 2. Oligomer composition of lysozyme crystallization solutions with precipitators from the CS1 and CS2 crystallization kits by SAXS

№	Precipitant	R_g, Å	Dimer, %	Octamer, %	χ^2	Crystallization result	Precipitant solution composition
1	CS1 1	14.3	0	0	3.26	–	0.01 M cobalt chloride 0.1 M sodium acetate pH 4.6 1.0 M 1,6-hexanediol
2	CS1 10	15.5	9.3	0	1.37	–	0.2 M magnesium chloride 0.1 M HEPES HEPES sodium salt pH 7.5 30% (v/v) isopropanol
3	CS1 11	15.0	5.4	0	1.25	–	0.2 M ammonium acetate 0.1 M Tris-HCl pH 8.5 30% (v/v) isopropanol
4	CS1 14	14.3	0	0	6.97	–	25% (v/v) ethylene glycol
5	CS1 15	14.3	0	0	2.24	–	0.02 M calcium chloride 0.1 M sodium acetate pH 4.6 30% (v/v) MPD (2-methyl-2,4-pentanediol)
6	CS1 16	14.5	1.7	0	1.18	–	0.2 M sodium chloride 0.1 M sodium acetate pH 4.6 30% (v/v) MPD
7	CS1 17	16.3	18.4	0	1.2	–	0.2 M ammonium acetate 0.1 M trisodium citrate pH 5.6 30% (v/v) MPD
8	CS1 2	16.3	18.4	0	1.69	–	0.1 M trisodium citrate pH 5.6 2.5 M 1,6-hexanediol
9	CS1 21	15.6	10.9	0	1.43	–	0.2 M ammonium phosphate 0.1 M Tris pH 8.5 50 %(v/v) MPD
10	CS1 23	14.3	0	0	2.17	–	0.1 M Tris pH 8.5 25% (v/v) tert-butanol
11	CS1 25	16	14.9	0	1.71	–	0.4 M ammonium phosphate
12	CS1 3	14.3	0	0	1.08	–	0.2 M magnesium chloride 0.1 M Tris pH 8.5 3.4 M 1,6-hexanediol
13	CS1 51	14.3	0	0	7.41	–	35% (v/v) dioxane
14	CS1 61	14.5	1.2	0	1.15	–	0.2 M magnesium formate
15	CS1 18	14.3	0	0	1.17	–	0.2 M magnesium acetate 0.1 M sodium cacodylate pH 6.5 30% (v/v) MPD
16	CS1 20	17.1	25.9	0.1	1.73	–	0.5 M ammonium sulfate 0.1 M HEPES pH 7.5 30% (v/v) MPD
17	CS1 24	17.6	33.5	0.1	3.06	–	0.1 M trisodium citrate pH 5.6 35% (v/v) tert-butanol
18	CS1 9	18	39.3	0.1	3.76	–	0.2 M trisodium citrate 0.1 M sodium cacodylate pH 6.5 30% (v/v) isopropanol
19	CS2 13	14.3	0	0.1	1.35	–	0.3 M magnesium formate 0.1 M Bis-Tris pH 5.5
20	CS1 56	17.5	20.8	0.6	1.14	–	0.1 M HEPES pH 7.5 20% (v/v) Jeffamine M-600
21	CS1 35	17.1	14.2	0.6	1.18	–	1.0 M imidazole pH 7
22	CS1 6	16	3.9	0.6	1.08	–	0.2 M calcium chloride 0.1 M sodium acetate pH 4.6 20% (v/v) isopropanol
23	CS1 8	18.1	29.6	0.7	1.76	–	0.2 M trisodium citrate 0.1 M HEPES sodium salt pH 7.5 20% (v/v) isopropanol

Note. Samples are arranged in increasing order of octamer volume fraction (0–0.7%).

Table 3. Oligomer composition of lysozyme crystallization solutions with precipitators from the CS1 and CS2 crystallization kits by SAXS

№	Precipitant	R_g, Å	Dimer, %	Octamer, %	χ^2	Crystallization result	Precipitant solution composition
24	CS1 39	17.4	14.8	0.9	1.32	Crystal	0.05 M cadmium sulfate 0.1 M HEPES pH 7.5 1.0 M sodium acetate
25	CS2 17	18.5	28.9	1	1.08	Aggregation	1.26 M sodium phosphate 0.14 M potassium phosphate
26	CS1 62	18.3	25.1	1	1.25	Crystal	0.1 M MES pH 6.5 1.6 M magnesium sulfate
27	CS1 46	18.3	24.5	1.1	1.17	Crystal	0.1 M HEPES sodium salt pH 7.5 0.8 M sodium phosphate 0.8 M potassium phosphate
28	CS1 50	18.3	20.5	1.2	1.28	Aggregation	1.6 M ammonium sulfate 0.1 M MES pH 6.5 10% (v/v) dioxane
29	CS1 27	19.2	29.1	1.6	1.26	Crystal	0.1 M Tris-HCl pH 8.5 2.0 M ammonium phosphate
30	CS1 37	19.1	24.5	1.7	1.28	Crystal	0.1 M HEPES sodium salt pH 7.5 0.8 M K/Na tartrate
31	CS1 58	19.5	28	1.9	1.28	–	0.01 M nickel chloride 0.1 M Tris pH 8.5 1.0 M lithium sulfate
32	CS1 28	19.2	19.2	2	1.2	Crystal	0.1 M HEPES pH 7.5 2.0 M ammonium formate
33	CS1 59	19.6	27.7	2.1	1.34	Aggregation	0.1 M HEPES sodium salt pH 7.5 1.5 M lithium sulfate
34	CS1 32	19.7	23.6	2.3	1.25	Aggregation	0.1 M sodium chloride 0.1 M HEPES pH 7.5 1.6 M ammonium sulfate
35	CS1 22	21.1	66.8	2.5	12.72	Crystal	0.1 M HEPES pH 7.5 70 % (v/v) MPD
36	CS2 22	19.9	22.8	2.5	1.18	Crystal	0.8 M succinic acid pH 7.0
37	CS1 33	20.1	23.9	2.7	1.26	Aggregation	0.01 M cobalt chloride 0.1 M MES pH 6.5 1.8 M ammonium sulfate
38	CS2 18	20.5	32.6	2.9	1.14	Aggregation	0.49 M sodium phosphate 0.91 M potassium phosphate
39	CS1 4	20.7	25.1	3.3	1.22	Aggregation	2.0 M ammonium sulfate 5% (v/v) isopropanol
40	CS1 57	20.8	27.6	3.4	1.27	Aggregation	0.5 M ammonium sulfate 0.1 M sodium citrate pH 5.6 1.0 M lithium sulfate
41	CS1 30	21.1	24.6	3.8	1.23	Aggregation	0.1 M Tris-HCl pH 8.5 2.0 M ammonium sulfate
42	CS2 19	21.4	29.8	4	1.06	Aggregation	0.056 M sodium phosphate 0.91 M potassium phosphate
43	CS1 29	21.3	23.7	4	1.09	Aggregation	0.1 M ammonium acetate pH 4.6 2.0 M ammonium sulfate
44	CS1 60	21.4	23	4.2	1.18	–	0.1 M BICINE pH 9.0 2.0 M magnesium chloride
45	CS1 31	21.5	24.6	4.3	1.2	Aggregation	2.0 M ammonium sulfate
46	CS1 47	21.6	22.4	4.4	1.13	Crystal	0.1 M sodium acetate pH 4.6 2.0 M sodium formate

Note. Samples are arranged in increasing order of octamer volume fraction (0.9–4.4%).

Table 4. Oligomer composition of lysozyme crystallization solutions with precipitators from the CS1 and CS2 crystallization kits by SAXS

№	Precipitant	R_g, Å	Dimer, %	Octamer, %	χ^2	Crystallization result	Precipitant solution composition
47	CS1 43	18	0	4.9	23.69	Denaturation	0.1 M HEPES pH 7.5 4.3 M sodium chloride
48	CS2 21	22.3	35.9	5.1	1.27	Denaturation	1.8 M ammonium citrate pH 7.0
49	CS1 42	22.2	24.4	5.2	1.15	Aggregation	0.1 M sodium phosphate 0.1 M potassium phosphate 0.1 M MES pH 6.5 2.0 M sodium chloride
50	CS1 41	22.8	21.3	6.2	1.12	Aggregation	0.1 M sodium acetate pH 4.62 M sodium chloride
51	CS2 24	23.4	23.9	7.1	1.13	Denaturation	2.8 M sodium acetate pH 7.0
52	CS1 34	23.5	25.1	7.4	1.17	Denaturation	0.2 M K/Na tartrate 0.1 M trisodium citrate pH 5.6
53	CS1 44	26.2	15.1	13.5	1.17	Denaturation	0.1 M HEPES sodium salt pH 7.5 1.4 M trisodium citrate
54	CS1 45	26.8	20.5	16	1.42	Denaturation	1.6 M trisodium citrate pH 6.5
55	CS1 48	28.2	0	21.1	18.85	Denaturation	4.0 M sodium formate

Note. Samples are arranged in increasing order of octamer volume fraction (4.9–21.1%).

1) only monomers are present in the solution (the lowest point of the unsaturated region);
2) only monomers and dimers are found in the solution (unsaturated region/approaching saturation); and
3) monomers, dimers, and octamers are observed in the solution, with the octamer concentration changing depending on the supersaturation degree as follows (four intervals in total):
   1. 0–1%: crystals or other solid formations are absent in the solution;
   2. 1–5%: monocrystal growth and aggregation are observed;
   3. 5–7%: either aggregation or denaturation occurs (amorphous formation); and
   4. > 7%: only denaturation is noted.

Figure 2 shows five experimental SAXS curves for a lysozyme solution with the precipitants CS1 18 (No. 15 in *Table 2*), CS1 17 (No. 7 in *Table 2*), CS1 28 (No. 32 in *Table 3*), CS1 31 (No. 45 in *Table 3*), and CS1 45 (No. 54 in *Table 4*). These curves present different cases of oligomeric composition of the lysozyme solution and crystallization results. In the case where CS1 18 was used, when only monomers were observed in the solution, clear drops were noted (neither crystals nor other solid phases were formed). For CS1 17 (monomers and dimers were observed, while octamers were not found in the solution), a clear drop was also noted (result "–"). The use of CS1 28 (monomers, dimers, and octamers were observed in the solution) resulted in crystal growth (result "crystal"). The precipitants CS1 31 and CS1 45 led to the formation of monomers, dimers, and octamers in the crystallization solutions, as well as aggregation and denaturation (CS1 31 and CS1 45, respectively).

Dependence of the probability of crystal growth on the precursor cluster concentration in the crystallization solution

Preparation of the crystallization solution of the protein can result in several evolutionary pathways depending on the supersaturation degree:

1) no precursor clusters form in the protein solution after addition of the precipitant: i.e., there is no intermediate and, therefore, solid phase, including monocrystals (in addition to monomers, dimers may be also present in the solution, (unsaturated region, approaching saturation));
2) precursor clusters form in the solution, the intermediate phase forms, with further transition to crystal growth;
3) the degree of solution supersaturation becomes so high that the precursor cluster concentration increases to the point where aggregation takes place

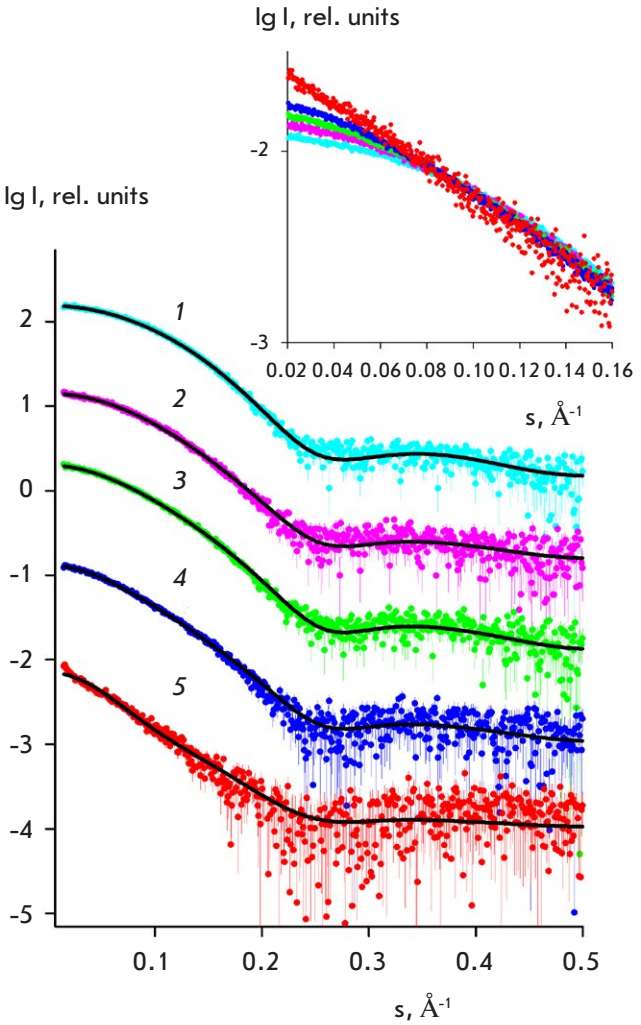

Fig. 2. Experimental SAXS curves (colored lines) for lysozyme crystallization solutions (black lines) and theoretical approximations using a mixture of oligomers calculated using the OLIGOMER program for the following solutions: *1* – lysozyme with CS1 18 precipitant (monomers only, no crystal), *2* – lysozyme with CS1 17 precipitant (dimers and monomers, no crystal), *3* – lysozyme with CS1 31 precipitant (monomers, dimers, octamers, and crystal), *4* – lysozyme with CS1 31 precipitant (monomers, dimers, octamers, and aggregation), *5* – lysozyme with CS1 45 precipitant (monomers, dimers octamers, and denaturation). The curves are shifted along the vertical axis for better visualization

(the state that can further evolve into a crystal); and

4) the supersaturation degree exceeds its limit, and the protein in the solution transforms into an amorphous state, when partial denaturation can occur.

Comparison of the results of a measuring of octamer concentrations and the peculiarities of lysozyme transition from solution to the solid phase denotes a relationship between them. In the absence of octamers in the solution (only monomers and dimers) at an octamer concentration < 1%, neither lysozyme monocrystals nor any other solid and amorphous forms were observed. Crystallization and aggregation are noted in a octamer concentration interval of 1–5%, with monocrystals forming mainly in the range of an octamer concentration of 2–3%. An increase in the octamer concentration to 5–7% leads to aggregation and denaturation (amorphous formation), while a further increase above 7% results in protein denaturation only (formation of amorphous precipitates).

In this regard, the data were converted into a different format. We considered the probability of successful crystal growth at different octamer fractions in the solution and rounded the octamer fractions to the nearest whole number (using the standard built-in Excel function). We considered the following cases and calculated their probability: 1 – crystal growth at 20 mg/ml; 2 – occurrence of visible aggregation (mass crystallization); and 3 – formation of an amorphous precipitate (denaturation). Therefore, the probability was calculated as the ratio of successful cases (when one of the abovementioned variants is observed in the drop) to the number of cases with the same octamer fraction (*Table 5*).

The highest probability of lysozyme crystal formation coincides with an octamer concentration range of 2–3% (*Fig. 3*). Neither crystal growth nor aggregation is observed for an octamer concentration of > 7%; the probability of denaturation in this case is 1. The general correlation between the formation of a given condensed phase as a result of crystallization and octamer concentration in the solution is as follows. The probability of any solid phase formation is zero (0) for a volume fraction of octamers of 0–1%. A higher octamer volume fraction corresponds to a higher probability of crystal formation and aggregation. Furthermore, the highest probability of crystal formation falls on an octamer concentration of 2%, while the maximum probability of aggregation shifts to a higher octamer concentration and stands at 4%. The probability of amorphous phase formation reaches its maximum at an octamer concentration of > 7%.

We would like to note that two points corresponding to an octamer fraction rounded to 6% were excluded from the general probability curves for aggregation and denaturation in *Fig. 3*. The reason why these points did not fit into the curves may have to do with the small statistical sample (only two cases).

In the section "The effect of the precipitant concentration on the supersaturation degree and its dependence on the octamer concentration", where we

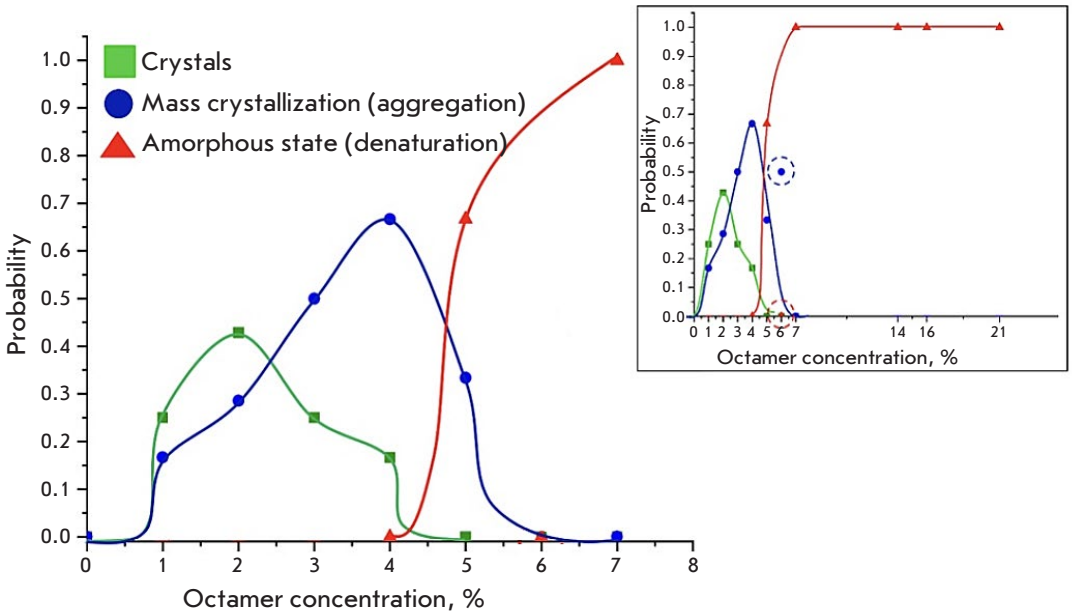

Fig. 3. General patterns of the changes in the probability of lysozyme crystal growth, aggregation, and denaturation as a function of the integer fraction of octamers (21% magnification of the interval of the volume fraction of octamers in the inset), for different cases of condensed phase formation: crystals (green line), mass crystallization (blue line), and amorphous precipitate/denaturation (red line)

Table 5. Probabilities calculated for the three cases: crystal growth at 20 mg/ml, occurrence of visible aggregation (mass crystallization), and occurrence of amorphous precipitation/denaturation

Octamer fraction (rounded to the nearest whole number), %	Total No. of cases	Crystal		Aggregation		Denaturation	
		Success	Probability	Success	Probability	Success	Probability
0	24	0	0	0	0	0	0
1	12	3	0.25	2	0.16667	0	0
2	7	3	0.42857	2	0.28571	0	0
3	8	2	0.25	4	0.5	0	0
4	6	1	0.16667	4	0.66667	0	0
5	3	0	0	1	0.33333	2	0.66667
6	2	0	0	1	0.5	0	0
7	2	0	0	0	0	2	1
14	1	0	0	0	0	1	1
16	1	0	0	0	0	1	1
21	1	0	0	0	0	1	1

compared octamer concentrations at different NaCl concentrations, the supersaturation degree, and solubility, we stated that an increase in the NaCl concentration (from 15 to 30 mg/ml) results in an increase in the proportion of octamer fractions in the solution ranging from 2.9 to 4.1%. Measurements of supersaturation at different NaCl concentrations demonstrated that, in the region of octamer concentration of > 4%, the probability of monocrystal formation should decrease, while the probability of aggregation and amorphous state formation should increase. This pattern is observed in *Fig. 3*: the probability of crystal growth decreased to 0, while the probability of aggregation and denaturation began to increase at an octamer concentration of > 4%.

Based on a comparison of the obtained graphs with regions in the phase diagram, we can state that an octamer concentration of 0% (either monomers only or both dimers and monomers are present in the solution) corresponds to the unsaturated region in the phase diagram. An increase in the octamer volume fraction results in an increase in the supersaturation

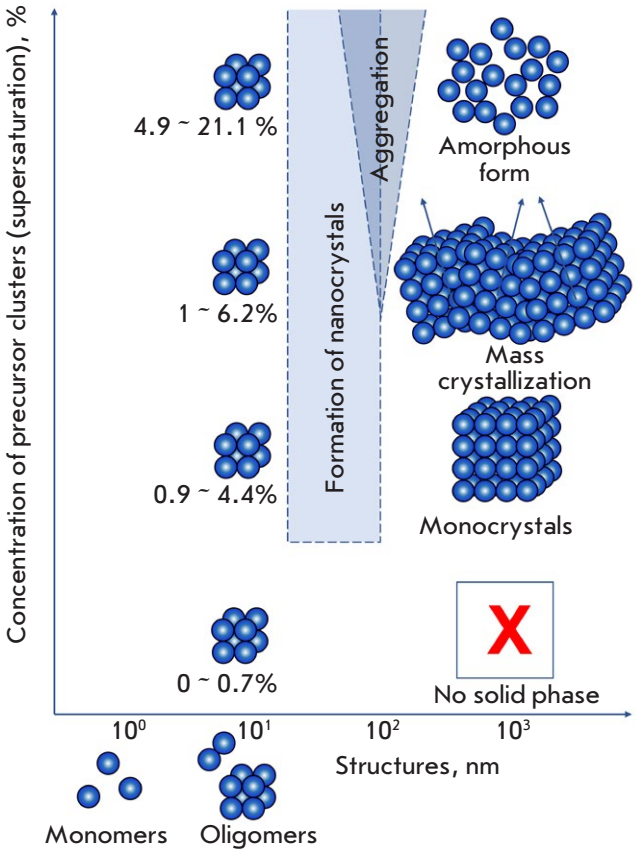

Fig. 4. Polymorphism of the structures formed during crystallization depending on the concentration of precursor clusters as exemplified by the lysozyme protein under tetragonal syngony crystallization conditions

degree, and an octamer concentration range of 1–5% corresponds to the region of nucleation. An octamer concentration of >5% corresponds to the region of precipitation.

CONCLUSIONS

Simultaneous measurement of oligomer concentrations and solid phase formation in 67 lysozyme solutions led us to the following conclusions:

- no crystals form at low octamer concentrations (< 0.8%);
- at an octamer concentration in the range of 0.7–4%, either individual crystals form or mass crystallization (aggregation) takes place, with the aggregation probability increasing with increasing precursor cluster concentration (solution supersaturation degree); and
- the probability of amorphous (denatured) phase formation shoots up, starting from an octamer concentration of 6%.

Based on our previous results on the link between the octamer concentration in a lysozyme solution at the initial crystallization stage and the crystallization results (formation of either monocrystals, aggregates, or an amorphous state), we can state that crystallization at the initial stage depends on the type of final solid phase the protein transforms into (*Fig. 4*). The obtained results make it possible to compare the processes under way in the region of 3–20 nm, which is the intermediate phase when precursor clusters form from 3D clusters, with the results of the transition to the solid phase (for sizes of 1–10 μm).

As noted above, the concentration of precursor clusters determines the solid phase type. Transition from clusters to crystals and an amorphous state was not studied in this work. This issue remains the least studied to date. It has been known since Faraday's times that a supercooled liquid can exist for an indefinite period of time without transitioning to a solid state. This process is usually initiated by the temperature and concentration gradients, the addition of foreign objects that can act as seeding agents, etc. In this work, we performed crystallization at the concentration gradient, while the solid phase formed almost three months after the preparation of the solution.

Nevertheless, the result of this study makes it possible to predict the solid phase type at an early stage of solution (melt) preparation by measuring (or calculating) the concentration of the precursor clusters.

In addition, the nucleation process [30] remains unstudied. However, the obtained results can be useful in furthering our understanding of this process. ●

This work was supported by the Ministry of Science and Higher Education within the State assignment of the Federal Research Center "Crystallography and Photonics" of the Russian Academy of Sciences as part of the study of the initial stage of lysozyme crystallization under external conditions (precipitant solutions and precipitant concentrations) on a BM29 beamline at the European Synchrotron Radiation Facility and Facility of SAXS Data Analysis (grant No. 075-15-2021-1362) as part of analysis of experimental SAXS data and results of crystallization and the iNEXT Consortium [6938] as part of providing financial support for SAXS data collection on a P12 beamline operated by EMBL Hamburg at the PETRA III storage ring.

REFERENCES

1. Gebauer D., Kellermeier M., Gale J.D., Bergström L., Cölfen H. // Chem. Soc. Rev. 2014. V. 43. P. 2348–2371.
2. Askhabov A.M. // Proceedings of the Russian Mineralogical Society. 2019. V. 148. № 6. P. 1–13.
3. Karthika S., Redhakrishnan T.K., Kalaichelvi P. // Cryst. Growth Des. 2016. V. 16. № 11. P. 6663–6681.
4. Ivanov V.K., Fedorov P.P., Baranchikov A.Ye., Osiko V.V. // Rus. Chem. Rev. 2014. V. 83. № 12. P. 1204–1222.
5. De Yoreo J.J., Gilbert P.U.P.A., Sommerdijk N.A.J.M., Penn R.L., Whitelam S., Joester D., Zhang H., Rimer J.D., Navrotsky A., Banfield J.F., et al. // Science. 2015. V. 349. № 6247. P. aaa6760-1-aaa6760-9.
6. Berman H.M., Westbrook J., Feng Z., Gilliland G., Bhat T.N., Weissig H., Shindyalov I.N., Bourne P.E. // Nucl. Acids Res. 2000. V. 28. № 1. P. 235–242.
7. Krauss I.R., Merlino A., Vergara A., Sica F. // Int. J. Mol. Sci. 2013. V. 14. № 6. P. 11643–11691.
8. McPherson A. // Methods. 2004. V. 34. № 3. P. 254–265.
9. Vekilov P.G., Vorontsova M.A. // Acta Cryst. F. 2014. V. F270. P. 271–282.
10. Kovalchuk M.V., Blagov A.E., Dyakova Yu.A., Gruzinov A.Yu., Marchenkova, M.A., Peters G.S., Pisarevsky Yu.V., Timofeev V.I., Volkov V.V. // Cryst. Growth Des. 2016. V. 16. № 4. P. 1792–1797.
11. Marchenkova M.A., Volkov V.V., Blagov A.E., Dyakova Yu.A., Ilina K.B., Tereschenko E.Yu., Timofeev V.I., Pisarevsky Yu.V., Kovalchuk M.V. // Cryst. Rep. 2016. V. 61. № 1. P. 5–10.
12. Boikova A.S., D'yakova Yu.A., Il'ina K.B., Konarev P.V., Kryukova A.E., Marchenkova M.A., Blagov A.E., Pisarevskii Yu.V., Koval'chuk M.V. // Cryst. Rep. 2017. V. 62. № 6. P. 837–842.
13. Boikova A.S., Dyakova Yu.A., Ilina K.B., Konarev P.V., Kryukova A.E., Kuklin A.I., Marchenkova M.A., Nabatov B.V., Blagov A.E., Pisarevsky Yu.V., et al. // Acta Cryst. D. 2017. V. 73. № 7. P. 591–599.
14. Dyakova Yu.A., Boikova A.S., Ilina K.B., Konarev P.V., Marchenkova M.A., Pisarevsky Yu.V., Timofeev V.I., Kovalchuk M.V. // Cryst. Rep. 2019. V. 64. № 1. P. 11–15.
15. Marchenkova M.A., Konarev P.V., Boikova A.S., Ilina K.B., Pisarevsky Yu.V., Kovalchuk M.V. // Cryst. Rep. 2021. V. 66. № 5. P. 751–757.
16. Kovalchuk M.V., Boikova A.S., Dyakova Y.A., Ilina K.B., Konarev P.V., Kryukova A.E., Marchenkova M.A., Pisarevsky, Yu.V., Timofeev V.I. // J. Biomol. Struct. Dyn. 2019. V. 37. № 12. P. 3058–3064.
17. Boikova A.S., D'yakova Yu.A., Il'ina K.B., Konarev P.V., Kryukova A.E., Marchenkova M.A., Pisarevskii Yu.V., Koval'chuk M.V. // Cryst. Rep. 2018. V. 63. № 6. P. 865–870.
18. Marchenkova M.A., Konarev P.V., Rakitina T.V., Timofeev V.I., Boikova A.S., Dyakova Yu.A., Ilina K.B., Korzhenevskiy D.A., Nikolaeva A.Yu., Pisarevsky Yu.V., et al. // J. Biomol. Struct. Dyn. 2020. V. 38. № 10. P. 2939–2944.
19. Kovalchuk M.V., Alekseeva O.A., Blagov A.E., Ilyushin G.D., Il'ina K.B., Konarev P.V., Lomonov V.A., Pisarevsky Y.V., Peters G.S. // Cryst. Rep. 2019. V. 64. № 1. P. 6–10.
20. Kordonskaya Yu.V., Timofeev V.I., Dyakova Yu.A., Marchenkova M.A., Pisarevsky Yu.V., Podshivalov D.D., Kovalchuk M.V. // Cryst. Rep. 2018. V. 63. № 6. P. 947–950.
21. Kordonskaya Yu.V., Marchenkova M.A., Timofeev V.I., Dyakova Yu.A., Pisarevsky Y.V., Kovalchuk M.V. // J. Biomol. Struct. Dyn. 2021. V. 39. № 18. P. 7223–7230.
22. Blanchet C.E., Spilotros A., Schwemmer F., Graewert M.A., Kikhney A., Jeffries C.M., Franke D., Mark D., Zengerle R., Cipriani F. // J. Appl. Crystallogr. 2015. V. 48. P. 431–443.
23. Round A., Felisaz F., Fodinger L., Gobbo A., Huet J., Villard C., Blanchet C.E., Pernot P., McSweeney S., Roessle M., et al. // Acta Cryst. D. 2015. V. D71. P. 67–75.
24. Franke D., Petoukhov M.V., Konarev P.V., Panjkovich A., Tuukkanen A., Mertens H.D.T., Kikhney A.G., Hajizadeh N.R., Franklin J.M., Jeffries C.M. // J. Appl. Crystallogr. 2017. V. 50. P. 1212–1225.
25. Konarev P.V., Volkov V.V., Sokolova A.V., Koch M.H.J., Svergun D.I. // J. Appl. Crystallogr. 2003. V. 36. P. 1277–1282.
26. Svergun D., Barberato C., Koch M.H.J. // J. Appl. Crystallogr. 1995. V. 28. P. 768–773.
27. Chen R.-Q., Lu Q.-Q., Cheng Q.-D., Ao L.-B., Zhang C.-Y., Hou H., Liu Y.-M., Li D.-W., Yin D.-C. // Sci. Rep. 2015. V. 5. № 1. P. 1–6.
28. Wiechmann M., Enders O., Zeilinger C., Kolb H.-A. // Ultramicroscopy. 2001. V. 86. № 1–2. P. 159–166.
29. Yaminsky I.V., Gvozdev N.V., Sil'nikova M.I., Rashkovich L.N. // Cryst. Rep. 2002. V. 47. № S1. P. S149–158.
30. Zhou R., Cao H., Zhang C., Yin D. // CrystEngComm. 2017. V. 19. P. 1143–1155.

Specificity of Penicillin Acylases in Deprotection of N-Benzyloxycarbonyl Derivatives of Amino Acids

I. A. Morozova[1], D. T. Guranda[1], N. V. Panin[1,2], V. K. Švedas[1,2,3*]
[1]Lomonosov Moscow State University, Belozersky Institute of Physicochemical Biology, Moscow, 119234 Russian Federation
[2]Lomonosov Moscow State University, Research Computing Center, Moscow, 119234 Russian Federation
[3]Lomonosov Moscow State University, Faculty of Bioengineering and Bioinformatics, Moscow, 119234 Russian Federation
*E-mail: vytas@belozersky.msu.ru
Received February 02, 2023; in final form, February 20, 2023
DOI: 10.32607/actanaturae.13703

ABSTRACT **Changes in the structure of the N-acyl group in N-acylated amino acid derivatives significantly affect both the recognition and activity of penicillin acylases on this series of substrates. However, penicillin acylases from both *Alcaligenes faecalis* and *Escherichia coli* are capable of removing the N-benzyloxycarbonyl protecting group in amino acid derivatives under mild conditions without the use of toxic reagents. Efficiency in using penicillin acylases in preparative organic synthesis can be improved by utilizing modern rational enzyme design methods.**

KEYWORDS **penicillin acylases, substrate specificity, enzymatic deprotection of functional groups, N-benzyloxycarbonyl derivatives of amino acids.**

ABBREVIATIONS **PA – penicillin acylase; HPLC – high-performance liquid chromatography; PMSF – phenylmethylsulfonyl fluoride; NIPAB – 2-nitro-5-[(phenylacetyl)amino]benzoic acid; o-FA – o-phtalaldehyde; NAC – N-acetyl-L-cysteine; Z – benzyloxycarbonyl protective group.**

INTRODUCTION

Masking functional groups is an important aspect of organic synthesis [1, 2]. The use of enzymes for introducing and removing protective groups significantly expands the possibilities in this area, up to the application of new reagents and changing the conditions for these stages. Thus, one set of reagents is used in the chemical synthesis of peptides, which is mainly carried out in organic solvents, while, when applying enzymes (e.g., to mask amino groups), one can introduce the phenylacetyl [3], phthalyl [4], and acetyl [5] protective groups. Biocatalysis in organic synthesis, and especially in drug preparation, also aims to search for enzymes that can catalyze traditional chemical reactions and make them more environmentally and economically attractive. One such example is the removal of the benzyloxycarbonyl protecting group in amino compounds, which is conventionally carried out by catalytic hydrogenation, sodium reduction in liquid ammonia, and acidolysis using hydrogen bromide in acetic acid [1, 2]. The following limitations and disadvantages of these methods can be distinguished as follows: the widely used hydrogenation on a palladium catalyst cannot be applied when the structure contains organic sulfides, including cysteine or methionine residues [6]. Deblocking can be carried out in the presence of cyclohexylamine or boron trifluoride etherate [7]. However, the method is not selective in the presence of reducible functional groups such as C=C, C=O, CN, NO_2, formyl, carbamoyl, etc. [8]. One should also take into account such factors as the toxicity of palladium and the lack of reliable methods for removing its traces from the final product, which is extremely important in drug synthesis [9]. During reductive cleavage with sodium in liquid ammonia [10], other protective groups are simultaneously cleaved off with the benzyloxycarbonyl residue. Ester groups are, at least partially, converted to amides, threonine residues are destroyed, methionine residues are partially demethylated, and some peptide bonds are cleaved. Side reactions of interesterification and acetylation of threonine and serine residues oc-

cur during acidolytic cleavage; tryptophan, nitroarginine residues, benzyl esters, and amide groups are destroyed [11]. Along with optimizing the conditions for these reactions in order to reduce the contribution of side processes, employing biocatalytic methods to remove the N-benzyloxycarbonyl protection of amino groups is of interest. New enzymes such as urethane hydrolases were discovered as progress was made in this direction [12, 13]. Enzymes capable of removing benzyloxycarbonyl protection were found in *Sphingomonas paucimobilis*, *Burkholderia phenazinium*, and *Arthrobacter sp.* [14–16]. The ability of *Escherichia coli* penicillin acylase to cleave the N-benzyloxycarbonyl derivatives of amino acids was also shown [17]. The aim of this work is to study how changes in the structure of the N-acyl group (replacement of the phenylacetyl residue with benzyloxycarbonyl) alter the specificity of penicillin acylases from *Alcaligenes faecalis* and *Escherichia coli*. Furthermore, this study aims to compare the ability of the two enzymes to remove the protective group.

EXPERIMENTAL

Reagents

We used phenylacetyl chloride (Sigma, USA), phenylmethylsulfonyl fluoride (Merck, Germany), and acetonitrile (Cryochrome, Russia) as reagents. The N-phenylacetyl derivatives of α-amino acids were synthesized according to the method described previously [18].

Penicillin acylase from *Escherichia coli* was prepared using the procedure described earlier [19], while penicillin acylase from *Alcaligenes faecalis* was procured from LLC Innovations and High Technologies of Moscow State University. The concentration of active sites of penicillin acylases was determined by titration with phenylmethylsulfonyl fluoride (PMSF) as described previously [20, 21].

Determining the k_{cat} and K_M values for penicillin acylase-catalyzed hydrolysis of N-acyl derivatives of amino acids

Kinetic experiments were carried out in a thermostated cell of a Shimadzu UV-1601 spectrophotometer at 400 nm and 25°C in 0.01 M phosphate buffer pH 7.5 in the presence of 0.1 M KCl. The values of the Michaelis constant K_M for the hydrolysis of the N-phenylacetyl and N-benzyloxycarbonyl derivatives of the amino acids were determined as the constants of competitive inhibition of the hydrolysis of the NIPAB chromogenic substrate by these compounds by analyzing the dependence between the observed Michaelis constants of NIPAB hydrolysis on the concentration of the N-phenylacetyl or N-benzyloxycarbonyl derivative of the amino acid. The catalytic constants of enzymatic hydrolysis of the N-phenylacetyl and N-benzyloxycarbonyl amino acid derivatives were determined at saturation with the substrate (concentration numerically equals to 10 K_M and 20 K_M) to determine the maximum rate of the enzymatic reaction.

The progress of the reaction was followed by sampling and spectrophotometric registration of the resulting amino groups after modification with o-phthalaldehyde. In a typical experiment, a solution of the N-acyl amino acid derivative in 0.01 M phosphate buffer (pH 7.5) containing 0.1 M KCl was placed in a thermostated cell at 25°C and the required amount of the enzyme was added under stirring. After some time, samples (15–30 μL) of the reaction mixture were taken, mixed with 50 μL of a 10 mM PMSF solution in isopropanol to stop the reaction, diluted to the desired concentration, and analyzed by HPLC. In order to determine the initial rates of enzymatic hydrolysis, 8–10 samples were typically taken; the substrate conversion did not exceed 10%.

HPLC analysis with pre-column modification of amino groups with o-phthalaldehyde

Primary amino groups were modified as follows: 50 μL of a methanol solution containing NAC (40 mM) and o-FA (20 mM) was added to 900 μL of a 0.5 mM solution of an amino compound in 0.4 M borate buffer (pH 9.6) at 25°C. The mixture was stirred, diluted with a chromatography eluent after 15 min, centrifuged for 3 min at 12,000 rpm, and analyzed. The chromatographic system consisted of a Waters M6000 eluent supply module, a Reodyne 7 125 type injector with a 50 μL loop, a Nucleosil C1-8 Chrompack Varian reverse phase chromatography column (250×4 mm, 5 μm), and a Waters M481 LC detector. Chromatograms were recorded using the Multichrome hardware-software system for collecting and processing chromatographic data (Ampersend, Russia). The flow rate was 1 mL/min. The resulting isoindoles were analyzed at 340 nm using 6 mM phosphate buffer (pH 6.8) containing acetonitrile (10–40 vol.%) as the mobile phase.

Direct HPLC analysis of the reaction mixture components

HPLC analysis of the reaction mixture components without pre-column modification of the formed amino groups was carried out using a Waters chromatographic system, a Kromasil Eternity-5-C18 column (Eka Chemicals, Sweden), 6 mM phosphate buffer pH 3.0 containing acetonitrile (30 vol.%) and 0.1 g/L so-

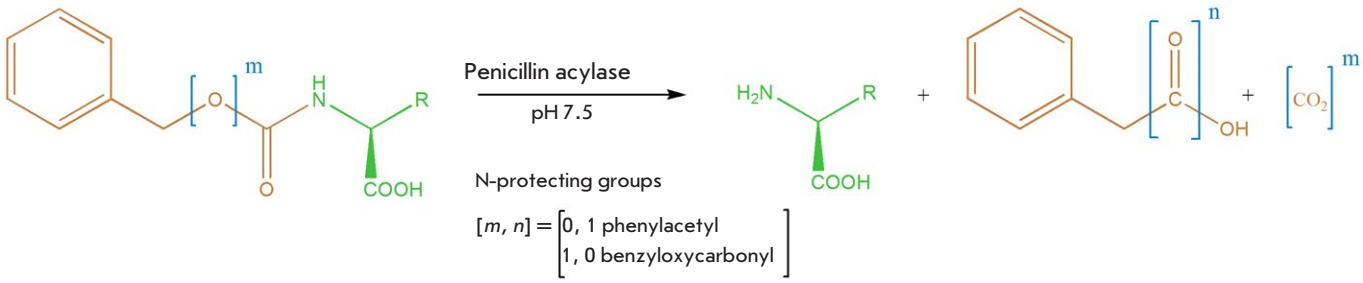

Fig. 1. Removal of phenylacetyl and benzyloxycarbonyl protecting groups catalyzed by penicillin acylases

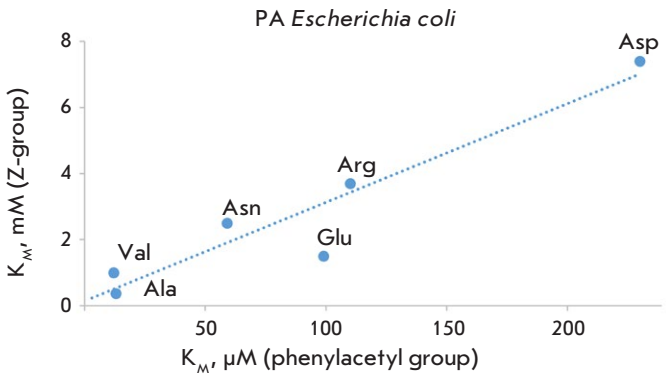

Fig. 2. The correlation between the Michaelis constant (K_M) values for the hydrolysis of the N-phenylacetyl (X axis) and N-benzyloxycarbonyl (Y axis) derivatives of amino acids catalyzed by penicillin acylase from *Eschericha coli*

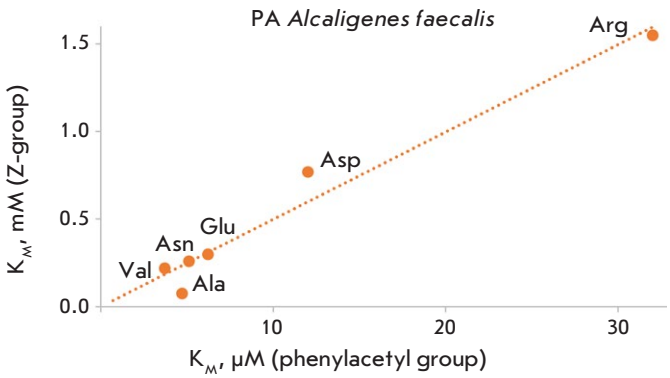

Fig. 3. The correlation between the Michaelis constant (K_M) values for the hydrolysis of the N-phenylacetyl (X axis) and N-benzyloxycarbonyl (Y axis) derivatives of amino acids catalyzed by penicillin acylase from *Alcaligenes faecalis*

dium dodecyl sulfate at 210 nm, and a flow rate of 1 mL/min.

RESULTS AND DISCUSSION

The scheme of enzymatic hydrolysis of the N-phenylacetyl and N-benzyloxycarbonyl derivatives of amino acids is presented in *Fig. 1*. It is noteworthy that the products of these two reactions differ: when the N-phenylacetyl protection is removed, an amino acid with a free amino group and phenylacetic acid are formed while removal of the N-benzyloxycarbonyl protection leads to the accumulation of benzyl alcohol, along with the amino acid and the release of CO_2.

The difference in acyl groups per oxygen atom significantly alters the efficiency of substrate binding in the active center of penicillin acylases, which is characteristic of both *Alcaligenes faecalis* penicillin acylase and *Escherichia coli* penicillin acylase. However, the change in the structure of the N-acyl group does not affect the enzymes' specificity toward the amino acid side chain radical as evidenced by the correlations between the Michaelis constants for the reactions of removal of the N-phenylacetyl and N-benzyloxycarbonyl protecting groups catalyzed by both penicillin acylases. Meanwhile, both enzymes differ in their specificities towards this structural fragment, as shown in *Figs. 2* and *3*, where the least effective binding substrates for penicillin acylase from *Escherichia coli* are derivatives of aspartic acid, while for penicillin acylase from *Alcaligenes faecalis* they are arginine derivatives.

When the phenylacetyl residue is replaced with benzyloxycarbonyl, the affinity of both enzymes for the substrate decreases by more than an order of magnitude, while penicillin acylase from *Alcaligenes faecalis* exhibits a higher affinity for new substrates (the K_M values lie in the range of 0.08–1.6 mM).

Whereas the affinity of both enzymes for substrates depends on the nature of the amino acid side chain, this structural fragment affects the reactivity of penicillin acylases in different ways (*Fig. 4*). The nature of the amino acid side chain in the series of N-phenylacetyl derivatives of amino acids has little effect on the catalytic activity of penicillin acylase

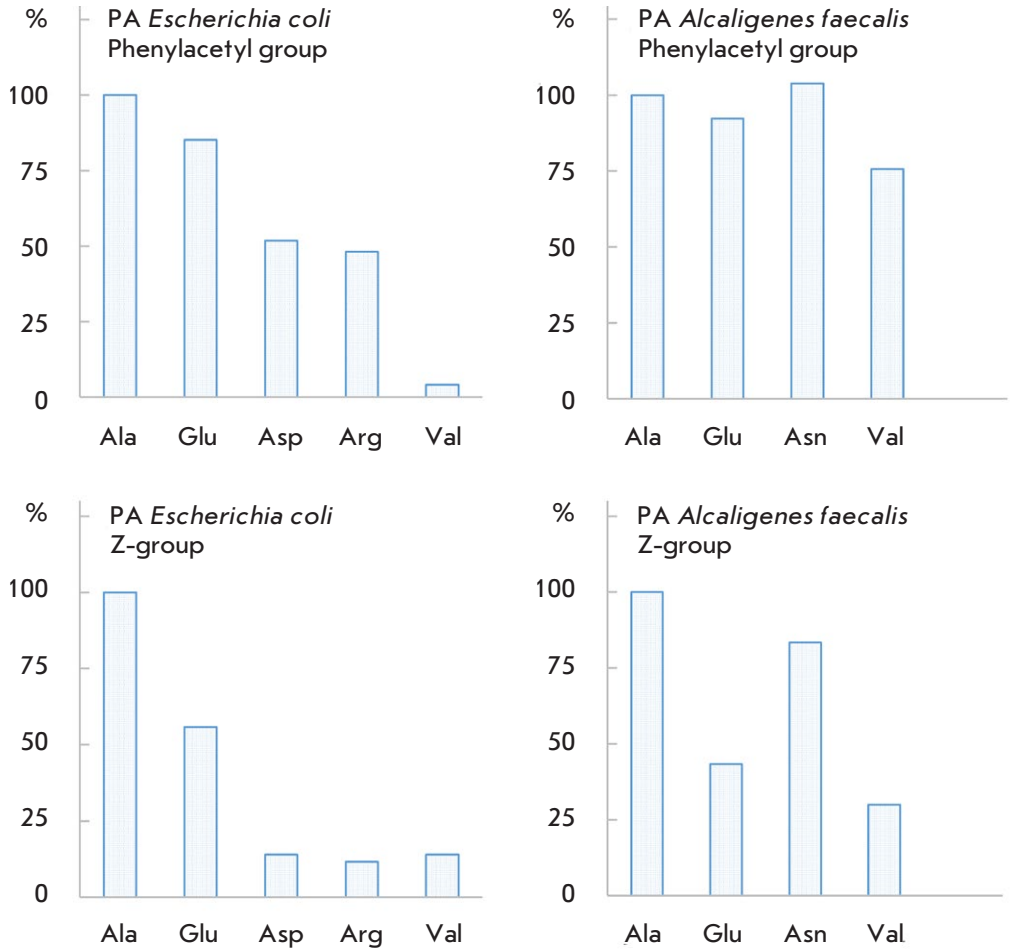

Fig. 4. The catalytic activity of penicillin acylases from *Eschericha coli* (left-hand side figures) and *Alcaligenes faecalis* (right-hand side figures) in the hydrolysis of the N-phenylacetyl and N-benzyloxycarbonyl (Z) amino acid derivatives expressed as the catalytic constant value (%) with respect to the corresponding alanine derivatives: the upper and lower graphs demonstrate the activity of the penicillin acylases with respect to the N-phenylacetyl and N-benzyloxycarbonyl derivatives of amino acids, respectively

from *Alcaligenes faecalis* (the upper right-hand side of the figure), while the reactivity of penicillin acylase from *Escherichia coli* strongly depends on this structural fragment and drops more than 20-fold in the series N-Phac-Ala, Glu, Asp, Arg, and Val (the upper left-hand side of the figure). When the phenylacetyl residue is replaced with benzyloxycarbonyl, the reactivity of the enzymes decreases. Thus, the activity of penicillin acylase from *Escherichia coli* decreases 10- to 49-fold depending on the structure of the side chain radical of the amino acid residue while penicillin acylase from *Alcaligenes faecalis* is even more sensitive to this structural change: the enzyme activity decreases by two orders of magnitude. Nevertheless, both penicillin acylases are able to remove the N-benzyloxycarbonyl protecting groups in the amino acid derivatives (*Fig. 5*); by introducing mutations in the enzyme structure, one can enhance the catalytic activity to these nonspecific substrates. The experience in studying penicillin acylase from *Escherichia coli* shows that both the catalytic activity

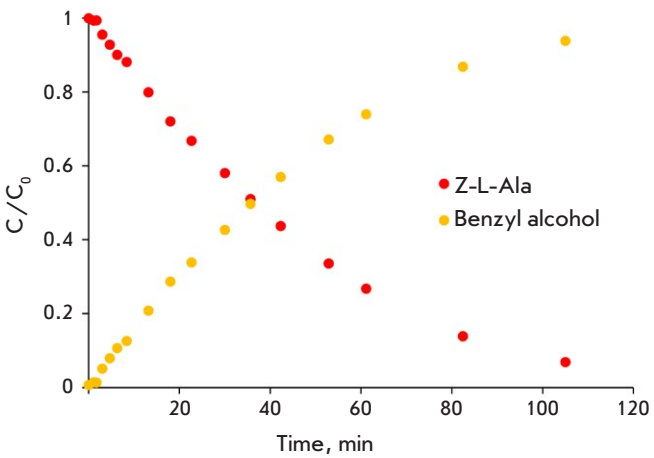

Fig. 5. Removal of the N-benzyloxycarbonyl protecting group catalyzed by penicillin acylase from *Alcaligenes faecalis*. The red dots show the changes in the concentration of the substrate (N-benzyloxycarbonyl-L-Ala); the yellow ones indicate the accumulation of the reaction product (benzyl alcohol). Reaction conditions: pH 7.5; 25°C; substrate concentration, 1 mM; enzyme concentration, 6 μM

and the affinity for the substrates can be improved by protein engineering [22].

CONCLUSIONS

This study demonstrated that changes in the structure of the N-acyl group in N-acylated amino acid derivatives have a significant impact on both the recognition and activity of penicillin acylases with respect to this series of substrates. Nevertheless, both enzymes (namely, penicillin acylase from *Alcaligenes faecalis* and penicillin acylase from *Escherichia coli*) can efficiently remove the N-benzyloxycarbonyl protecting group in amino acid derivatives under mild conditions without the use of toxic reagents, which makes them useful in organic synthesis. The efficiency of such biocatalytic deprotection can be further enhanced using modern methods of rational enzyme design. ●

This work was supported by the Russian Science Foundation (grant No. 21-71-30003).

REFERENCES

1. Kadereit D., Waldmann H. // Chem. Rev. 2001. V. 101. № 11. P. 3367–3396.
2. Sartori G., Maggi R. // Chem. Rev. 2010. V. 113. P. 1–54.
3. Didziapetris R.J., Drabnig B., Schellenberger V., Jakubke H.-D., Švedas V.K. // FEBS Lett. 1991. V. 287. P. 31–33.
4. Costello C.A., Kreuzman A.J., Zmijewski M.J. // Tetrahedron Lett. 1996. V. 37. № 42. P. 7469–7472.
5. Simons C., van Leeuwen J.G.E., Stemmer R., Arends I.W.C.E., Maschmeyer T., Sheldon R.A., Hanefeld U. // J. Mol. Catal. B Enzym. 2008. V. 54. № 3–4. P. 67–71.
6. Sewald N., Jakubke H.-D. // Peptides: Chemistry and Biology, 2nd ed. Weinheim: Wiley. 2009. 594 p.
7. Yajima H. // Chem. Pharm. Bull. Japan. 1968. V. 16. P. 1342
8. Medzihradszky K., Medzihradszky-Schweiger H. // Acta Chem. Acad. Sci. Hung. 1965. V. 44. P. 15–18.
9. Ojha N.K., Zyryanov G.V., Majee A., Charushin V.N., Chupakhin O.N., Santra S. // Coordination Chem. Rev. 2017. V. 353. P. 1–57.
10. Sifferd R.H., Vigneaud V. // J. Biol. Chem. 1935. V. 108. P. 753.
11. Wunsch E., Drees F. // Chem. Ber. 1966. V. 99. P. 110.
12. Matsumura E., Shin T., Murao S., Sakaguchi M., Kawano T. // Agric. Biol. Chem. 1985. V. 49. № 12. P. 3643–3645.
13. Matsumura E., Yamamoto E., Kawano T., Shin T.H., Murao S. // Agric. Biol. Chem. 1986. V. 50. № 6. P. 1563–1571.
14. Patel R.N., Nanduri V., Brzozowski D., McNamee C., Banerjee A. // Adv. Synth. Catal. 2003. V. 345 P. 830–834.
15. Chu L.N., Nanduri V.B., Patel R.N., Goswami A. // J. Mol. Catal. B Enzym. 2013. V.85–86. P.56–60.
16. Maurs M., Acher F., Azerad R. // J. Mol. Catal. B Enzym. 2012. V. 84. P. 22–26.
17. Alvaro G., Feliu J.A., Caminal G., Lopez-Santin J., Clapes P. // Biocatal. Biotransformation. 2000. V. 18. № 3. P. 253–258.
18. Guranda D.T., van Langen L.M., van Rantwijk F., Sheldon R.A., Švedas V.K. // Tetrahedron: Asymmetry. 2001. V. 12. P. 1645–1650.
19. Yasnaya A.S., Yamskova O.V., Guranda D.T., Shcherbakova T.A., Tishkov V.I., Švedas V.K. // Mosc. Univ. Chem. Bull. 2008. V. 49. № 2. P. 103–107.
20. Shvyadas V.K., Margolin A.L., Sherstyuk S.F., Klyosov A.A., Berezin I.V. // Bioorgan. Khimiya. 1977. V. 3. № 4. P. 546–554.
21. Švedas V., Guranda D., van Langen L., van Rantwijk F., Sheldon R. // FEBS Letters. 1997. V. 417. P. 414–418.
22. Shapovalova I.V., Alkema W.B.L., Jamskova O.V., de Vries E., Guranda D.T., Janssen D.B., Švedas V.K. // Acta Naturae. 2009. V. 1. № 3. P. 94–98.

Creation of Recombinant Biocontrol Agents by Genetic Programming of Yeast

S. O. Pipiya[1*], N. Z. Mirzoeva[1], M. N. Baranova[1], I. E. Eliseev[1], Yu. A. Mokrushina[1,2], O. V. Shamova[3], A. G. Gabibov[1,2], I. V. Smirnov[1,4], S. S. Terekhov[1,2]

[1]Institute of Bioorganic Chemistry, Russian Academy of Sciences, academicians M.M. Shemyakin and Yu.A. Ovchinnikov, Russian Academy of Sciences, Moscow, 117997 Russian Federation
[2]Lomonosov Moscow State University M.V. Lomonosov, Moscow, 119234 Russian Federation
[3]Institute of Experimental Medicine, St. Petersburg, 197022 Russian Federation
[4]Federal State Budgetary Institution "National Medical Research Center of Endocrinology" of the Ministry of Health of the Russian Federation, Moscow, 115478 Russian Federation
*E-mail: pipiyasofiya@ibch.ru

Received December 14, 2022; in final form, February 21, 2023
DOI: 10.32607/actanaturae.11878

ABSTRACT **Bacterial infections caused by antibiotic-resistant pathogens pose an extremely serious and elusive problem in healthcare. The discovery and targeted creation of new antibiotics are today among the most important public health issues. Antibiotics based on antimicrobial peptides (AMPs) are of particular interest due to their genetically encoded nature. A distinct advantage of most AMPs is their direct mechanism of action that is mediated by their membranolytic properties. The low rate of emergence of antibiotic resistance associated with the killing mechanism of action of AMPs attracts heightened attention to this field. Recombinant technologies enable the creation of genetically programmable AMP producers for large-scale generation of recombinant AMPs (rAMPs) or the creation of rAMP-producing biocontrol agents. The methylotrophic yeast *Pichia pastoris* was genetically modified for the secreted production of rAMP. Constitutive expression of the sequence encoding the mature AMP protegrin-1 provided the yeast strain that effectively inhibits the growth of target gram-positive and gram-negative bacteria. An antimicrobial effect was also observed in the microculture when a yeast rAMP producer and a reporter bacterium were co-encapsulated in droplets of microfluidic double emulsion. The heterologous production of rAMPs opens up new avenues for creating effective biocontrol agents and screening antimicrobial activity using ultrahigh-throughput technologies.**

KEYWORDS **Antimicrobial peptides (AMPs), yeast *Pichia pastoris*, heterologous expression, protegrin-1 (PG-1), microfluidic compartmentalization, emulsion microcultivation.**

ABBREVIATIONS **AMP – antimicrobial peptide; rAMP – recombinant antimicrobial peptide; AR – antibiotic resistance; ESKAPE – a group of pathogens including *Enterococcus faecium, Staphylococcus aureus, Klebsiella pneumoniae, Acinetobacter baumannii, Pseudomonas aeruginosa* and species of the genus *Enterobacter*; MIC – minimum inhibitory concentration; PG-1 – protegrin-1; rPG-1 – recombinant protegrin-1; GAP – glyceraldehyde-3-phosphate dehydrogenase; sfGFP – superfolder green fluorescent protein; MDR – multidrug resistance; AOX1 – alcohol oxidase-1.**

INTRODUCTION

Antibiotic resistance (AR) poses a major challenge to the global healthcare system. According to some estimates, infections caused by antimicrobial-resistant bacterial strains were responsible for the death of 4.95 million people in 2019 [1]. The number of strains acquiring resistance to antibiotics, including last-resort ones, is also increasing. Yet, the number of novel antibacterial agents approved for clinical use continues to decrease with every year, in opposition to the AR spread rate [2], which makes it necessary to search for alternative approaches to infectious disease control.

The global community has identified the top-priority pathogens that necessitate prompt action to develop novel approaches aimed at combating them [3]. These pathogens are known under the acronym "ESKAPE" and include such bacteria as *Enterococcus faeci-*

um, Staphylococcus aureus, Klebsiella pneumoniae, Acinetobacter baumannii, Pseudomonas aeruginosa, and species that belong to the genus *Enterobacter*. Antimicrobial peptides (AMPs) are particularly effective against bacterial infections caused by antibiotic-resistant members of this group of bacteria [4]. AMPs are produced by a broad range of organisms and exhibit antibacterial, antifungal, and immunomodulatory activities [5]. The mechanisms of action and the molecular targets of AMPs differ from the targets of low-molecular-weight antibiotics. AMPs are often membrane-targeting; they form pores in the lipid bilayer or affect cell wall biosynthesis, thus disrupting the integrity of bacterial cells and causing pathogen death [6]. Due to this mechanism of action, bacteria develop lower resistance to AMPs [7, 8].

A limited number of AMPs is currently available for therapeutic use; however, the number of AMPs undergoing preclinical and clinical trials is increasing, thus proving that this field of research is very promising [9, 10]. The cost of AMP production by solid-phase synthesis can be as high as US$ 50–400 per gram of the product, which is economically feasible mainly for short peptides [11]. Furthermore, chemical synthesis technologies do not allow one to perform large-scale screening of antimicrobial activity employing the principles of combinatorial chemistry and biology [12]. An alternative approach is to use heterologous systems for recombinant production of AMPs. The heterologous production systems based on the methylotrophic yeast *Pichia pastoris* allow one to easily scale up manufacturing of recombinant biologics, thus minimizing their production costs [13, 14].

Biocontrol agents are living organisms, either natural or modified, that can inhibit the spread of pathogens and harmful organisms [15]. This term is most often used in the context of biopesticide design. Since yeast cells are not the targets of most AMPs, they can be used to create biocontrol agents that secrete active AMPs into the extracellular environment in order to inhibit the growth of pathogenic bacteria (*Fig. 1*) [16] or phytopathogenic fungi [17]. The application of this approach for controlling pathogens, including those from the ESKAPE group, can be promising in limiting the spread of antibiotic resistance.

This study focuses on the genetic programming of the methylotrophic yeast *P. pastoris* in order to generate recombinant biocontrol agents, with antimicrobial peptide acting as the active component. A genetic construct ensuring constitutive production of mature AMP secreted into the culture medium was generated. The yeast *P. pastoris* transfected with this construct exhibited antimicrobial activity against both gram-negative and gram-positive target bacteria. A significant antimicrobial effect was also observed in the emulsion microculture mimicking natural bacterial microcompartments. Co-encapsulation of target bacteria and AMP-secreting yeast cells in droplets of microfluidic double emulsion effectively inhibited bacterial growth through the heterologous production of rAMP, protegrin-1 (rPG-1). The elaborated approach to designing recombinant biocontrol agents is rather promising for further development of alternative strategies to combat antibiotic resistance.

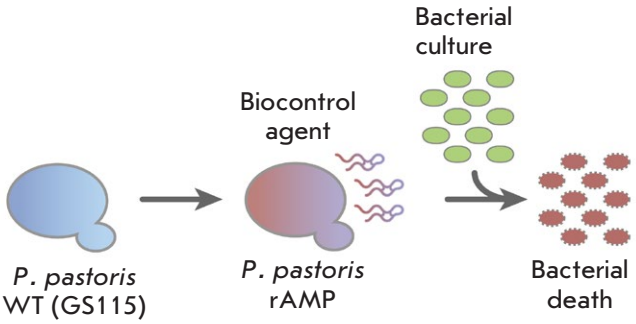

Fig. 1. Schematic representation of the genetic programming of *P. pastoris* yeast strains and the creation of a recombinant biocontrol agent: wild-type yeast (*P. pastoris* WT GS115) is transfected with a genetic construct for the secretory production of AMP, and cocultivation of the resulting biocontrol agent (*P. pastoris* rAMP) with a target bacterium leads to bacterial elimination

EXPERIMENTAL

Bacterial and yeast strains

The *P. pastoris* GS115 strain (Invitrogen, U.S.) was used as a heterologous producer of AMP. Antimicrobial activity was checked for the bacterial strains *Escherichia coli* Δ*lptD* (kindly provided by I.A. Osterman) and *Bacillus megaterium* B-512 (kindly provided by S.A. Dubiley). For generating the *E. coli* Δ*lptD* sfGFP reporter strain, *E. coli* Δ*lptD* cells were transfected with a plasmid that constitutively expressed the green fluorescent protein sfGFP [18].

Plasmid construction and transfection into yeast cells

The codons of the sequence coding for recombinant protegrin-1 (rPG-1) were optimized using the GeneArt GeneOptimizer software (Thermo Fisher Scientific Inc., U.S.). The optimized *rPG-1* gene sequence was cloned into the pGAPZalpha A expression vector (Thermo Fisher Scientific Inc.) by homologous recombination. The resulting pGAP-PG-1 plasmid was linearized at the AvrII restriction site

and transfected into yeast cells by electroporation [19]. The transfected clones were chosen on selective YPDS agar medium (2% peptone, 1% yeast extract, 2% glucose, 1 M sorbitol, 2% agar) supplemented with the zeocin antibiotic until the final concentration of 100 μg/mL was attained.

Analysis of the growth inhibition zones of target bacteria

In order to measure the diameter of the growth inhibition zones, *P. pastoris* clones were cultured in plates containing YPD agar (1% yeast extract, 2% peptone, 2% glucose, 100 mM potassium phosphate pH 6.0, and 1.8% agar) during 2 days at 30°C. Soft agar (8 g/L tryptone, 2.5 g/L NaCl, 5 g/L yeast extract, and 0.5% agar) was melted, cooled down to 42°C, and *E. coli* Δ*lptD* or *B. megaterium* B-512 was inoculated until a final concentration of ~10^6 CFU/mL. The *P. pastoris* colonies were then covered with inoculated soft agar and incubated at 37°C overnight. The presence of antimicrobial activity was analyzed based on the diameter of the growth inhibition zones of the reporter bacterium.

Estimation of the concentration of recombinant protegrin-1 in the culture medium

The rPG-1 producer yeast strain was cultured in the YPD medium (1% yeast extract, 2% peptone, 2% glucose, and 100 mM potassium phosphate pH 6.0) in shake flasks at 37°C and 250 rpm during 3 days. The culture medium was used to analyze the antimicrobial activity against the target bacterium *E. coli* Δ*lptD* using the two-fold serial dilution method. A synthetic analog of protegrin-1 produced by solid-phase synthesis was used as a reference standard for determining the peptide concentration.

Encapsulation of yeast strains and the target bacterium into droplets of microfluidic double emulsion and flow cytometry

The reporter strain *E. coli* Δ*lptD* sfGFP producing sfGFP under control of the pJ23119 promoter was cultured in the YPD medium (1% yeast extract, 2% peptone, 2% glucose, and 100 mM potassium phosphate pH 6.0) in shake flasks at 37°C and 250 rpm until they reached the logarithmic growth phase. *P. pastoris* GS115 and rPG-1 were cultured in the YPD medium in shake flasks at 30°C and 180 rpm during 16 h. Next, the cell cultures were filtered using 40 μm cell strainers (Greiner Bio-One, Germany) and diluted to the optical densities of OD_{600} = 0.45 (occupancy (λ) ~ 5 cells per droplet) for *E. coli* Δ*lptD* and OD_{600} = 1.5 (occupancy (λ) ~ 1 cell per droplet) for the yeast strains. The cells were then encapsulated into droplets of microfluidic double emulsion (MDE) using 20 μm microfluidic chips produced by soft lithography according to the procedure described previously [20]. The filled MDE droplets were cultured at 30°C in an incubator saturated with water vapor. After incubation for 24 h, the fluorescence signal from the MDE droplets was analyzed using a Novocyte Flow Cytometer system (ACEA Biosciences Inc., USA). The droplets were visualized using an Eclipse Ti inverted fluorescent microscope (Nikon, Japan) with the standard FITC filter. The experiment involving cocultivation of yeasts and bacteria in a 96-well plate was conducted in the YPD medium with the initial optical densities OD_{600} = 0.25 for yeasts and OD_{600} = 0.005 for *E. coli* Δ*lptD* sfGFP. The plate was incubated at 30°C under constant stirring. The growth of the target bacterium was assessed by counting colonies after inoculation of serial ten-fold dilutions of the coculture onto an agar medium. The measurements were performed in three replicates.

RESULTS

Antimicrobial peptides as effective antibacterial agents

Antimicrobial peptides can be simultaneously characterized by a high antimicrobial efficacy and a broad spectrum of antimicrobial activity. *Table 1* summarizes the results of our analysis of the published data on the antimicrobial activity of a number of highly active AMPs.

Highly effective AMPs can belong to different structural classes. Protegrin-1 and arenicin-1 are β-hairpin AMPs, while temporin L, pleurocidin, and melittin have an α-helical structure. Despite the differences in their secondary structures, they exhibit a broad spectrum of antimicrobial activity and are also efficient against ESKAPE pathogens and opportunistic pathogenic fungi such as *Candida albicans*.

Among the peptides under study, protegrin-1 (PG-1) has a low minimum inhibitory concentration (MIC) and exhibits a broad spectrum of activity against various pathogens, including the ESKAPE ones. Therefore, taking into account the high antimicrobial activity of PG-1, we decided to use its amino-acid sequence in the design of a biocontrol agent that is based on methylotrophic yeast *P. pastoris*.

Genetic programming of the yeast

Protegrin-1 consists of 18 amino acid residues and contains two intramolecular disulfide bonds maintaining the β-hairpin structure (*Fig. 2A*). Unlike recombinant protegrin, the natural peptide carries an amidated C-terminal arginine residue. The absence of a

Table 1. Antibiotic activity of a panel of representative highly effective AMPs

Susceptible bacteria	MIC, μg/mL				
	protegrin-1	arenicin-1	temporin L	pleurocidin	melittin
Klebsiella pneumoniae	0.5–4	ND	16	4–8	4–64
Acinetobacter baumanii	0.25	4	4	1–2	0.25–0.5
Pseudomonas aeruginosa	4	2–4	16	16–32	2–8
Staphylococcus aureus	4	2–4	2–4	4–16	1–4
Candida albicans	2	24	8	ND	25

*ND – no data; the MIC data were adapted from [21] for protegrin-1; from [22, 23] for arenicin-1; from [24] for temporin L; from [25] for pleurocidin; and from [26–29] for melittin.

modification of the C-terminus may affect the stability and activity of AMP; however, efficient *in situ* production of recombinant protegrin-1 (rPG-1) in a heterologous system can minimize these effects.

The nucleotide sequence of the *P. pastoris* GS115 protegrin-1 gene was optimized in accordance with the codon frequency and cloned into the shuttle expression vector pGAPZalpha A. The resulting pGAP-PG-1 genetic construct ensured constitutive production of protegrin-1 due to the strong constitutive promoter of the glyceraldehyde-3-phosphate dehydrogenase (GAP) gene, while secretion into the extracellular environment was ensured by the yeast's alpha factor signal sequence (*Fig. 2B*). The generated rPG-1 yeast strain, transfected with plasmid pGAP-PG-1, secreted the mature peptide into the extracellular environment, forming distinct zones of growth inhibition of the reporter strains of gram-positive (*B. megaterium*) and gram-negative (*E. coli* Δ*lptD*) bacteria (*Fig. 2C*).

The level of rPG-1 production by the yeast cells was assessed according to the antimicrobial activity of the culture medium against the reporter bacterium *E. coli* Δ*lptD*. A chemical analog of rPG-1 was used as a reference standard. The rPG-1 concentration in the culture medium was 540 ng/mL.

Therefore, we have demonstrated that artificial antimicrobial activity can be reconstructed in rPG-1-producing *P. pastoris* cells.

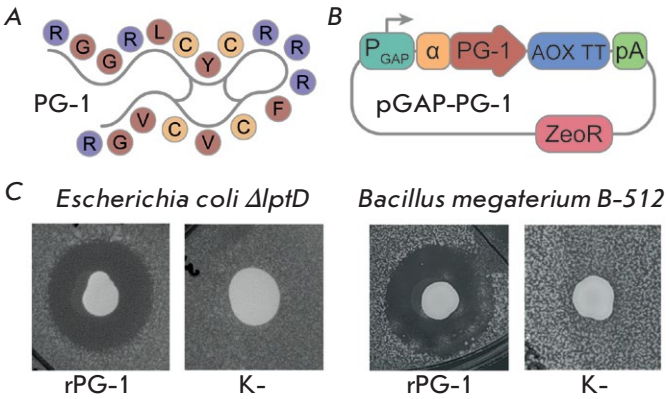

Fig. 2. Genetic programming of the *P. pastoris* yeast: (*A*) a structural scheme of protegrin-1, where purple denotes the positively charged amino acid residues, red represents uncharged amino acid residues, yellow represents cysteine residues; (*B*) diagram of the genetic construct for protegrin-1 production in yeast: P_{GAP} – glyceraldehyde-3-phosphate dehydrogenase (GAP) promoter; α – alpha factor signal sequence; PG-1 – codon-optimized protegrin-1 sequence; AOX TT – AOX1 transcription terminator; pA – polyadenylation signal; ZeoR – zeocin resistance; (*C*) test of the antimicrobial activity of the protegrin-producing strain (rPG-1) and control yeast producing the mCherry fluorescent protein (K-). The diameter of the growth inhibition zones was 12 and 14 mm for reporter bacteria *E. coli ΔlptD* and *B. megaterium*, respectively

Cocultivation in droplets of microfluidic double emulsion

Effective biocontrol agents can limit the spread of pathogens they are targeted to. Microbial competition often occurs within certain microcompartments of their habitat, both in soil communities and in the gut microbiome [30]. Hence, when designing biocontrol agents and probiotic organisms, one needs to assess their ability to inhibit the growth of the target bacteria in microcompartments, as well as when bacteria are numerically superior. Droplets of microfluid-

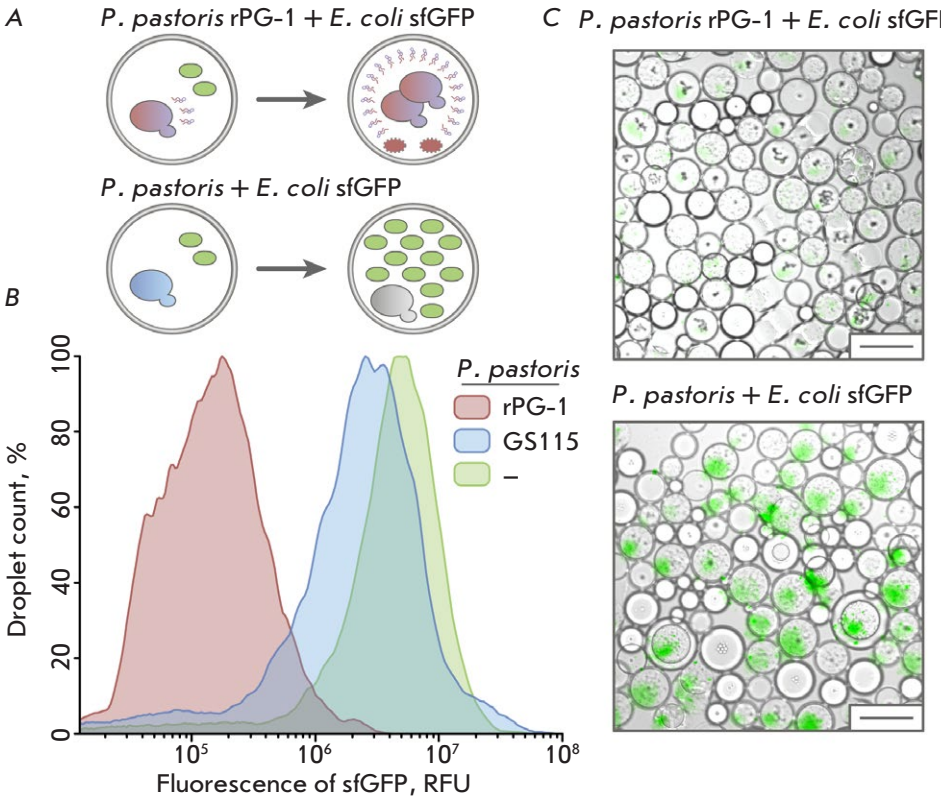

Fig. 3. An analysis of the antimicrobial properties of a recombinant biocontrol agent: (*A*) the scheme of cocultivation of effector yeast with a target bacterium in double emulsion drops; (*B*) the results of flow cytometry of droplets after cocultivation: the fluorescence signal distribution is marked with color: for *E. coli* Δ*lptD* sfGFP encapsulated with strain rPG-1, red; with control yeast *P. pastoris* GS115, blue; without yeast, green; (*C*) microfluidic double emulsion droplet microscopy of the target bacterium *E. coli* Δ*lptD* sfGFP encapsulated with effector yeast *P. pastoris* rPG-1c and the control *P. pastoris* GS115. Scale bar: 50 μm

ic double emulsion make it possible to co-encapsulate effector yeast cells and the reporter bacterial strain in order to evaluate their antimicrobial properties. This model can be further modified to perform large-scale screening of antimicrobial activity.

In this study, the recombinant yeast strain producing protegrin (rPG-1) was co-encapsulated with *E. coli* Δ*lptD* sfGFP reporter cells constitutively producing the green fluorescent protein sfGFP in microfluidic double emulsion droplets (*Fig. 3A*). Co-encapsulation of *E. coli* Δ*lptD* sfGFP and wild-type yeast (GS115), as well as encapsulation of *E. coli* Δ*lptD* sfGFP without yeast, was used as the control. The antimicrobial activity of the recombinant *P. pastoris* yeast strains was detected according to death or proliferation of the reporter bacterial target and the accompanying sfGFP fluorescence in the microfluidic double emulsion droplets.

After incubation for 24 h, the droplets were analyzed by flow cytometry. Co-encapsulation of the target bacterium and yeast strain rPG-1 reduced the intensity of the fluorescence signal of the reporter compared to that of the droplets containing *E. coli* Δ*lptD* sfGFP, either individually encapsulated or co-encapsulated with the control strain GS115 (*Fig. 3B*). The reduced fluorescence levels in the droplets were indication that growth of the *E. coli* Δ*lptD* sfGFP cells in the presence of yeast rPG-1 had been inhibited. Meanwhile, GS115 yeast had no significant effect on the proliferation of *E. coli* Δ*lptD* sfGFP, increasing the fluorescence signal in the corresponding droplets.

Microscopic examination of the incubated samples showed highly efficient inhibition of the growth of the *E. coli* Δ*lptD* sfGFP reporter strain, accompanied by the proliferation of *P. pastoris* rPG-1 (*Fig. 3C*). Meanwhile, droplets filled with the proliferating cells of the reporter bacterium predominated in the case of co-encapsulation of the reporter bacterium and the control GS115 strain (*Fig. 3C*). A similar effect was achieved when effector yeasts were cocultured with the target bacterium in a 96-well plate. Growth of *E. coli* Δ*lptD* sfGFP was inhibited in the *P. pastoris* rPG-1 suspension, while their growth in the control *P. pastoris* GS115 suspension was not affected.

Hence, the generated rPG-1-producing yeasts can inhibit the growth of the target bacterium in the co-culture within the first day of incubation. These findings can be used for the design of probiotic organisms based on rAMP-producing yeasts and to generate programmable recombinant biocontrol agents.

DISCUSSION

The rapid spread of antibiotic resistance poses a serious problem in the fight against infectious diseases.

The emergence of multidrug-resistant (MDR) bacterial strains further reduces the number of available treatment regimens. Therefore, searching for alternative antimicrobial compounds is an urgent issue. Antimicrobial peptides can become a source of novel antimicrobial agents, since they exhibit activity against a wide range of pathogens, including those associated with multidrug resistance [31].

AMPs include members of various structural classes. Among them, there are β-hairpins, α-helices, as well as linear, combined, and cyclic peptides [32]. The wide structural variability of AMPs allows one to implement different mechanisms of impact on bacterial cells, thus affecting the spectrum of antimicrobial activity. The rational design methods make it possible to fine-tune the physicochemical properties of AMPs and generate a peptide with improved activity and toxicity [33]. Therefore, AMPs constitute a flexible basis for designing effective antimicrobials.

Protegrin-1, which belongs to the β-hairpin AMPs, consists of 18 amino acid residues and contains two intramolecular disulfide bonds. It exhibits broad antimicrobial activity through its interaction with the bacterial membrane and pore formation in it [34, 35]. Taking into account its high antimicrobial activity and the broad range of pathogens susceptible to it, protegrin-1 was selected as an active component for designing a recombinant biocontrol agent.

Heterologous production of AMPs is an important bioengineering issue and also serves as a basis for the design of systems for the large-scale screening of antimicrobial compounds. *P. pastoris* methylotrophic yeast is widely used in biotechnology, because it allows one to produce recombinant proteins at high yields within short time periods [13, 14]. Generation of recombinant proteins under control of a methanol-inducible alcohol oxidase-1 (AOX1) promoter is the most commonly employed method [36]. However, methanol is easily flammable and a toxic substance; furthermore, induced expression makes it impossible to assess the competitive characteristics of recombinant yeasts *in vivo*. In our study, the antimicrobial peptide was synthesized in *P. pastoris* cells under control of a strong constitutive glyceraldehyde-3-phosphate dehydrogenase (GAP) promoter. Therefore, we managed to generate a recombinant yeast strain capable of effectively inhibiting the growth of gram-positive (*B. megaterium*) and gram-negative (*E. coli* Δ*lptD*) bacterial targets.

Biocontrol agents can inhibit the growth of the pathogens they are targeted to [15]. To ensure effective protection against pathogens, biocontrol agents need to be able to compete with these pathogens under conditions of limited resources and space. In this study, such conditions were simulated by microcompartmentalization of the bacterial target and yeast effector in droplets of microfluidic double emulsion and bacterial cells were numerically superior over yeast cells during encapsulation. The yeast strain secreting recombinant protegrin-1 (rPG-1) into the culture medium was found to effectively inhibit the growth of the target bacteria as early as on day 1 after encapsulation. Due to the constitutive production of rPG-1, recombinant yeast exhibits constant antimicrobial activity and can control the growth of microorganisms without the need to add an inducer. Therefore, genetic programming of *P. pastoris* yeast resulted in the generation of a recombinant biocontrol agent capable of inhibiting the growth of the target bacteria under conditions of competition for space and nutrients.

CONCLUSIONS

A recombinant biocontrol agent based on methylotrophic yeast *P. pastoris*, with rAMP protegrin-1 as its active component, has been designed in this study. The resulting yeast strain inhibited reporter target growth both on an agar medium and during cocultivation in droplets of microfluidic double emulsion. The developed strategy for the production of recombinant biocontrol agents is an important stage in elaborating alternative methods for combatting pathogens. Furthermore, the studied approaches can be used to search for novel compounds exhibiting antimicrobial activity by deep functional profiling [37]. ●

This work was supported by the Russian Science Foundation (project No. 21-14-00357).

REFERENCES

1. Murray C.J.L., Ikuta K.S., Sharara F., Swetschinski L., Robles Aguilar G., Gray A., Han C., Bisignano C., Rao P., Wool E., et al. // Lancet. 2022. V. 399. № 10325. P. 629–655.
2. Chahine E.B., Dougherty J.A., Thornby K.-A., Guirguis E.H. // Ann. Pharmacother. 2022. V. 56. № 4. P. 441–462.
3. Oliveira D.M.P.D., Forde B.M., Kidd T.J., Harris P.N.A., Schembri M.A., Beatson S.A., Paterson D.L., Walker M.J. // Clin. Microbiol. Rev. 2020. V. 33. № 3. P. e00181–00119.
4. Lin Q., Deslouches B., Montelaro R.C., Di Y.P. // Int. J. Antimicrob. Agents. 2018. V. 52. № 5. P. 667–672.
5. Mookherjee N., Anderson M.A., Haagsman H.P., Davidson D.J. // Nat. Rev. Drug Discov. 2020. V. 19. № 5. P. 311–332.
6. Mahlapuu M., Håkansson J., Ringstad L., Björn C. // Front. Cell. Infect. Microbiol. 2016. V. 6. № 194. P. 1–20.
7. Spohn R., Daruka L., Lázár V., Martins A., Vidovics F., Grézal G., Méhi O., Kintses B., Számel M., Jangir P.K., et

al. // Nat. Commun. 2019. V. 10. № 1. P. 4538.
8. Assoni L., Milani B., Carvalho M.R., Nepomuceno L.N., Waz N.T., Guerra M.E.S., Converso T.R., Darrieux M. // Front. Microbiol. 2020. V. 11. № 593215. P. 1–20.
9. Zhu Y., Hao W., Wang X., Ouyang J., Deng X., Yu H., Wang Y. // Med. Res. Rev. 2022. V. 42. № 4. P. 1377–1422.
10. Koo H.B., Seo J. // Pept. Sci. 2019. V. 111. № 5. P. e24122.
11. Moretta A., Scieuzo C., Petrone A.M., Salvia R., Manniello M.D., Franco A., Lucchetti D., Vassallo A., Vogel H., Sgambato A., et al. // Front. Cell. Infect. Microbiol. 2021. V. 11. № 668632. P. 1–26.
12. Tucker A.T., Leonard S.P., DuBois C.D., Knauf G.A., Cunningham A.L., Wilke C.O., Trent M.S., Davies B.W. // Cell. 2018. V. 172. № 3. P. 618–628.e613.
13. Popa C., Shi X., Ruiz T., Ferrer P., Coca M. // Front. Microbiol. 2019. V. 10. № 1472. P. 1–13.
14. Chen X., Li J., Sun H., Li S., Chen T., Liu G., Dyson P. // Sci. Rep. 2017. V. 7. № 1. 14543.
15. Stenberg J.A., Sundh I., Becher P.G., Björkman C., Dubey M., Egan P.A., Friberg H., Gil J.F., Jensen D.F., Jonsson M., et al. // J. Pest Sci. 2021. V. 94. № 3. P. 665–676.
16. Pipiya S.O., Mokrushina Y.A., Gabibov A.G., Smirnov I.V., Terekhov S.S. // Antibiotics. 2020. V. 9. № 9. P. 527.
17. Huang Y., Gao L., Lin M., Yu T. // Postharvest. Biol. Technol. 2021. V. 171. № 11. P. 1298.
18. Baranova M.N., Babikova P.A., Kudzhaev A.M., Mokrushina Y.A., Belozerova O.A., Yunin M.A., Kovalchuk S., Gabibov A.G., Smirnov I.V., Terekhov S.S. // Antibiotics. 2021. V. 10. № 10. P. 1161.
19. Wu S., Letchworth G.J. // BioTechniques. 2004. V. 36. № 1. P. 152–154.
20. Terekhov S.S., Smirnov I.V., Stepanova A.V., Bobik T.V., Mokrushina Y.A., Ponomarenko N.A., Belogurov A.A., Rubtsova M.P., Kartseva O.V., Gomzikova M.O., et al. // Proc. Natl. Acad. Sci. USA. 2017. V. 114. № 10. P. 2550–2555.
21. Edwards I.A., Elliott A.G., Kavanagh A.M., Zuegg J., Blaskovich M.A.T., Cooper M.A. // ACS Infect. Dis. 2016. V. 2. № 6. P. 442–450.
22. Orlov D.S., Shamova O.V., Eliseev I.E., Zharkova M.S., Chakchir O.B., Antcheva N., Zachariev S., Panteleev P.V., Kokryakov V.N., Ovchinnikova T.V., et al. // Mar. Drugs..2019. V. 17. № 6. P. 376.
23. Park C., Cho J., Lee J., Lee D.G. // Biotechnol. Lett. 2011. V. 33. № 1. P. 185–189.
24. Manzo G., Ferguson P.M., Hind C.K., Clifford M., Gustilo V.B., Ali H., Bansal S.S., Bui T.T., Drake A.F., Atkinson R.A., et al. // Sci. Rep. 2019. V. 9. № 1. P. 10934.
25. Manzo G., Hind C.K., Ferguson P.M., Amison R.T., Hodgson-Casson A.C., Ciazynska K.A., Weller B.J., Clarke M., Lam C., Man R.C.H., et al. // Commun. Biol. 2020. V. 3. № 1. P. 697/
26. Dosler S., Karaaslan E., Alev Gerceker A. // J. Chemother. 2016. V. 28. № 2. P. 95–103.
27. Akbari R., Hakemi-Vala M., Pashaie F., Bevalian P., Hashemi A., Pooshang Bagheri K. // Microb. Drug Resist. 2018. V. 25. № 2. P. 193–202.
28. Jang W.S., Kim C.H., Kim K.N., Park S.Y., Lee J.H., Son S.M., Lee I.H. // Antimicrob. Agents Chemother. 2003. V. 47. № 8. P. 2481–2486.
29. Sung W.S., Park S.H., Lee D.G. // FEBS Lett. 2008. V. 582. № 16. P. 2463–2466.
30. Donaldson G.P., Lee S.M., Mazmanian S.K. // Nat. Rev. Microbiol. 2016. V. 14. № 1. 20–32.
31. Park S.C., Park Y., Hahm K.S. // Int. J. Mol. Sci. 2011. V. 12. № 9. P. 5971–5992.
32. Huan Y., Kong Q., Mou H., Yi H. // Front. Microbiol. 2020. V. 11. № 582779. P. 1–21.
33. Elliott A.G., Huang J.X., Neve S., Zuegg J., Edwards I.A., Cain A.K., Boinett C.J., Barquist L., Lundberg C.V., Steen J., et al. // Nat. Commun. 2020. V. 11. № 1. P. 3184.
34. Bolintineanu D., Hazrati E., Davis H.T., Lehrer R.I., Kaznessis Y.N. // Peptides. 2010. V. 31. № 1. P. 1–8.
35. Fahrner R.L., Dieckmann T., Harwig S.S., Lehrer R.I., Eisenberg D., Feigon J. // Chem. Biol. 1996. V. 3. № 7. P. 543–550.
36. Karbalaei M., Rezaee S.A., Farsiani H. // J. Cell. Physiol. 2020. V. 235. № 9. P. 5867–5881.
37. Terekhov S.S., Smirnov I.V., Malakhova M.V., Samoilov A.E., Manolov A.I., Nazarov A.S., Danilov D.V., Dubiley S.A., Osterman I.A., Rubtsova M.P., et al. // Proc. Natl. Acad. Sci. USA. 2018. V. 115. № 38. P. 9551–9556.

Characterization of the C6D7-RBD Human Monoclonal Antibody Specific to the SARS-CoV-2 S Protein Receptor-Binding Domain

Ya. O. Romanenko*, M. V. Silkina, A. S. Kartseva, M. A. Marin, M. A. Shkuratova, M. A. Makarova, A. K. Ryabko, D. A. Konyshkova, N. A. Zeninskaya, A. E. Khlyntseva, I. G. Shemyakin, V. V. Firstova

Federal Budget Institution of Science State Research Center for Applied Microbiology and Biotechnology, Obolensk, Moscow region, 142279 Russian Federation

*E-mail: muntian.jana@yandex.ru

Received November 01, 2022; in final form, February 20, 2023

DOI:

ABSTRACT **The new coronavirus infection COVID-19 is an acute viral disease that affects primarily the upper respiratory tract. The etiological agent of COVID-19 is the SARS-CoV-2 RNA virus (Coronaviridae family, *Betacoronavirus* genus, *Sarbecovirus* subgenus). We have developed a high-affinity human monoclonal antibody, called C6D7-RBD, which is specific to the S protein receptor-binding domain (RBD) from the SARS-CoV-2 Wuhan-Hu-1 strain and exhibits virus-neutralizing activity in a test with recombinant antigens: angiotensin-converting enzyme 2 (ACE2) and RBD.**

KEYWORDS **COVID-19, SARS-CoV-2, receptor-binding domain, human monoclonal antibody, virus-neutralizing activity.**

ABBREVIATIONS **COVID-19 – (COronaVIrus Disease 2019); SARS-CoV-2 – severe acute respiratory syndrome-related coronavirus 2; WHO – World Health Organization; FDA – Food and Drug Administration; hMAb – human monoclonal antibody; mAb – monoclonal antibody; ACE-2 – angiotensin-converting enzyme 2; TMPRSS2 – transmembrane serine protease 2; RBD – receptor-binding domain; PBS – phosphate-buffered saline; FBS – fetal bovine serum; ELISA – enzyme-linked immunosorbent assay; TMB – 3,3',5,5'-tetramethylbenzidine; PBS–TW – phosphate-buffered saline containing Tween-20; PAG – polyacrylamide gel.**

INTRODUCTION

The new coronavirus infection COVID-19 (COronaVIrus Disease 2019), which is caused by the severe acute respiratory syndrome-related coronavirus 2 (SARS-CoV-2), was first detected in Wuhan, the capital of China's Hubei province, at the end of 2019. Despite all efforts to contain the disease in China, the virus spread across the world, and soon the World Health Organization (WHO) had declared a COVID-19 pandemic [1]. To date, the ongoing pandemic continues, claiming many more lives. Many effective vaccines have been developed around the world over that short period of time. However, there remains a need for agents that can be used for passive immunotherapy of moderate and severe cases of the disease; in particular, human monoclonal antibody (hMAb)-based medications.

The SARS-CoV-2 virus genome encodes four structural proteins: the surface spike (S) glycoprotein, the membrane (M) protein, nucleocapsid (N) protein, and the envelope (E) protein. The S protein mediates viral attachment, fusion, and entry into the host cell. The transmembrane serine protease 2 (TMPRSS2) cleaves the S protein into two subunits, S1 and S2 [2, 3]. The receptor interaction between the virus and the host cell is mediated by RBD that is located in the S1 subunit. Next, the S2 subunit promotes fusion of the viral membrane with that of the host cell [4]. Therefore, RBD is the main target in developing hMAbs capable of neutralizing the virus [5].

As the disease has spread and mortality rates have increased, researchers around the world have scrambled to come up with innovative agents with high clinical efficacy and safety.

In October 2020, the Ministry of Health of the Russian Federation approved the use of plasma from convalescent donors (surviving patients diagnosed with COVID-19) for the treatment of patients with a new severe coronavirus infection because of the lack of drugs for a specific treatment. According to their guidelines, the age range of potential donors should be 18 to 55 years, the body weight should exceed 55 kg, and the blood plasma should be collected no earlier than 14 days after resolving clinical symptoms and receiving a double negative oropharyngeal swab for SARS-CoV-2 RNA performed in a 24-hour or more interval. The blood plasma should exhibit virus-neutralizing activity at a 1 : 160 dilution; the total protein concentration in the blood should not be less than 65 g/L [6].

In the Russian Federation, there is no experience of the use of monoclonal antibody-based drugs on severely-ill patients, but there is one patented hMAb that exhibits neutralizing activity and selectively interacts with a SARS-CoV-2 S protein RBD fragment [7].

The development of hMAbs specific to the SARS-CoV-2 S protein RBD is promising. This study characterizes the developed hMAb, which may be used for the treatment of COVID-19.

EXPERIMENTAL

For this study, we chose a blood donor who had recovered from the new coronavirus infection COVID-19 and was vaccinated with the Sputnik Light vaccine (manufactured by the Gamaleya National Research Center for Epidemiology and Microbiology, the Russian Academy of Medical Sciences) 6 months after recovery. The donor provided written informed consent to participate in the study. On day 7 after vaccination, peripheral blood was collected and the B lymphocyte fraction was isolated using a RosetteSep™ Human B Cell Enrichment Cocktail kit (Stemcell technologies, Canada), in accordance with the manufacturer's instructions. The isolated B lymphocytes were electrofused with the K6H6/B5 myeloma cell line (ATCC® CRL1823™) using an ECM 2001 device (BTX Harvard Apparatus, USA), according to a previously published procedure [8].

The produced hybridomas were cultured at a temperature of 37°C in a humid atmosphere with 5% CO_2. The culture medium was replaced once every three days. After the hybrid culture reached the monolayer, an enzyme-linked immunosorbent assay (ELISA) was performed to identify hybridomas producing SARS-CoV-2 S protein RBD specific to mAbs.

Enzyme-linked immunosorbent assay

The culture fluid from the wells with grown hybrid cells was tested using ELISA for specific interactions with a recombinant RBD from the SARS-CoV-2 Wuhan-Hu-1 strain (his-sars2-rbd, Invivogen). For this, 100 μL of a solution of the recombinant RBD (his-sars2-rbd, Invivogen) at a concentration of 1 μg/mL per well in PBS was added to the wells of a 96-well polystyrene plate and incubated at a temperature of 37°C on an orbital plate shaker (Elmi, Latvia) at 370 rpm for 2 h. Then, each well of the plate was washed three times with 200 μL of PBS containing 0.05% Tween-20 (PBS–TW). Later, the free binding sites on the wells were blocked with milk with a fat content of no more than 0.5% (200 μL per well) and incubated at 37°C h under the same conditions for 1h. After incubation, the wells were washed with PBS-TW three times. Next, 100 μL of the culture liquid was added to the plate and the plate was incubated and washed under the same conditions. The wells containing PBS alone were used as a negative control; the donor's pretested blood serum with a high titer of anti-RBD antibodies at a 1 : 25 dilution was used as a positive control. After incubation, the wells were washed with PBS-TW three times. Then, anti-human IgG (whole molecule) rabbit antibodies conjugated with horseradish peroxidase (Sigma, USA) at a 1 : 20 000 dilution were added to the wells. A plate was incubated under the same conditions for 40 min. At the end of the incubation, the plate was washed 6 times and 100 μL of a developing solution containing 3,3',5,5'-tetramethylbenzidine (TMB) was added to the wells of the plate. The reaction was assessed based on the development of a blue color. The staining intensity was measured on a microplate spectrophotometer (Bio-Rad xMark) at a wavelength of 655 nm.

Hybrid cell colonies displaying high absorbance (3-fold higher than the negative control value) in ELISA were cloned and scaled in Corning® T-25 and T-75 culture flasks. Then, the hybrid culture was cultivated in 1.6 L Optimum Growth™ flasks (Thomson Instrument Company, USA) to produce hMAbs.

Affinity chromatography

To produce the C6D7-RBD hMAb, the culture liquid used for culturing hybridomas was purified by affinity chromatography on a Protein G-sepharose column (HiTrap™ Protein G, Sweden) using an ÄKTA Start system (GE Healthcare, USA). The isolated IgG was transferred into PBS and purified by gel filtration on a Superdex 200 10/300 GL sorbent (GE Healthcare, USA). The purity of the resulting immunoglobulin fraction was evaluated by Laemmli SDS electrophoresis in 10% polyacrylamide gel (PAG) under reducing and non-reducing conditions. Gels were stained with Coomassie Brilliant Blue R-250.

Immunoblot analysis

The immunological specificity of the purified C6D7-RBD hMAb was assessed by immunoblotting. For this, the recombinant RBD (1 μg per lane) was separated by PAG electrophoresis under reducing conditions. Further, the protein was horizontally transferred from the gel to a Hybond-C Extra nitrocellulose membrane (GE Healthcare) using a standard procedure. After transfer, the membrane was immersed in skimmed milk (less than 0.5% fat) to block the free binding sites on the nitrocellulose and incubated at a temperature of 37°C with shaking for 1 h. After incubation, the membrane was washed with PBS-TW three times and immersed in a 10 μg/mL C6D7-RBD hMAb solution in PBS. The membrane was incubated and washed under the same conditions. The hMAb on the membrane was detected using anti-human IgG goat antibodies conjugated with horseradish peroxidase (Sigma) at a 1 : 10 000 dilution in PBS. The membrane was incubated under the same conditions for 40 min. After incubation, the membrane was washed with PBS-TW 6 times and developed with a 1% diaminobenzidine solution in PBS supplemented with nickel and cobalt chlorides and 33% hydrogen peroxide (1 μL per 1 mL of a developing solution).

Class assignment of C6D7-RBD hMAb

The subclass and isotype of the purified C6D7-RBD hMAb were assessed using an immunochromatographic rapid test (Iso-Gold™ Rapid Human Antibody Isotyping Kit, Canada). All reagents were brought to room temperature before the testing. A C6D7-RBD hMAb test sample was diluted 100-fold with 200 μL of sample dilution buffer (Part Number SDB-004). Then, a test strip was immersed in a tube with the test sample. The result was analyzed after 5–10 min.

Determination of the equilibrium dissociation constant for C6D7-RBD hMAb and the target RBD protein

The equilibrium dissociation constant for C6D7-RBD hMAb and the target RBD protein was determined using surface plasmon resonance (SPR) spectroscopy on a BIAcore X-100 instrument (Biacore, Sweden). The experiment was performed on a CM5 sensor chip in HBS-EP buffer (10 mM Hepes, 150 mM NaCl, 3 mM EDTA, and 0.005% P20 surfactant, pH 7.4). Anti-histidine antibodies were conjugated to the sensor chip using a His Capture Kit Type 2 and an Amine Coupling Kit (Cytiva, Sweden), according to the manufacturer's instructions. The recombinant RBD (10 μg/mL) was applied to the prepared chip at a rate of 30 μL/min for 3 min. After a 10-minute stabilization period, the antibody (concentrations of 6.25 to 100 nM) was injected at a constant flow rate of 40 μL/min for 3 min. Dissociation was monitored for 90 min. Next, the chip was regenerated with 10 mM glycine pH 1.7 at a flow rate of 50 μL/min for 30 s. Sensorograms were normalized by subtracting baseline RU values from the reference flow cell (no hMAb capture) and analyzed by fitting the data to a 1 : 1 Langmuir binding model using the Biacore T200 Evaluation software.

C6D7-RBD hMAb-mediated inhibition of the ACE-2–RBD interaction

The virus-neutralizing activity of C6D7-RBD hMAb was evaluated using competitive ELISA. For this purpose, the recombinant RBD protein was immobilized on the wells of a 96-well polystyrene plate at a concentration of 1 μg/mL according to the above-described procedure. Then, the C6D7-RBD hMAb was added to the wells at concentrations of 10 to 0.078125 μg/mL in a twofold serial dilution step. The plate was incubated at 37°C for 1 h. After incubation, the wells were washed with PBS-TW three times. Then, recombinant human ACE-2 (fc-hace2, Invivogen) conjugated with horseradish peroxidase was added to the wells using a LYNX Rapid HRP Antibody Conjugation kit (Bio-Rad). The plate was incubated and washed using the same conditions. Then, 100 μL of a TMB developing solution was added to the wells. The reaction was evaluated based on the development of a blue color. The staining intensity was measured on a microplate spectrophotometer (Bio-Rad xMark) at a wavelength of 655 nm. The mean background optical density (control of the wells without RBD immobilization, which is equivalent to the RBD completely blocked by antibodies) was considered as 100% neutralizing activity. The mean optical density of the control wells where ACE-2–HRP interacted with RBD in the absence of antibodies was considered as a lack of neutralizing activity (0%). The control values were used to generate a linear function in order to quantify absorbance in the experimental wells with varying antibody amounts as the percentage of neutralizing activity.

RESULTS

Electrofusion of plasmablasts with K6H6/B5 partner cells resulted in 5 hybridomas. Of these, one hybridoma, called C6D7-RBD, was selected based on the results of a screening for the specificity of the anti-RBD antibodies synthesized by the hybridomas. Subsequent scaling of the hybridoma culture provided a large amount of supernatant with antibodies. A pure immunoglobulin fraction was produced using chromatographic purification techniques.

Chromatographic purification of C6D7-RBD hMAb

The purity of the immunoglobulin fraction produced by affinity chromatography and subsequent gel filtration was assessed by Laemmli SDS-electrophoresis in 10% PAG under reducing and non-reducing conditions (*Fig. 1*). The position of the purified C6D7-RBD hMAb on the electropherogram corresponds to its molecular weight. Based on densitometry data (GE Typhoon FLA 9500, Sweden), the purity of C6D7-RBD hMAb amounted to at least 95%.

Immunological specificity of C6D7-RBD hMAb to the SARS-CoV-2 S protein receptor-binding domain

The specificity of C6D7-RBD hMAb to the recombinant RBD protein was confirmed by immunoblotting. The C6D7-RBD hMAb was shown to exhibit specific activity against the recombinant RBD protein (*Fig. 2*).

Immunochromatographic test results

According to the immunochromatographic test data, the C6D7-RBD hMAb is the G1 isotype of class G immunoglobulins and contains the $\varkappa$-chain (*Fig. 3*).

Determination of the equilibrium dissociation constant for the C6D7-RBD hMAb and the target RBD protein (Wuhan)

The parameters of the affinity interaction between the C6D7-RBD hMAb and the recombinant RBD protein were evaluated using surface plasmon resonance (SPR) spectroscopy. The equilibrium dissociation constant (K_D) for the C6D7-RBD hMAb was $K_D = 5.525 \times 10^{-9}$ M (*Fig. 4*).

RBD–ACE2-neutralizing activity of the C6D7-RBD hMAb

Figure 5 shows a dose-dependent increase in the neutralizing activity of C6D7-RBD hMAb. Almost complete (97%) inhibition of the ACE-2–RBD (Wuhan) interaction was observed at a maximum C6D7-RBD hMAb concentration of 10 μg/mL. Addition of the C6D7-RBD hMAb to a concentration of 0.625 μg/mL blunted the ACE-2–RBD (Wuhan) interaction by 36%; there was almost no neutralizing activity (2%) at the minimum C6D7-RBD hMAb concentration (0.078125 μg/mL).

DISCUSSION

Production of hMAb with naturally paired heavy and light chains which is specific to a chosen target and exhibits virus-neutralizing activity is quite difficult. We used cytometric sorting to produce a pool of plasmablasts. We chose the strategy of sorting the entire population of plasmablasts (regardless of their specificity), but blood sampling was performed on day 7 after vaccination of the donor with the Sputnik Light vaccine. Several studies have reported that the number of specific plasmablasts increases in the blood on day 7 or 8 after vaccination or infection [9–11]. To increase the number of produced hybridomas, we used electrofusion, whose efficiency is an order of magnitude higher than that of fusion with PEG [8]. The use of the K6H6/B5 cell line as partner cells reduced the risk of subsequent segregation of human chromosomes from hybridomas [12]. A total of 12 hybridomas were produced, but only five were RBD-specific, and only one hybridoma (C6D7-RBD) was able to stably synthesize the antibody.

Further analysis revealed that C6D7-RBD belongs to the IgG1 subclass and contains the $\varkappa$-light chain. C6D7-RBD hMAb is specific to SARS-CoV-2 RBD, with $K_D = 5.525 \times 10^{-9}$ M.

Traditional techniques used to identify the ability of mAbs to neutralize the SARS-CoV-2 virus are based on assessing the ability of antibodies to inhibit plaque formation or the viral cytopathogenic effect in a sensitive cell culture. Working with the wild-type SARS-CoV-2 virus requires biosecurity and a laboratory environment that meets the safety requirements for working with risk-group II pathogens. Surrogate techniques can be used to facilitate the screening for the neutralizing activity of monoclonal antibodies or sera from recovered/vaccinated donors. These techniques include competitive ELISA that analyzes the effect of antibodies on the interaction between recombinant RBD proteins and ACE-2. This technique reflects the ability of antibodies to inhibit virus entry into the cell. A number of studies have shown that most virus-neutralizing antibodies are specific to the SARS-CoV-2 S glycoprotein RBD, and that their mechanism of action is related to the inhibition of virus binding to the viral receptor ACE-2 on the target cell surface. This technique was used to show that 10-μg/mL C6D7-RBD hMAb almost completely blocks the RBD–ACE-2 interaction.

In world practice, there is experience in the use of hMAb-based drugs. To date, the FDA has only approved three such drugs for emergency treatment of COVID-19. In 2021, the British pharmaceutical company GlaxoSmithKline (GSK) and its American partner Vir Biotechnology introduced sotrovimab (VIR-7831) to the market [13]. The drug comprises a single hMAb specific to the SARS-CoV-2 S protein RBD [14]. In the same year, AbCellera, together with the U.S. Vaccine Research Center at the National Institute of Allergy and Infectious Diseases (NIAID), developed LY-CoV555/bamlanivimab and LY-CoV016/etesevimab [15]. This drug consists of a cocktail of hMAbs specific to the RBD S protein and

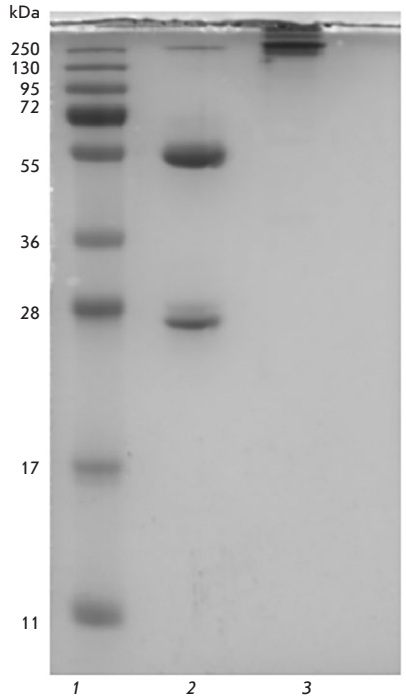

Fig. 1. Electrophoregram of C6D7-RBD hMAb.
1 – PageRuler™ SM1811 molecular weight markers (Fermentas, USA).
2 – C6D7-RBD hMAb sample, reducing conditions.
3 – C6D7-RBD hMAb sample, non-reducing conditions

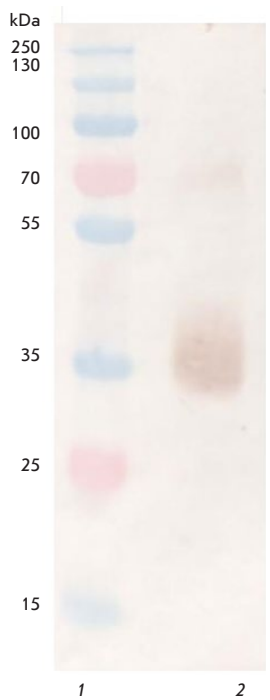

Fig. 2. C6D7-RBD hMAb specificity to the recombinant RBD protein.
1 – PageRuler™ SM1811 molecular weight markers (Fermentas, USA).
2 – Recombinant RBD detected with C6D7-RBD hMAb

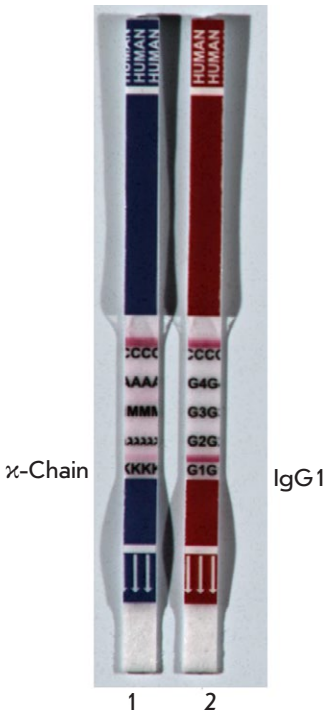

Fig. 3. Class assignment of C6D7-RBD hMAb.
1 – Strip for determining the light chain type and immunoglobulin class.
2 – Strip for determining the IgG subclass

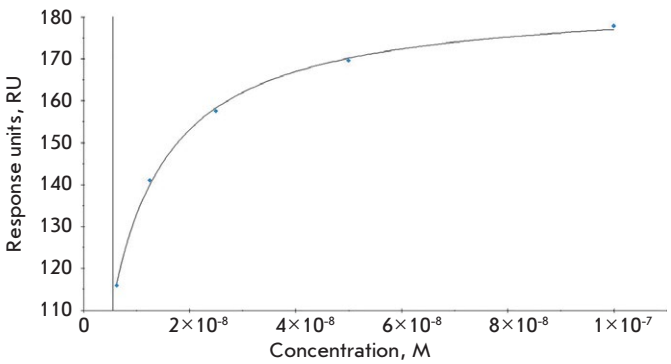

Fig. 4. Determining K_D for C6D7-RBD hMAb and the target RBD protein

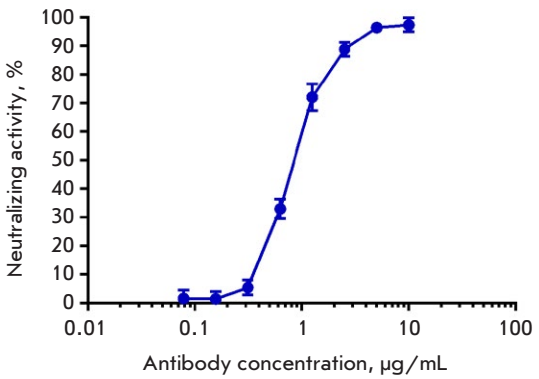

Fig. 5. RBD–ACE2-neutralizing activity of C6D7-RBD hMAb

ACE-2 [16]. The third approved drug, Casirivimab and Imdevimab (REGN10933 and REGN10987), developed by the American biotechnology company Regeneron Pharmaceuticals, consists of two hMAbs specific to the SARS-CoV-2 S protein RBD [17, 18]. Clinical trials have demonstrated that a cocktail of SARS-CoV-2 S protein RBD specific monoclonal antibodies more effectively neutralizes the SARS-CoV-2 virus.

Therefore, the developed C6D7-RBD hMAb is promising and needs further study of its efficacy as a separate hMAb or a component of a mAb cocktail for neutralizing the SARS-CoV-2 virus.

CONCLUSION

Using cytometric sorting and hybridoma technology, we were able to generate the C6D7-RBD hMAb-producing hybridoma. The C6D7-RBD hMAb belongs to the IgG subclass 1; the light chain is represented by the κ-isotype. The C6D7-RBD hMAb is specific to the SARS-CoV-2 virus in the ability to neutralize its entry into the cell. ●

This work was supported by the state task R&D 3.1.3.
Conflict of interest. The authors declare no conflict of interest.

REFERENCES

1. Yan Y., Chang L., Wang L. // Rev. Med. Virol. 2020. V. 30. № 3. P. e2106.
2. Huang Y., Yang C., Xu X.F., Xu W., Liu S.W. // Acta Pharmacologica Sinica. V. 41. № 9. P. 1141–1149.
3. Kumar S., Chandele A., Sharma A. // PLoS Pathogens. 2022. V. 17. № 9. P. e1009885.
4. Raybould M.I., Kovaltsuk A., Marks C., Deane C.M. // Bioinformatics. 2021. V. 37. № 5. P. 734–735.
5. Xia S., Yan L., Xu W., Agrawal A.S., Algaissi A., Tseng C.T.K., Wang Q., Du L., Tan W., Wilson I.A., et al. // Sci. Adv. 2019. V. 5. № 4. P. eaav4580.
6. Kamkin E.G. Prevention, diagnosis, and treatment of novel coronavirus infection (COVID-19). Temporary guidelines. M: Ministry of Health of the Russian Federation, 2020.
7. Shakhparonov M.I., Pavlyukov M.S., Antipova N.V. Monoclonal antibody to rdb fragment in composition of sars-cov-2 s protein. RF patent RU2744274. 2021.
8. Silkina M.V., Kartseva A.S., Ryabko A.K., Maryin M.A., Romanenko Ya.O., Kalmantaeva O.V., Khlyntseva A.E., Shemyakin I.G., Dyatlov I.A., Firstova V.V. // Biotechnology. 2021. V. 37. № 2. P. 77–87.
9. Scholzen A., Nahrendorf W., Langhorne J., Sauerwein R.W. // PLoS One. 2014. V. 9. № 7. P. e102885.
10. Traggiai E., Becker S., Subbarao K., Kolesnikova L., Uematsu Y., Gismondo M.R., Murphy B.R., Rappuoli R., Lanzavecchia A. // Nat. Medicine. 2004. V. 10. № 8. P. 871–875.
11. Ušaj M., Trontelj K., Miklavčič D., Kandušer M. // J. Membrane Biol. 2010. V. 236. № 1. P. 107–116.
12. Yu X., McGraw P.A., House F.S., Crowe J.E., Jr. // J. Immunol. Meth. 2008. V. 336. № 2. P. 142–151.
13. Tuccori M., Ferraro S., Convertino I., Cappello E., Valdiserra G., Blandizzi C., Maggi F., Focosi D. // MAbs. 2020. V. 12. № 1. P. 1854149.
14. Cathcart A.L., Havenar-Daughton C., Lempp F.A., Ma D., Schmid M.A., Agostini M.L., Guarino B., Di Julio J., Rosen L.E., Tucker H., et al. // bioRxiv. 2021. P. 2021.03.09.434607.
15. Jones B.E., Brown-Augsburger P.L., Corbett K.S., Westendorf K., Davies J., Cujec T.P., Wiethoff C.M., Blackbourne J.L., Heinz B.A., Foster D., et al. // Sci. Translat. Med. 2021. V. 13 № 593. P. eabf1906.
16. Chen P., Nirula A., Heller B., Gottlieb R.L., Boscia J., Morris J., Huhn G., Cardona J., Mocherla B., Stosor V., et al. // New Engl. J. Med. 2021. V. 384. № 3. P. 229–237.
17. Hansen J., Baum A., Pascal K.E., Russo V., Giordano S., Wloga E., Fulton B.O., Yan Y., Koon K., Patel K., et al. // Science. 2020. V. 369. № 6506. P. 1010–1014.
18. VanBlargan L.A., Errico J.M., Halfmann P., Zost S.J., Crowe J.E., Purcell L.A., Kawaoka Y., Corti D., Fremont D.H., Diamond M.S. // Nat. Medicine. 2022. V. 28. № 3. P. 490–495.

Distortion of Population Statistics due to the Use of Different Methodological Approaches to the Construction of Genomic DNA Libraries

F. S. Sharko[1*], K. V. Zhur[1], V. A. Trifonov[1,2], E. B. Prokhortchouk[1]
[1]Laboratory of vertebrate genomics and epigenomics, Federal Research Centre "Fundamentals of Biotechnology" of the Russian Academy of Sciences, Moscow, 119071 Russian Federation
[2]Institute for the History of Material Culture of the Russian Academy of Sciences, Saint Petersburg, 191186 Russian Federation
*E-mail: fedosic@gmail.com
Received December 26, 2022; in final form, March 02, 2023
DOI: 10.32607/actanaturae.11898

ABSTRACT **Several different methods of DNA library preparation for paleogenetic studies are now available. However, the chemical reactions underlying each of them can affect the primary sequence of ancient DNA (aDNA) in the libraries and taint the results of a statistical analysis. In this paper, we compare the results of a sequencing of the aDNA libraries of a Bronze Age sample from burials of the Caucasian burial ground Klady, prepared using three different approaches: (1) shotgun sequencing, (2) strategies for selecting target genomic regions, and (3) strategies for selecting target genomic regions, including DNA pre-treatment with a mixture of uracil-DNA glycosylase (UDG) and endonuclease VIII. The impact of the studied approaches to genomic library preparation on the results of a secondary analysis of the statistical data, namely F4 statistics, ADMIXTURE, and principal component analysis (PCA), was analyzed. It was shown that preparation of genomic libraries without the use of UDG can result in distorted statistical data due to postmortem chemical modifications of the aDNA. This distortion can be alleviated by analyzing only the single nucleotide polymorphisms caused by transversions in the genome.**
KEYWORDS **ancient DNA, ADMIXTURE, UDG.**
ABBREVIATIONS **UDG – uracil-DNA glycosylase; aDNA – ancient DNA; SNP – single nucleotide polymorphism; PCA – principal component analysis.**

INTRODUCTION

The Russian Federation is a rich source of archaeological material for paleogenetic studies. Materials from Russia have been used in one way or another in almost all discoveries that have involved ancient DNA (aDNA): the discovery of the Denisovan man [1], the Ancient North Eurasians (ANE) population [2], Eastern hunter-gatherers (EHG) [3], and the population of Yamnik [4]. Yet, paleogenetic studies sited in Russia have had limited success, which has mostly involved the donation of bone material [5]. However, a number of interdisciplinary teams have recently been established. These teams are focused on comprehensive studies: expeditionary finds, synthesis of archaeological and paleogenetic data, and the generation of new historical hypotheses. This work summarizes the methodological approaches tested at the Federal Research Center "Fundamentals of Biotechnology" of the Russian Academy of Sciences and provides the most effective algorithms for the construction of genomic libraries that can be used by other laboratories in the field.

Ancient DNA sequence analysis has become a powerful tool to study ancient human populations [6–8]. However, there is a number of difficulties associated with postmortem degradation of genetic material due to the action of endogenous nucleases, random hydrolysis, and oxidation. The most common aDNA damage is deamination of cytosine residues, i.e. cleavage of the amino group from the nucleobase, followed by the formation of uracil residues, which, in turn, are converted to thymine during the polymerase chain

reaction at the stage of preparation of DNA fragment libraries [9]. As a result, when sequencing libraries of aDNA fragments, researchers observe substitutions in either the C→T direction at the 5' end of the DNA molecule or G→A direction at the 3' end, depending on the sample preparation protocol used. The presence of these substitutions (false nucleotides) reduces the accuracy of mapping reads to the reference sequence, meaning that the reads containing non-reference alleles are less likely to be mapped than those containing reference alleles [6].

The total number of false nucleotides present in a reconstructed genome depends on the amount of sequencing data obtained and postmortem DNA damage and whether or not DNA was pre-treated with a mixture of uracil-DNA glycosylase (UDG) and endonuclease VIII (the mixture makes it possible to remove uracil with the formation of a single-nucleotide gap) during the preparation of genomic libraries [10]. Reconstructed ancient genomes usually contain sequences with both genuine and artefactual variants, which can affect the allele frequency analysis and determination of the population structure [6].

Analysis of ancient genome databases (Allen Ancient DNA Resource, https://reich.hms.harvard.edu/allen-ancient-dna-resource-aadr-downloadable-genotypes-present-day-and-ancient-dna-data) shows that the majority of sequenced genomes were obtained by constructing shotgun (SG) libraries either with or without UDG treatment or by selecting the target regions using various enrichment approaches. Among the latter, kits produced by the manufacturers Twist, Agilent, and Arbor are the ones used most often. Enrichment kits have recently been characterized by D. Reich et al. [11], who concluded that Twist kits are the most effective. However, their study does not discuss such important aspects as the effect of sample preparation methods on the results of the secondary statistical analysis. These include F-statistics, ancestral ADMIXTURE analysis components, and multivariate principal component analysis (PCA) projections.

Population structure analysis plays an important role in human evolutionary genetics, which makes it possible to characterize genetic variability [12]; i.e. the presence of different levels of genetic relationship between subgroups in the population. For instance, this is important for establishing the time of divergence between populations originating from different geographic locations [13, 14]. In order to solve this task mathematically, a formal assumption of the existence of so-called ancestral populations that gave rise to the analyzed groups is made. These ancestral populations are a mathematical abstraction; they are characterized by specific allele frequencies, and the contribution of these frequencies to real samples allows one to make brief visual summaries illustrating the presence of a population structure in the sample.

Genetic clustering algorithms implemented in such tools as STRUCTURE [15] and ADMIXTURE [16] are widely used for the characterization of individual samples and populations based on genetic data. ADMIXTURE effectively estimates individual ancestries by computing maximum likelihood estimates in a parametric model. This model states that the genotype n_{ij} for individual i at single nucleotide polymorphism (SNP) j is a number of type "1" alleles observed. Given K ancestral populations, the success likelihood in binomial distribution $n_{ij} \sim \mathrm{Bin}(2, p_{ij})$ is a function of the fraction q_{ik} of ancestry i for population k and the frequency f_{kj} for allele 1 in population k. ADMIXTURE maximizes the log-likelihood of a model using a block relaxation algorithm:

$$p_{ij} = \sum_{k=1}^{K} q_{ik} f_{kj}$$

$$L(Q,F) = \Sigma_{ij}\{n_{ij} \times \mathrm{In}p_{ij} + (2-n_{ij}) \times \mathrm{In}(1-p_{ij})\},$$

where q_{ik} and f_{kj} comprise the matrices Q and F, respectively [17].

The F4-statistics used in this study estimates the probability of independence of the two graph branches, each of which contains two populations. In the frequency space, the statistics are a mathematical expectation of the product of the frequency difference between two populations in each of the two graph branches for all SNPs:

$$\mathrm{F4(A,B;C,D)}=\{(a-b)(c-d)\},$$

where A, B, C, and D are populations, while a, b, c, and d are the corresponding frequencies.

The result is considered statistically significant if the absolute value of the z score for the distribution of F4-statistics elements is > 3. In paleogenetics, it is often impossible to obtain populations frequencies due to the lack of a sufficient number of samples. In this case, the ABBA-BABA test is used as an F4-statistics analogue to genotype individual genomes. To be able to establish the likelihood that ABBA-BABA test values differ from zero, the absolute value of the z score should be > 3, while ABBA-BABA test values for uniform genomic windows are used as sample elements [18]. If one of the populations tested using F4 (or the ABBA-BABA test in the case of genotypes) is historically, morphologically, or genetically very distant from the studied groups (outgroup), then the intuitive explanation of the non-zero F4-statistics comes down to evaluating the contribution of the population located

in the same branch with the outgroup to one of the two populations in the other graph branch.

If we present the genome as a vector with genotype values as coordinates that can be either 1, 0, or -1 (which stand for homozygotes AA and BB and heterozygote AB, respectively), then genotyped samples can be presented as a set of multidimensional (based on the total number of SNPs identified) vectors that can be projected onto lower dimensional spaces. PCA is one of the projection methods; it makes it possible to visualize relative to the position of objects. In particular, in ethnogeographic studies, pairwise distances between the samples of modern genomes obtained by using the PCA analysis correlate with the pairwise geographic distances between the residential locations of the donors of genetic material. Plotting ancient genomes on PCA maps constructed in the vector space of modern genomes is a convenient tool for estimating the genetic relationship between ancient and modern humans.

In this work, we compare the results of a population ADMIXTURE analysis and PCA analysis, as well as F4-statistics values for a Bronze Age sample from the Caucasian burial ground Klady (Tsarskaya village) [19], obtained using three approaches. The following methods were used for preparing genomic libraries: 1) shotgun sequencing strategy; 2) selection of target genomic regions using the Arbor kit; 3) selection of target genomic regions using the Arbor kit with UDG pre-treatment of DNA; and 4) selection of target genomic regions using the Agilent kit with UDG pre-treatment of DNA.

EXPERIMENTAL

DNA isolation and genomic library preparation

All experiments with aDNA were carried out in a clean room at the Federal Research Center "Fundamentals of Biotechnology" of the Russian Academy of Sciences (Skryabin Institute of Bioengineering). DNA isolated from an anthropological sample, namely the remains (fragments of jaws and teeth) of an adult from the Maykop culture megalithic tombs of the Bronze Age (Northwest Caucasus), was used. DNA was isolated from 100 mg of bone powder using Dabney buffer (5 M guanidine hydrochloride, 40% (v/v), isopropanol, 0.12 M sodium acetate, and 0.05% (v/v) Tween 20) and silica-coated magnetic beads [20]. The resulting DNA was used to prepare high-complexity libraries of single-stranded DNA fragments using the ACCEL-NGS 1S Plus DNA Library Kit (Swift Biosciences, USA) according to the original protocol with the following modifications: polymerase that had been developed in a way that uracil residues did not abrogate DNA synthesis (KAPA HiFi HS Uracil+RM, USA) was used at indexing PCR stages.

Three different types of DNA libraries were prepared from the same extract for next-generation sequencing. The first (I) library (KLD_SG) was obtained using shotgun sequencing of the total genome. For the second (II) library (KLD_CAP), the same preparation protocol was used, followed by enrichment of the genomic regions of interest (target enrichment). Unlike in library II, in the third library (III) (KLD_UDG), DNA was pre-treated with a mixture of uracil-DNA glycosylase (UDG) and endonuclease VIII, which removes uracil from the DNA and converts the resulting abasic sites to single-nucleotide gaps [21]. Treatment with the mixture of UDG and endonuclease VIII successfully removes uracils in aDNA, while preserving a significant part of them at the end of fragments: the so-called "whiskers of ancientry," which are indicative of the ancient nature of DNA. Data on the fourth (IV) library type, which was synthesized from the same bone remains based on the principle of selecting target regions using the Agilent kit with pre-treatment of intact aDNA with UDG, were obtained from professor Pinhasi (University of Vienna, Austria) and designated with the index I6268 from the previously published study [22].

Target enrichment

The MyBaits Expert Human Affinities Prime Plus Kit [MyBaits Manual v.1.0 – Population Genomics Hybridization Capture for Target NGS, 2021. https://arborbiosci.com/wp-content/uploads/ 2021/03/myBaits_Expert_HumanAffinities_v1.0_Manual.pdf] was used to capture 1.6 million SNPs from human aDNA. Reagents for enriching the selected genomic regions contained biotinylated single-strand DNA probes, which are a mixture of three probe sets: prime 1240K panel [23], Y Chr 46K (Y chromosome sites identified by the International Society of Genetic Genealogy ISOGG) and MitoTrio (probe set for three different mitochondrial genomes, including the revised Cambridge Reference Sequence (rCRS), Reconstructed Sapiens Reference Sequence (RSRS), and the Vindija Neanderthal sequence [24]). The protocol for MyBaits Expert Human Affinities Prime Plus kit includes two successive rounds of enrichment.

Sequencing

All three genomic libraries (both shotgun libraries and the ones enriched in the genomic regions of interest) were sequenced using the Illumina Hiseq 4000 platform (1 × 75 + 8 + 8 cycles) with single DNA reads.

Table 1. Sequencing statistics

Library	Number of input reads	Number of reads after filtration	Read average length for analysis	Number of mapped reads	After elimination of PCR duplicates	Coverage	Endogenous DNA, %	SNPs (for analysis)
KLD_SG (I)	1,473,546,011	1,469,259,287	78.02	65,025,843	46,813,163	1.17	3.18	321,229
KLD_CAP (II)	100,874,292	100,870,259	79.06	85,406,013	3,865,852	0.09	3.83	615,991
KLD_UDG (III)	58,364,547	58,329,170	63.95	52,565,836	4,392,304	0.08	7.53	690,148
I6268	*	*	*	*	1,091,304	0.81	4.02	372,480

Note. The study by Wang et al. [22] does not provide scores designated as *.

Bioinformatics analysis

To remove contaminating DNA reads from the sequencing data, we used the BBDuk software [25] included in the BBMap package (www.sourceforge.net/projects/bbmap/) and bacterial, fungal, plant, viral, and "others" databases (http://jgi.doe.gov/data-and-tools/bbtools/bb-tools-user-guide/). The output of the BBDuk tool was analyzed using the PALEOMIX pipeline (version 1.2.14) [26]. Sequencing adapters were trimmed using the Cutadapt v3.4 tool [27]. Sequences were aligned to the reference human genome sequence (hg19/GRCh37) using BWA (version 0.7.17) [28]. Aligned reads were filtered to provide the maximum mapping quality of 20 using the Samtools view v1.9 program [29]. Samtools v1.9 was used to index, sort, and remove duplicates (rmdup) [29].

PileupCaller (https://github.com/stschiff/sequenceTools) was used to call genotypes from the aligned reads using the "--randomHaploid" mode, which calls haploid genotypes by random selection of one high-quality base (phred base quality score $\geqslant$ 30) on the 1240K SNP panel (https://reich.hms.harvard.edu/).

Postmortem DNA damage patterns were analyzed using the MapDamage2 software [30], which offers a series of tools for imaging and modeling postmortem damage patterns observed in ancient samples. MapDamage2.0 also makes it possible to recalculate base quality scores in order to mitigate the impact of postmortem damage on further analysis.

We used the ADMIXTURE v.1.3.0 software [16] to determine the genetic clustering of a Bronze Age sample from the burial mound Klady (Caucasus) using each of the three methods of genomic library preparation, as well as other samples from the Allen Ancient DNA Resource (AADR) panel. SNPs were trimmed for sites with linkage disequilibrium using PLINK v1.9 [31]. The sliding window was 50 SNPs; the step was 5 SNPs; the r2 threshold was 0.2 (–indep-pairwise 50 5 0.2). There were 10 runs with random starting values for a number of clusters (K) in the range of 4–13; the run with the lowest cross-validation error was selected to plot the graph of population admixture.

RESULTS AND DISCUSSION

Characterization of genomic libraries

The contribution of postmortem DNA modifications in the distortion of the statistical analysis results was assessed using three genomic libraries prepared from an archeological bone sample from the burial mound Klady (Tsarskaya village): (I) shotgun library KLD_SG; (II) library enriched for the target regions KLD_CAP; and (III) library enriched for the target regions and treated with the mixture of UDG and endonuclease VIII, which removes uracil residues from DNA strands and converts the resulting abasic sites to single-nucleotide gaps (KLD_UDG). Thus, we expected to find C→T substitutions in libraries I and II. These substitutions have the potential to distort the results of the genetic analysis. They are artificially deleted in library III. However, this library is expected to contain shorter fragments, which is due to UDG-mediated introduction of single-strand breaks in the original DNA.

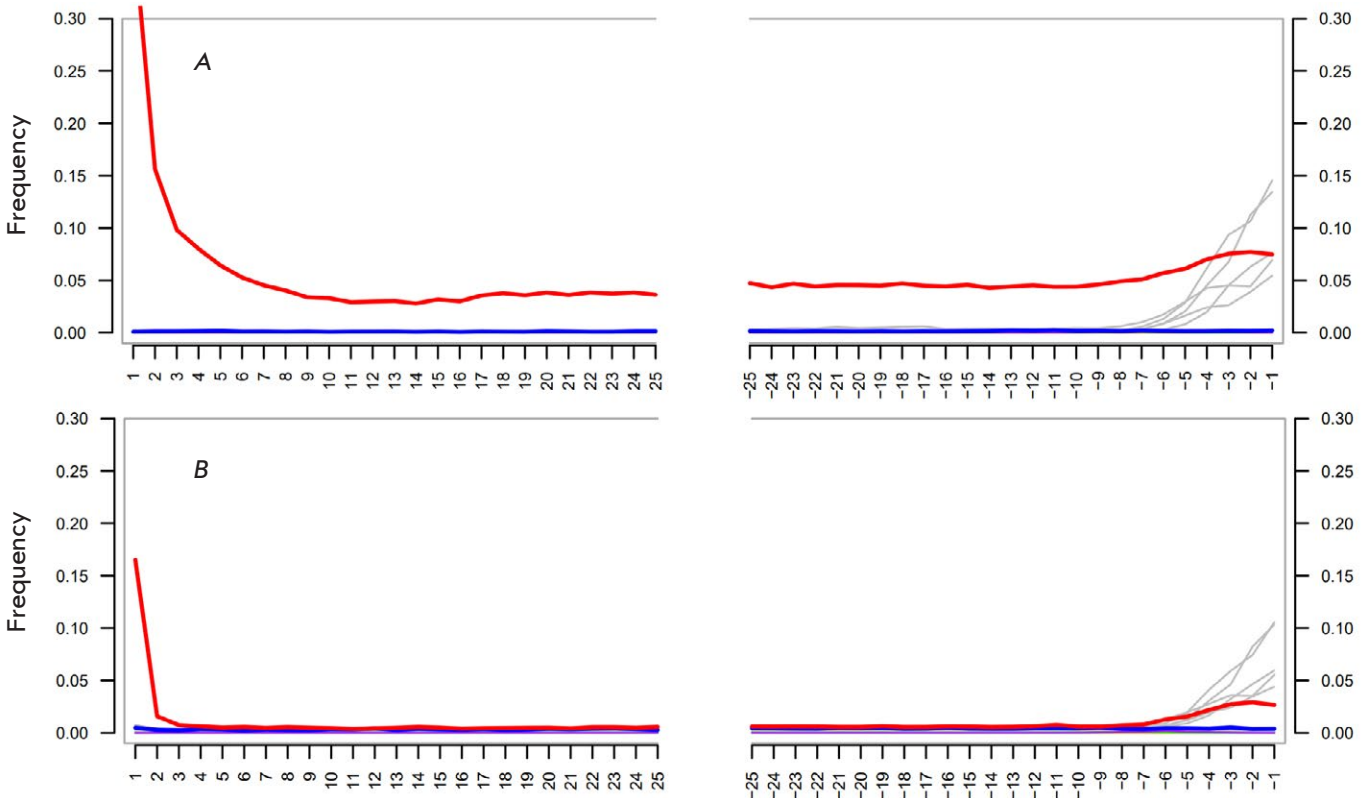

Fig. 1. Postmortem damage patterns of DNA libraries generated using MapDamage 2.0. (*A*) – Library without UDG treatment (KLD_SG), false C→T transitions are represented by the red line (the blue line denotes complementary G→A transitions) at 5′ (positive coordinates) and 3′ ends (negative coordinates) of the last 25 nucleotides. The presence of C→T substitutions after the second reading (right half of the graph) of the complementary strand is due to the particulars of the single-strand library preparation. The drop in the deamination level for the nucleotides -5 and -1 is due to A-tailing and the experimental protocol used. (*B*) – Damage pattern in the library partially treated with UDG (KLD_UDG) and obtained from the same extract

The total number of DNA reads generated for these three libraries varied from 58,364,547 to 1,473,546,011 per DNA library, while the fraction of endogenous DNA (i.e., reads mapped on human genome hg19/GRCh37) was 3.18–7.53% (*Table 1*).

It is important to note that evaluation of the number of SNPs suitable for analysis was conducted for the 1,2K panel used in the experiments with aDNA [32]. The number of SNPs determined for library I was almost two times lower than those in other libraries, despite the 10-fold excess of the number of reads compared to the libraries II and III.

The authenticity of the ancient DNA was determined using the MapDamage version 2.0 software, which utilizes postmortem damage patterns (*Fig. 1*). Taking into account that libraries treated with UDG retain a certain number of C→T substitutions at terminal 2 bp in mapped fragments, 2 bp should be deleted from both ends of the reads using trimBam from the bamUtil repository [33].

ADMIXTURE analysis

The results of the ADMIXTURE analysis for K = 7 for three libraries prepared in this study with the previously sequenced Novosvobodnaya cultural variant sample I6268 [22], to which the Klady burials belong, demonstrated additional components in non-UDG-treated samples (samples KLD_CAP and KLD_SG; green and purple components in *Fig. 2A*). Based on the identity of the bone sample, the false effect of postmortem aDNA modifications on the ADMIXTURE analysis results when preparing libraries without using UDG was hypothesized.

We proposed a bioinformatics approach for reducing the negative effect of postmortem modifications. The approach is based on masking all the SNPs asso-

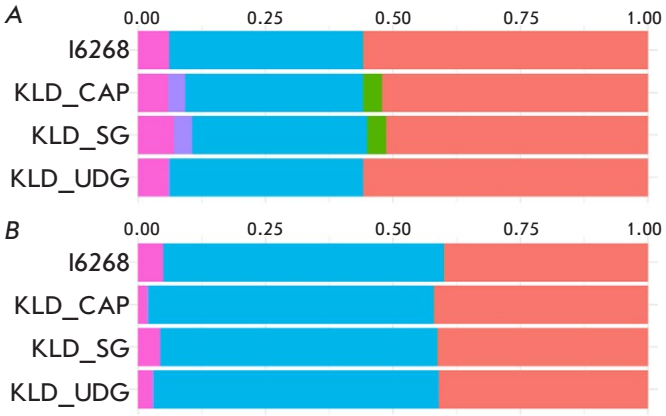

Fig. 2. ADMIXTURE analysis (K = 7) of a genome sequenced using various methodological approaches. (*A*) – Standard admixture analysis based on David Reich's 1240k SNP panel. Additional basic green and purple populations in the form of additional components caused by postmortem changes can be seen. (*B*) – Admixture analysis conducted for transversions only

ciated with transitions (C→T and G→A). After all transitions are eliminated, ADMIXTURE analysis results for libraries not treated with UDG correlate with the analysis results for UDG-treated libraries (*Fig. 2B*).

The fact that the proportional composition of ancestral populations changes due to the elimination of false green and purple components when analyzing transversions draws attention: the ratio of the blue component increases, while the ratios of red and pink components increase. This can be explained by the significant decrease in the number of SNPs at the input point for ADMIXTURE. Indeed, the number of transversions is approximately five times lower than the total number of SNPs. Detailed numerical parameters for all three libraries, KLD_CAP, KLD_SG, and I6268, are presented in *Fig. 3*.

Thus, the use of transversions in a ADMIXTURE analysis eliminates false positive signals in the form of ancestral populations that occur due to postmortal DNA modifications, but not real historical population upheavals. However, such a genetic reductionism should be used with caution, since a decrease in the total number of input data due to the exclusion of transitions can affect the reliability of the analysis results. Our empirical data show that the confidence threshold is reached when using < 30,000 SNPs.

Having analyzed all samples from the Allen Ancient DNA Resource (AADR) V44.3 panel (January 2021), we found a significant negative correlation (-0.5844) between the additional ADMIXTURE component and treatment with UDG in 3,284 European samples from the Allen Ancient DNA Resource (AADR) database (*Fig. 4*). It is also important to note that enrichment for target regions makes it possible to save resources during sequencing. Indeed, the generation of 58 million reads in the KLD_UDG library yields results on the structure of ancestral populations similar to those obtained using KLD_SG (~1,500 million reads).

F4 statistics

To study the role of sample preparation in population analysis data interpretation, we calculated the F4 statistics in the F4(Wang_3, Y;X, Yoruba) configuration. The Wang_3 population consists of three samples (I6267, I6266, and I6272) of the Novosvobodnaya cultural variant, to which sample I6268 belongs. Population X was used from a list proposed by archaeologists (provided on the left of the Y axis in *Fig. 5*) based on their historical hypotheses. The Yoruba population was used as the outgroup. Four SNP sets determined for KLD_SG, KLD_CAP, KLD_UDG, and I6268 were used as Y populations. As stated above, the intuitive meaning of non-zero significant statistics will indicate which population from the X list contributes the most both to the Wang_3 population in case of positive statistics and the experimental sample Y in case of negative statistics. Interpretation of the archaeological and historical meaning of the difference between population Wang_3 and the sample used for the preparation of the four test libraries is beyond the scope of this paper. Calculations were presented only as an example to demonstrate that reliable non-zero F4 statistics can be interpreted differently depending on the method of sample preparation.

Figure 5A presents F4 statistics data for all SNPs. For KLD_SG used as Y, all populations on the right were sorted in descending order of statistical value. When using the three other libraries as Y, the sorting order changes significantly. Furthermore, reliable statistical results with the absolute z score value > 3 change: 12, 9, 8, and 2 for KLD_SG, KLD_CAP, KLD_UDG, and I6268, respectively. Only one population from the X list, namely Russia_HG_Tyumen, is reliable for all four libraries from the Y list. However, when analyzing transversions, the sorting order for all four libraries changes compared to the original F4 sorting (Wang_3; KLD_SG; X; Yoruba). The number of reliable X populations is 7, 9, 4, and 1 for KLD_SG, KLD_CAP, KLD_UDG, and I6268, respectively. Furthermore, there is no X population that can be reliably determined using F4 statistics for all four libraries when using transversions. *Figure 5B* shows that even Russia_HG_Tyumen, which is the total significant population X in the analysis of all

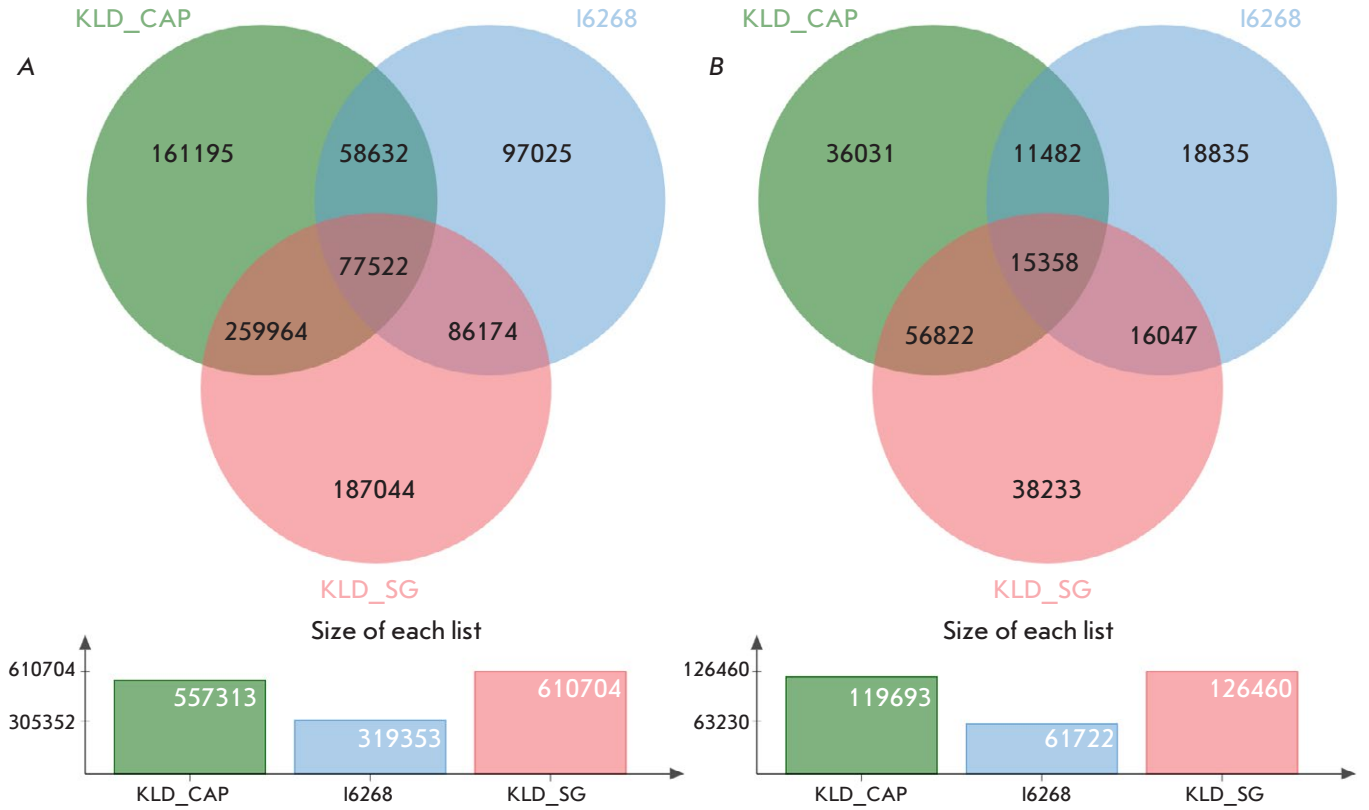

Fig. 3. Venn diagrams for the SNPs of the three libraries (KLD_CAP, KLD_SG, and I6268). The total number of SNPs for each library is shown below the charts. (*A*) – Transversions and transitions; (*B*) – Transversions only

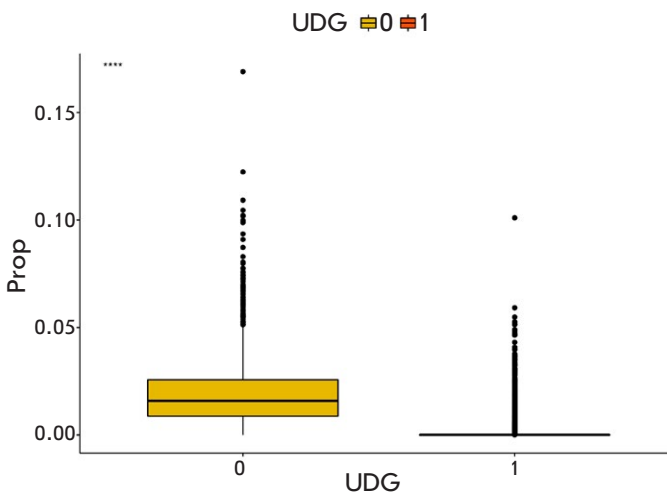

Fig. 4. Distribution of the relative content of additional components in the ADMIXTURE analysis between samples from the Allen Ancient DNA Resource V44.3 panel treated with UDG (1) - 2,376 samples and without treatment (0) - 908 samples. Prop – the proportion of admixtures

SNPs, is significant for only three libraries: KLD_SG, KLD_CAP, and KLD_UDG, but not I6268.

The conclusions of this part of the study are the following: F4 statistics is extremely sensitive to the number of input SNPs compared to ADMIXTURE, and it is important to use SNP sets obtained from uniformly prepared genomic libraries for F4 statistics. Otherwise, there is a chance of incorrect interpretation of reliable and positive absolute values of F4.

Genetic PCA maps

We also assessed the impact of sample preparation on PCA projections on the PC1–PC2 plane. A total of 253 ancient samples were used for PCA, which was first obtained for vectors of representatives of different modern Eurasian populations [34]. In order to simplify the interpretation, all ancient samples in *Fig. 6* are colored in light gray, except for the four libraries studied. Samples I6268 and KLD_UDG have a minimal difference in PC1–PC2 coordinates, while KLD_SG is shifted from them in the northeast direction. To obtain a detailed idea of how the four test libraries are grouped in the analysis of both all SNPs and transver-

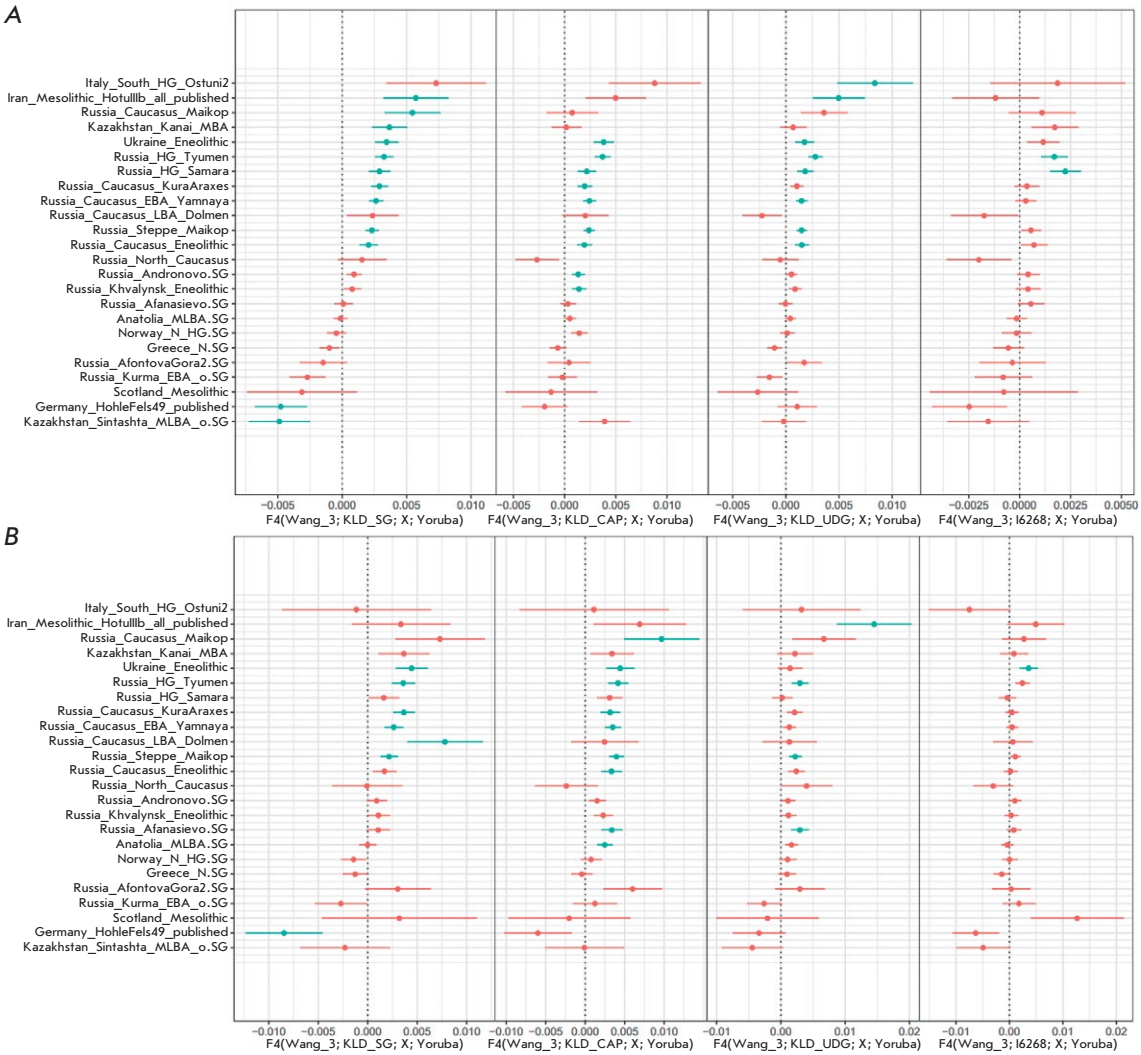

Fig. 5. F4 statistics in the F(Wang_3, Y;X, Yoruba) configuration. The reliable metrics for $|z| > 3$ are colored in blue. (*A*) – F4 calculated for all SNPs from the 1240k panel. (*B*) – F4 calculated for transversions only

sions only, the PCA analysis was conducted using only 17 samples related historically to the Novosvobodnaya cultural variant (*Fig.* 7). It is important to clarify that the new PCA with 17 samples is based on the generation of new PC1–PC2 vectors which differ from those in *Fig. 6*. The figure shows that it is impossible to reduce even two libraries to one point on the PC1–PC2 plane when using both all SNPs (*Fig. 7A*) and transversions only (*Fig. 7B*). We see that Fst for the group KLD_SG, KLD_CAP, KLD_UDG, and I6268 is 11% when using all SNPs and 19% when using transversions only. This indicates an increase in sample concordance when using transversions, which is illustrated in a slightly tighter grouping of the four test libraries in the PCA maps.

CONCLUSIONS

This works shows that modern statistical approaches, especially F4 statistics, are extremely sensitive to the method of sample preparation used for obtaining aDNA genomic libraries. We consider the selection of target regions with pre-treatment of aDNA with UDG as the optimal approach to generating genomic libraries. Even with this approach, the use of enrichment kits from different manufacturers can generate false positive results in the statistical analysis. In order to minimize the effect of the methodological approaches, we recommend increasing the expeditionary samples of bone remains of representatives of the same culture/population and, if possible, consolidating sample preparation in one study. ●

This work was financially supported by the Ministry of Education and Science of the Russian Federation, project No. 075-10-2020-116 (grant No. 13.1902.21.0023).

Fig. 6. Principal component analysis (PCA). Ancient samples were projected onto the vectors of modern samples that were used only to construct PCA and are not shown in this figure

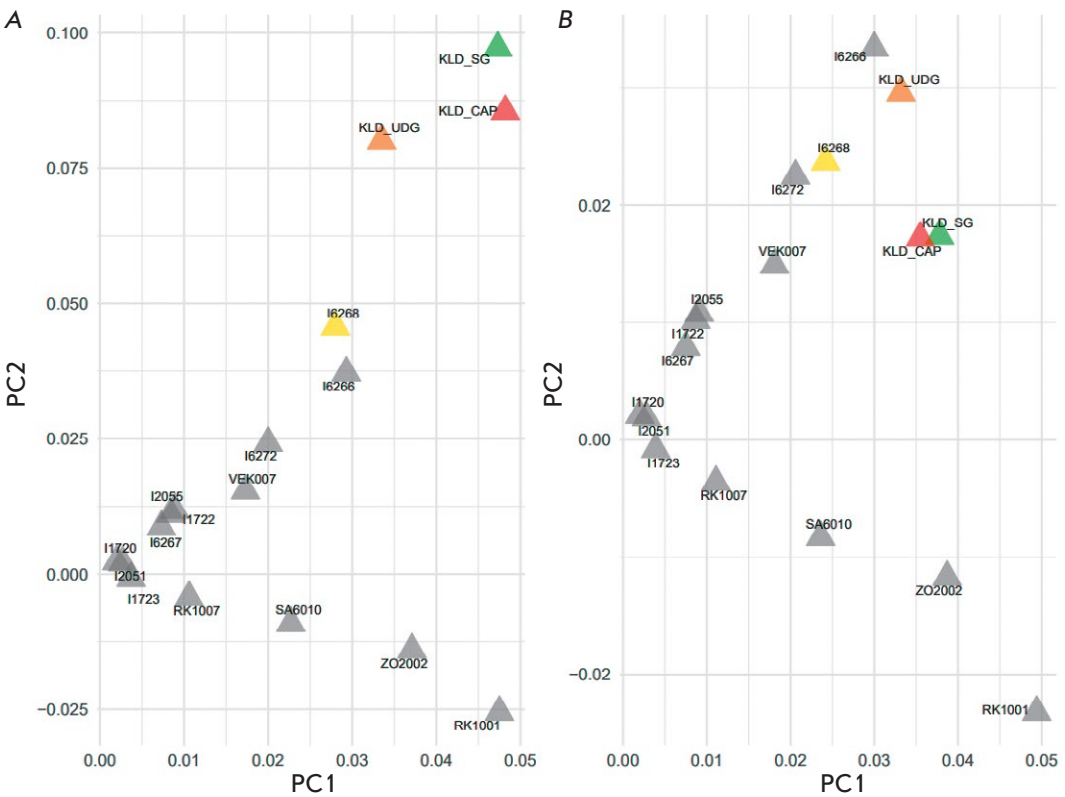

Fig. 7. Principal component analysis (PCA) for KLD_SG, KLD_CAP, KLD_UDG, I6268 (highlighted in color), and other Caucasian samples (shown in grey) calculated for all SNPs from the 1240k panel (*A*) and transversions only (*B*)

REFERENCES

1. Krause J., Fu Q., Good J.M., Viola B., Shunkov M.V., Derevianko A.P., Pääbo S. // Nature. 2010. V. 464. № 7290. P. 894–897.
2. Long J. // Hum. Biol. 2017. V. 89. № 4. P. 303–304.
3. Haak W., Lazaridis I., Patterson N., Rohland N., Mallick S., Llamas B., Brandt G., Nordenfelt S., Harney E., Stewardson K., et al. // Nature. 2015. V. 522. № 7555. P. 207–211.
4. Morgunova N. // Radiocarbon. 2013. V. 55. № 3–4. P. 1286–1296.
5. Grigorenko A.P., Borinskaya S.A., Yankovsky N.K., Rogaev E.I. // Acta Naturae. 2009. V. 1. № 3. P. 58–69.
6. Orlando L., Allaby R., Skoglund P., Der Sarkissian C., Stockhammer P.W., Ávila-Arcos M.C., Fu Q., Krause J., Willerslev E., Stone A.C., et al. // Nat. Rev. Methods Primers. 2021. V. 1. № 1. P. 14.
7. Sokolov A.S., Nedoluzhko A.V., Boulygina E.S., Tsygankova S.V., Sharko F.S., Gruzdeva N.M., Shishlov A.V., Kolpakova A.V., Rezepkin A.D., Skryabin K.G., et al. // J. Archaeol. Sci. 2016. V. 73. P. 138–144.
8. Erlikh V.R., Gak E.I., Kleshchenko A.A., Sharko F.S., Boulygina E.S., Tsygankova S.V., Slobodova N.V., Rastorguev S.M., Nedoluzhko A., Godizov G.L., et al. // J. Archaeol. Sci. Repts. 2021. V. 39. P. 103198.
9. Axelsson E., Willerslev E., Gilbert M.T.P., Nielsen R. // Mol. Biol. Evol. 2008. V. 25. № 10. P. 2181–2187.
10. Llamas B., Valverde G., Fehren-Schmitz L., Weyrich L.S., Cooper A., Haak W. // STAR: Sci. Technol. Archaeol. Res. 2017. V. 3. № 1. P. 1–14.
11. Rohland N., Mallick S., Mah M., Maier R., Patterson N., Reich D. // Genome Res. 2022. V. 32. № 11–12. P. 2068–2078.
12. Hellenthal G., Busby G.B.J., Band G., Wilson J.F., Capelli C., Falush D., Myers S. // Science. 2014. V. 343. № 6172. P. 747–751.
13. Gopalan S., Smith S.P., Korunes K., Hamid I., Ramachandran S., Goldberg A. // Philos. Trans. R. Soc. Lond. B Biol. Sci. 2022. V. 377. № 1852. P. 20200410.
14. Sjödin P., McKenna J., Jakobsson M. // Genetics. 2021. V. 217. № 4. iyab008.
15. Hubisz M.J., Falush D., Stephens M., Pritchard J.K. // Mol. Ecol. Resour. 2009. V. 9. № 5. P. 1322–1332.
16. Alexander D.H., Novembre J., Lange K. // Genome Res. 2009. V. 19. № 9. P. 1655–1664.
17. Zhou H., Alexander D., Lange K. // Stat. Comput. 2011. V. 21. № 2. P. 261–273.
18. Sinharay S. International encyclopedia of education. Amsterdam: Elsevier, 2010. P. 229–231.
19. Trifonov V.A., Shishlina N.I., Hommel P. // Brief Communications of the Institute of Archaeology. 2019. №. 257. P. 35–47.
20. Rohland N., Glocke I., Aximu-Petri A., Meyer M. // Nat. Protoc. 2018. V. 13. № 11. P. 2447–2461.
21. Gansauge M.-T., Meyer M. // Nat. Protoc. 2013. V. 8. № 4. P. 737–748.
22. Wang C.-C., Reinhold S., Kalmykov A., Wissgott A., Brandt G., Jeong C., Cheronet O., Ferry M., Harney E., Keating D., et al. // Nat. Commun. 2019. V. 10. № 1. P. 590.
23. Mathieson I., Lazaridis I., Rohland N., Mallick S., Patterson N., Roodenberg S.A., Harney E., Stewardson K., Fernandes D., Novak M., et al. // Nature. 2015. V. 528. № 7583. P. 499–503.
24. Green R.E., Malaspinas A.-S., Krause J., Briggs A.W., Johnson P.L.F., Uhler C., Meyer M., Good J.M., Maricic T., Stenzel U., et al. // Cell. 2008. V. 134. № 3. P. 416–426.
25. Bushnell B., Rood J., Singer E. // PLoS One. 2017. V. 12. № 10. P. e0185056.
26. Schubert M., Ermini L., Der Sarkissian C., Jónsson H., Ginolhac A., Schaefer R., Martin M.D., Fernández R., Kircher M., McCue M., et al. // Nat. Protoc. 2014. V. 9. № 5. P. 1056–1082.
27. Martin M. // EMBnet J. 2011. V. 17. № 1. P. 10.
28. Li H., Durbin R. // Bioinformatics. 2009. V. 25. № 14. P. 1754–1760.
29. Li H., Handsaker B., Wysoker A., Fennell T., Ruan J., Homer N., Marth G., Abecasis G., Durbin R., 1000 Genome Project Data Processing Subgroup. // Bioinformatics. 2009. V. 25. № 16. P. 2078–2079.
30. Jónsson H., Ginolhac A., Schubert M., Johnson P.L.F., Orlando L. // Bioinformatics. 2013. V. 29. № 13. P. 1682–1684.
31. Purcell S., Neale B., Todd-Brown K., Thomas L., Ferreira M.A.R., Bender D., Maller J., Sklar P., de Bakker P.I.W., Daly M.J., et al. // Am. J. Hum. Genet. 2007. V. 81. № 3. P. 559–575.
32. Allentoft M.E., Sikora M., Sjögren K.-G., Rasmussen S., Rasmussen M., Stenderup J., Damgaard P.B., Schroeder H., Ahlström T., Vinner L., et al. // Nature. 2015. V. 522. № 7555. P. 167–172.
33. Jun G., Wing M.K., Abecasis G.R., Kang H.M. // Genome Res. 2015. V. 25. № 6. P. 918–925.
34. Triska P., Chekanov N., Stepanov V., Khusnutdinova E.K., Kumar G.P.A., Akhmetova V., Babalyan K., Boulygina E., Kharkov V., Gubina M., et al. // BMC Genet. 2017. V. 18. № Suppl. 1. P. 110.

GENERAL RULES

Acta Naturae publishes experimental articles and reviews, as well as articles on topical issues, short reviews, and reports on the subjects of basic and applied life sciences and biotechnology.

The journal *Acta Naturae* is on the list of the leading periodicals of the Higher Attestation Commission of the Russian Ministry of Education and Science. The journal Acta Naturae is indexed in PubMed, Web of Science, Scopus and RCSI databases.

The editors of *Acta Naturae* ask of the authors that they follow certain guidelines listed below. Articles which fail to conform to these guidelines will be rejected without review. The editors will not consider articles whose results have already been published or are being considered by other publications.

The maximum length of a review, together with tables and references, cannot exceed 50,000 characters with spaces (approximately 30 pages, A4 format, 1.5 spacing, Times New Roman font, size 12) and cannot contain more than 16 figures.

Experimental articles should not exceed 30,000 symbols (approximately 15 pages in A4 format, including tables and references). They should contain no more than ten figures.

A short report must include the study's rationale, experimental material, and conclusions. A short report should not exceed 12,000 symbols (5–6 pages in A4 format including no more than 12 references). It should contain no more than three figures.

The manuscript and all necessary files should be uploaded to www.actanaturae.ru:

1) text in Word 2003 for Windows format;
2) the figures in TIFF format;
3) the text of the article and figures in one pdf file;
4) the article's title, the names and initials of the authors, the full name of the organizations, the abstract, keywords, abbreviations, figure captions, and Russian references should be translated to English;
5) the cover letter stating that the submitted manuscript has not been published elsewhere and is not under consideration for publication;
6) the license agreement (the agreement form can be downloaded from the website www.actanaturae.ru).

MANUSCRIPT FORMATTING

The manuscript should be formatted in the following manner:

- Article title. Bold font. The title should not be too long or too short and must be informative. The title should not exceed 100 characters. It should reflect the major result, the essence, and uniqueness of the work, names and initials of the authors.
- The corresponding author, who will also be working with the proofs, should be marked with a footnote *.
- Full name of the scientific organization and its departmental affiliation. If there are two or more scientific organizations involved, they should be linked by digital superscripts with the authors' names. Abstract. The structure of the abstract should be very clear and must reflect the following: it should introduce the reader to the main issue and describe the experimental approach, the possibility of practical use, and the possibility of further research in the field. The average length of an abstract is 20 lines (1,500 characters).
- Keywords (3 – 6). These should include the field of research, methods, experimental subject, and the specifics of the work. List of abbreviations.
- INTRODUCTION
- EXPERIMENTAL PROCEDURES
- RESULTS AND DISCUSSION
- CONCLUSION

  The organizations that funded the work should be listed at the end of this section with grant numbers in parenthesis.
- REFERENCES

  The in-text references should be in brackets, such as [1].

RECOMMENDATIONS ON THE TYPING AND FORMATTING OF THE TEXT

- We recommend the use of Microsoft Word 2003 for Windows text editing software.
- The Times New Roman font should be used. Standard font size is 12.
- The space between the lines is 1.5.
- Using more than one whole space between words is not recommended.
- We do not accept articles with automatic referencing; automatic word hyphenation; or automatic prohibition of hyphenation, listing, automatic indentation, etc.
- We recommend that tables be created using Word software options (Table → Insert Table) or MS Excel. Tables that were created manually (using lots of spaces without boxes) cannot be accepted.
- Initials and last names should always be separated by a whole space; for example, A. A. Ivanov.
- Throughout the text, all dates should appear in the "day.month.year" format, for example 02.05.1991, 26.12.1874, etc.
- There should be no periods after the title of the article, the authors' names, headings and subheadings, figure captions, units (s – second, g – gram, min – minute, h – hour, d – day, deg – degree).
- Periods should be used after footnotes (including those in tables), table comments, abstracts, and abbreviations (mon. – months, y. – years, m. temp. – melting temperature); however, they should not be used in subscripted indexes (T_m – melting temperature; $T_{p.t}$ – temperature of phase transition). One exception is mln – million, which should be used without a period.
- Decimal numbers should always contain a period and not a comma (0.25 and not 0,25).
- The hyphen ("-") is surrounded by two whole spaces, while the "minus," "interval," or "chemical bond" symbols do not require a space.
- The only symbol used for multiplication is "×"; the "×" symbol can only be used if it has a number to its

right. The "·" symbol is used for denoting complex compounds in chemical formulas and also noncovalent complexes (such as DNA·RNA, etc.).
- Formulas must use the letter of the Latin and Greek alphabets.
- Latin genera and species' names should be in italics, while the taxa of higher orders should be in regular font.
- Gene names (except for yeast genes) should be italicized, while names of proteins should be in regular font.
- Names of nucleotides (A, T, G, C, U), amino acids (Arg, Ile, Val, etc.), and phosphonucleotides (ATP, AMP, etc.) should be written with Latin letters in regular font.
- Numeration of bases in nucleic acids and amino acid residues should not be hyphenated (T34, Ala89).
- When choosing units of measurement, SI units are to be used.
- Molecular mass should be in Daltons (Da, KDa, MDa).
- The number of nucleotide pairs should be abbreviated (bp, kbp).
- The number of amino acids should be abbreviated to aa.
- Biochemical terms, such as the names of enzymes, should conform to IUPAC standards.
- The number of term and name abbreviations in the text should be kept to a minimum.
- Repeating the same data in the text, tables, and graphs is not allowed.

GUIDENESS FOR ILLUSTRATIONS

- Figures should be supplied in separate files. Only TIFF is accepted.
- Figures should have a resolution of no less than 300 dpi for color and half-tone images and no less than 600 dpi.
- Files should not have any additional layers.

REVIEW AND PREPARATION OF THE MANUSCRIPT FOR PRINT AND PUBLICATION

Articles are published on a first-come, first-served basis. The members of the editorial board have the right to recommend the expedited publishing of articles which are deemed to be a priority and have received good reviews.

Articles which have been received by the editorial board are assessed by the board members and then sent for external review, if needed. The choice of reviewers is up to the editorial board. The manuscript is sent on to reviewers who are experts in this field of research, and the editorial board makes its decisions based on the reviews of these experts. The article may be accepted as is, sent back for improvements, or rejected.

The editorial board can decide to reject an article if it does not conform to the guidelines set above.

The return of an article to the authors for improvement does not mean that the article has been accepted for publication. After the revised text has been received, a decision is made by the editorial board. The author must return the improved text, together with the responses to all comments. The date of acceptance is the day on which the final version of the article was received by the publisher.

A revised manuscript must be sent back to the publisher a week after the authors have received the comments; if not, the article is considered a resubmission.

E-mail is used at all the stages of communication between the author, editors, publishers, and reviewers, so it is of vital importance that the authors monitor the address that they list in the article and inform the publisher of any changes in due time.

After the layout for the relevant issue of the journal is ready, the publisher sends out PDF files to the authors for a final review.

Changes other than simple corrections in the text, figures, or tables are not allowed at the final review stage. If this is necessary, the issue is resolved by the editorial board.

FORMAT OF REFERENCES

The journal uses a numeric reference system, which means that references are denoted as numbers in the text (in brackets) which refer to the number in the reference list.

For books: the last name and initials of the author, full title of the book, location of publisher, publisher, year in which the work was published, and the volume or issue and the number of pages in the book.

For periodicals: the last name and initials of the author, title of the journal, year in which the work was published, volume, issue, first and last page of the article. Must specify the name of the first 10 authors. Ross M.T., Grafham D.V., Coffey A.J., Scherer S., McLay K., Muzny D., Platzer M., Howell G.R., Burrows C., Bird C.P., et al. // Nature. 2005. V. 434. № 7031. P. 325–337.

References to books which have Russian translations should be accompanied with references to the original material listing the required data.

References to doctoral thesis abstracts must include the last name and initials of the author, the title of the thesis, the location in which the work was performed, and the year of completion.

References to patents must include the last names and initials of the authors, the type of the patent document (the author's rights or patent), the patent number, the name of the country that issued the document, the international invention classification index, and the year of patent issue.

The list of references should be on a separate page. The tables should be on a separate page, and figure captions should also be on a separate page.

The following e-mail addresses can be used to contact the editorial staff: actanaturae@gmail.com, tel.: (495) 727-38-60.